NUMERICAL TOOLS FOR FRACTURE MECHANICS PREDICTION OF PASSIVELY AND ACTIVELY COUPLED STRUCTURAL SYSTEMS

Department of Mechanical and Aerospace Engineering
Doctorate of Mechanics
XXVI Cycle (2011-2014)

Settore Scientifico-Disciplinare
ING-IND/14

Ph.D. Thesis

NUMERICAL TOOLS FOR FRACTURE MECHANICS PREDICTION OF PASSIVELY AND ACTIVELY COUPLED STRUCTURAL SYSTEMS

Author
Mehdi Mohammadzadeh Sari
matr. 179472

Tutor
Prof. Eugenio Brusa

Co-Tutor
Prof. Naman Recho

Coordinator
Prof. Luigi Garibaldi

February 2014

AKNOWLEDGEMENT

This is the end of my journey in obtaining my PhD. I have not traveled in a vacuum in this journey. This thesis has been seen through to completion with the support and encouragement of numbers people including my well wishers, my friends and colleagues. At the end of my thesis I would like to thank all those people who made this thesis possible and an unforgettable experience for me.

First of all, I would like to thank to my PhD advisors, Professor Eugenio Brusa, for supporting me during these past three years and sharing his great knowledge and experience with me. Without his supervision and constant help this dissertation would not have been possible. Under his guidance I successfully overcame many difficulties and learned a lot. It has been an honor to be his first PhD student.

I would also thank to Professor Naman Recho for his guidance and suggestions as my co-advisers during this project in the EPF School of Engineering, France and Eng. Marco Faraldi for helping me to complete a part of my thesis.

I will forever be thankful to Mr. Mauro Parodi, Technical Manager of Exemplar Srl, for his helping and teaching to complete the final goal of my thesis, he always followed my research work even after our contract and it was so valuable for me.

My times at Torino was made enjoyable in large part due to the many friends that became a part of my life. I am grateful for time spent with the.

Least but not last, I would like to pay high regards to my father, mother, sister and who I love for their sincere encouragement and inspiration thorough my research work and lifting me uphill this phase of life. I owe everything to them.

Table of Contents

LIST OF FIGURES

LIST OF TABLES

INTRODUCTION

This study is aimed at developing a numerical tool to predict the fracture mechanics of passively and actively coupled structural systems. These definitions are related to the wide recently growing up in the technology of composite materials equipped with functional layers made of smart materials such as piezoelectric, electrostrictive, magnetostrictive and others. Their main function is providing a local conversion of energy for several goals. Very often they are used as a sensor to monitor the static and dynamic behaviour of structures. In active control of shape and of vibration energy is supplied to the transducer, which applies a suitable force or moment to the structure. Moreover, quite recently conversion is activated to store the energy by using some effect like vibration or temperature increasing, which could be dissipated otherwise.

A critical issue of design of those systems is prevention of damage propagation, in case of cracking. This task can be performed in both the case of PASSIVE COUPLING in which the smart layer is only connecting the energy associated to the deformation of the structure and of ACTIVE COUPLING in which an external source of energy is connected to the smart layer and it converts this power into a suitable actuation of the mechanical system.

To predict the crack propagation inside the material there are analytical and numerical approaches already assessed in the literature for classical applications where functional materials are not yet used. Among analytical approaches, there are many procedures, which require huge mathematical solutions and are effective in case of simple structures, while their application to some complicated geometries is rather different because of the lack of formulations suitable for each relevant and specific case. Numerical approaches were already widely used in fracture mechanics and in several applications, nevertheless literature show a

lack of procedures applicable to the smart materials, such as the piezoceramics, which can be used for both the PASSIVELY COUPLED SYSTEMS (energy harvester and sensor) and the ACTIVE DEVICES (actuators).

A main goal of this study is developing a numerical tool able to predict the mechanical behaviour of smart structures equipped with piezoelectric layers in case of crack damage. It could be used in the design activity for a consistent prediction of the smart system reliability. A comprehensive approach is described. As it is used in fracture mechanics the smart material behaviour is described by calculating the so-called Stress Intensity Factor (SIF), the J-integral and the crack propagation in fracture of the electromechanical coupling, in passive and active configuration.

For this investigation the commercial software ABAQUS was selected. It implements the Finite Element Method and is currently providing a dedicated tool for the analysis of the piezoelectric phenomenon as well as a very efficient section for fracture mechanics. A relevant obstacle to an easy development of this investigation was the absence of a procedure in the ABAQUS code to make cooperating the two tools above described, dealing with piezoelectricity and fracture, respectively. A relevant activity of this thesis was therefore dedicated to a programming code, which could perform the whole investigation, by analyzing the crack propagation inside the piezoelectric layers, when the electromechanical coupling is fully considered.

The final goal was reached in some steps. At the beginning modeling activity just considered the pure metal. Single and mixed modes of crack propagation were analyzed to understand how the code works in case of both static and dynamic analysis. The AISI steel 4340 was used in this first activity because it is widely used in mechanical engineering and several references were available to validate the numerical prediction performed by means of the ABAQUS code. After that some preliminary benchmarking among analytical, numerical and experimental results available in the literature to validate the models, a deeper validation was performed in case of welded joints in tight cooperation together with the EPF School of Engineering in Sceaux (France), where several tests were completed.

In the next step, the case of composite material with ceramic and metal is considered, to investigate the behaviour of crack inside the two materials, which have different fracture toughness. In particular, the speed of crack in its propagation inside the composite material and the direction followed were calculated. The Aluminum Nitride is used as ceramic metal. This preliminary section of the thesis allows describing the main tools available in the literature for fracture mechanics, How they could be implemented inside the ABAQUS code, a preliminary procedure was assumed and validated in case of a single material, with double layers of different materials, to predict the effect of static loads and dynamic excitation.

In a second section of the thesis the case of piezoceramic materials was deeply investigated, a preliminary description of some piezoceramics widely used in industrial application was documented. A collection of typical values of mechanical and electrical properties was performed to allow comparing the performance of some materials. After this introduction, which revealed that PZT-4 is still the material most analyzed and known in terms of characterization, the fracture mechanics of piezoceramic was analyzed.

Since the ABAQUS code cannot perform the fracture analysis in case of smart materials because its not able to connect the electro-mechanical properties of the piezoceramic to the tool used for fracture analysis the ISIGHT program was used to connect these two tools inside the ABAQUS together to perform the required analysis. Programming the ABAQUS code in case of coupled numerical solution to predict simultaneously the behaviour of piezoelectric material under the effect of electro mechanical coupling and the crack propagation inside the material was rather difficult and some procedures need to be assessed. In particular calculation of Stress Intensity factor and J-integral was performed by resorting to a dedicated tool, based on a suitable loop between the fracture analysis module and the piezoelectric solution task, then a new loop was implemented to analysis the crack propagation.

In case of calculation of SIF and J-integral the solution could be found as a result of a sequence of steps and by separating the pure mechanical analysis from the prediction of electrical behaviour. It is known that if small increments of either loading condition or displacements are applied to find the solution, it is possible for each value of force predicting

the solution in terms of displacements to be inputted into the electrical analysis to predict the voltage and charge distribution inside and across the piezoelectric material and vise versa. Therefore SIF and J-integral could be obtained by solving separately and in sequence the two related domains. In case of crack propagation this sequential approach can be even used but it is also possible resorting to a piezoelectric-thermal analogy by assuming that a thermal gradient is equivalent to the voltage distribution and properties of materials converted into equivalent thermo-mechanical coefficient.

As a relevant result of this work a new tool for the coupled analysis of electro mechanical piezoelectric structures for fracture mechanics was assumed and preliminarily tested. Numerical results revealed that a very interesting phenomenon of “crack regression” is exhibited by the piezoelectric material as its J-integral may decrease after reaching a maximum value as far as its analyzed as a function of the crack length and of voltage.

Future actions include a deeper experimental activity to confirm some interesting conclusions here drawn and a straight application of these design tools to vibration energy harvester with piezoelectric materials.

Part One

The State of the Arts on Fracture Mechanics, tools and codes

CHAPTER 1

BASIC CONCEPTS OF FRACTURE MECHANICS

1 Fracture mechanics

1.1 Nucleation of damage in structures

Static or dynamic loads may induce in structural components made by brittle material a rupture and crack propagates fairly fast. In case of ductile material rupture follows a first yielding, being associated to plastic strain [1]. In several applications damage is induced by dynamic loads, thus making the structure undergoing the so – called fatigue phenomenon. If fatigue is dominating in the failure process it can be recognized that are two steps, for damage; a preliminary nucleation of crack on the surface, being associated to same local phenomena of band slips and to plastic behavior, these cracks propagate through the cross section of the mechanical component and induce a final brittle rupture of the structure. Nucleation is controlled entirely by local stresses around slip or twin bands [2]. Crack growth is governed both by the applied stress acting on the solid and by local stress. A critical issue of design is crack propagation, i.e. the number of loading cycles to reach the rupture of the mechanical components and the related lifetime. It depends on the size and shape of the structure and the external loading. More generally, for a given material under a

given load, there will be a rate of crack nucleation per unit volume and per unit time and a certain speed in propagation. Therefore prediction is never easy. Cracks nucleate where are in-homogeneities of material such as grain boundaries, surface heterogeneities, pre-existing micro cracks and dislocation tangles [3]. These heterogeneities usually evolve in time being associated to fatigue, work hardening, electro migration and void formation.

1.2 Fracture modes

Once the crack is nucleated on the surface of the mechanical structure its growth occurs in presence of a very high gradiant associated stress field. Three basic modes for crack growth are defined in the literature and are shown in Fig 1.1. Mode I is the “opening” or “tensile mode”, where the crack faces separate symmetrically with respect to the x_1-x_2 and x_1-x_3 planes. In Mode II, the “sliding” or in “plane shearing” mode, the crack faces slide each other symmetrically about the x_1-x_2 plane but anti-symmetrically with respect to the x_1-x_3 plane. In the “tearing” or “anti-plane” mode, Mode III, the crack faces also slide each other but anti symmetrically with respect to the x_1-x_2 and x_1-x_3 planes. In several practical cases, loads excite simultaneously two modes and make the crack propagation depending on a so-called “mixed-mode fracture mechanism” [4].

It can be remarked that as crack propagates a certain amount of energy is released because of the rupture of the internal ligaments of the material. This energy released has a rate, being termed G_I, G_{II}, and G_{III} respectively for the three modes. In mixed-mode problems the energy release rates of different contributing modes are usually added to obtain the total energy release rate [5].

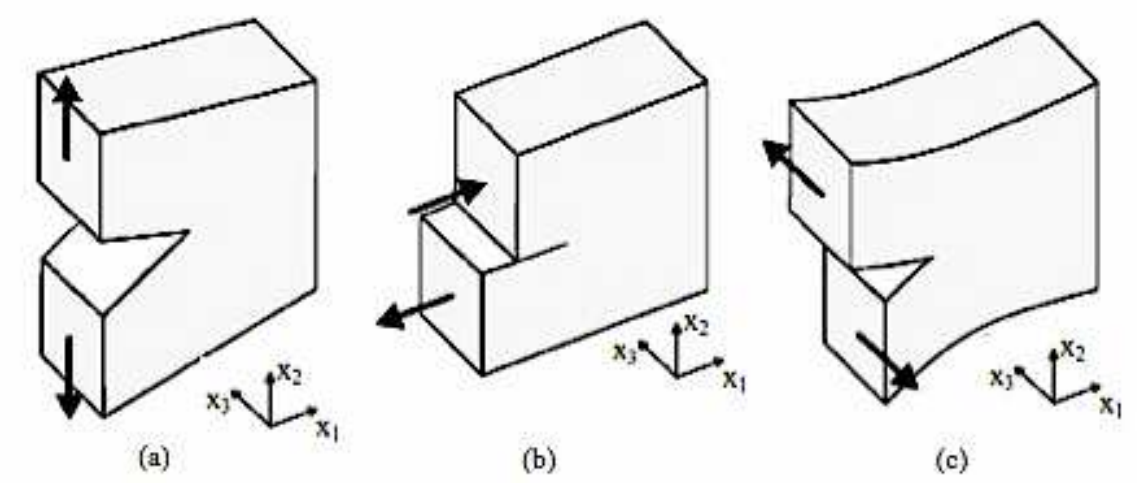

Fig. 1.1: Three basic loading modes for a cracked body: (a) Mode I, “opening mode”; (b) Mode II, “sliding mode”; (c) Mode III, “tearing mode”. [6]

1.3 Linear Elastic (LEFM) and Elastic Plastic (EPFM) Fracture Mechanics

Literature proposed some analytical tools to predict the fracture mechanics, which are based on the assumption of the linear elastic behaviour of material. In the so-called “Linear Elastic Fracture Mechanics (LEFM)”, prediction of crack growth is based on the energy balance. Griffith states “crack growth will occur, when there is enough energy available to generate new crack surface.” The “energy release rate” is an essential quantity in energy balance criteria. The resulting crack growth criterion is referred to as being “global”, because a rather large volume of material is considered. The crack growth criterion can also be based on the stress state at the crack tip. This stress field can be determined in several cases through an analytical approach. It is characterized by the definition of the “stress intensity factor” (In the following simply SIF) [7].

The resulting crack growth criterion is referred to as “local”, because attention is focused on a small material volume just around the crack tip. Assumption of linear elastic material behavior leads to infinite stresses at the crack tip. In reality, this is obviously not possible, because in ductile materials plastic deformation will occur in the crack tip region. Using

some yield criteria (Von Mises, Tresca), the crack tip plastic zone can be determined. When this zone is small enough (Small Scale Yielding, SSY), LEFM concepts can be used. Fig. 1.2

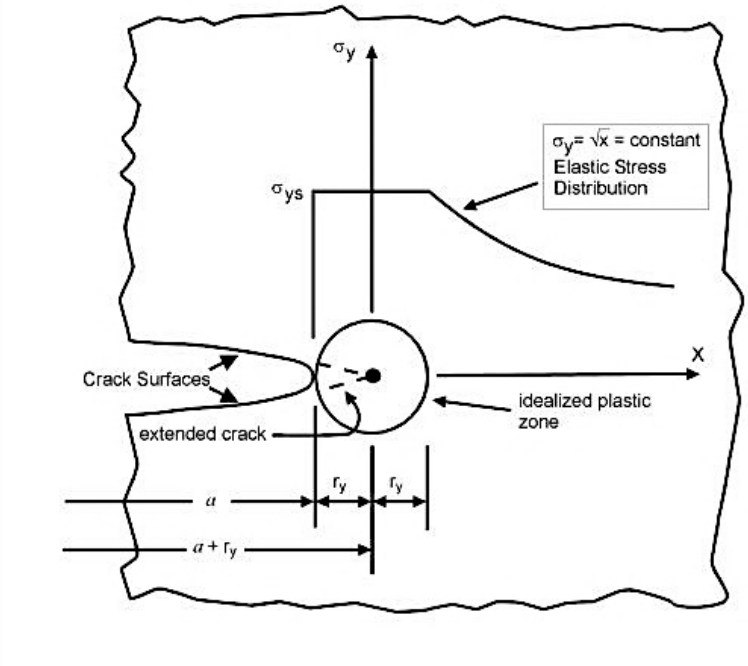

Fig 1.2: Plastic strain zone at the crack tip [8]

When the global stress-strain response of the body is linear and elastic (LEFM), the elastic energy release rate, G, and the stress intensity factor in the literature defined as K can be used for characterizing cracks in structures.

To make clear to the Reader the approach proposed by the LEFM, the following steps are usually performed:

1. The critical stress intensity factors that cause fracture for the material are first measured, for the three modes (K_{CI}, K_{CII}, K_{CIII}).
2. Size and location of cracks in the structure or component are detected.
3. The stress intensity factors for the cracks in the structure or component are calculated for the foreseen loading conditions, these are compared to the strength of the material.

In the elastic-plastic fracture mechanics (EPFM) also called “yielding fracture mechanics” (YFM), the fracture characterizing parameters are the “J-integral” and the “crack-tip-opening displacement”, CTOD. Due to finite strength of materials, there is always a small damaged

zone around the crack tip. For metals, this damaged zone is referred to as the “crack tip plastic zone”. If the size of the plastic zone is small enough that it can be contained within the K-dominant region, we may use K and G as the LEFM parameters. This condition is also referred to as the “small-scale-yielding condition” (SSY) [9]. On the other hand, if this zone is larger than the K-dominant region, then the linear elastic assumptions are no more valid, i.e., LEFM is not applicable and nonlinear models must be used. Fig. 1.3 shows three different situations regarding the spread of crack tip plastic zone. The first one represents the SSY condition. The second one shows the situation when the crack tip plastic zone is large enough to cause some nonlinearity in the overall response of the component. However, if this nonlinearity is not very significant, it can be handled with a non-linear elastic model, for which a non-linear-elastic energy release rate is expressed as J (usually known as the J-Integral) is computed. However, there is a limit to the validity of J-integral with regard to the size of the plastic zone compared to the J-dominant region. The energy release rate is no more constant in case of elastic plastic behaviour since it depends on the contour which is selected for the definition of J-integral.

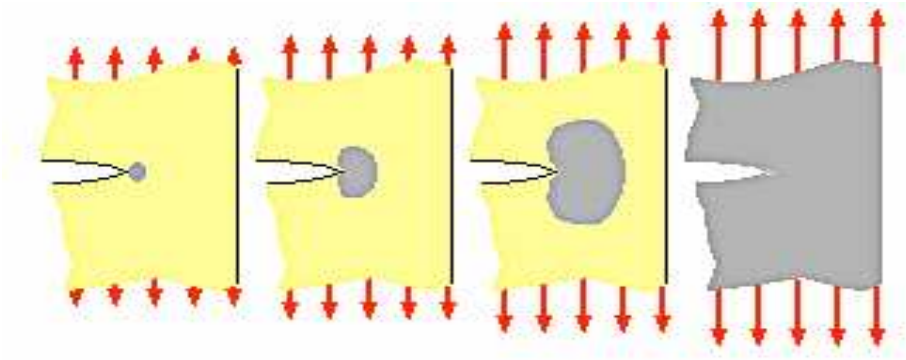

Fig 1.3: From left, a) Linear Elastic, b) Elastic-Plastic, c) Fully Plastic, d) Overall Plasticity [10]

For situations where the crack tip plasticity is so widespread that even plastic ligaments may form within the component (Fig. 1.3 c) the appropriate parameter would be the “crack-tip opening displacement” (CTOD). Finally, when the loading causes overall plastic deformation even in presence of cracks (Fig. 1.3 d), the failure mode is “plastic collapse” more than fracture.

1.4 Stress and strain distribution around the crack tip

Predicting the size of plastic region is crucial, therefore many authors worked in this field such as Irwin and Dugdale. Their estimations of the crack-tip-plastic-zone size assume that deformation is uniaxial and plastic. Nevertheless, the actual state of stress at the crack tip region is triaxial. In order to investigate how this 2D state of stress can develop a roll of material, the interior of the specimen at the crack tip, as depicted in Fig. 1.4, is usually considered [11].

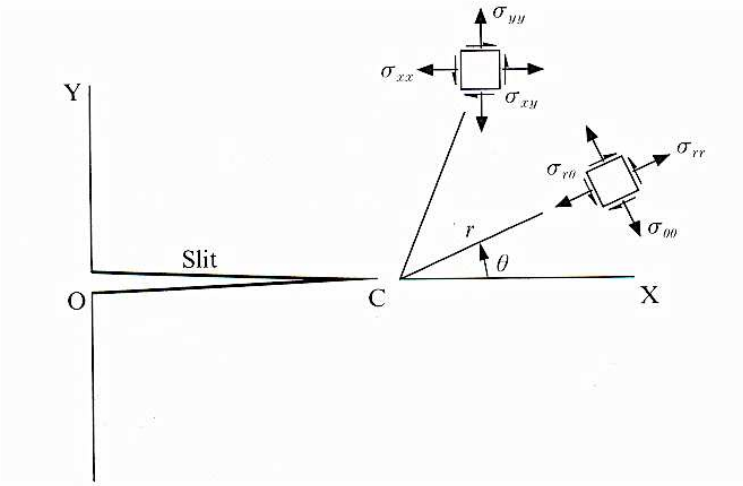

Fig 1.4: Stress distribution around the crack tip [12]

Due to very high stresses in this region, material undergoes a large extension along the x_2 direction and also tends to contract along the x and z directions to maintain the condition of constant volume required by plastic deformation.

$$\varepsilon_{xx} + \varepsilon_{yy} + \varepsilon_{zz} = 0 \tag{1.1}$$

However, material in this zone is part of a larger mass, which stress undergoes lower without contraction. As a result, tensile stresses develop in the other two directions, as shown in Fig. 1.5. Thus, in the interior of the specimen, the material in the crack tip region experiences a state of plane strain, being due to the constraints imposed by the surrounding material.

However, at the surfaces of the specimen there can be no stress in the x_3 direction and a state of plane stress exists. Due to the above motivations, it is clear that a very precise determination of the shape and size of the plastic zone is rather difficult, because behaviour is locally associated to a plane stress or a plane strain condition.

Plane Stress/Plane Strain Transition

According to the literature [13] the plane stress is defined to be a state of stress in which the normal stress and the shear stresses directed perpendicular to the plane are assumed to be zero and plane strain is defined to be a state of strain in which the strain normal to the x-y plane □z and the shear strains □xz and □yz are assumed to be zero (Fig 1.5).

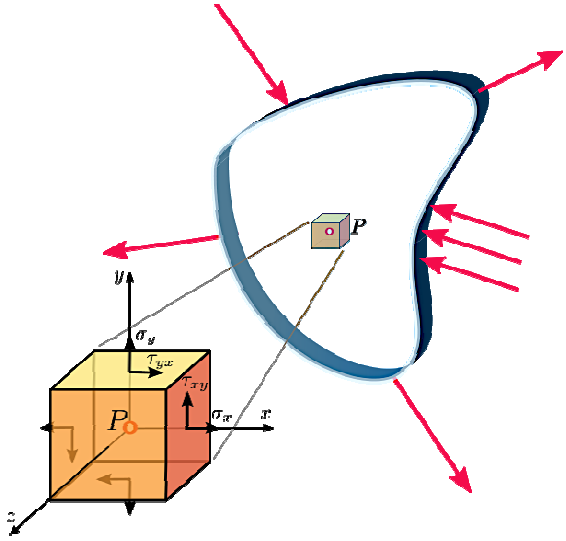

Fig 1.5: Plane stress state in a continuum [14]

As the above Fig presents, for the plane stress and plane strain:

$\sigma_{xx}, \sigma_{yy}, \tau_{xy} \neq 0$

$\sigma_{zz} = \tau_{zx} = \tau_{zy} = 0$ (plane stress)

$\varepsilon_{xx}, \varepsilon_{yy}, \tau_{xy} \neq 0$

$\varepsilon_{zz} = \tau_{yx} = \gamma_{zy} = 0$ (plane strain) (1.2)

In case of principal reference frames the two assumptions simply define that:

$\sigma_1, \sigma_2 \neq 0$ $\varepsilon_1, \varepsilon_2 \neq 0$

$\sigma_3 = 0$ (plane stress) $\varepsilon_3 = 0$ (plane strain) (1.3)

For a given crack tip, it can be found that plastic region around the tip is larger on the surface, where the state of plane stress holds and is smaller in the interior of the component, where plane strain occurs. (Fig 1.6). This phenomenon has very important implications for toughness evaluation, i.e., different toughness values may be measured depending on the dimensions of the specimens.

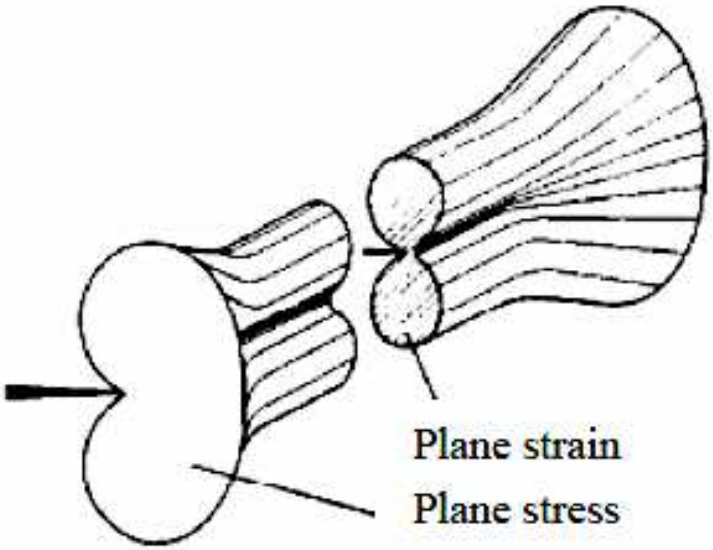

Fig 1.6: The different plastic zone size in plane strain and plane stress [15]

It has long been observed that thicker components are less prone to be cracked. This effect can be attributed to the size of crack tip plastic zone relative to the thickness. In thin components, the plastic zone is large compared to the thickness, whereas in thick components it is very small. In general, fractures of thick specimens are more brittle in appearance (being flat with no evidence of ductility) while the fractures of thin specimen often show 45° shear bands over parts of the fracture surface.

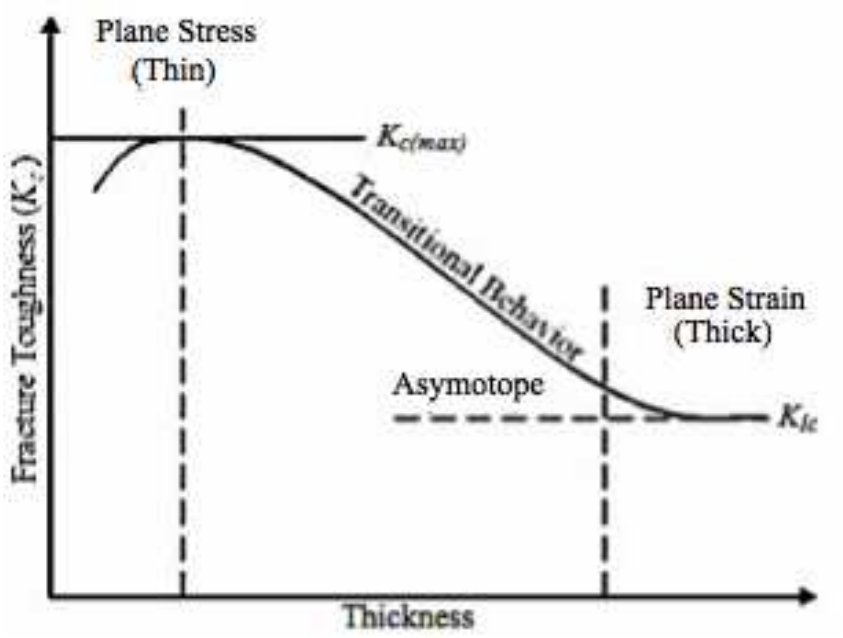

Fig 1.7: Difference in toughness across the thickness of specimen [8]

Moreover, as Fig. 1.7 shows in the case of plane stress the planes of maximum shear stress are located at angles $\propto = 45°$ from the directions of σ_1 and σ_3 as well as the Mohr's circle can describe. Although in the plane strain condition σ_1 and σ_2 have the same magnitude as in plane stress, the third principal stress is $\sigma_3 = \nu\,(\sigma_1 + \sigma_2)$:

Plane stress $\sigma_3 = 0$

$$\varepsilon_1 = 1/E\,(\sigma_1 - \nu\sigma_2 - \nu\sigma_3) \quad (1.4)$$

$$\varepsilon_2 = 1/E\,(\sigma_2 - \nu\sigma_1 - \nu\sigma_3) \quad (1.5)$$

Plane strain $\varepsilon_3 = 0$

$$\varepsilon_3 = 1/E\,(\sigma_3 - \nu\sigma_2 - \nu\sigma_1) = 0,\ \sigma_3 = \nu\,(\sigma_1 + \sigma_2) \quad (1.6)$$

1.5 Stable and unstable propagation of crack

Very often a crack already exists in the mechanical component before it goes into service, therefore the issue of design is predicting how the fatigue failure process will proceed with the incremental crack growth and when the final fracture will occur. Most fatigue failures are in the low stress region (much less than the yield stress) where the LEFM is likely to be valid. Hence, the LEFM principles can be applied to predict incremental fatigue crack growth. In fact, extensive fatigue tests on a wide variety of materials show that the SIF is a much more effective parameter in describing fatigue propagation than the stress amplitude [16]. The key point of these tests is that the rate of crack propagation, measured in terms of incremental crack growth per cycle of loading, is primarily a function of the range of crack tip stress intensity [17]:

$$da/dN = f(\Delta K) \tag{1.7}$$

The most widely used expression, proposed by Paris, is:

$$da/dN = C(\Delta K)^n \tag{1.8}$$

In which C and m are constant coefficients dependent on the material properties and are obtained from experiments. The standard methods for fatigue crack growth tests can be found in ASTM E647. The most commonly used specimen in fatigue crack propagation studies is the (CT) or compact tension specimen (see Fig 1.8).

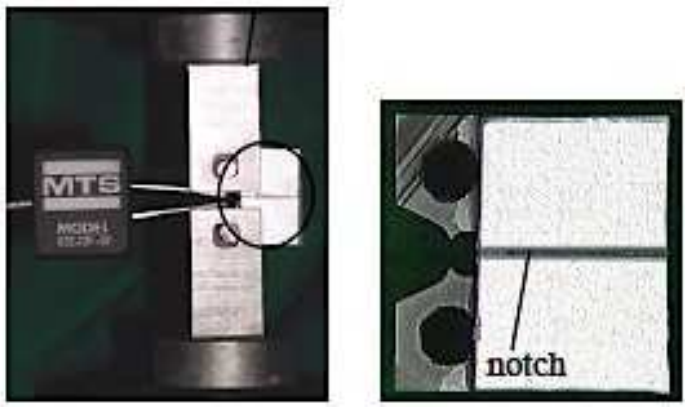

Fig 1.8: The (CT) or compact tension specimen in fatigue crack propagation [18]

As Fig. 1.9 shows a typical crack-growth-rate versus stress-intensity-range diagram includes three regions of different behavior [19]:

1. The “threshold region” is attributed to very low levels of ΔK, where the crack does not propagate. The “threshold region” is strongly influenced by the mean stress.
2. The “stable propagation region” where the crack grows incrementally according to the Paris law.
3. The “final unstable region” where the crack propagates more rapidly, often in a less uniformly incremental manner. In the unstable region, various mechanisms are responsible for the increased growth rate, which loads uncontrolled.

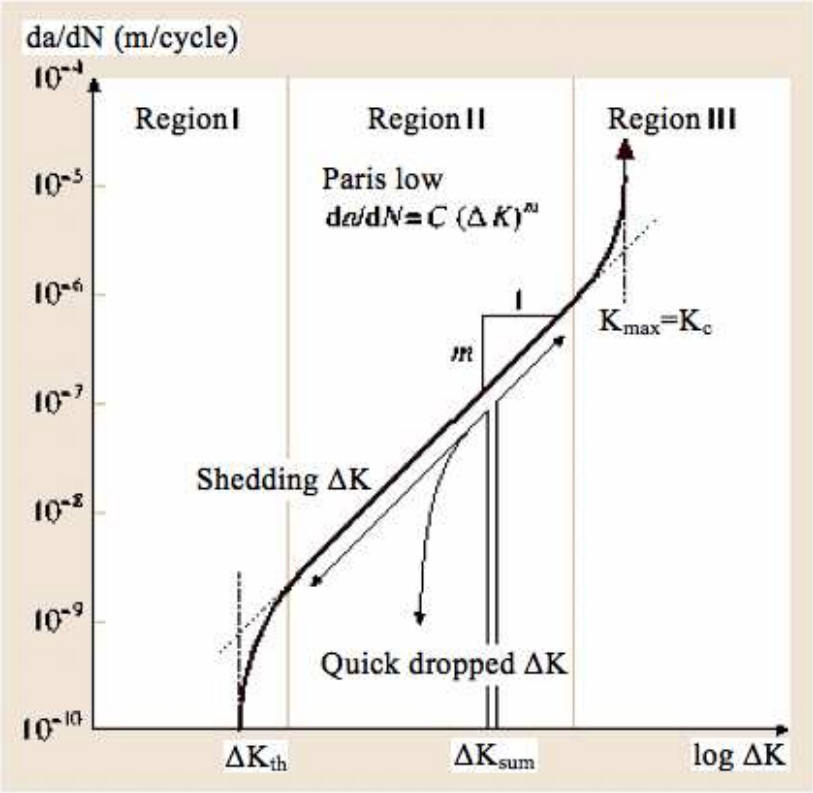

Fig 1.9: Typical crack-growth-rate versus stress-intensity-range diagram [19]

1.6 Toughness of material

Toughness describes the amount of total energy required for the material break. In general, if the material requires a lot of energy before breaking, then it looks like “tough”. If only a little energy is needed to break the material it is weak or brittle, depending on whether the material exhibits a yielding phenomenon followed by a plastic behaviour as load is increased or not.

Toughness is the resistance opposed by material to be broken. When crack propagates through the structure, fracture occurs. The amount of energy absorbed during the fracture depends on the size of the component, which is broken. The amount of energy absorbed *per unit area* of crack is constant for a given material corresponds to its toughness.

High toughness is particularly important for components, which may suffer impact (cars, toys, bikes, impact tools and hammer), or for components where a fracture would be catastrophic (pressure vessels, aircraft). Toughness varies with temperature, some materials change from being tough to brittle as temperature decreases (e.g. some steels, rubber). A famous example of this problem in steels was the battleships that broke in two in cold seas during the Second World War; some dangerous embitterment occurs in hydrogen storage [20].

Detailed toughness tests use specimens with initial cracks, and measure the energy per unit area as the crack grows. This can be applied to all materials, and the selection charts show toughness data measured this way. Simple toughness tests use specimens of fixed size with a machined notch, and just measure the energy needed to break the specimen.

Crack grows as soon as the crack tip stress exceeds a critical value. The SIF determines the amplitude of the crack tip stress for a given geometry and loading case, thus allowing to assume that a crack grows when K reaches a critical value. This implies that a crack growth criterion can be formulated, where the SIF is compared to this critical value. Therefore value of the SIF has to be calculated. The critical value has to be found in some experimental measurements. It is referred to as “Fracture Toughness “, K_C, where an additional subscript is used to describe the fracture mode analyzed: K_{Ic}, K_{IIc}, K_{IIIc} [21].

2 Classical fracture criteria and parameters

2.1 The Stress Intensity Factor

A major activity in the design process based on fracture mechanics is the determination of the Stress Intensity Factor (in the following simply SIF). In the following sections some of the pertinent analytical, experimental, and numerical methods are discussed.

Analytical determination of SIF

SIF can be coupled by an analytical approach in some relevant cases. In case of an infinite plate with a central crack of length '2a', under remote stress σ_0, the calculating of SIF is as follow: (see Fig. 1.10)

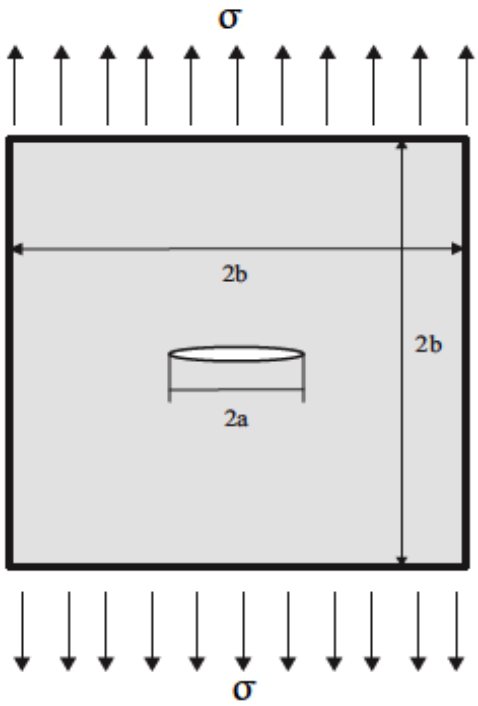

Fig 1.10: An infinite plate with a central elliptic crack [22]

Because the linear elastic fracture mechanics approach is based on elasticity, one can determine the effects of more than one type of loading on the crack tip stress field by linearly adding the SIF due to each type of loading. The process of adding SIF solutions for the same geometry is sometimes referred to as "principle of superposition". The only constraint on the

summation process is that the SIF must be associated with the same structural geometry, including crack geometry. Thus, for the geometries shown in Fig. 1.11, the equation is as follow:

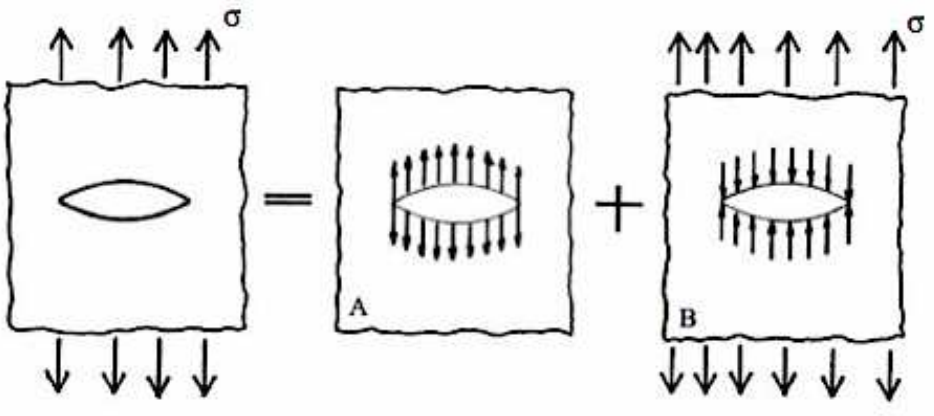

Fig 1.11: The geometries of superposition of K expression [8]

$$K_{IA} + K_{IB} = \sigma\sqrt{\pi a} \quad (1.9)$$

$$K_{IA} + 0 = \sigma\sqrt{\pi a} \quad (1.10)$$

$$K_{IA} = \sigma\sqrt{\pi a} \quad (1.11)$$

The stress distribution around the tip in mode I is described by Westergaard [23] as follow (Fig 1.12):

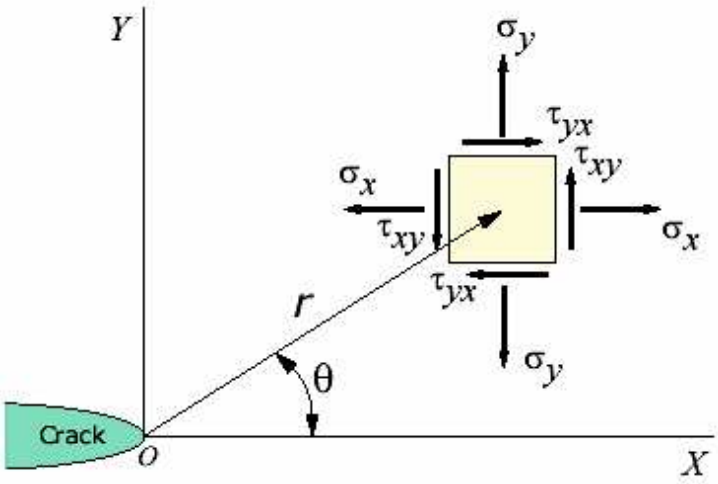

Fig 1.12: The stress distribution around the crack tip. [24]

$$\sigma_i = \frac{KI}{\sqrt{2\,\pi r}}\, f(\theta) \tag{1.12}$$

$$\sigma_{xx} = \frac{KI}{\sqrt{2\,\pi r}} \cos\frac{\theta}{2}\left(1 - \sin\frac{\theta}{2}\sin\frac{3\theta}{2}\right) + \ldots \tag{1.13}$$

$$\sigma_{yy} = \frac{KI}{\sqrt{2\,\pi r}} \cos\frac{\theta}{2}\left(1 + \sin\frac{\theta}{2}\sin\frac{3\theta}{2}\right) + \ldots \tag{1.14}$$

$$\tau_{xy} = \frac{KI}{\sqrt{2\,\pi r}} \cos\frac{\theta}{2}\cos\frac{3\theta}{2}\sin\frac{\theta}{2} \ldots \tag{1.15}$$

For distances close to the crack tip ($r \leq 0.1a$), the second and higher order terms indicated by dots may be neglected. The I subscript is used to denote the crack opening mode, but similar relations apply in modes II and III. Above equations show three factors relevant to depict the stress state near the crack tip: denominator $\sqrt{2\pi r}$ shows the singular nature of the stress distribution; σ approaches infinity as the crack tip is approached, with a $\sqrt{r}$ dependency. Depend on angle θ; it can be separated if a suitable factor is introduced. $f_x = \cos\theta/2 \cdot (1 - \sin\theta/2 \sin 3\theta/2) + \ldots$. Factor K_I contains the dependence on applied stress 'σ_∞', the crack length a, and the specimen geometry. The K_I factor gives the overall intensity of the stress distribution, hence its name. For the specific case of a central crack of width 2a or an edge crack of length 2a in a large sheet, $K_I = \sigma\alpha\sqrt{\pi a}$ and $K_I = 1.12\sigma\alpha\sqrt{\pi a}$ for an edge crack of length 'a' in the edge of a large sheet. Expressions for K_I for some additional geometry are given in Table 1.1 The literature [25] contain expressions for K for a large number of crack and loading geometries, and both numerical and experimental procedures exist for determining the stress intensity factor is specific actual geometries.

Table 1.1: Expressions of K_I for different geometries

Type of Crack	Stress Intensity Factor, K_I
Center crack, length 2a, in an infinite plate	$\sigma\alpha\sqrt{\pi a}$
Edge crack, length a, in a semi infinite plate	$1.12\ \sigma\alpha\sqrt{\pi a}$
Central penny shaped crack, radius a, in infinite body	$K_I = 2\ \sigma\alpha\sqrt{\pi/a}$
Center crack, length 2a in plate of width W	$\sigma\alpha\sqrt{W \tan\left(\frac{\pi a}{w}\right)}$
Two symmetrical edge cracks, each length a, in plate of total width W	$\sigma\alpha\sqrt{W \tan\left(\frac{\pi a}{w}\right) + 0.1 \sin\left(\frac{2\pi a}{w}\right)}$

These SIF's are used in design and analysis by arguing that material can withstand crack tip stresses up to a critical value of stress intensity, termed K_{Ic}, beyond which the crack propagates very fast. This critical SIF is then a measure of material toughness. The failure stress σ_f is then related to the crack length a and the fracture toughness by:

$$\sigma_f = \frac{KIc}{\alpha\sqrt{\pi a}} \qquad (1.16)$$

Where α is a geometrical parameter equal to 1 for edge cracks and generally on the order of unity for other boundary conditions. Expressions for α are tabulated for a wide variety of specimen and crack geometries.

Typical values of G_{Ic} and K_{Ic} for various materials are listed in Table 1.2 [26, 27 and 28]], and it is seen that they vary over a very wide range from material to material. Some polymers can be very tough, especially when rated on per-pound bases, but steel alloys are hard to beat in terms of absolute resistance to crack propagation.

Table 1.2: Typical values of K_{IC} for various materials

Material type	Material	K_{IC} (MPa.$\sqrt{m}$)
Metal	Aluminum alloy (7075)	24
	Steel alloy (4340)	50
	Titanium alloy	44–66
	Aluminum	14–28
Ceramic	Aluminium oxide	3–5
	Silicon carbide	3–5
	Soda-lime glass	0.7–0.8
	Concrete	0.2–1.4
Polymer	Polymethyl methacrylate	0.7–1.6
	Polystyrene	0.7–1.1
Composite	Mullite-fibre composite	1.8–3.3
	Silica aerogels	0.0008–0.0048

2.2 The Energy Release Rate

By the analysis of the energy balance, the energy release rate, denoted as G, was introduced. It is defined by the energy necessary to make the crack fronts extending the crack length by a unit length. It corresponds to the decrease of the total potential energy W_{pot} of the cracked body, when it passes from an initial configuration with a given crack length, to another configuration where the crack is increased by a unit of length "da" [29]:

$$G = -\frac{dW_{pot}}{da} \qquad (1.17)$$

$$W_{pot} = W_{\varepsilon} - W_{ext}$$

Where: W_{ext} is the work of external forces and W_{pot} is the total potential energy of crack body and W_{ε} is strain energy of structure.

Using the stress field in the singular zone, one can relate G to the stress intensity factors:

$$G = \frac{(KI^2 + KII^2)}{E'} + \frac{KIII^2}{2\mu} \quad (1.18)$$

With $E' = E$ in plane stress

$E' = E/(1-\nu^2)$ in plane strain

μ: Shear modulus

2.3 The J-Integral

The contour integral is the other way to characterize the singularity of the stress field in the vicinity of the crack, which one can deduce from the law of conservation of energy. In 2D crack linear elastic an integral of contour can be defined as follow [29]:

$$J = \int_\Gamma \left(W_e n_1 - \sigma_{ij} \frac{\delta U_i}{\delta x_i} \right) ds \quad (1.19)$$

Where W_e is the density of strain elastic energy and Γ is a contour around the crack. The crack is supposed as straight following the crack axis n is the normal vector to the contour, $\sigma_{ij}.n_j$ is the applied stress to the contour and U_i is the corresponding displacement. (See Fig 1.13):

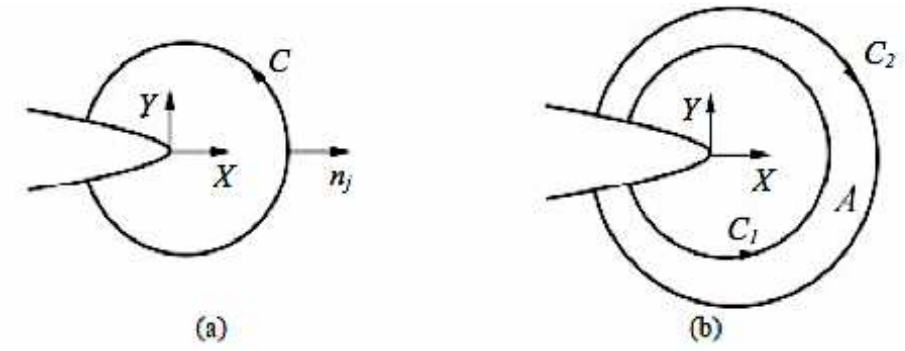

Fig 1.13: (a) Arbitrary contour surrounding the crack tip;
(b) Area to be employed to calculate the J-integral [30] *C C_2 X Y C_1 n_j*

The J-integral as the difference in potential energy Wpot of two cracked bodies is expressed by:

$$J = -\lim_{\Delta a \to 0} \frac{Wpot(a+\Delta a) - Wpot\,(a)}{\Delta a} = -\frac{dWpot}{\Delta a} \quad (1.20)$$

By comparison with G defined previously, one can realize that in the case of an elastic material or a very weak plastic deformation near the crack zone:

$$J = G = -\frac{dWpot}{da} \quad (1.21)$$

Relation between J and K

In LEFM, the stress and displacement components at the crack tip are known as a function of the position relative to the crack tip. For multi-mode loading, they are characterized by the stress intensity factors K_I, K_{II} and K_{III}.

Because the J-integral is path-independent, the integration path can be chosen to be a circle with the crack tip as its center. Integration over this circular path reveals that the J-integral is related to the SIF.

For Mode I loading of the crack, it follows immediately that the J-integral is equivalent to the energy release rate G. This means that J-integral can be used in the crack growth criteria of LEFM as a replacement for K and G [29].

Plane stress $J = \frac{1}{E} K_I^{\,2}$ (1.22)

Plane strain $J = \frac{(1-\nu^2)}{E} K_I^{\,2}$ (1.23)

J-integral crack growth criterion

J-integral can replace the energy release rate in LEFM and is related to the SIF. In NLFM, where the material behavior is described by the general Ramberg-Osgood relation [31], the J integral characterizes the stress at the crack tip. It is thus obvious that it can be used in a crack growth criterion. Calculation of its value is easily done, due to the fact that the

integration path can be chosen arbitrarily. Critical values have to be measured according to normalized experiments.

$$J = J_c \tag{1.24}$$

2.4 Crack Opening Displacement (CTOD)

In LEFM the displacement of material points in the region around the crack tip can be calculated. With the crack along the x-axis, the displacement u_y in y-direction is known as a function of r (distance) and θ (angle), both for plane stress and plane strain. Displacement of points at the upper crack surface results for $\theta = \pi$ and can be expressed in the coordinate x, by taking:

$$r = a - x \tag{1.25}$$

Where a is the half crack length. The origin of this xy-coordinate system is at the crack center. The crack opening (displacement) (COD) δ is two times this displacement. It can be easily appreciated that the opening at the crack tip (CTOD), δt, is zero [32].

$$u_y = \frac{\sigma\sqrt{\pi a}}{2\mu}\sqrt{\frac{r}{2\pi}}\left[\sin\left(\frac{\theta}{2}\right)\left(k+1-2\cos^2\left(\frac{\theta}{2}\right)\right)\right] \tag{1.26}$$

Displacement in crack plane $\theta = \pi$; $r = a - x$:

$$u_y = \frac{(1+\nu)(k+1)}{E}\frac{\sigma}{2}\sqrt{2a(a-x)} \tag{1.27}$$

Crack Opening Displacement (COD):

$$\delta(x) = 2u_y(x) = \frac{(1+\nu)(k+1)}{E}\sigma\sqrt{2a(a-x)} \tag{1.28}$$

Crack Tip Opening Displacement (CTOD):

$$\delta t = \delta(x = a) = 0 \qquad (1.29)$$

This CTOD can be used in a crack growth criterion (Fig 1.14), when plasticity at the crack tip is taken into account and the actual crack length is replaced by the effective crack length.

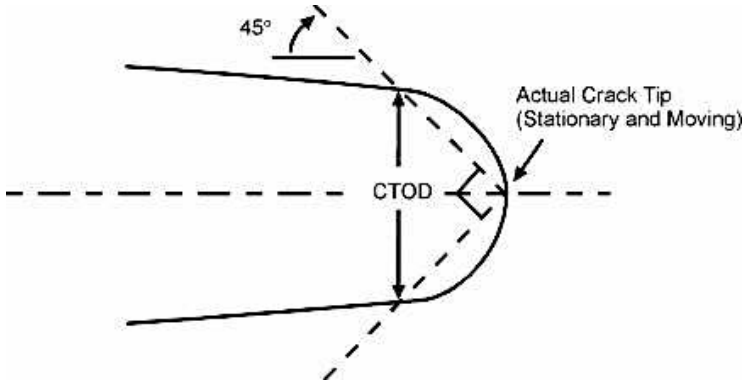

Fig 1.14: Definition of the Crack Tip Opening Displacement (CTOD) [8]

3 Fatigue crack propagation and life of structure

When a subcritical crack (a crack whose SIF is below the critical value) is under either cyclic or fatigue load, or is subjected to a corrosive environment, crack propagation will occur. Fatigue crack propagation occurs through repeated crack tip blunting and sharpening effects, which are in turn caused by micro plastic deformation mechanisms operating at the crack tip. The application of repeated loading will cause crack growth. The loading is usually caused by vibration. To predict the minimum fatigue life of metallic structures, and to establish safe inspection intervals, an understanding of the rate of fatigue crack propagation is required. Historically, fatigue life prediction was based on the Wöhler curve (Fig. 1.15).

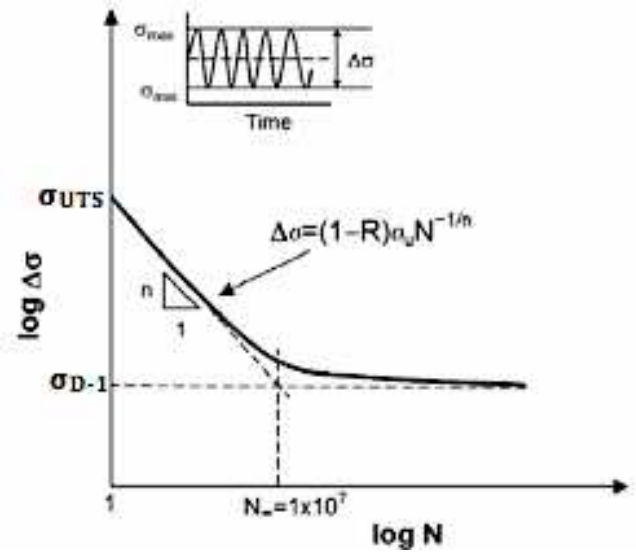

Fig 1.15: Fatigue life prediction was based on Wohler curve [33]

Where $\sigma_a = \frac{\sigma max - \sigma min}{2}$, and σ_{max} and σ_{min} are maximum and minimum of total cycle.

It can be started with a plate that has no crack and subject it to a series of repeated loading between σ_{min} and σ_{max}, it would observe three distinct stages. (Fig 1.16)

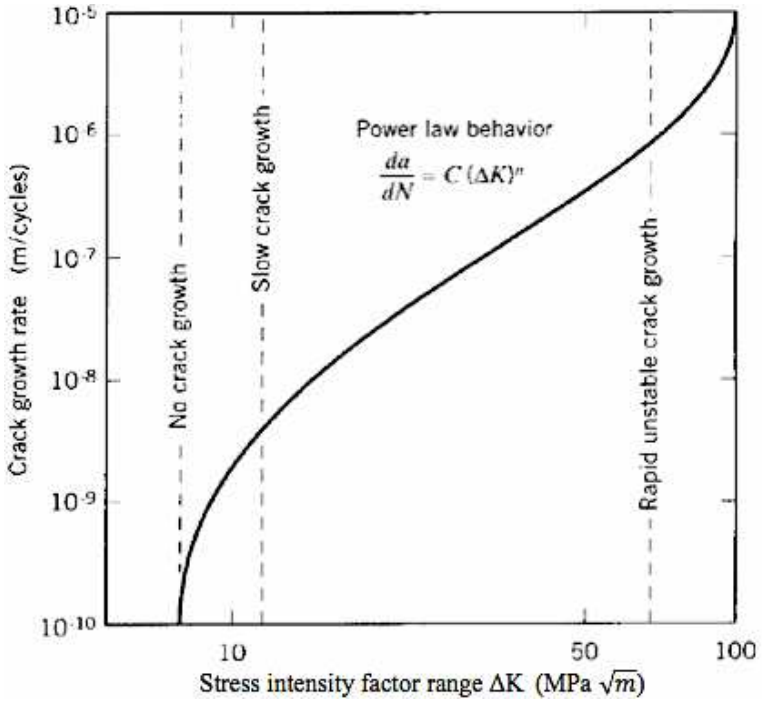

Fig 1.16: Three different stage of crack growth [34]

First stage is difficult to capture and is most appropriately investigated by metallurgists or material scientists law based on experimental observations. Most other empirical fatigue laws can be considered as direct extensions, or refinements of this one, given by:

$$\frac{da}{dN} = C\,(\Delta K_I)^n \tag{1.30}$$

Which is a straight line on a log-log plot of $\frac{da}{dN}$ vs ΔK_I, and:

$$\Delta K = K_{max} - K_{min} = (\sigma_{max} - \sigma_{min})\, f(g)\, \sqrt{\pi a} \tag{1.31}$$

"a" is the crack length; "N" the number of load cycles; "C" the intercept of line along da/dN and is of the order of 10^{-6} and has units of length/cycle; and n is the slope of the line and ranges from 2 to 10. Equation 9.1 can be rewritten as:

$$\Delta K = \frac{\Delta a}{C[(\Delta N(a)]^n} \tag{1.32}$$

The useful aspect of fatigue crack growth laws is that they can be used to calculate the number of cycles required to propagate a crack from a given initial size to some final size, which is critical for failure. Thus if the initial size is a_i and the final size a_f it may be writen:

$$N = \int_0^N dN = \int_{a_i}^{a_f} \frac{\Delta a}{C[\beta \Delta\sigma(\pi a)\text{^}1/2]^n} da \tag{1.33}$$

In the above equation (1.30) the geometric factor β is assumed to be constant because the inclusion of a function of $\frac{a}{W}$ within the integral sign will usually lead to a formulation, which cannot be integrated analytically. In practice, it is more straightforward and very often sufficiently accurate to solve the fatigue life equation by splitting the crack growth history into a series of crack increments. An average value within each step may then be used to calculate β and hence an average K is considered during each step. The average propagation rate within the step can then be calculated from the Paris law. In the case of a pressure vessel,

a_f may simply be defined in terms of a crack big enough to cause leakage, or one which results in the limiting fracture toughness being reached. Then, it will briefly introduce two software tools commonly used for fatigue crack growth studies. Thus, it is apparent that a small error in the SIF calculation would be magnified greatly as n ranges from 2 to 6. Because of the sensitivity of N upon ΔK, it is essential to properly determine the numerical values of the SIF.

However, in most practical cases, the crack shape, boundary conditions, and load are in such a combination that an analytical solution for the SIF does not exist and large approximation errors have to be accepted. Unfortunately, analytical expressions for K are available for only few simple cases. Thus the stress analyst has to use some formulas for them [35].

4 Advanced Problem in Fracture Mechanics

4.1 The Mixed Mode Operation

A more complicated case is that of crack, which shows an angle with the loading direction, even in this investigation a key issue is finding the magnitude of the far-field stress σ at which the crack starts to grow, but even determining the direction of crack growth is crucial [36]. (Fig 1.17)

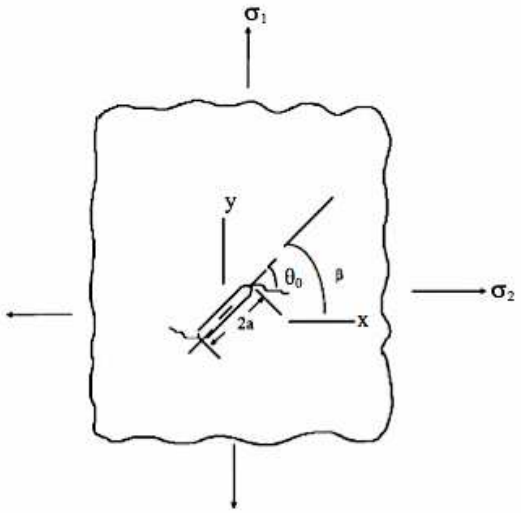

Fig 1.17: case of angled crack [37]

The first investigation is performed by resorting to the methods described in previous sections, while two are the general approaches used for predicting the direction of crack growth. In the first one, it is assumed that crack growth occurs along the direction perpendicular to the maximum tangential stress at (or near) the crack tip.

A second approach considers crack growth along the direction for which the strain energy density is minimal, since this condition corresponds to a maximum of energy release rate. The strain energy density just around crack tip can be written as [38]:

$$\psi = \frac{1}{r}\left(a_{11}K_I^2 + 2a_{12}K_IK_{II} + a_{22}K_{II}^2\right) = \frac{s(\theta)}{r} \tag{1.31}$$

$$a_{11} = \frac{1}{16\mu}\left[(1 + \cos\theta)(k - \cos\theta)\right] \tag{1.32}$$

$$a_{12} = \frac{1}{16\mu}\sin\theta\,\left[2\cos\theta - k + 1\right] \tag{1.33}$$

$$a_{22} = \frac{1}{16\mu}\left[(k + 1)(1 - \cos\theta) + (1 + \cos\theta)(3\cos\theta - 1)\right] \tag{1.34}$$

Where k = (3− 4ν) for plane strain state, and k = (3−ν) /(1+ν) for plane stress state, being ν as Poisson ratio.

According to this criterion the crack starts to grow when “s” reaches a critical value, referred to as S_c, and the direction of crack growth is given when S is a minimum:

$$\frac{ds}{d\theta} = 0, \qquad \frac{d^2s}{d\theta^2} > 0 \tag{1.35}$$

For instance, when only mode I is considered:

$$[S_I(\theta)]_{min} = S_I(\theta=0) = a_{11}K_c^2 \rightarrow \qquad S_c = \frac{2(k-1)}{16\mu}K_c^2 \tag{1.36}$$

For the angled crack shown in Fig. 1.17, the strain energy density can be obtained by means of following expressions:

$$\sigma_{rr} = \left[\frac{K_I}{\sqrt{2\pi r}}\right]\left[\frac{5}{4}\cos\frac{\theta}{2} - \frac{1}{4}\cos\frac{3\theta}{2}\right] + \left[\frac{K_{II}}{\sqrt{2\pi r}}\right]\left[-\frac{5}{4}\sin\frac{\theta}{2} + \frac{3}{4}\sin\frac{3\theta}{2}\right] + \sigma_t \cos^2\theta \quad (1.37)$$

$$\sigma_{\theta\theta} = \left[\frac{K_I}{\sqrt{2\pi r}}\right]\left[\frac{3}{4}\cos\frac{\theta}{2} + \frac{1}{4}\cos\frac{3\theta}{2}\right] + \left[\frac{K_{II}}{\sqrt{2\pi r}}\right]\left[-\frac{3}{4}\sin\frac{\theta}{2} - \frac{3}{4}\sin\frac{3\theta}{2}\right] + \sigma_t \sin^2\theta \quad (1.38)$$

$$\sigma_{r\theta} = \left[\frac{K_I}{\sqrt{2\pi r}}\right]\left[\frac{1}{4}\sin\frac{\theta}{2} + \frac{1}{4}\sin\frac{3\theta}{2}\right] + \left[\frac{K_{II}}{\sqrt{2\pi r}}\right]\left[\frac{1}{4}\cos\frac{\theta}{2} + \frac{3}{4}\cos\frac{3\theta}{2}\right] - \sigma_t \sin\theta\cos\theta \quad (1.39)$$

Where, according to F. 1.18:

$$K_I = \sigma\sqrt{\pi a}\sin^2\beta, \qquad K_{II} = \sigma\sqrt{\pi a}\sin\beta\cos\beta \quad (1.40)$$

$$\sigma_t = \sigma\sin^2\beta \quad (1.41)$$

4.2 Crack path direction under mixed mode loading

Many loading conditions in mechanical structures lead to a mixed mode crack tip propagation. Defects arising from fabrication processes such as welding or casting, residual tensile stresses, embrittled microstructures and fatigue may lead to have crack propagation under the effect by combined modes I, II and III.

Broberg [39] discussed some aspects of the stability of the crack path under pure and mixed mode loads and concluded that crack paths remain straight under homogeneous remote stress fields. However, engineering structures in service rarely experience such well-defined uniform stress fields. Stress and strain gradients arising from geometric features, multiple cracks and non-uniform, non-proportional remote loads commonly occur.

Applied mixed mode loading and interaction among multiple cracks are main causes of a major loss of directional stability. Highly anisotropic microstructures can also lead to significant changes in crack orientation but more often are responsible for local deviations, or ‘zigzags’, in the overall mode I crack trajectory.

The shape of plastic zone under pure mode III conditions differs substantially from that of mode I. In mode III, plastic zone is essentially circular and extends some four to six times further ahead of the crack than the symmetrical inclined shear distribution seen ahead of a pure mode I crack at the same SIF. The center of the circular plastic zone lies somewhere

between the tip of the crack and one radius distance ahead, depending on the work hardening coefficient.

Furthermore, the extent of crack tip plasticity in torsional loading, and hence the prevalence of flat mode growth, is also dependent upon the size of the cylindrical component; small diameter shafts being more prone to flat crack growth than large shafts for the same stress, or strain, intensity factor. In these cases, a large ratio of the applied torque to plastic collapse limit torque of the shaft, as would occur in a small diameter shaft, extends the crack tip plasticity beyond that expected for the level of strain intensity factor applied.

The path of a fatigue crack under proportional loading from an initially mixed mode condition, as created by angled or inclined cracks in laboratory specimens, is surprisingly stable. One might expect major variations, as a function of mean stress for example, but there is little evidence to this effect. Nevertheless, there are some differences in the crack trajectory in specimens under identical test conditions. These small-scale fluctuations in crack path are worthy of detailed investigation but, until recently, experimental techniques to evaluate the strength of mixed mode crack field have not been reliable enough to yield some useful information.

Understanding the behaviour of mixed mode cracks in general, and the path of such cracks requires a combination of high quality experimental data and observations as well as robust mathematical models. Good data on the crack tip stress state, crack closure and contact, and the crack trajectory is hard to obtain and there has been much recent work in this area [29].

5 Functional materials and electromechanical coupling

Functional materials exploit coupling among multiple variables for example, by transforming mechanical energy into electrical energy in piezoelectric materials. Electromechanical coupling coefficient is a numerical measure of the conversion efficiency between the electrical and mechanical energy in piezoelectric material. Qualitatively the electromechanical coupling coefficient, K (to be distinguish from SIF) can be determined as:

$$K^{-2} = \frac{1}{\text{energy converted per input energy}} \tag{1.42}$$

5.1 Modified criteria and tools for the fracture of piezoelectric materials

Piezoelectric materials have been extensively used in smart devices such as sensors and actuators. The combined mechanical and electric loads give rise to sufficiently high stresses in these devices, which result in catastrophic failure. Piezoelectric ceramics have become preferred materials for a wide variety of electronic and mechatronic devices due to their pronounced piezoelectric, dielectric, and pyro electric properties. However, piezoelectric ceramics are brittle and susceptible to cracking at all scales ranging from electric domains to devices. Various defects, such as domain walls, grain boundaries, flaws and pores, impurities and inclusions, etc., exist in piezoelectric ceramics. Defects cause geometric, electric, thermal, and mechanical discontinuities and thus induce high stress and/or electric field concentrations, which may induce crack initiation, crack growth, partial discharge, and dielectric breakdown, fracture or failure. Due to the importance of the reliability of these devices, an effective prediction of their reliability is important for the design activity [40].

Fracture behavior of piezoelectric ceramics is more complex than in other materials, because of the nonlinear nature of the mechanical and electrical properties. There are new challenges in studying the fracture behavior of piezoelectric ceramics, e.g., determination of the electric boundary conditions on crack faces, effect of electric fields on the piezoelectric fracture behavior, calculation of the global and local energy release rates, etc.

Analysis of fracture behaviour in piezoelectric material is never simple because there is much nonlinearity repurposed. Polarization is linked to the electric field nonlinearly. Somehow relation between strain and electric field might because nonlinear above a certain amplitude of voltage. Moreover material may exhibit a nonlinear relation between stress and strain. To face the problem of solving this kind of problem, some approached based on micromechanical modeling of materials are used as well as methods based on some phenomenological approaches. This motivated the large number of criteria proposed for fracture of piezoceramics [41].

Modeling the piezoelectric material inside some FEM code exhibits the problem of inputting the electromechanical properties of these materials. ABAQUS is usually used to analyze the fracture mechanics, but there are some difficulties in case of piezoelectric materials. Electromechanical properties can be inputted only as loading and boundary condition inside

the software properly and also the fracture properties of piezo have to be assigned into the model. Unfortunately this software doesn’t have a suitable tool to connect the electromechanical and fracture modeling together. That’s why it was strictly required writing a dedicated subroutine by using either Python or Isight.

CHAPTER 2

MODELING OF THE FRACTURE OF THE LINEAR ELASTIC MATERIAL

1 Numerical approach for the description of fracture

As it was already described in pervious chapter, three are the modes of propagation of crack which have to be predicted when an analytical approach is applied.

Opening sliding and tearing crack modes are analyzed. Literature of fracture mechanics provide some very well known and assessed models, which will be here, briefly summarized.

If one assumed that a local reference frame could be described as in Fig 2.1, the stress components to be calculated are: $\sigma_{\theta\theta}$, σ_{rr}, $\tau_{r\theta}$.

Being $\sigma_{\theta\theta}$ the local tangential component, expressed in terms of normal stress, σ_{rr} is the radial component along the z-direction, while $\tau_{r\theta}$ is the shear stress lying on the plane.

It is worthy noticing that analytical approach is simply discretized inside the finite element method, when the prediction of fracture behaviour is performed by a numerical solution. In particular, the polar reference frame described in the analytical approach is used and the same stress component is calculated.

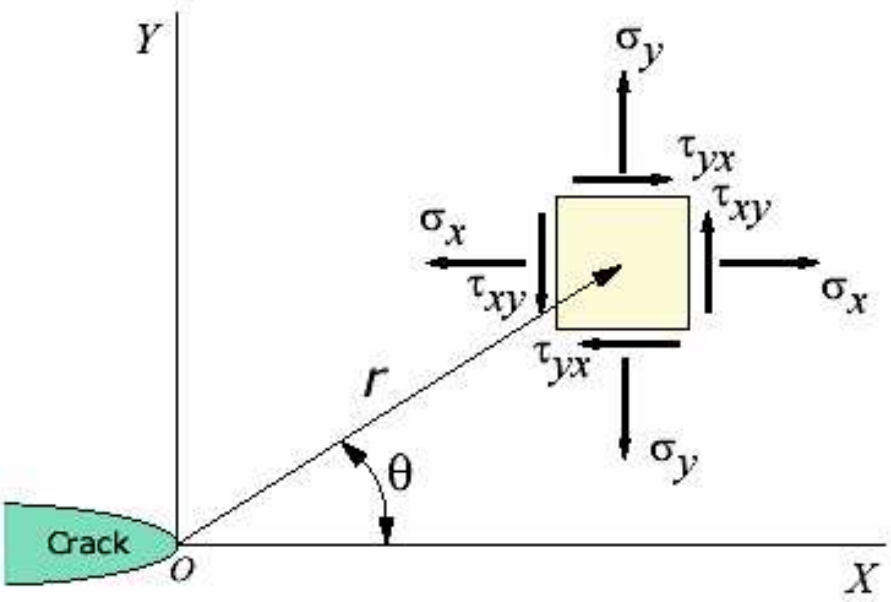

Fig 2.1: Stress field at crack tip.[24]

The stress field at the crack tip is shown in Fig 2.1. For mode I, stresses and displacements at the crack tip are given by Lawn [42]:

$$\begin{Bmatrix}\sigma_{rr}\\ \sigma_{\theta\theta}\\ \tau_{r\theta}\end{Bmatrix} = \frac{K_I}{(2\pi r)^{\frac{1}{2}}}\begin{Bmatrix}\cos(\frac{\theta}{2})[1+sin^2(\frac{\theta}{2})\\ cos^3(\frac{\theta}{2})\\ \sin(\frac{\theta}{2})\,cos^2(\frac{\theta}{2})\end{Bmatrix} \tag{2.1}$$

$$\begin{Bmatrix}u_r\\ u_\theta\end{Bmatrix} = \frac{K_I}{2E}\,(\frac{r}{2\pi})^{\frac{1}{2}}\begin{Bmatrix}(1+\nu)[(2K-1)\cos\left(\frac{\theta}{2}\right)-\cos(\frac{3\theta}{2})\\ (1+\nu)[-(2K+1)\sin\left(\frac{\theta}{2}\right)+\sin(\frac{3\theta}{2})\end{Bmatrix}$$

For mode II they are

$$\begin{Bmatrix}\sigma_{rr}\\ \sigma_{\theta\theta}\\ \tau_{r\theta}\end{Bmatrix} = \frac{K_{II}}{(2\pi r)^{\frac{1}{2}}}\begin{Bmatrix}\sin(\frac{\theta}{2})[1-3sin^2(\frac{\theta}{2})\\ -\sin(\frac{\theta}{2})\,cos^2(\frac{\theta}{2})\\ \cos(\frac{\theta}{2})[1-3csin^2(\frac{\theta}{2})]\end{Bmatrix} \quad (2.2)$$

$$\begin{Bmatrix}u_r\\ u_\theta\end{Bmatrix} = \frac{K_{II}}{2E}\,(\frac{r}{2\pi})^{\frac{1}{2}}\begin{Bmatrix}(1+\nu)[-(2K-1)\sin\left(\frac{\theta}{2}\right)+3\sin(\frac{3\theta}{2})\\ (1+\nu)[-(2K+1)\cos\left(\frac{\theta}{2}\right)+3\cos(\frac{3\theta}{2})\end{Bmatrix}$$

Parameters K changes in case of either plane stress or plane strain as follow:

K = (3 - ν)/(1 + ν) Plane stress (2.3)

K = (3 - 4ν) Plane strain (2.4)

In above equations, E is the Young's modulus, ν is the Poisson's ratio. u_r is the displacement parallel to the r coordinate, and u_θ is the displacement normal to the coordinate. According to the literature stress and displacement equations in (2.1, 2.2) can be summarized as follow:

$$\sigma_{ij} = K\frac{1}{\sqrt{2\pi r}}f_{ij}(\theta) \quad (2.5a)$$

$$u_i = K\frac{1}{2E}\sqrt{\frac{r}{2\pi}}f_i(\theta) \quad (2.5b)$$

The *K* factor depends on the loading condition σ_{ij}, and also on the specimen geometry (r, θ, u_i) For r = 0, which is at the tip of the fracture, a singularity exists in the linear stress and strain field.

2 The Stress Intensity Factor

To calculate the SIF for mode I in a finite element mesh three points of the crack are considered as “A”, “B” and “C”. Under the unique effect of mode I, at a finite grid block A-B, $\theta = 180$ and $r = r_{AB}$

Displacement parallel to the r−coordinate is zero. Only displacement along the direction, being normal to the r−coordinate, is active. From (2.1) difference of displacements between points A and B is: [43]

$$u_{\theta B} - u_{\theta A} = -\frac{K_I(1+\nu)(K+1)}{E}\sqrt{\frac{r_{AB}}{2\pi}} \tag{2.6}$$

Therefore SIF of mode I, K_I, is computed as

$$K_I = \frac{E}{(1+\nu)(K+1)\,E}\sqrt{\frac{2\pi}{r_{AB}}}\,(u_{\theta B} - u_{\theta A}) \tag{2.7}$$

In case of pure mode II, there is no displacement along the direction normal to the coordinate, and u_θ is null. Displacement parallel to the r−coordinate is:

$$u_{rB} - u_{rA} = -\frac{K_{II}(1+\nu)(K+1)}{E}\sqrt{\frac{r_{AB}}{2\pi}} \tag{2.8}$$

And SIF of mode II, K_{II}, is computed as:

$$K_{II} = \frac{E}{(1+\nu)(K+1)}\sqrt{\frac{2\pi}{r_{AB}}}\,(u_{rB} - u_{rA}) \tag{2.9}$$

Equations (2.6) and (2.8) are applicable for cracks with symmetrical structure, i.e. displacements at points B and C are identical in magnitude and opposite in sign. In a mixed mode I-II free surface may overlying the fracture [44]. Under mixed mode I-II condition displacements at the two sides of the crack face are different. In the above discussed case, displacement normal to the crack axis at points B and C, $u_{\theta B}$ and u_α, respectively, are different; as well as displacement parallel to the crack axis at these two points, u_{rB} and u_{rC}, at point C, $\theta = 180$ and $r = r_{AC}$

Normal displacement u_θ at point B only results from mode I:

$$u_{\theta B} = -\frac{K_I(1+v)(K+1)}{E}\sqrt{\frac{r_{AB}}{2\pi}} \tag{2.10}$$

as for point C

$$u_{\theta C} = \frac{K_I(1+v)(K+1)}{E}\sqrt{\frac{r_{AC}}{2\pi}} \tag{2.11}$$

where $r_{AB} = r_{AC}$. If one subtracts (2.10) and (2.11), and solve for K_I:

$$K_I = -\frac{E}{2(1+v)(K+1)}\sqrt{\frac{2\pi}{r_{AB}}}(u_{\theta B} - u_{\theta A}) \tag{2.12}$$

Under mode II with asymmetric mix-mode loading condition, displacement normal to the crack axis is null at both points B and C. However, displacement parallel to the crack axis at point B is:

$$u_{rB} = -\frac{K_{II}(1+v)(K+1)}{E}\sqrt{\frac{r_{AB}}{2\pi}} \tag{2.13}$$

while at point C

$$u_{rC} = \frac{K_{II}(1+v)(K+1)}{E}\sqrt{\frac{r_{AC}}{2\pi}} \tag{2.14}$$

These equations lead to:

$$K_I = -\frac{E}{2(1+v)(K+1)}\sqrt{\frac{2\pi}{r_{AB}}}(u_{rB} - u_{rC}) \tag{2.15}$$

This approach is referred to as "displacement correlation method", which is one among three methods widely used to calculate the stress intensity factor in some FEM codes. In the displacement correlation method, displacement values computed at the finite element grid nodes near crack tip are correlated with analytical solutions [45].

3. Propagation Criterion for crack

The critical value of the SIF, K_{IC}, which is also recognized as fracture toughness [Lawn, 1993], is a material property used to describe the resistance of a material to fracture propagation. The fracture toughness of a material is related to the strength of bonds between constituent particles and the size of flaws in the material. Fracture toughness is widely used to describe fracture propagation through rock, and it appears to be a valid predictor of fracture propagation in cohesive soils. In rock, fracture toughness values are typically on the order of 1 MPa$\sqrt{m}$, whereas the fracture toughness of partially saturated silty clay is less than 0.05 MPa$\sqrt{m}$ [46].

Propagation criterion which, will be used in this work is that under mode I, the onset of crack propagation will appear, and propagation will continue as far as:

$$K_I \geq K_{IC} \tag{2.16}$$

Propagation when will stop as soon as:

$$K_I < K_{IC} \tag{2.17}$$

In case of pure mode-I fracture crack will propagate in the same direction as it was initiated. However, under mixed mode-I and mode-II, initiation and propagation of a crack depend upon both modes I and II of the SIF and critical values. In the FEM analysis to simulate mixed mode I and II propagation the maximum circumferential tensile stress, $\sigma_{\theta max}$, near the crack tip [43] and some assumptions are made:

1) Crack extension starts at crack tip along the radial direction.

2) Crack extension starts in a plane normal to direction of the greatest tensile stress.

3) Crack extension begins when $\sigma_{\theta max}$ reaches a critical material-constant value.

According to the theory [43]:

$$\sigma_\theta\sqrt{2\pi r} = \cos\frac{\theta}{2}\left(K_I\cos^2\frac{\theta}{2} - \frac{\theta 3}{2}K_{II}\sin\theta\right) = K_{IC} \tag{2.18}$$

and

$$\tau_{r\theta} = 0 \rightarrow \cos\frac{\theta}{2}\left[K_I \sin\theta + K_{II}(3\cos\theta - 1)\right] = 0 \quad (2.19)$$

Therefore from equation (2.23), direction of the initial fracture increment, θ, can be found from

$$K_I \sin\theta + K_{II}(3\cos\theta - 1) = 0\,. \quad (2.20)$$

For instance, in case of mode I,

$$K_{II} = 0 \quad (2.21)$$

$$K_I \sin\theta = 0 \Rightarrow \theta = 0^\circ \quad (2.22)$$

Therefore crack will propagate in its own plane. However, for pure mode II,

$$K_I = 0 \quad (2.23)$$

$$K_{II}(3\cos\theta - 1) = 0 \Rightarrow \theta = -70.5^\circ\,. \quad (2.24)$$

i.e. crack will tend to follow a skew- path with an angle of 70.5 degree. Under mixed mode conditions, crack will propagate along a direction identified by an angle between 0° and 70.5°, according to the mixed condition of K_I and K_{II}.

4 Analytical approach of crack tip energy release rate for piezoelectric material

Electrostatic, dielectric, piezoelectric and elastic behavior will be accepted in the standard form since they have been verified rigorously over many years. The state of a material will be assumed to be given by its strain s and its polarization P and the behavior of the material will be assumed to be linear and reversible with nonlinearities and irreversibility

confined to the crack tip. The stored electrostatic energy in the material is due to its polarization P, but it is useful for the calculations of stored work to introduce the electric displacement D such that [47]:

$$D_i = e_0 E_i + P_i \tag{2.25}$$

Where e_0 is the permittivity of free space and E is the electric field. With these variables, it is possible to account simultaneously for the stored energy of polarization and the interaction energy among external and other charges necessary to permeate the electric field E into the space occupied by the material. x_i the electric field is given by:

$$E_i = \frac{\partial \Phi}{\partial x_i} \tag{2.26}$$

Where x is position in space and Φ is the electric potential. The electric displacement satisfies the condition:

$$\frac{\partial D_i}{\partial x_i} = q_v \tag{2.27}$$

where q_v is the density of free charge per unit volume. Throughout, we take $q_v = 0$.

The strain S is given by:

$$S_{ij} = \frac{1}{2}\left(\frac{\partial u_i}{\partial x_i} + \frac{\partial u_j}{\partial x_i}\right) \tag{2.28}$$

Where u is the displacement of continuum material points. Stress σ satisfies condition:

$$\frac{\partial \sigma_{ij}}{\partial x_i} + b_j = 0 \quad (2.29)$$

Where b is a body force per unit volume and quasi-static conditions are assumed. Since q_v =0, there are no Coulomb's forces acting on free charge within the material. The effect of forces acting on bound charges involved in the polarization process will be treated as being accounted for in the stored energy of the polarized state. Therefore, the body force b is zero and the stress s balances only loads applied externally to the body. In principle, some of these external loads could be due to electrostatic Coulomb's forces acting on the free charges at interfaces with electrodes or other surfaces. We will argue later that these are sufficiently small and can be neglected.

The constitutive laws connecting the electric displacement, stress, electric field and strain are:

$$\sigma_{ij} = C_{jkl}(S_{kl} - S^r_{kl})\text{-}e_{kij}E_k \quad (2.30)$$

$$D_i = e_{ijk}(S_{jk} - S^r_{jk}) + \varepsilon_{ij}E_j + P^r_i \quad (2.31)$$

Where C_{jkl} is the elasticity tensor at constant electric field, ε_{ij} is the tensor of dielectric permittivities at constant strain, e_{ijk} is a tensor of piezoelectric coefficients, S_r is the remanent strain of polarization and P^r is the remanent polarization. The stored energy per unit volume (in the absence of remanent strain and polarization) is given by:

$$U = \frac{1}{2}\sigma_{ij}S_{ij} + \frac{1}{2}E_iD_i \quad (2.32)$$

We address the problem of calculating of the crack tip energy release rate in a loaded compact tension specimen subject to an applied electric field. The material is piezoelectric, poled in the positive $\mathbf{x}_3$-direction and transversely isotropic about the poling axis. The needed relationships for plane strain:

$$\sigma_{11} = C_{11} s_{11} + C_{13} s_{33} - e_{31} E_3 \quad (2.33)$$

$$\sigma_{33} = C_{13} s_{11} + C_{33} s_{33} - e_{33} E_3 \quad (2.34)$$

$$\sigma_{13} = 2C_{44} s_{13} - e_{15} E_1 \quad (2.35)$$

$$D_1 = 2e_{15} s_{13} + e_{11} E_1 \quad (2.36)$$

$$D_3 = e_{31} s_{11} + e_{33} s_{33} + e_{33} E_3 \quad (2.37)$$

Where the datum for strain and electric displacement is the polarized state. That is, the remanent strain and polarization are present in the material but because the remanent state is the reference configuration for the measurement of strain, s_r and P_r are numerically equal to zero. Due to plane strain and the fact that the electric field is applied in the $x_1 \pm x_3$ plane, the strains s_{22}, s_{12}, and s_{23}, the stresses s_{12} and s_{23} plus the electric field component E_2 and the electric displacement component D_2 are all zero. The stress component s_{22} is nonzero to maintain plane strain constraint, but is not given above. W is the electrical enthalpy given by:

$$W = \frac{1}{2} (\sigma_{ij} S_{ij} - E_i D_i) \quad (2.38)$$

A is the planar area of the specimen, S is the perimeter of the specimen and D is the displacement of one of the load points in the direction of its prescribed applied force F. The integral over is taken only where the tractions are imposed in the case of the term involving displacements and only where the surface charge is imposed in the case of the term involving the potential. Variation of the displacements and the potential are constrained to be zero where they are imposed on S.

The J-integral is used for the fracture mechanics analysis of the specimen. The form suitable for piezoelectric materials is:

$$J = \int_{\Gamma} [W dx_3 + (n_i D_i E_1 - T_i (\frac{\partial u_i}{\partial x_i}) ds] \quad (2.39)$$

Where Γ is the contour from the crack tip on the lower surface to the crack tip on the upper surface and is traversed in the direction shown, n is the outward unit normal to the contour Γ and ds is arc length along the contour. Elementary considerations can be used to show that for homogeneous materials J is path independent (as long as the contour begins and ends at the crack tip and encloses the tip, encompassing the singularity there) and that J is equal to Γ, the crack tip energy release rate on propagation of the crack. That is, J gives the reduction of potential energy of the specimen per unit area of crack advance. [47]

5 Numerical tools

There are many numerical approaches currently available to solve the problems concerning LEFM and to calculate the SIF. Research activity in this domain has produced a very large number of papers and it would be extremely difficult, and perhaps useless in the frame of this thesis, to extensively review all the literature on this subject. Therefore, following state of the art only briefly includes some of the basic references and proposes a classification of proposed methods by defining categories.

a) The Finite Element Method (FEM)

Usually, displacement-type finite elements (based on the virtual work principle) are widely used. According to the so-called “direct approach”, the SIF are deduced from the displacement field, this is the case of the Crack Opening Displacement method (COD).

In the “energy approach” which is generally more precise, the SIF are deduced from the energy distribution in the proximity of the crack tip, either from the energy release as in

the method of the Virtual Crack Extension or from the J-integral as in the Equivalent Domain Integral Method [48].

b) The Boundary Elements Method (BEM)

In this method, only the boundaries of the solid are discretized. The partial differential equations of the Theory of Elasticity are transformed into integral equations on the boundaries of the domain. Basically, the primary unknowns of the numerical problem are the displacements.

This is the case for the “crack Green’s function method”, the “displacement discontinuity method” and the “sub regions method”. In dual method has been developed, which the surface tractions as primary unknowns [49].

c) The Mesh less method

This method has been applied to fracture mechanics since 1994 and, subsequently, different improvements have been introduced, for example to couple this approach with the finite element method, to ensure the continuity of displacements in the vicinity of crack and improve the representation of the singularity at the crack tip, by using an arbitrary Lagrangian-Eulerian formulation to enrich the displacement approximation near the crack tip or to enrich the weighting functions [50].

d) The Extended Finite Element Method

The Extended Finite Element Method (XFEM) allows some discontinuities in the assumed displacement field. Discontinuities can be due to the presence of cracks and do not have to coincide exactly with the finite element edges: they can be located anywhere in the domain independently of the finite element mesh [51]. This approach is extremely used in the recent literature of fracture mechanics and is highly supported by the ABAQUS © code.

5.1 The Finite Element Method

Many issues of structural integrity can be cast as problem of linear elastic fracture mechanics (LEFM). These can include fatigue crack propagation and life prediction, other types of sub-critical crack growth, residual strength estimation, and brittle fracture.

In these and other related problems, it is essential to be able to predict the onset of crack growth, and its rate, shape, and stability. the finite element method, as performed within modern high-performance and low cost computing environments, is a natural tool for analyzing such LEFM problems.

A) Singular finite elements

A fundamental difficulty when modeling linear elastic fracture mechanics (LEFM) problems through FEM is that polynomial basis functions used for most conventional elements cannot represent the singular crack-tip stress and strain fields predicted by the theory. This means that mesh doesn't assure the numerical convergence to the theoretical solution, although it is highly refined around the crack tip.

A significant improvement in the use of FEM for LEFM problems was the simultaneous, and independent, development of the quarter-point element. Crack tip displacement, stress and strain fields are modeled by standard quadratic order isoparametric finite elements if one simply moves the element's mid-side node to the position one quarter of the way from the crack tip to the far end of the element. This procedure introduces a singularity into the mapping between the element's parametric coordinate space and the Cartesian space [52]. The quadratic quarter-point element is illustrated in Fig 2.2.

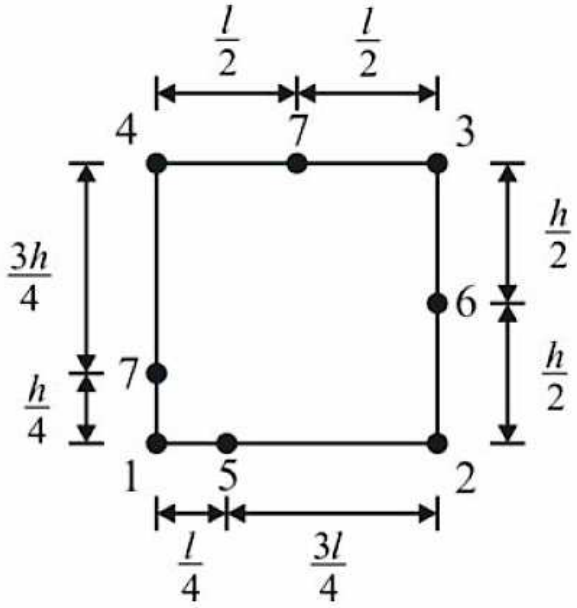

Fig 2.2: The quadratic quarter-point element [53]

The introduction of quarter-point elements was a significant milestone in the development of finite element procedures for LEFM. With these elements standard and widely available, finite element programs can be used to model crack tip fields accurately, with only minimal preprocessing required.

B) Extracting SIF and Energy Release Rate from FEM

Under LEFM assumptions, the stress, strain and displacement fields in the near crack-tip region are determined by the SIF. Therefore, extraction of accurate SIF is a fundamental task of FEM modeling. A large number of techniques for extracting SIF have been presented in the literature [54]. Among those, four are very often applied: displacement correlation, virtual cracks extension, modified crack closure integral and the J-integral, these techniques look more accurate and simples.

It is worthy motivated that techniques for extracting SIF's fall into one of two categories above-mentioned. Some belong the direct approaches, which correlate the SIF's with FEM results directly and energy approach, which compute the energy release rate. In general, the energy approaches are more accurate and should be used preferentially. However, the direct approaches are especially useful as a check on energy approaches because expressions are simple enough to handle the calculations. a brief description of four mentioned techniques follow:

Generalized Displacement correlation method is one of the simplest first techniques proposed to extract SIF's from the FEM displacements for a node of the mesh, by substituting directly displacement value into the analytical expressions for near-tip displacement, after subtracting the displacements of the crack tip. Usually, a node on the crack face where the displacements will be greatest is selected and thus the relative error in the displacements is expected to be smallest. A generalized form displacement correlation method (GDC) can use any linear or quadratic finite element type with homogeneous meshing without local refinement. These two features are critical for modeling dynamic fracture propagation problems where locations of fractures are not known a priori. Because regular finite elements' shape functions do not include the square-root terms, which are required for accurately representing the near-tip displacement field, the GDC method is enriched via a correction multiplier term. The proposed method using quadratic elements is accurate for mode-I and mode-II fracturing, including for very coarse meshes. An alternative formulation using linear elements is also

demonstrated to be accurate for mode-I fracturing, and acceptable mode-II results for most engineering applications can be obtained with appropriate mesh resolution, which remains considerably less than that required by most other methods for estimating stress intensities [55]. The configuration for this simple approach is shown in Fig 2.3.

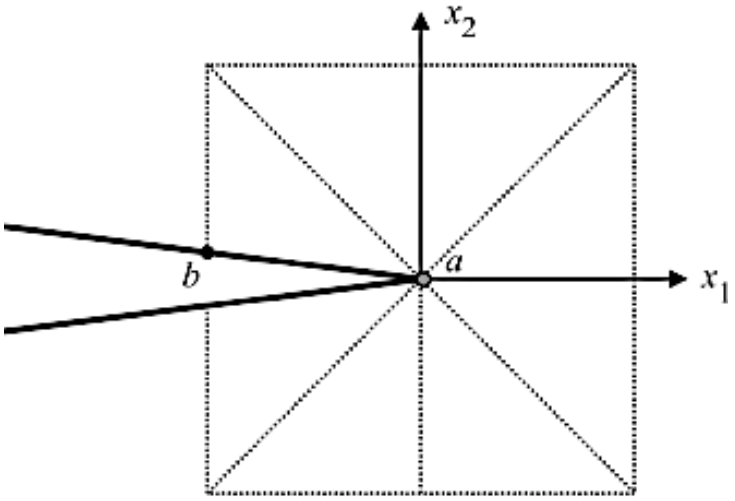

Fig 2.3: Possible sample point location for simple displacement correlation [54]

The virtual crack extension method is an energy approach that computes the rate of change in the total potential energy of a system for a small extension of the crack. Under LEFM assumption, this is equal to the energy release rate. In general, the virtual extension crack is more accurate than the displacement correlation approach for a given finite element mesh. However, as originally proposed, only a total energy release rate is computed. It is not separated for the three modes of fracture [56].

The modified crack closure integral (MCCI) technique was originally proposed by Rybicki and Kanninen [57], They observed that Irwin's crack closure integral could be used as computational tool (Fig 2.4). Release the energy release rate to the crack-tip stress and displacement fields for a small crack increment.

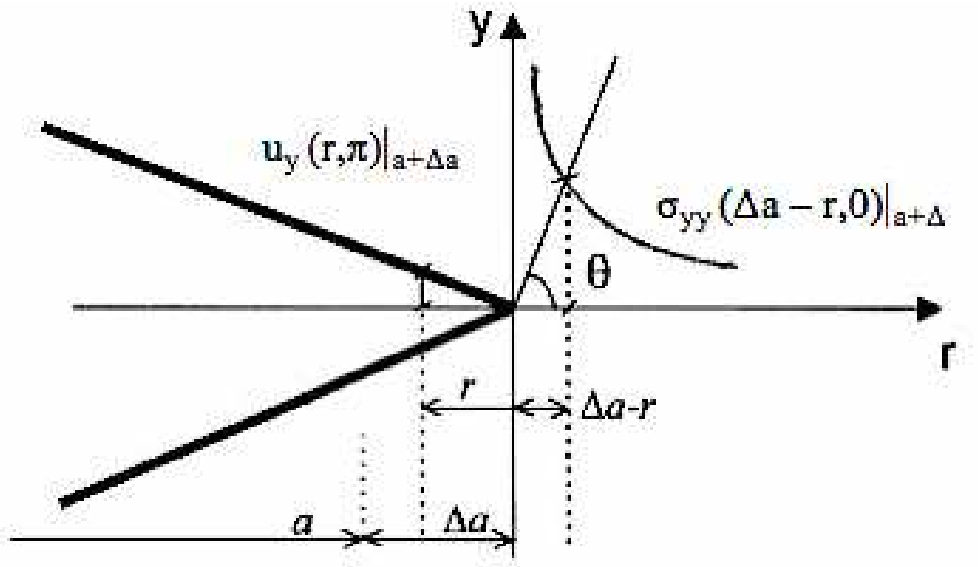

Fig 2.4: Crack-tip stress and displacement fields used in Irwin crack closure integral [58]

The MCCI procedure has been extended for use with higher order element. Of particular interest is its formulation for quadratic-point elements is insensitive. These elements express the crack-tip displacement and stress fields in terms of second order polynomials that were consistent with the quarter-point behavior.

In general, for a given mesh the MCCI technique yields SIF's that are more accurate than the displacement correlation approach, but less accurate than the J-integral approach. However, it gives surprisingly accurate results for its simplicity and requires nodal forces and displacements only, which are standard outputs from many finite element programs.

The J-integral is well-known parameter of nonlinear fracture mechanics. Under linear elastic material assumptions, the J-integral can be interpreted as being equivalent to the energy release rate, G. In its original formulation, it relates the energy release rate of a two dimensional body to a contour integral. The contour integral in the simple form can be shown to be path-independent providing there are no body forces inside the integration area, there are no tractions on the crack surface and the material behavior is elastic [29].

C) Available tools and softwares

In the FEM, the structure is subdivided into discrete elements. Different Element types can be used to cover the problem. Elements are connected at node, where continuity of displacement field is imposed. Displacements at nodes depend on the element stiffness

and computational of the nodal forces. For structural problems, numerical solution consists of computing nodal displacements. Stress and strain distributions throughout the body, as well as the crack parameters such as SIF, can be inferred from the nodal displacements. A number of commercial FEM packages have the ability of crack modeling and performing the fracture mechanics calculations. There is also some noncommercial code, as the FRANC2D, which is developed by the Cornell University, being surprisingly easy to learn and offering many capabilities. Finite element analysis can be carried out by several available software like ABAQUS, ANSYS, and LS- DYNA etc. These softwares are user friendly and give a wide range of analysis options. Static, dynamic, fluid, thermal and electromechanical problems can be analyzed by means of those codes.

In this thesis, the ABAQUS© was used, it can solve linear and nonlinear problems. It was designed to be able to investigate many links of nonlinearities such as geometrical material or multi-physic domains. Some specialized modules allow investigation of several behaviour of material in presence of plasticity, buckling, electromechanical coupling and even fracture. Numerical tools are evaluated to solve nonlinear problems by an automatic updating of the set-up to assure the numerical convergence and an accurate result.

5.2 The Extended Finite Element Method

The extended finite element method (XFEM), also known as generalized finite element method (GFEM) or partition of unity method (PUM) is a numerical technique that extends the classical finite element method (FEM) approach. Tools for solving to differential equations with discontinuous functions are included. The XFEM was developed to analyze problems with localized features, which cannot efficiently solved by a mesh refinement. A relevant application is modeling of fracture in the materials. Discontinuous basis functions are added to the standard polynomial basis functions for elements that are intersected by a crack, to include the crack opening displacements. A key advantage of XFEM is that in such problems the finite element mesh does not need to be updated to track the crack path. Subsequent research has demonstrated the more general use of the method for problems involving singularities, material interfaces, regular meshing of micro structural features such as voids, and other problems where a

localized feature can be described by an appropriate set of basis functions. It was shown that for some problems, such an embedding of the problem's feature into the approximation space could significantly improve convergence rates and accuracy. Moreover, treating problems with discontinuities with XFEM suppresses the need update and refine the mesh of discontinuity surfaces, thus alleviating the computational costs and errors associated with conventional finite element methods [51].

In XFEM, a discontinuous function and the two-dimensional asymptotic crack-tip displacement fields are added to the finite element approximation to account for the crack, by using the notion of “partition of unity”. This enables the domain to be modeled by finite elements with no explicit meshing of the crack surfaces. The initial crack geometry is represented by level set functions, and subsequently signed distance functions are used to compute the enrichment functions that appear in the displacement-based finite element approximation. The method has basically been developed in Northwestern University.

5.3 The Crack Box Technique

In order to use this technique one has to automatically create a transition zone between the ‘‘crack box’’ and the whole structural unchanged mesh. According to Fig 2.5 three regions can be detected around the crack tip:

• Zone (A): “Crack box”. It contains a specific and regular mesh. It is affected by the asymptotic solution at the crack tip. For elastic calculations, few elements are needed. The crack tip is modeled with degenerated quadratic elements with one side collapsed and mid side nodes are moved to the quarter point nearest the crack tip to create a strain singularity in $\frac{1}{\sqrt{r}}$ (r is the distance from the crack tip). For plastic calculations, more elements are needed to precisely determine the J-integral. To introduce a $\frac{1}{r}$ singularity for perfectly plastic material strains, degenerated quadratic elements are also used but crack tip nodes are allowed to move independently and mid side nodes remain at the mid side point. For Ramberg–Osgood materials, it has been checked that the latter mesh allows to globally approximating the $\frac{1}{\sqrt[n+1]{r^n}}$ strain field (n is the hardening coefficient).

• Zone (B): “Transition region”. It contains an optimized linear (for elastic calculations) or quadratic (to increase precision for elastic and plastic calculations) displacement field associated to triangular mesh obtained with the Delaunay triangulation procedure from NAG (Numerical Algorithms Group). This allows connecting the specific crack box with the whole ABAQUS model, which can be either a 2D model or a 3D shell model. The border of this region is automatically defined as a function of the crack path previously calculated.

• Zone (C): “Whole Model”. It represents a usual finite element mesh. It is to be noted that this mesh is unchanged during the crack propagation.

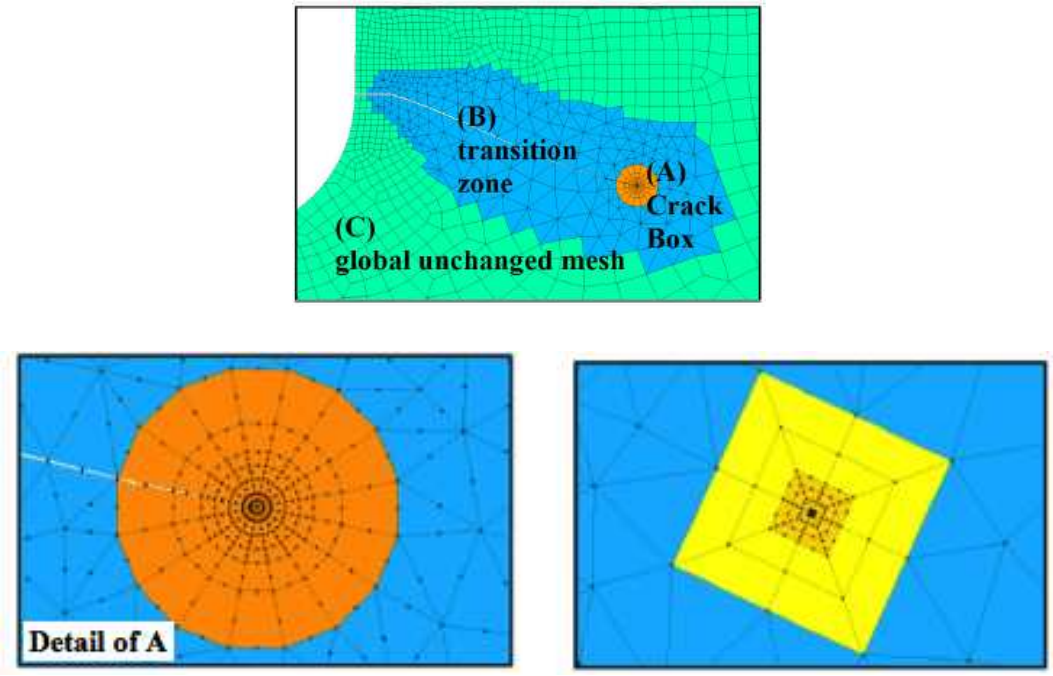

Fig 2.5: Crack box technique and different zone around crack tip and different mesh [29]

Creation of a crack box by an automatic procedure was used in this thesis is to develop a numerical tool by using the ABAQUS© code. Some steps are foreseen:

1) Meshing of the three regions for the initial crack.

2) Performing FEM calculation. An elastic or elastic–plastic criterion is used to calculate the direction of the crack extension.

3) Increasing the crack length in the calculated direction. The increment of crack Δa is mesh dependent. Influence of the crack extension can be taken into account by calculating the crack direction for different values of Δa until convergence. In this work the crack box size was set at the crack increment and the ratio dJ/da was then checked to be lower than a prescribed value. This criterion can be introduced during the crack simulation by subdividing the crack extension in the case it is not fulfilled with the default value.

4) Updating the local crack tip region mesh and connecting it to the whole structure by region B. Actually the region (B) works such a moving contour around the crack tip. It looks like a static condensation of the structural behaviour to the crack tip region. This technique is almost similar to boundary integral equations in which the transition zone replaces the contour [59].

5.4 The boundary element method (BEM)

Boundary elements show considerable promise as a means of both elastic and elasto-plastic analysis of the crack propagation. The boundary element method (BEM) is a numerical computational method of solving linear partial differential equations, which have been formulated as integral equations (i.e. in boundary integral form). It can be applied in many areas of engineering and science including fluid mechanics, acoustics, electro magnetics, and fracture mechanics. In electro magnetics, the more traditional term "method of moments" is often, though not always, synonymous with "boundary element method".

The integral equations may be regarded as an exact solution of the governing partial differential equation. The BEM attempts to use the given boundary conditions to fit boundary values into the integral equation, rather than values throughout the space defined by a partial differential equation. Once this is done, in the post-processing stage, the integral equation can then be used again to calculate numerically the solution directly at any desired point in the interior of the solution domain.

BEM is applicable to problems for which Green's functions can be calculated. These usually involve fields in linear homogeneous media. This places considerable restrictions

on the range and generality of problems to which boundary elements can be usefully applied. Nonlinearities can be included in the formulation, although they will generally introduce volume integrals, which then require the volume to be discretized before solution, removing one of the most often cited advantages of BEM. A useful technique for treating the volume integral without discretizing the volume is the “dual-reciprocity method”. This technique approximates part of the integrand by using radial basis functions (local interpolating functions) and converts the volume integral into boundary integral after collocating at selected points distributed throughout the volume domain (including the boundary). In the dual-reciprocity BEM, although there is no need to discretize the volume into meshes, unknowns at chosen points inside the solution domain are involved in the linear algebraic equations approximating the problem being considered [60].

The Green's function elements connecting pairs of source and field patches defined by the mesh form a matrix, which is solved numerically. Unless the Green's function is well behaved, at least for pairs of patches near each other, the Green's function must be integrated over either or both the source patch and the field patch. The form of the method in which the integrals over the source and field patches are the same is called "Galerkin's method". Galerkin's method is the obvious approach for problems, which are symmetrical with respect to exchanging the source and field points. The cost of computation involved in naive Galerkin implementations is typically quite severe. One must loop over elements twice (so we get n^2 passes through) and for each pair of elements it loops through Gauss points in the elements producing a multiplicative factor proportional to the number of Gauss-points squared. Also, the function evaluations required are typically quite expensive, involving trigonometric/hyperbolic function calls. Nonetheless, the principal source of the computational cost is this double-loop over elements producing a fully populated matrix [61].

The Green's functions, or fundamental solutions, are often problematic to integrate as they are based on a solution of the system equations subject to a singularity load (e.g. the electrical field arising from a point charge). Integrating such singular fields is not easy. For simple element geometries (e.g. planar triangles) analytical integration can be used. For more general elements, it is possible to design purely numerical schemes that adapt to the singularity, but at great computational cost. Of course, when source point and target element (where the integration is done) are far-apart, the local gradient surrounding the

point need not be quantified exactly and it becomes possible to integrate easily due to the smooth decay of the fundamental solution. It is this feature that is typically employed in schemes designed to accelerate boundary element problem calculations.

The BEM is often more efficient than other methods, including FEM, in terms of computational resources for problems where there is a small surface/volume ratio. Conceptually, it works by constructing a "mesh" over the modeled surface. However, for many problems boundary element methods are significantly less efficient than volume-discretization methods (finite element method, finite difference method, finite volume method). Boundary element formulations typically give rise to fully populated matrices. This means that storage requirements and computational time will tend to grow according to the square of the problem size. By converse, FEM matrices are typically banded (elements are only locally connected) and storage requirements for the system matrices typically grow quite linearly with the problem size. Compression techniques can be used to ameliorate these problems, though at the cost of added complexity and with a success-rate that depends heavily on the nature of the problem being solved and the geometry involved.

Some BEM advantages can be highly defined:

- The mesh is reduced in one dimension only.
- Automatic satisfaction of the radiation conditions at infinity is assured.
- Ability to capture high stress gradients is provided.
- Easy implementation of elements modeling crack-tip fields in fracture is offered.

Nevertheless the BEM exhibits some disadvantages like, singular integrations and need appropriate fundamental solution [62].

Part Two

Prediction of fracture mechanics in passive structures

CHAPTER 3

MODELING FRACTURE MECHANICS IN SINGLE LAYER OF METALLIC MATERIAL

1 INTRODUCTION

To assure a suitable design tool for fracture mechanics using the ABAQUS© code a preliminary implementation in case of a single layer of metal was performed. To develop this activity the AISI 4340 steel was selected and numerical investigations were performed by analyzing what happens during a standard fracture test upon three points bending specimen.

1.1 Material selection: AISI Steel 4340

Practical industrial applications currently use many kinds of steel, being either cast directly to shape, or into ingots, which are reheated and hot worked into a wrought shape by forging, extrusion, rolling, or other processes [63]. Wrought steels are the most common engineering material used, and come in a variety of forms with different finishes and properties. Alloy steels are steels that exceed the element limits for Carbon. However, they containing more than 3.99% Chromium are classified differently as stainless and tool steels. Alloy steels also contain elements not found in carbon steels such as nickel, chromium (up to 3.99%), cobalt, etc.

The typical elastic modulus of alloy steels at room temperature (25°C) ranges from 190 to 210 GPa. The density of alloy steels is about 7.85 g/cm^3 and tensile strength varies between 758 and 1882 MPa. The wide range of ultimate tensile strength is largely due to different heat treatment conditions.Among the number of steels used, the AISI 4340 is quite popular and very often was used to test design tool against fracture in the literature. The AISI 4340 is a low alloy steel containing nominally 0.4% C, 0.8% Cr, 0.25% Mo and 1.8% Ni. Higher strength levels up to 1,03 GPa may be achieved by suitable heat treatment. It is often used in instead of AISI 4140 at the higher strength levels because of its better hardenability. Due to availability this grade is often substituted with European based standards 817M40, EN24 and 1.6528 34CrNiMo6; which are similar but have a slightly lower nominal nickel content of 1.5% and higher nominal chromium content of 1.3%. The hardenability limitations of this grade (depth to which it will harden / obtain the specified mechanical properties after heat treatment) must always be taken into account when designing and selecting equipment. Component of the AISI 4340 is described in Table 3.1.

Table 3.1: Composition of AISI 4340 steel [63]

Element	**Weight %**
C	0.38-0.43
Mn	0.60-0.80
P	0.035 (max)
S	0.04 (max)
Si	0.15-0.30
Cr	0.70-0.90
Ni	1.65-2.00
Mo	0.20-0.30

Tables 3.2 and 3.3 show some mechanical, thermal and electrical properties of the AISI 4340 steel.

Table 3.2: Thermal properties of AISI 4340 steel [63]

Properties		Conditions	
		T (°C)	Treatment
Thermal Expansion (10^{-6}/ºC)	11.5	20-100	Oil hardened, tempered 630°C

Table 3.3: Mechanical and electrical properties of AISI 4340 steel [63]

Properties		Conditions	
		T (°C)	Treatment
Density (g/cm^3)	7.7-8.03	25	
Poisson's Ratio	0.27-0.30	25	
Elastic Modulus (GPa)	190-210	25	
Tensile Strength (MPa)	744.6	25	annealed at 810°C
Yield Strength (MPa)	472.3		
Elongation (%)	22.0		
Reduction in Area (%)	49.9		
Hardness (HB)	217	25	annealed at 810°C
Electric Resistivity (10^{-9}W-m)	248	20	-

The AISI 4340 steel is often used for structural applications, such as aircraft landing gear, power transmission gears and shafts and other structural parts. It uses in heavy-duty axles, shafts, heavy-duty gears, spindles, pins, studs, collets, bolts, couplings, sprockets, pinions, torsion bars, connecting rods, crowbars, conveyor parts etc. The Table 3.4 shows the characteristics of AISI 4340 steel in different process and situations.

Table 3.4: characteristics of AISI 4340 steel in different processes [63]

Principal Design Features	AISI 4340 is heat treatable, low alloy steel containing nickel, chromium and molybdenum. It is known for its toughness and capability of developing high strength in the heat-treated condition while retaining good fatigue strength.
Machinability	Machining is best done with this alloy in the annealed or normalized and tempered condition. It can be machined by all conventional methods. However in the high strength conditions of 200 ksi or greater the machinability is only from 25% to 10% that of the alloy in the annealed condition.
Forming	4340 has good ductility in the annealed condition and most forming operations are carried out in that condition. It can be bent or formed by spinning or pressing in the annealed state.
Welding	The alloy can be fusion or resistance welded. Preheat and post heat weld procedures should be followed when welding this alloy by established methods.
Heat Treatment	Heat treatment for strengthening is done at 1525 °F followed by an oil quench. For high strength (over 200 ksi) the alloy should first be normalized at 1650 °F prior to heat treatment. See "Tempering" for strength levels.
Hot Working	4340 has very good cold forming capability so that hot working should not be needed. Hot working in any but the annealed condition can affect the strength level. Consult the alloy supplier in regard to hot working.
Cold Working	The 4340 alloy may be cold worked, in the annealed condition, by conventional methods and tooling. It has good ductility.
Hardening	The alloy will harden by cold working or by heat treatment -- see "Heat Treatment" and "Tempering".

1.2 Test case for modeling

Numerical model was aimed at predicting the behaviour of material in a structural fracture test performed by bending a specimen. Three loading conditions were analyzed to evaluate several parameters of fracture mechanic such as SIF, J-Integral, crack propagation and life prediction. Specimen looks like in Fig 3.1 and is the so-called “three point bending specimen” (3PB). Dimensions are specified in Table 3.5.
Three modes were investigated in this analysis. A first sample is operated in first mode category of fracture mechanics, while the two others are operated in mixed mode fracture.

Table 3.5: Dimension of specimen

Specimen	Length	Width	Thickness	Length of Crack
Dimension [mm]	180	40	30	20

A first loading condition corresponds to the first mode of fracture mechanics (single mode). As Fig 3.1 shows load is applied in the middle of specimen being supported at the two ends. Crack located in the middle of specimen length, and has a initial length of 20 mm.

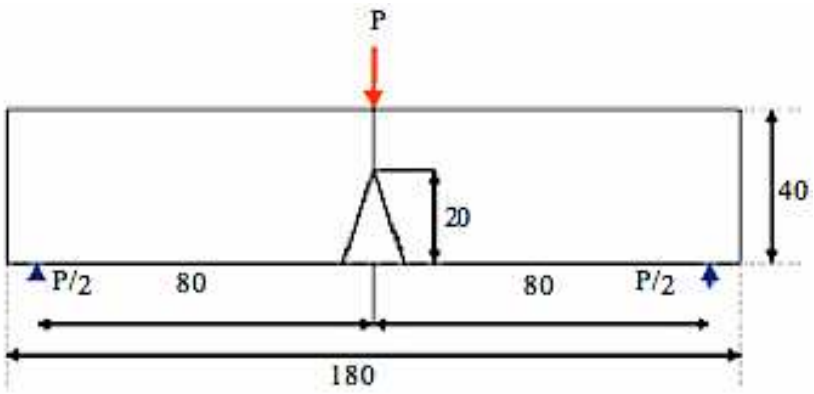

Fig 3.1: Test with fracture mode “A” [64]

The second test case corresponds to mixed mode of fracture mechanics, which is shown in Fig 3.2. Load is in the middle of specimen so as mixed mode fracture is no more applied. Crack excited closer to the left hinge and has an initial length of 20mm.

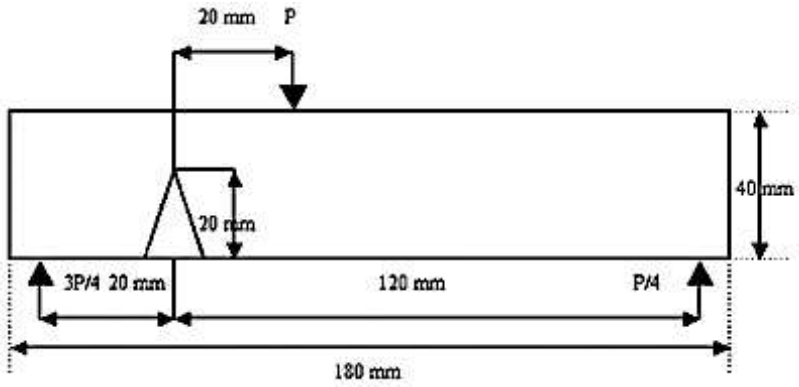

Fig 3.2: Test case of “mode B” [64]

A third case was then analyzed. Even in this one a mixed mode of fracture mechanics is operated. A Fig 3.3 shows, two load points with different amplitude of load are defined. Load at left side is 3/8 of other one; supports are positioned differently with pervious case, no more and simply at the two ends of specimen. Initial crack is 20 mm long. 3P/8 86 24 180 36 74

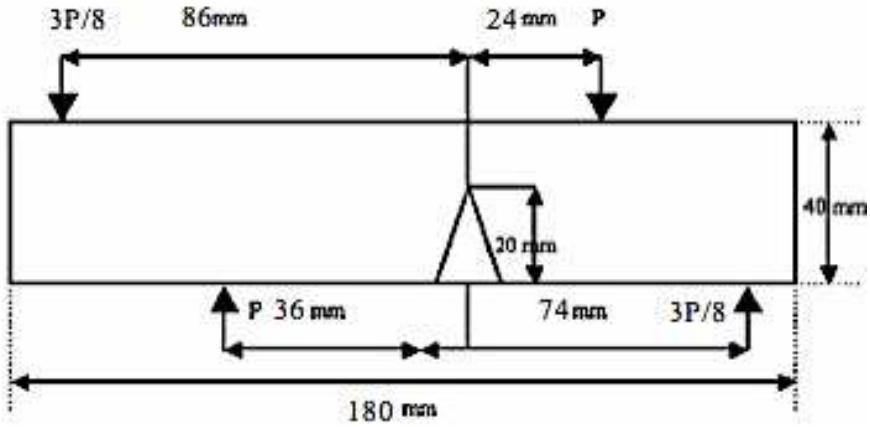

Fig 3.3: Test case of “mode C” [64]

2 Fracture analysis performed by analytical approach

2.1 Calculation of Stress Intensity Factor

To perform a fracture analysis the Stress Intensity Factor (SIF) of the mode tested is preliminary computed. Magnitude of this parameter depends on several factors, such as, the geometry of structure, the size of crack and its location and the loading condition in case of 3PB specimen and test mode A previously described. (Fig 3.4)
Condition for propagation is:

$$K_I=K_{IC} \tag{3.1}$$

Where K_I is SIF for mode I and K_{IC} the toughness of material for propagation mode I and critical force P_c required to have propagation is found.

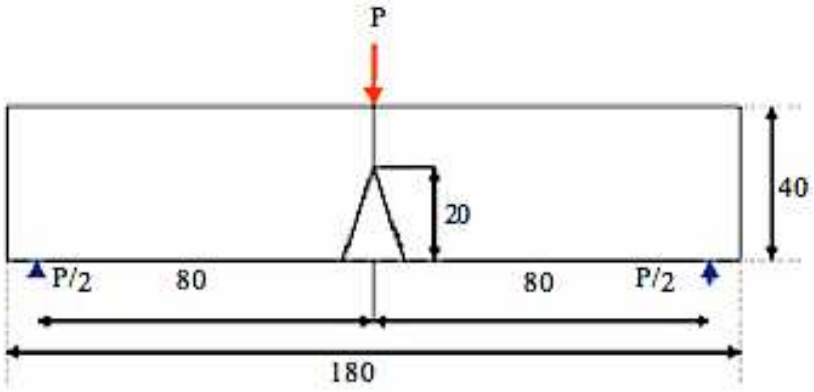

Fig 3.4: Three point bending specimen's sketch (3PB) [64]

Fracture toughness of the AISI 4340 is K_{IC}=48MPa. Expression for K_I is [65]:

$$K_I=\frac{Ps}{tW^{3/2}} f_{11}\left(\frac{a}{W}\right) \tag{3.2}$$

$$f_{11}\left(\frac{a}{W}\right)=\frac{\sqrt[3]{\frac{a}{W}}}{2\left(1+2\frac{a}{W}\right)\left(1-\frac{a}{W}\right)^{3/2}}\left[1.99-\frac{a}{W}\left(1-\frac{a}{W}\right)\left(2.15-3.93\frac{a}{W}+2{,}7\left(\frac{a}{W}\right)^2\right)\right] \tag{3.3}$$

Where: s is the length of the beam (between the two supports)
a is the crack height in beam
t is the thickness of beam
W is the width of beam
P is the force applied
f_{11} (a/w) is the geometric function, depending on a and W, respectively.

As Fig 3.4 shows, a=20 mm, s=160 mm, t=30 mm, W=40 mm, while P is the unknown force applied, therefore:

$$f_{11}(\frac{a}{W})=\frac{\sqrt[3]{\frac{a}{W}}}{2\left(1+2\frac{a}{W}\right)(1-\frac{a}{W})^{3/2}}\left[1.99-\frac{a}{W}\left(1-\frac{a}{W}\right)\left(2.15-3.93\frac{a}{W}+2{,}7\left(\frac{a}{W}\right)^2\right)\right] \quad (3.4)$$

- so, $f_{11}(\frac{a}{W})$= 2.67.

$$K_I=\frac{Ps}{tW^{3/2}}f_{11}(\frac{a}{W}) \quad (3.5)$$

Provided that K_{IC}= 48 MPa, so critical load is:

P_{cr} =28.17 KN

To investigate the behaviour of the 3PB specimen, load P was increased from low N up to P_C, by some steps and K_I was computed.

P_1=10 KN so K_I=17.75 MPa
P_2=15 KN so K_I=26.62 MPa
P_3=20 KN so K_I=35.5 MPa

It is worthy noticing that very often material undergoes cyclic loading. In this case distribution of stress inside the specimen and around the crack tip changes accordingly to instantaneous load applied. This effect is important when plastic region is analyzed since material undergoes tensile and compressive stress alternately, Moreover, fatigue of

material affects the fracture behaviour, therefore fracture analysis is faced an alternate stress which lead to have an alternate SIF.

Maximum and minimum values of stress intensity factor during the load period, usually K_{Imax} and K_{Imin} are computed and their ratio is defined as $R = K_{Imax} / K_{Imin}$. Life of cracked component is strongly affected by the amplitude and frequency of cyclic load as well as environmental factors, such as corrosion and temperature.

An example of cyclic loading is shown in Fig 3.5. When crack propagation is undergoing this condition stress intensity factor range ΔK_I is analyzed instead of a single value K_I, like in statics.

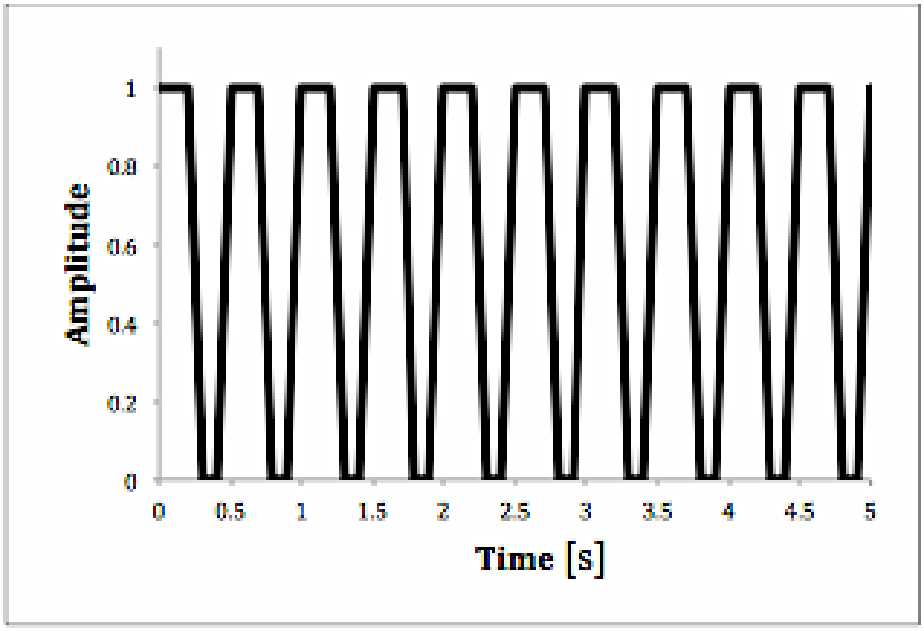

Fig 3.5: Example of applied cyclic loading.

In particular dynamic definition of stress intensity factor K_I is:

$\Delta K_I = K_{Imax} - K_{Imin}$ if $K_{Imin} \geq 0$

$\Delta K_I = K_{Imax}$ if $K_{Imin} < 0$

$\Delta K_I = 0$ if $K_{Imax} > 0$

2.2 J-Integral

An alternative way of analyzing fracture mechanics in Abaqus is by computing the J-Integral. J-integral allows characterizing the singularity of the stress field in proximity of the crack. In a pure 2D cracked and linear elastic medium, Rice (1968) defined as J the follow integral of contour:

$$J=\int\Gamma\{W_e n_1 - \sigma_{ij}\, n_j \frac{\delta ui}{\delta x1}\}ds \quad (3.6)$$

Where W_e is the density of elastic strain energy and Γ is a contour around the crack tip. Since the crack is supposed as straight along its axis. n is the normal vector to the contour, $\sigma_{ij}\, n_j$ is the applied stress to the contour and u_i is the corresponding displacement. (See Fig 3.6):

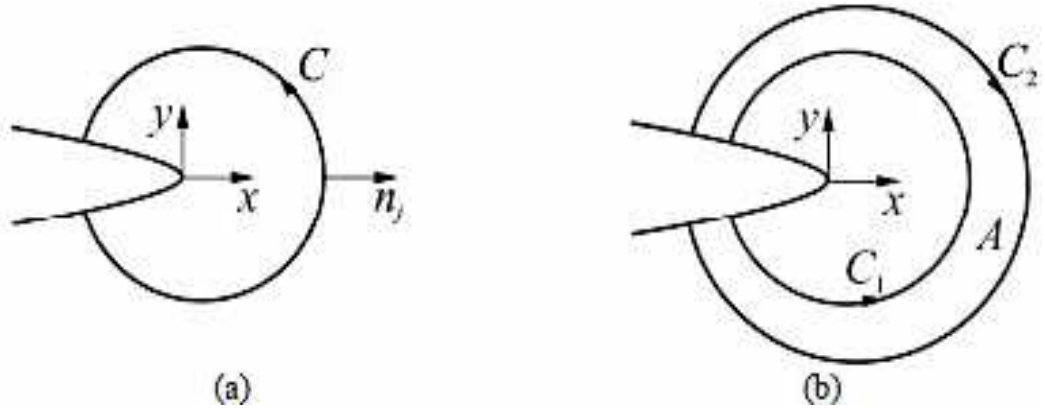

Fig 3.6: Integral path for the J integral [30]

As it was already mentioned stress intensity factor and J integral are selected as follow (for linear elastic media):

$$J=K_I^2/ E' \quad (3.7)$$

Being $E'=E$ for plane stress, $E' = E/(1-\nu^2)$ for plane strain and E is the Young's modulus, while ν is Poison's ratio.

2.3 Crack Propagation in standard specimen under bending

According to the Paris's law, the fatigue growth rate da/dN is related to range ΔK_I as in Fig 3.7, being "a" crack length and N the number of loading cycles.

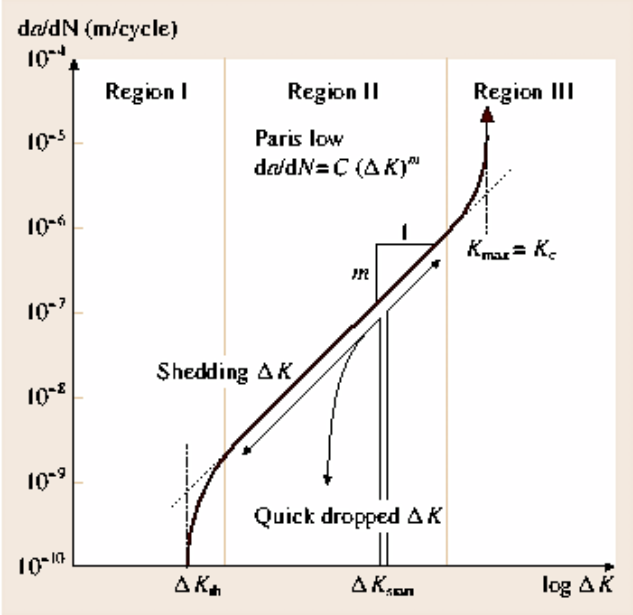

Fig 3.7: Fatigue growth rate by Paris's law [19]

Fracture behaviour is characterized by three regions, crack starts to grow when $\Delta K_I > \Delta K_{th}$, i.e. the threshold value. After a preliminary transient growth, crack propagates with a good speed and Paris' law can predict this behaviour. Only when $\Delta K_I > \Delta K_{IC}$ propagation suddenly becomes faster and unstable.

In region II, Paris' low states that:

$$\log \frac{da}{dN} = n \log \Delta K_I + C \qquad (3.8)$$

Above equation (3.6) describes the original formulation:

$$\frac{da}{dN} = C\,(\Delta K_I)^n \qquad (3.9)$$

C and n can be considered as the material properties. Paris also points out that for metallic materials, often 2 < n < 4 (n is dimensionless). Like in other domains of structural mechanics a safety factor n_S can be applied. It is always larger than unity, to assure safety against collapse.

If safety factor is assumed to be n_s=1.8, the other parameters are in the test case:

C= 1 e-11 (MPa^4m), n=3 and so far if ΔK_I = 17.75 ($MN/m^{3/2}$), fracture behaviour of AISI 4340 is described by: $\frac{da}{dN} = C\,(\Delta K_I)^n = 5.5 * e^{10}$.

It can be observed that if variables, are separated the crack length "a" can be selected to the number of cycles N as follows:

$$\int_{a_0}^{a_1} \frac{da}{\{\sqrt{a} f(a)\}^n} = C\,(\Delta\sigma\sqrt{\Pi})^n \int_0^N dN \qquad (3.10)$$

This analytical approach is very useful if one would predict the number of cycles N required to reach a certain length of:

$$N = \frac{1}{C\,(\Delta\sigma\infty\sqrt{\Pi} f_0)^{2.8}} \left(\frac{a_1^{\frac{2.8}{2}+1} - a_0^{-\frac{2.8}{2}+1}}{-\frac{2.8}{2}+1}\right) \qquad (3.11)$$

In particular when $\Delta K_I = \Delta K_{IC}$ the number of cycles required for the rupture to material propagation can be found. Nevertheless, a very often designer is prone to assume a safety factor to avoid that this condition might occur. Hence fracture toughness K_{IC} is usually divided by the safety factor, for instance n_S=1.8. In this case:

$K_{ICS} = (K_{IC}/n_s)$= 27.777 $MN/m^{3/2}$.

According to the above interpretation maximum stress can be found as $K_I = \sigma_\infty . \sqrt{\Pi a} f$, f is the function of geometry and in test case f=2.67, therefore σ_∞ = 26.596 ≈2 7 MPa.
Model allows predicting the crack length for given number of cycles, if K_{IC} is used the final length is a_f = 45.12 mm, which is bigger than the specimen width.

$$N= \frac{1}{C\,(\Delta\sigma\infty\sqrt{\Pi}f_0)^{2.8}} \left(\frac{a_1^{\frac{2.8}{2}+1}-a_0^{-\frac{2.8}{2}+1}}{-\frac{2.8}{2}+1}\right) = 3.4553*e5.$$

Therefore it can be found that to have a complete propagation of crack through the specimen width (40 mm) are required $3.4553*e^5 \approx 34500$ cycles if load is P=10KN and initial crack length is 20mm.

3 FEM analysis by means of the ABAQUS© code

3.1 Static analysis

In the PRE-PROCESSING activity of the FEM modeling the specimen geometries sketched. This is done by creating a "part" in which the 2D geometry is first drawn, elements are then defined, type deformable and shell's shape. As the sketch is carried out by using various commands, like lines, auto trim, fillet etc. and result looks like in Fig 3.8.

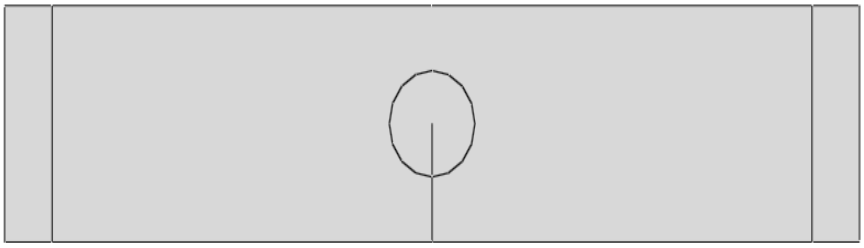

Fig 3.8: Model of specimen created inside the part module of the ABAQUS

Material for the sketched part then is selected directly from the "material" menu, and properties are inputted. In case of 4340 steel, it is elastic defined as having Young's modulus equal to 210 GPa and Poisson's ratio 0.29. Moreover to predict even the plastic behaviour curve σ-ε is given as in Fig 3.9.

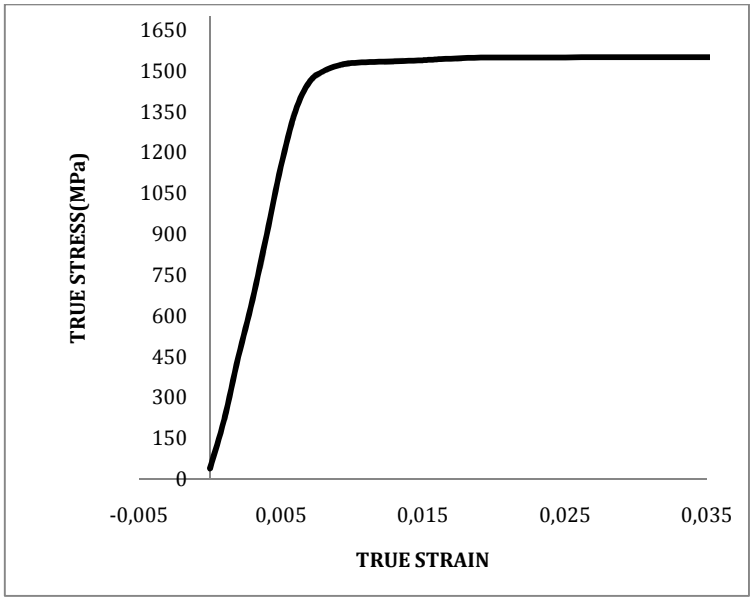

Fig 3.9: Stress vs. strain curve of the AISI 4340 Steel [66]

Once the material and its properties are defined. It can be defined by using the “sections” menu and selecting category “solid” and type “homogenous”.

Sub-menu “instances” under “assembly” allows creating some independent parts. Since the model involves analysis of a crack, never defined until now, it can be defined in the sub-menu “engineering features” under “assembly”. Defining crack requires defining the crack contour, tip and propagation direction. In particular crack propagation direction is defined through q-vectors, i.e. by selecting the crack start and end point, respectively. As soon as these parameters are defined data in the dialog box are filled. It is even required specifying that analysis is being carried out for half-section of the model and singularity parameters. For static analysis with elastic fracture mechanics, in the second-order mesh options field, size is described by entering a value of 0.25 for the mid side node parameter, to move the mid side nodes to the quarter points. In the degenerate element control at crack Tip/Line field, option “Collapsed element side, single node” is entered. The type of analysis can be chosen from menu ”steps” and analysis type chosen is “general static”.

To prepare the post-processing ABAQUS requires even “Field output requests” and “History output requests”, being sub-menus of (type of analysis). Field outputs as J-

integral and Stress Intensity Factors were selected to perform the J-integral computation. Ten contours were required.

Load is a concentrated force and can be created in ABAQUS in the “load” menu, by selecting the mechanical category and “concentrated force” in type of selected step. Two boundary conditions were defined in the “boundary condition-menu” concerning the displacement/rotation conditions at the two supports.

Mesh assignment was done at the “Mesh part”, inside the circle around the crack, the “sweep technique” was chosen while the technique was preferred in the outer portion of the specimen. The plane strain assumption was selected inside the element options (CPE4R). Fig 3.10 shows the model after meshing.

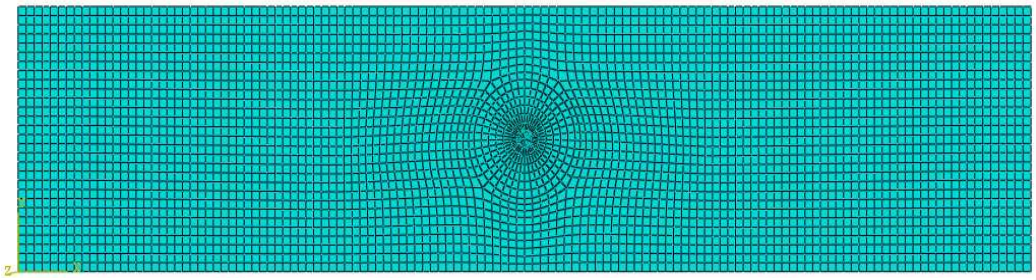

Fig 3.10: Meshed model of specimen

Solution starts by opening a new job inside the selected “job” menu, computed results are then analyzed by selecting the “result menu” where the stress intensity factor and energy release rate are included.

Fig 3.11 shows some results of the ABAQUS© code and stress distribution around the crack tip, it should be mentioned that, stress distribution in all cases inside the thesis is Von mises stress.

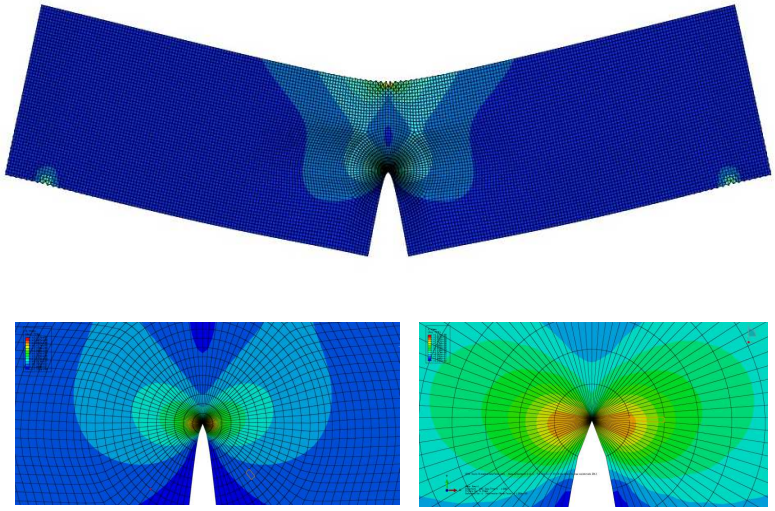

Fig 3.11: Stress distribution around the crack tip after analyzing in Abaqus

Numerical results are obtained for the test case where these correspond to those computed by the analytical approach, as it shall be deeply described later in this thesis.

3.2 Dynamic analysis

When applied load is cyclic a dynamic analysis is required. Procedure looks similar to the static analysis, although some parameters have to be changed.

Value of 0.5 for the mid-side node parameters is selected instead of 0.25 to keep the midside nodes at the midside points. and in the degenerate element control at crack tip field, “collapsed element side, duplicate node” is suggested. In the “step module”, dynamic and implicit is the type of analysis step and a proper time period and step interval time have to be defined. In the general dynamic analysis the loading is “cyclic impulse”. A tabular format is available in this menu to create the cycle for the specific time period.

In static analysis, the axis which describes the value of time strictly depends on the law of increasing loading condition for bending imposed during the fracture test, inparticular absolute value of time, which are described inside the graph depends on the rate of the applied load which can be different, test by test. In case of dynamic analysis, this is related to the frequency of the cycles which simulate the fatigue condition, from this point of you, inside the analysis, time axis describes the sequence of loading condition

and related crack length applied during simulation, in this case the absolute values are more significant because they are related to the time history of the cycles applied.

3.3 Preliminary numerical results of SIF and J-Integral

After modeling the specimen inside the Abaqus code and running, results were collected and discussed. A first comparison between the set of results obtained through the FEM and those found by the analytical approach is proposed in Table 3.6.

Table 3.6: Computation of SIF for several values of static load

Load [KN]	Analytical [MPa]	FEM Plane stress [MPa]	FEM Plane strain [MPa]	Error
10	17.75	17.35	17.35	About 2.2%
15	26.625	26.03	26.03	
20	35.5	34.7	34.7	

Stress intensity factor for several values of static load were computed by the FEM code and compared to those obtained by the analytical approach. It can be observed that option about the plane state poorly changes the results and the different between those analytical and numerical approaches are quite small (2.2-2.3%). To investigate the role of mesh refinement a dedicated activity was performed and results are shown in Table 3.7.

Table 3.7: Stress intensity factor computed by FEM code with different number of elements according to mesh size

Load case	Number of elements	Stress Intensity Factor (Plane stress) [MPa]
10KN, Static	3970	17.12
10KN, Static	8654	17.27
10KN, Static	15230	17.35

It can be observed that approximation improves but with an increasing computational effort Figs 3.12 and 3.13 show the value of energy release rate and stress intensity factor during the static analysis. As it was expected energy release rate nonlinearly grown up with load while SIF linearly follows the increasingly values of load.

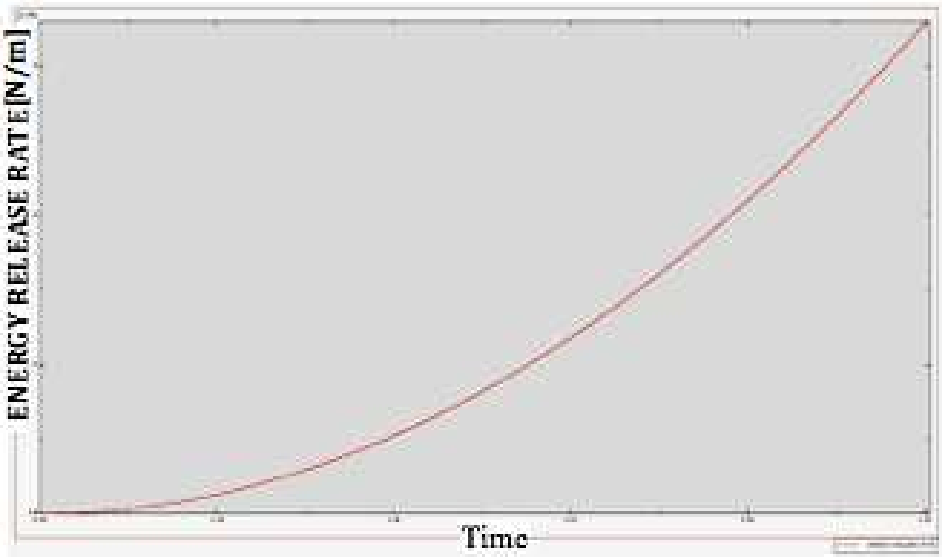

Fig 3.12: Energy release rate as computed by Abaqus.

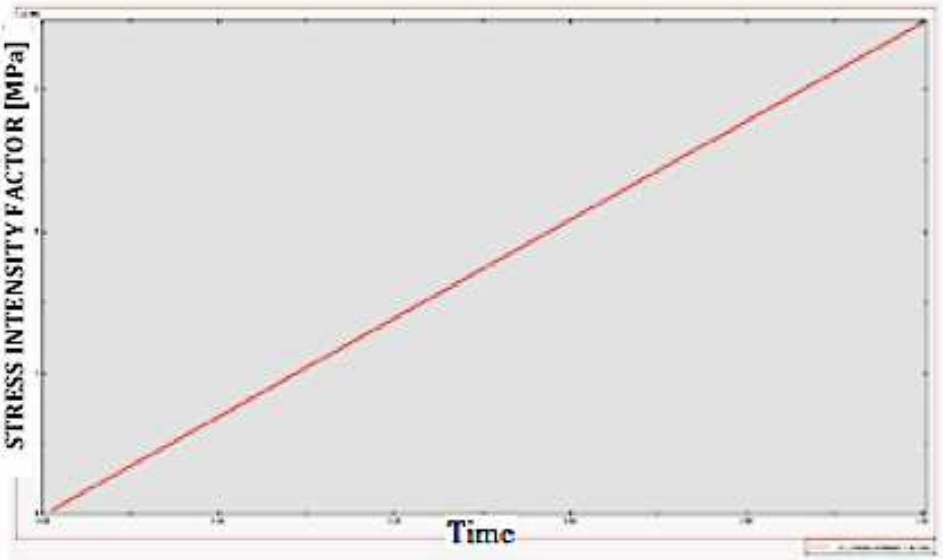

Fig 3.13: Stress Intensity Factor as computed by Abaqus.

The number of contours used to perform the analysis is greatly important to reach a good approximation. In particular, it is known that in case of plastic behaviour the results are not independent on the contours seleced. Figs 3.14 and 3.15 present the energy release

rate and stress intensity factors for different number of counters. First three contours show fairly different values, it's due to the fact that they are too close to singularity.

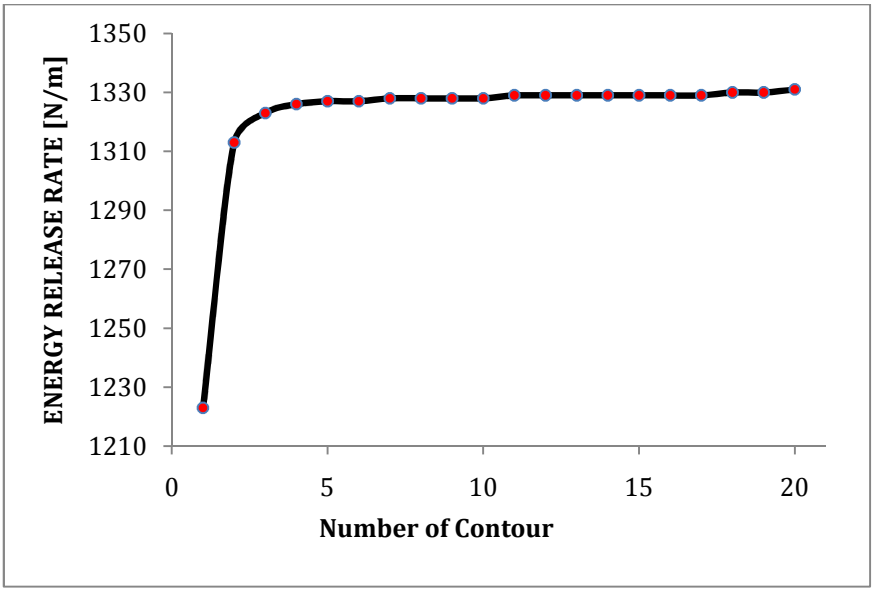

Fig 3.14: J-Integral vs. number of contours

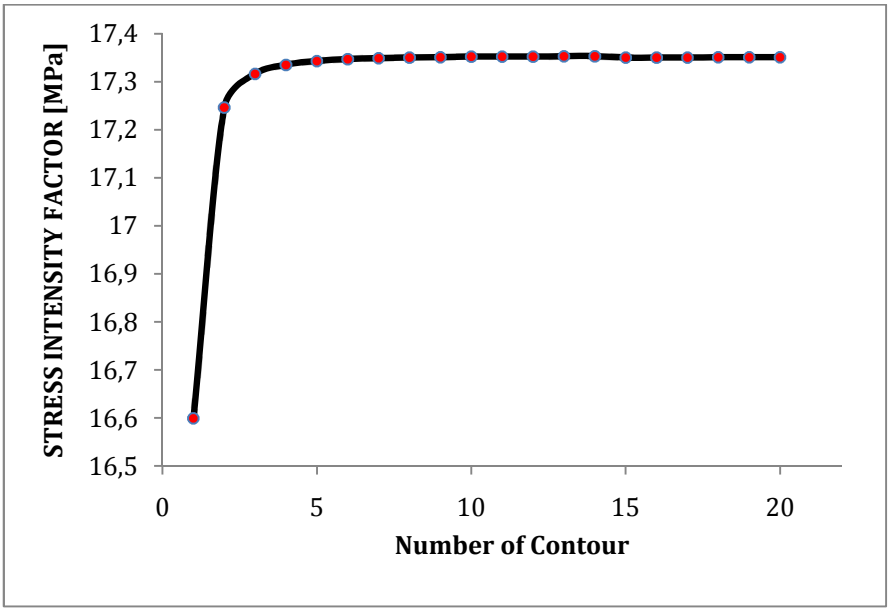

Fig 3.15: Stress intensity factor vs. number of contours

As Figs show contour selected to perform the computation of J and SIF respectively has to be sufficiently for the crack tip to avoid any numerical problem of singularity, but then they are stable even when selected counters are more far from the tip. Cyclic load in dynamic analysis was considered, some results are collected, Table 3.8 shows the value

of stress intensity factor and energy release rate in two cyclic load conditions, 120 cycles per minute and 240 cycles per minute, i.e. for cycles with different geometry. The value of SIF in two conditions is so close and three numbers after dot is used to show the difference between these conditions.

Table 3.8: J-integral and Stress Intensity Factor computed by Abaqus with cycles of different frequency

Dynamic Analysis	Stress Intensity factor [MPa]	Energy Release rate [K/N]
10 KN (120 cycles per min)	17.852	1376
10 KN (240 cycles per min)	17.854	1377

In this case, for given maximum load, SIF ΔK is very close to the theoretical value and a little bit higher than in static analysis for given mesh size. This is a consequence of selecting a large value in second-order mesh option, nevertheless values are compatible with the applied load. Following Figs present the graph of stress intensity factor and energy release rate during the time period under the cyclic load (120 cycle/min).

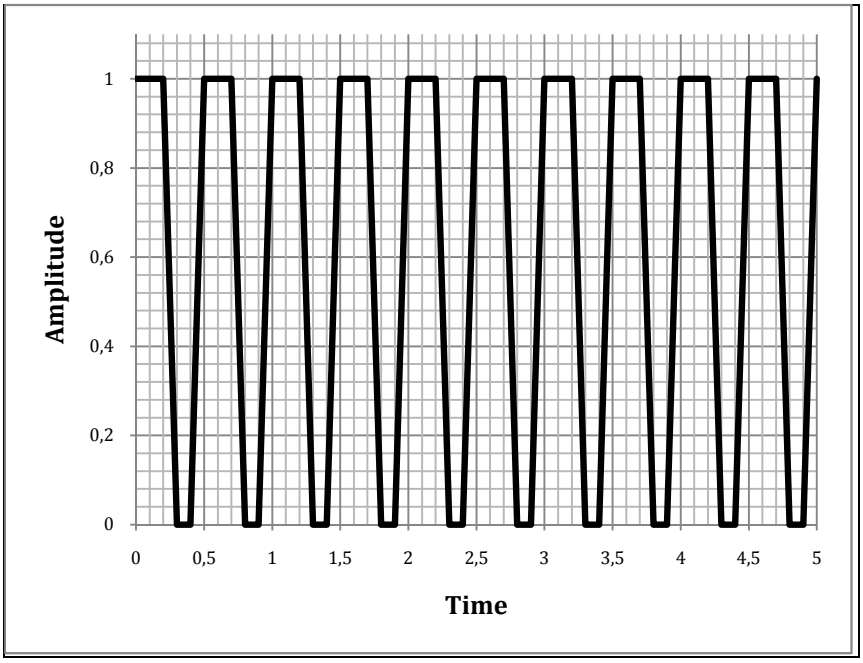

Fig 3.16: Load amplitude factor vs. time for 120 cycles/min

The following Fig 3.17 presents the value of Stress Intensity Factor of steel in dynamic load (120 cycle per minute).

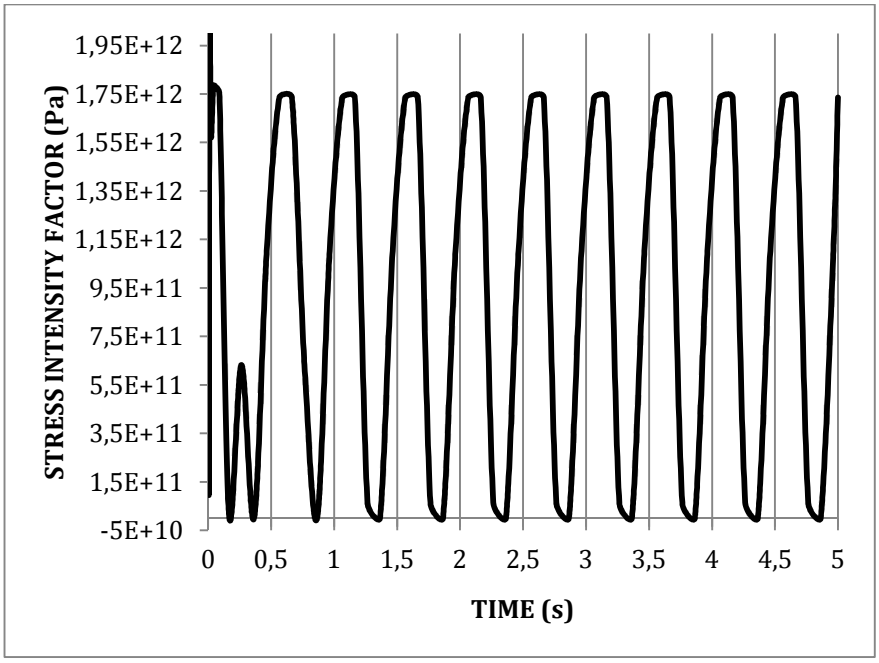

Fig 3.17: Stress Intensity Factor vs. time

The following Fig 3.18 presents the value of J-integral of steel in dynamic load (120 cycle per minute).

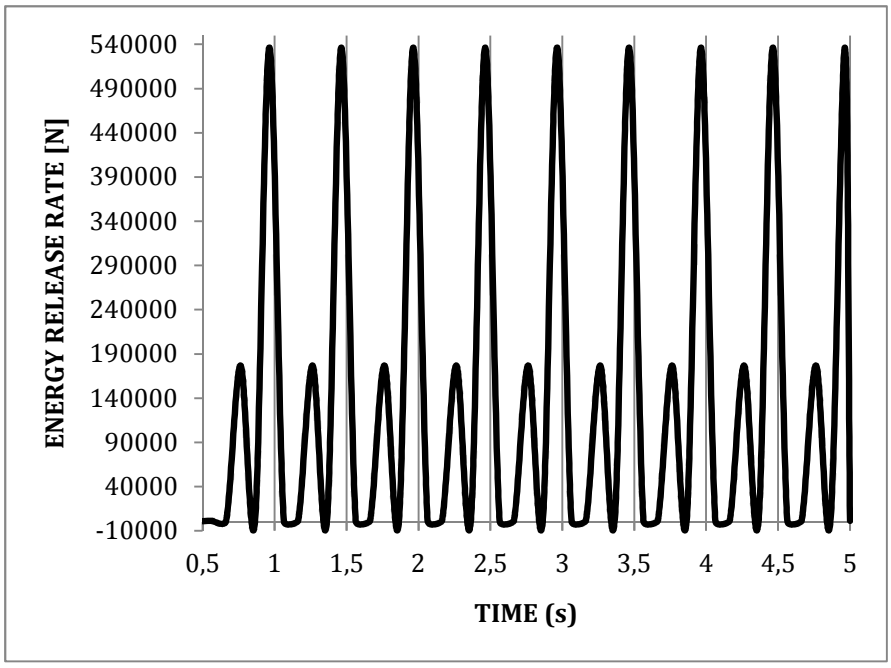

Fig 3.18: The J-integral values diagram during the time in 120 cycles

The following Fig 3.19 and 3.20 present the value of Stress Intensity Factor and J-integral diagram obtained from Abaqus results in dynamic load (240 cycle per min):

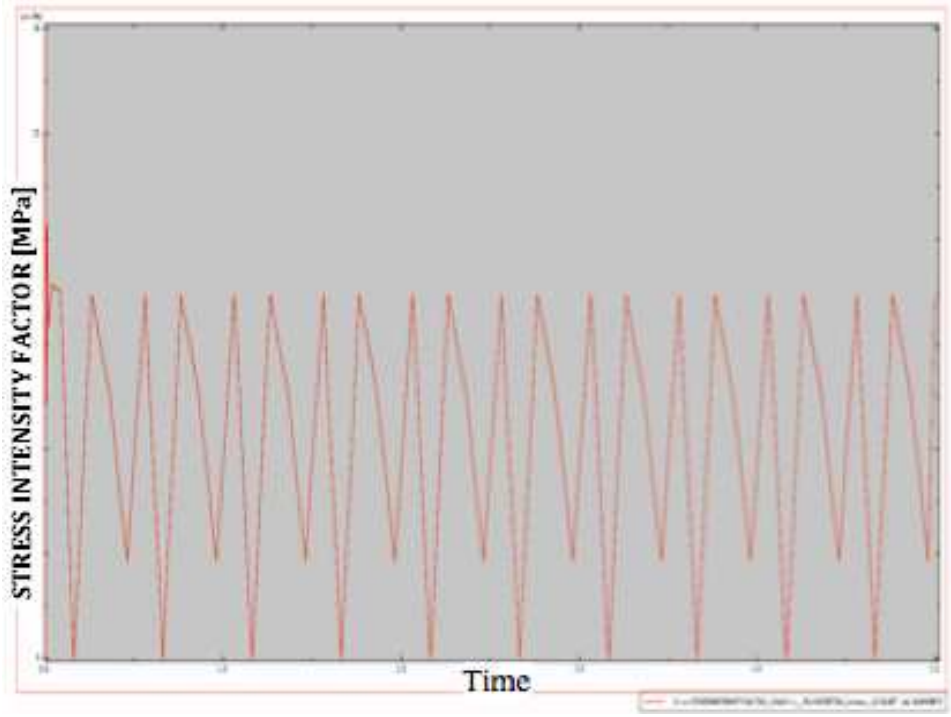

Fig 3.19: The stress intensity factor values diagram in 240 cycles/min

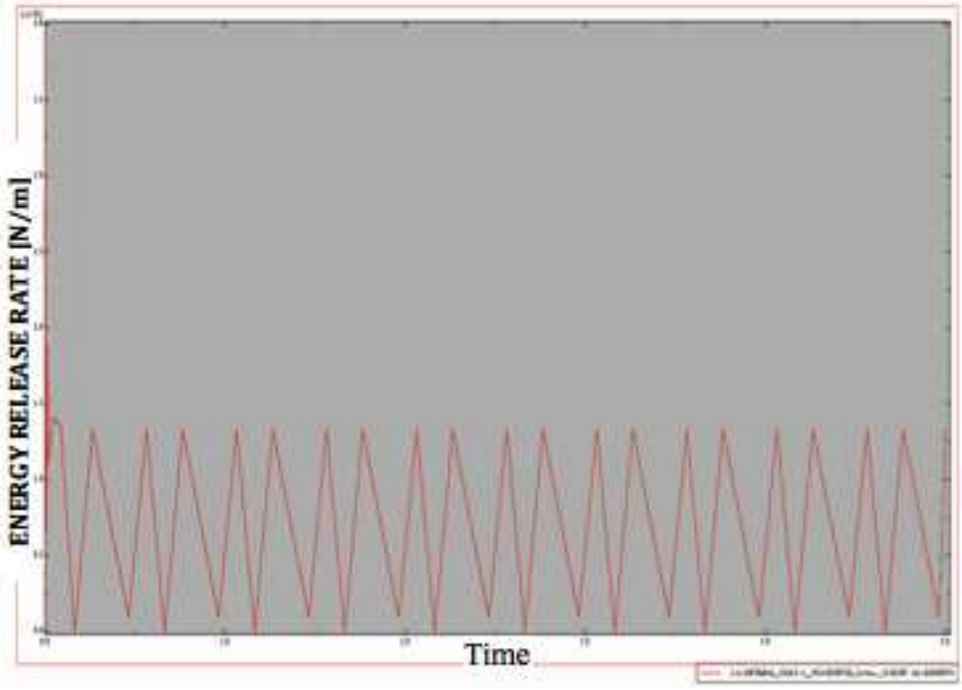

Fig 3.20: The J-integral values diagram in 240 cycles/min

3.4 Numerical investigation in mixed mode

In the second part of the analyses of 4340 steel, the mixed mode B was selected to the complete this preliminary investigation. Specimen used for modeling activity is depicted in Fig 3.2.

As Fig 3.21 shows distribution of stress is partly irregular and no were symmetric like it looked in mode A. Procedure follows in the numerical investigation was the same of previous case, but here load and crack location are different.

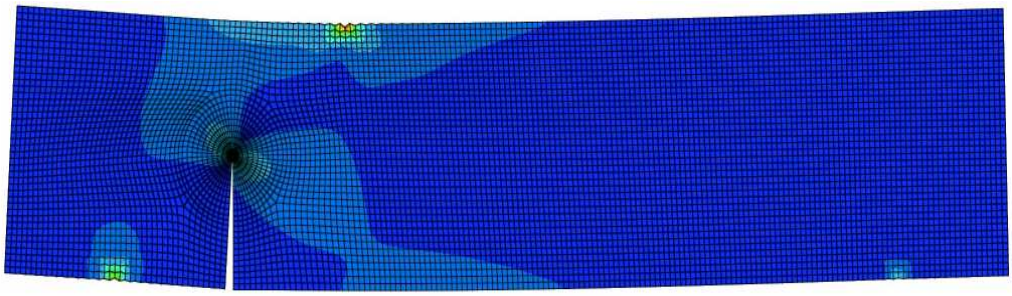

Fig 3.21: Stress distribution around the crack tip in mode B

The J integral and stress intensity factor in case of both mode II and I are described in Tables 3.9 and 3.10.

Table 3.9: The J-integral for different contours and mixed mode analysis

Contour	1	2	3	4	5	6	7	8	9	10
J-Integral [N/m]	200	214.4	216	216.4	216.6	216.7	216.8	216.8	216.9	216.9

Table 3.10: The K_I and K_{II} for different contours and mixed mode analysis

Contour	1	2	3	4	5	6	7	8	9	10
K_I [MPa]	6.904	6.658	6.684	6.691	6.694	6.696	6.696	6.697	6.697	6.698
K_{II} [MPa]	1.958	2.034	2.042	2.045	2.046	2.046	2.046	2.046	2.046	2.046

Energy release rate and Stress intensity factor graph per contours are shown in Figs 3.22 and 3.23.

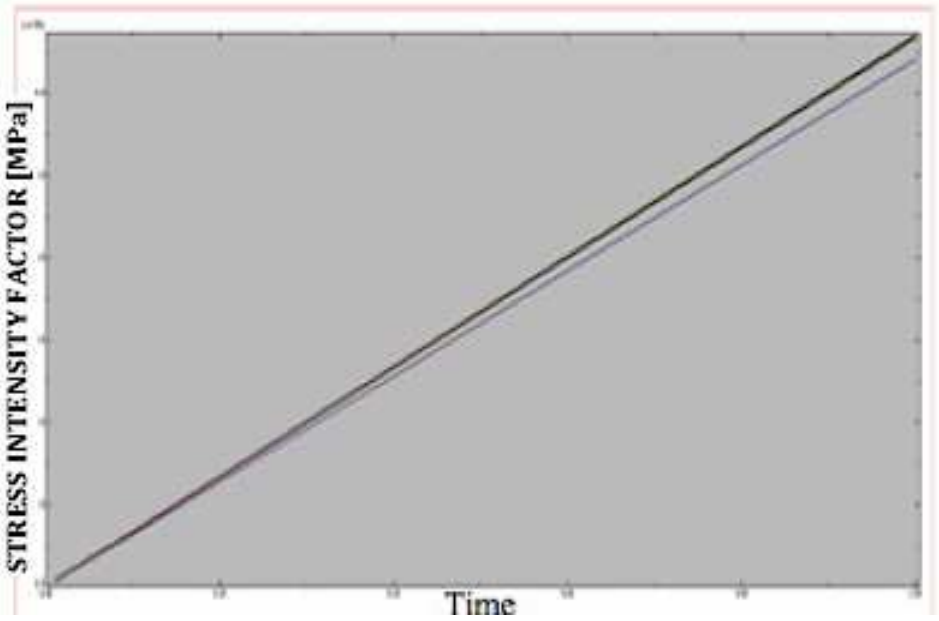

Fig 3.22: The stress intensity factor values during the time.

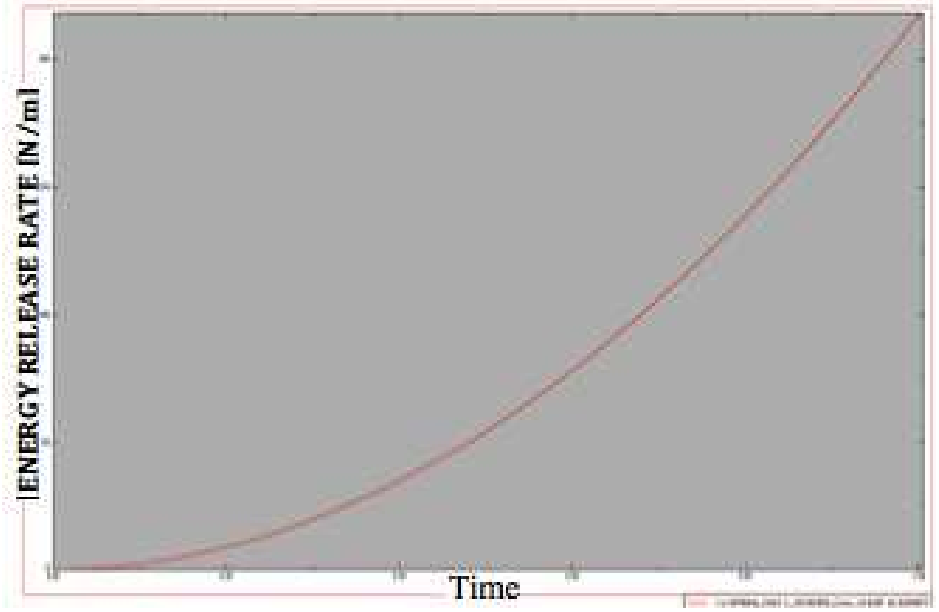

Fig 3.23: The J-integral values during the time.

According to the above tables of stress intensity factor K_I could be set at $6.697*10^6$ and K_{II} at 2.046 and J integral to 216.8.

Mixed mode C was finally evaluated, specimen is sketched in Fig 3.3 Numerical investigation was performed like in previous cases. Fig 3.24 describes the stress distribution inside the specimen, while Table 3.11 do for SIF and J-Integral.

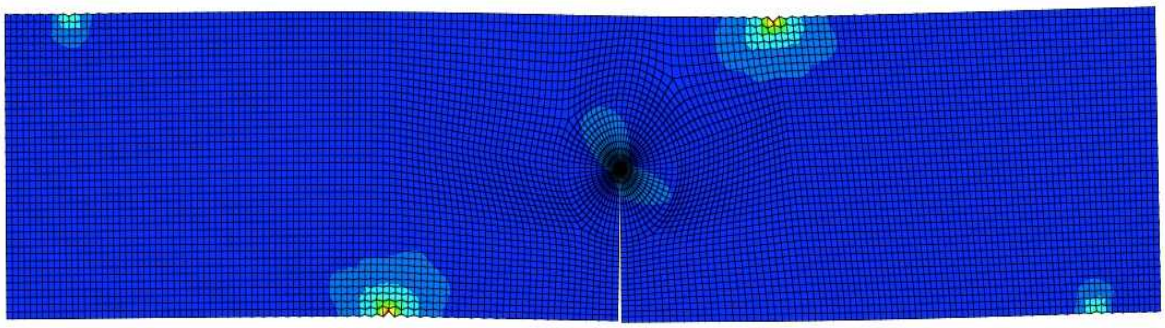

Fig 3.24: Stress distribution inside the model after analysis.

Table 3.11: The J integral value in different contours for mixed mode analysis

Contour	1	2	3	4	5	6	7	8	9	10
J-Integral [N/m]	25.99	28.05	28.28	28.34	28.37	28.38	28.39	28.39	28.4	28.41

Table 3.12: The K_I and K_{II} and different integral contours of mixed mode analysis

Contour	1	2	3	4	5	6	7	8	9	10
K_I [MPa]	1.7371	1.804	1.811	1.813	1.814	1.815	1.815	1.815	1.815	1.815
K_{II}[MPa]	1.7159	1.782	1.789	1.79	1.792	1.792	1.793	1.793	1.793	1.793

As tables point out K_I is about 1.18152 e6, and K_{II} is $1.7936*10^6$ the J integral is 28.4.

3.5 Discussion about numerical results

- Summarized results for mode A, B, C

Results collected in Tables 3.13 and 3.14 show that SIF and J integral in mode A are larger than of other modes, Although in mode B they are greater than mode C. Stress intensity factor is depending on the sample geometry, size and location of crack, and the magnitude and distribution of loads. Larger value of K_I and J in mode A are due to the location of crack and loads, being leading to a stress distribution around the crack tip larger than in the other cases.

Table 3.13: Stress intensity factor in three modes analyzed.

Modes	Stress Intensity Factor Values KI [MPa]
Mode A	17.35
Mode B	6.69
Mode C	1.18

Table 3.14: J-integral in three modes analyzed

Modes	J-Integral [N/m]
Mode A	1383
Mode B	216.8
Mode C	28.4

- Comparison of stress distribution in the three modes analyzed

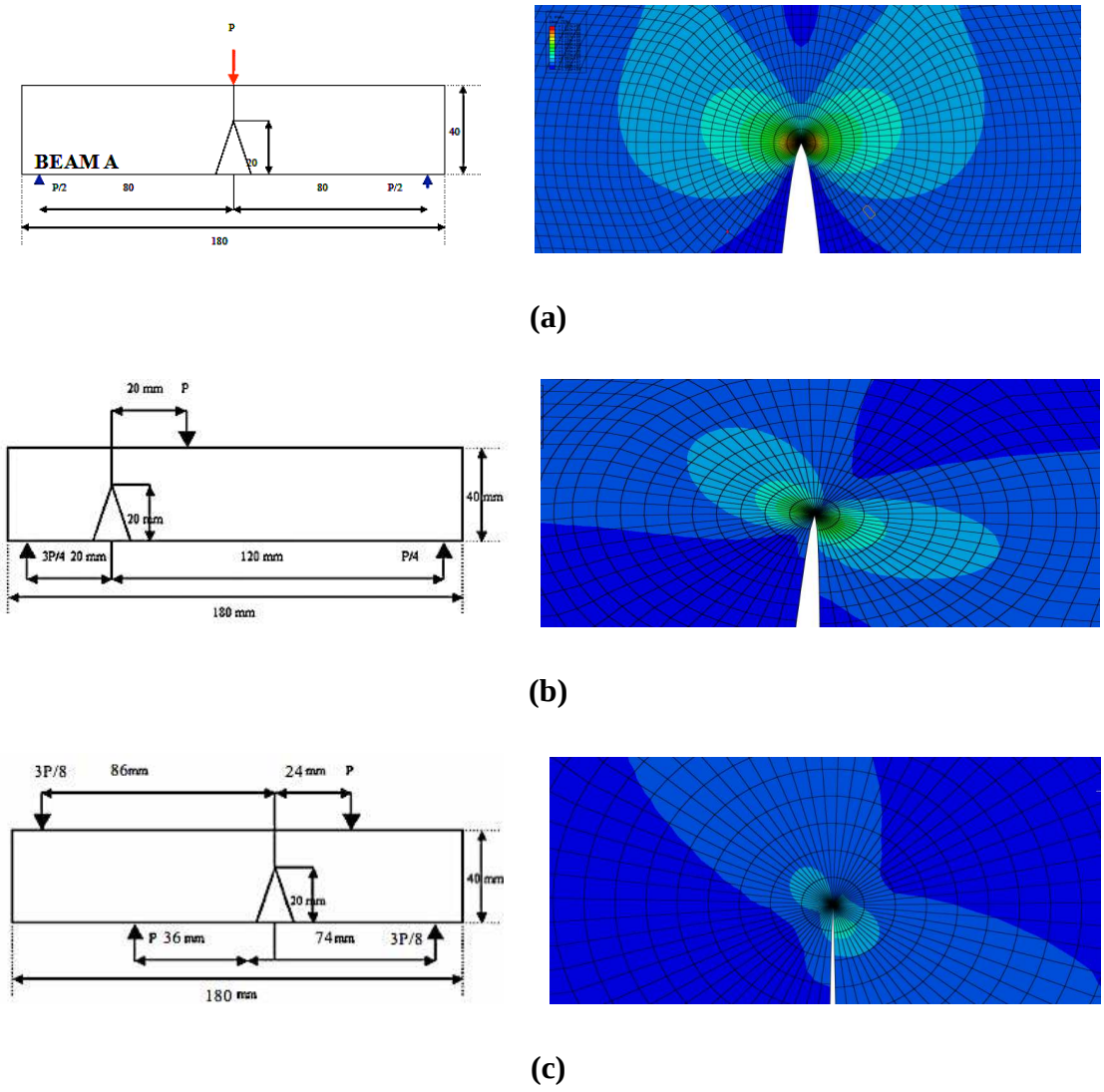

Fig 3.25: Stress distribution around the crack tip in mode A, B and C

Fig 3.25 points out that crack opening is fairly different in the three analyzed modes. Location of load, constraints and crack in stress concentration is larger in A, slightly less in B and smaller in C. Therefore K tend to be bigger, intermediate and smaller in the sequence.

- Analysis of numerical results and model validation

To validate the model developed inside the ABAQUS© code, the test case used by Kwiatkowski and Dębski [67] was used. The Authors of that paper performed numerical calculation of the stress intensity factor and of the J-Integral in case of the three point bending of SENB (single edge notched beam) composites samples with a matrix made of two thermoplastics: PP and PA6 glass fiber. Numerical calculations were aimed at predicting the experimental behavior and at determining the conditions of crack process initiation of the composite material. Results were then verified by experiments. Specimen analyzed and tested is shown in sketch of Fig 3.26.

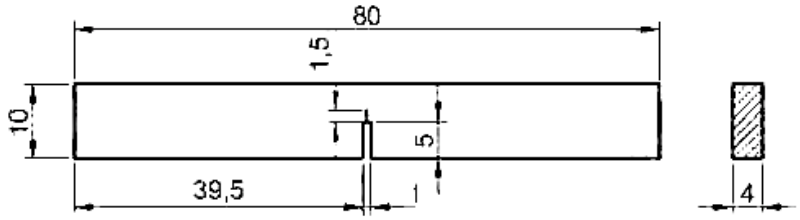

Fig 3.26**:** Sketch of the standard specimen SENB used as a test case by kwiatkowski and Dębski [67]

It can be remarked that the analyzed test case looks a like test more complicated than the characterized of the AISI 4340 steel because the SENB in composite material exhibits a non-isotropic behaviour because of the different mathematical properties along two orthogonal directions. Nevertheless it could be appreciated that a good agreement between the ABAQUS model here in developed and the test case could confirm the validity of the proposed numerical implementation.

After modeling the specimen inside the ABAQUS code and once those properties of this composite were inputted, analysis was performed for some values of the initial crack length. Numerical results of SIF were then compared to those obtained in. As Fig 3.27 shows values of K_I agree with the test case.

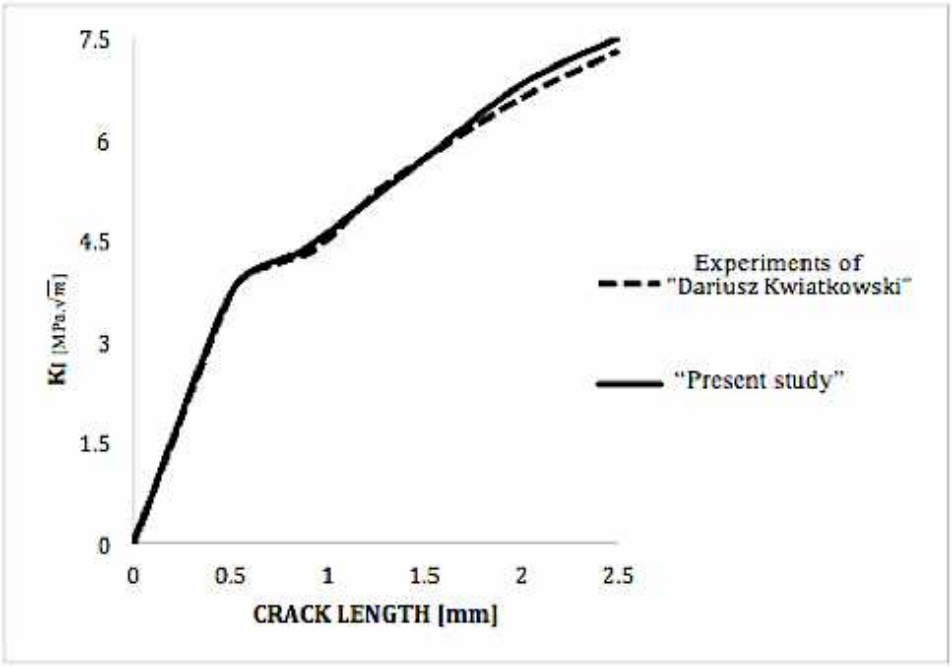

Fig 3.27: Comparison of K_I of SENB component material between Kwiatkowski - Dębski and ABAQUS results

- Sensitivity analysis upon fracture

After a preliminary assessment of the numerical procedure in the Abaqus code, the tool was used to investigate the sensitivity of SIF and of J-integral on some parameters like the magnitude of load, the thickness of the structure and the crack length. In the case of the computation of the J-integral, both the conditions of elastic and elastic-plastic behavior of material were considered. Material used as a test case was the AISI 4340 steel.

A) Influence of the loading condition on the failure criteria

Magnitude of applied load affects quite a lot the energy release rate and the stress intensity factor of the proposed test case. The energy release rate of crack was evaluated by calculating the J-integral. As Fig 3.28 shows for increasing values of applied load the energy release rate nonlinearly grows up, but the assumption of elastic-plastic behavior involves a larger rate, in accordance with the literature [68].

It can be noticed that for the material tested difference is appreciable. Up to the critical

value of load crack propagation is stable and difference between the two assumptions looks limited. Above the critical load (P_{cr}= 28KN) propagation becomes faster and differences are more evident. For this material the influence of the plastic region around the tip tends to be relevant since the increment of localized energy is correspondingly quite high. Table 3.15 presents values of J-Integral for different load magnitude in both elastic and elastic-plastic conditions.

Table 3.15: Values of J-integral for different load magnitudes

Loads [KN]	5	10	15	20	25	30	35	40	45	50
J-Integral Elastic [N/m]	332	1330	2992	5320	8312	11970	16299	21288	26943	33263
J-Integral Elastic-Plastic [N/m]	369	1914	4818	9021	14483	21164	29035	38076	48273	59655

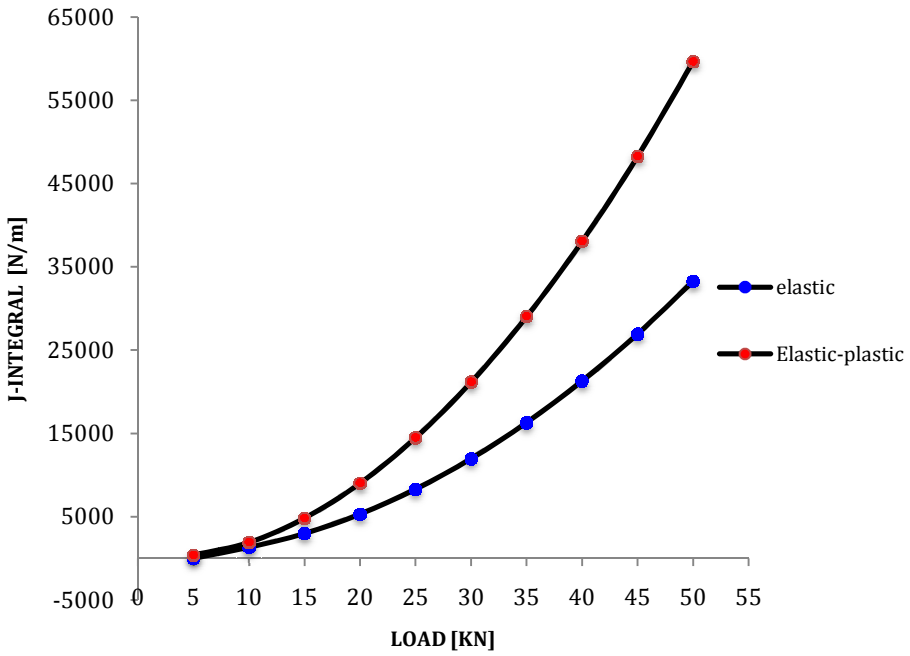

Fig 3.28: Computed value of J-Integral with thickness of 30 mm, crack length of 20 mm made of AISI 4340

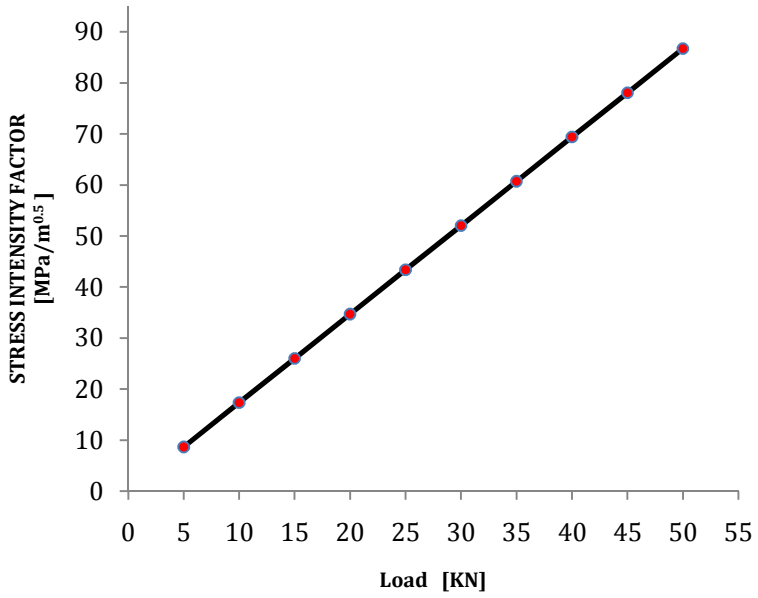

Fig 3.29. Stress Intensity Factor vs. applied load for specimen with thickness of 30 mm, crack length of 20 mm for the AISI 4340 steel

Above numerical results are agreeing with the analytical computation of the S.I.F., under the assumption of elastic behavior. Fig 3.29 points out that relation between S.I.F. and applied load is almost linear, for the given configuration.

Table 3.16 collects values of Stress Intensity Factor calculated for several load magnitudes in both elastic and elastic-plastic behaviors.

Table 3.16: Values of SIF for different load magnitudes

Loads [KN]	5	10	15	20	25	30	35	40	45	50
S.I.F [MPa]	8.67	17.35	26.02	34.7	43.37	52.05	60.72	69.4	78.07	86.75

Influence of load was analyzed by using the same model, but with different materials, to compare their performance. Fig 3.30 shows the case of the EH 36 steel.

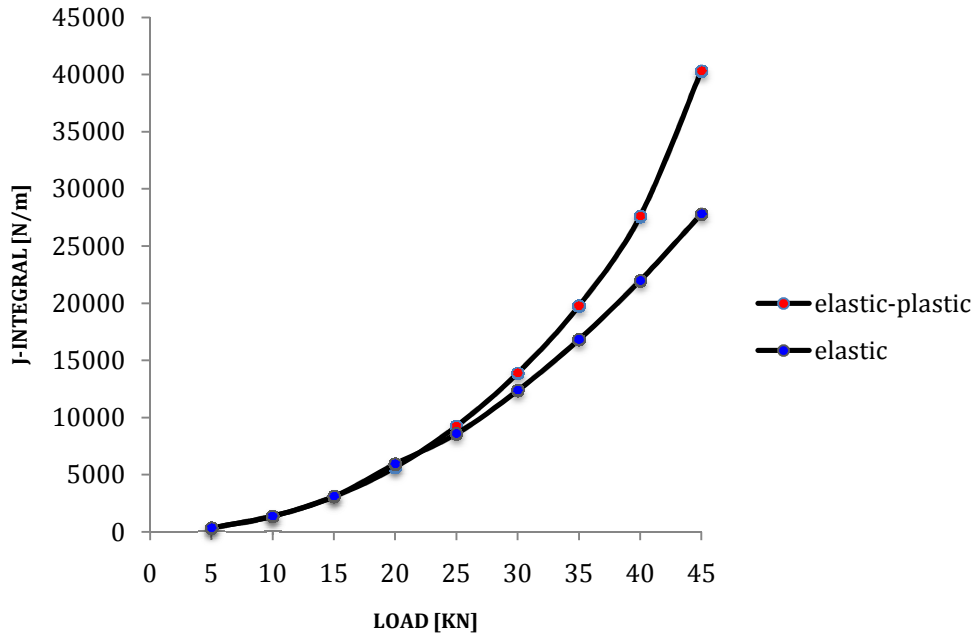

Fig 3.30. J-Integral vs. load for specimen with thickness of 30 mm, crack length of 20 mm, for the EH36 steel

As far as Fig 3.28 and Fig 3.30 show the analyzed steel AISI 4340 exhibits a behavior against the crack propagation fairly different if effect of plasticity is included. This result is motivated by the mechanical properties of the selected steel, whose mechanical strength is fairly high, but the behavior is ductile, with a large plastic effect in the stress vs. strain curve (Fig 3.10). A suitable prediction of the plastic region around the tip is a key issue of design of mechanical components made of this material. Moreover, in case of stress concentration and notches the steel AIAS 4340 offers a good recovery of the stress, thus increasing the potential life of the component against fatigue.

B) Influence of the crack length on the failure criteria

Sensitivity upon the initial crack length was even analyzed. Some values of crack length were assumed to perform the numerical investigation through the computation of the J-integral first and the S.I.F. Table 3.17 summarizes some values of J-integral in obtained for some values of crack lengths in both elastic and elastic-plastic conditions.

Table 3.17: Values of J-integral calculated for some crack lengths

Crack length (mm)	5	10	15	20	25	30
J-Integral Elastic [N/m]	158.7	322.4	687.8	1330	2880	10984
J-Integral Elastic-Plastic [N/m]	168	364.2	850.7	1903	4742	19717

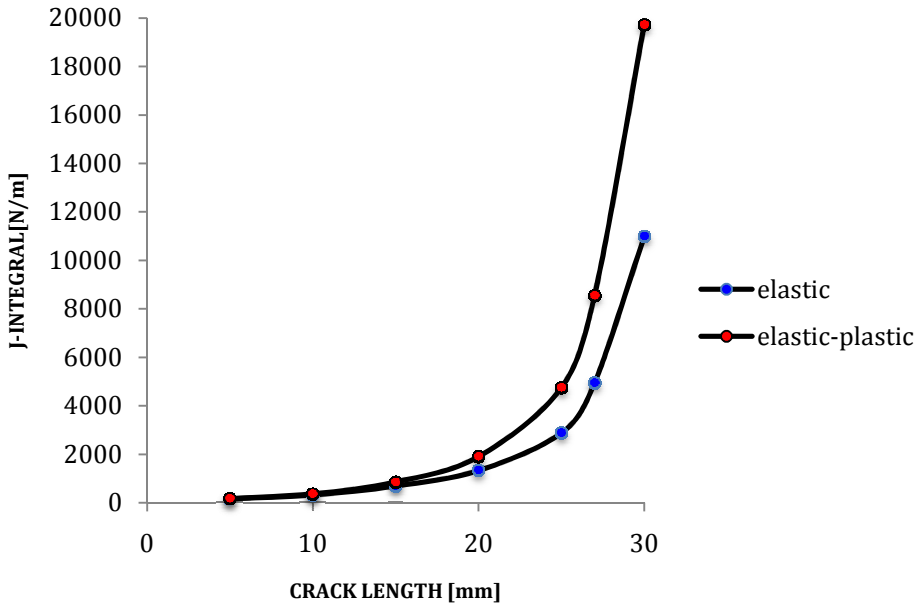

Fig 3.31: J-Integral vs. crack length for applied load of 10 KN, thickness of 30 mm and AISI 4340 steel.

Table 3.18 presents values of Stress Intensity Factor for different crack lengths.

Table 3.18: Stress Intensity Factor for different crack lengths

Crack length [mm]	5	10	15	20	25	30
S.I.F [MPa]	6.09	8.86	12.24	17.35	27.11	49.71

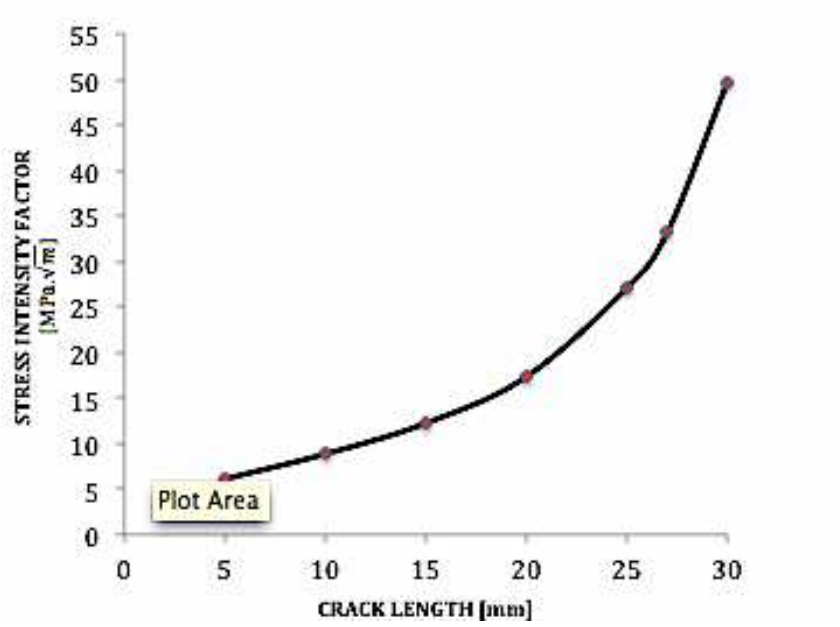

Fig 3.32: Stress Intensity Factor, for applied load of 10 KN, thickness of 30 mm and AISI 4340 steel

In this case longer initial cracks induce an evident effect upon the Stress Intensity Factor and energy release rate. It can be remarked that a discontinuity in both the diagrams of Fig 3.31 and 3.32 respectively is detected in correspondence of the critical condition, for the unstable propagation (P_{CR}=28 KN). This result is motivated, by the facts that as crack length is increased for a given applied load, stress distribution around the crack tip increases as well as the S.I.F. and the energy release rate grows up. When critical value of load is reached, the J-Integral and the Stress Intensity Factor show a magnified rate, i.e. the curve slope is much more evident.

C) Influence of thickness on the failure criteria

Above investigation did not consider yet the variability of thickness of tested specimen, being a significant parameter in terms of bending of the structure, since it affects its transversal inertia and the crack propagation. Once again results were monitored in terms of S.I.F. and energy release rate. Fig 3.33 describes the second parameter and shows a drastic reduction as the thickness of specimen is increased. This trend is mainly due to the increased cross section of structure link undergoes the same load in all the simulations, thus reducing the stress concentration around the crack tip. It can be remarked that difference between the two assumptions of elastic and elastic-plastic behavior

respectively disappears above a value of thickness, which is lower than the standard one. This result is compatible with the assumptions of plane stress or strain, usually proposed for different aspect ratios of the geometry of the specimen. Table 3.19 resumes values of J-integral computed for different thickness of specimens (in both elastic and elastic-plastic conditions).

Table 3.19: The value of J-integral in different thickness

Thickness (mm)	5	10	20	30	40	50
J-Integral Elastic [N/m]	47822	11955	2989	1330	747.2	478.2
J-Integral Elastic-Plastic [N/m]	86719	21164	4828	1914	963	516.6

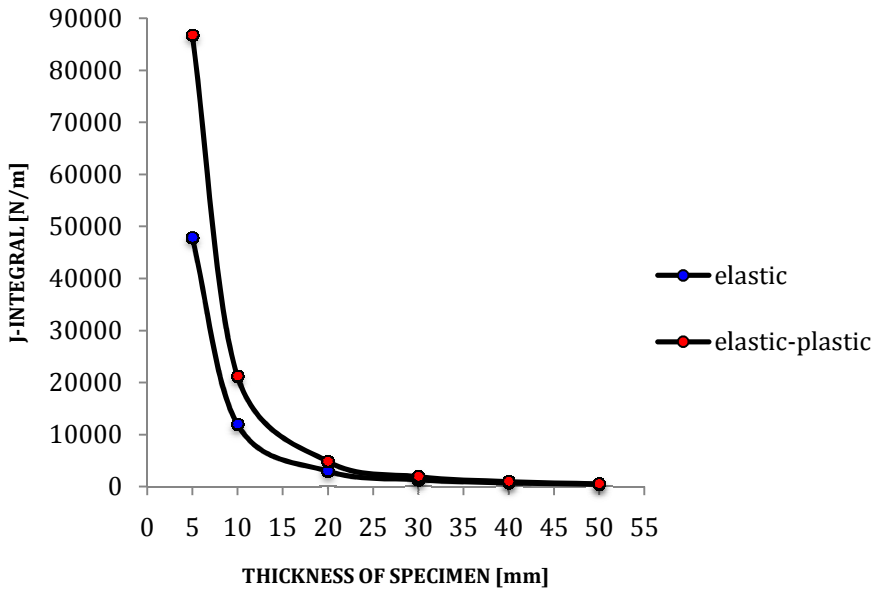

Fig 3.33: J-Integral vs. thickness of specimens for applied load of 10 KN, crack length of 20 mm and AISI 4340 steel

Table 3.20 shows values of Stress Intensity Factor for several thicknesses of specimens.

Table 3.20: Stress Intensity Factor in different thickness

Thickness (mm)	5	10	20	30	40	50
S.I.F [MPa]	104.11	52.05	26.02	17.35	13.01	10.41

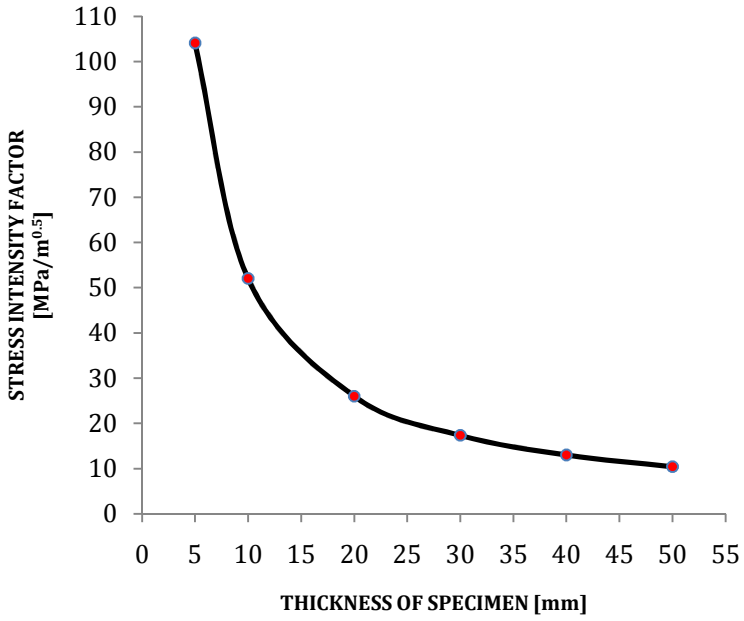

Fig 3.34: Stress Intensity Factor, for applied load of 10 KN, crack length of 20 mm and AISI 4340 steel

S.I.F evenly follows the trend of the J-Integral and inversely depends on the thickness of specimen, for given loading condition.

All the numerical investigations above described motivate some typical peculiarities of the AISI 4340 steel, as the very good balance of strength, toughness and wear resistance, being suitable for several industrial applications like heavy-duty axles, shafts, gears and spindles or bolts, torsion bars and connecting rods.

3.5 Crack propagation in Single and mixed mode

Crack propagation in steel AISI 4340 for three conditions of failure modes were analyzed (single and mixed mode) is analyzed. This numerical investigation was performed by section of the XFEM available inside the ABAQUS code and the related procedure was assumed and tested.

In the “part module” of ABAQUS a first task is modeling the specimen geometry, as it is then it is possible drawing and locating the crack by defining the section and the initial geometry. Even inputs in the “property module”, have to be updated. In addition to the Young modulus, Poisson ratio of steel material, for crack propagation it is required the maximum principal stress and fraction energy. For this kind of steel, it was assumed 745 MPa for maximum principal stress and to compute the fracture energy, the fracture toughness of AISI 4340 steel is used. It should mention that, it is not necessary to assign any property for the crack. The crack and specimens volume are merged as separated parts inside the “dependent module”.

The crack is created by ABAQUS through the “ interaction module” where the XFEM method is used to model the propagation inside the specimen. Dynamic implicit solution is then used to analysis the model, by selecting the NGlom, on option. Steps for calculation are kept small. Total time and step time are even assigned. Before applying load and boundary conditions a refinement of mesh can be performed and the analysis is run. The ABAQUS code makes avaiable several results as the crack growth maps, crack angles and crack propagation speed, being firstly described.

Crack Growth Map

Crack growth direction and stress distribution along the crack tip can be seen in the maps and crack propagation attitude can be analyzed deeply in these maps.

Crack Propagation Angle

Once the crack has started, direction along which it propagates is a issue of failure prevention. Unfortunately, no reference solution exists since, as already stated, simulations in which the convergence is achieved are those where just a single element has been cracked. One single element cracked has been thought to do not provide any valuable information about the actual direction of crack propagation. Thus, in this

section, results are provided in terms of real angles. In order to uniquely identify the crack growth direction.

Crack Propagation Speed

Along with the crack propagation direction, the second relevant parameter of crack growth is speed. Evaluation of such parameter has been studied for the three modes. Crack growth is analyzed by the integration the model equations in the time domain.

A) Crack Propagation in case of Single mode– MODE A

FEM model of MODE A specimen is introduced the crack fracture as shows in Fig 3.35.

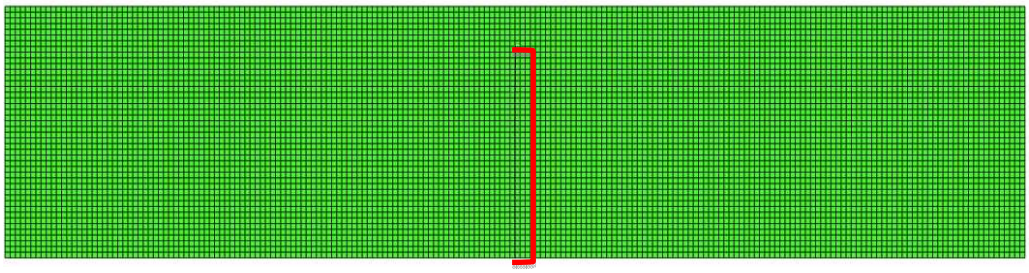

Fig 3.35: The crack growth propagation map in mode A

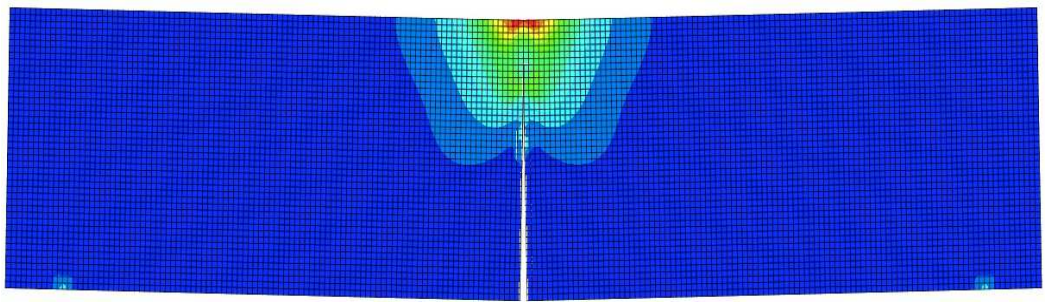

Fig 3.36: The stress distribution when crack growth in mode A

The XFEM approach allows propagating the crack across the specimen as the load increases, in mode A the crack is propagating along a straight line along from the tip and

stress distribution around the crack tip is symmetric as in Fig 3.36. From previous section it is known that a higher Stress Intensity Factor is found in this mode.

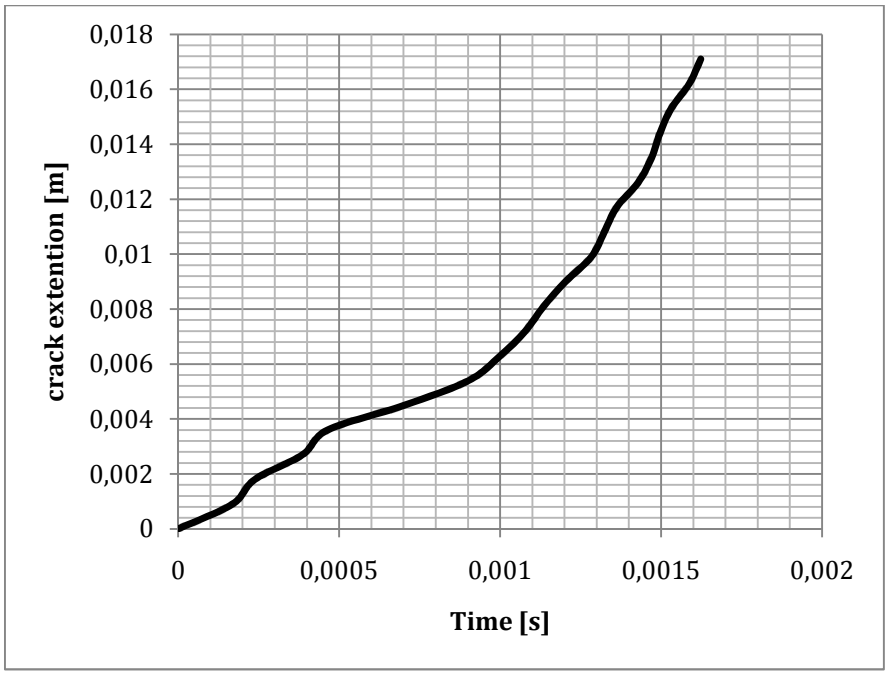

Fig 3.37: Crack length vs. time for mode A

Fig 3.37 shows the crack length vs. time for mode A. Crack propagation has a moderate increase in the time; at least propagation is stalk and controlled.

B) Crack Propagation in case of Single mode– MODE B

Mode B is conceived to induce a mixed mode propagation of crack as it can be approximated in Fig 3.38.

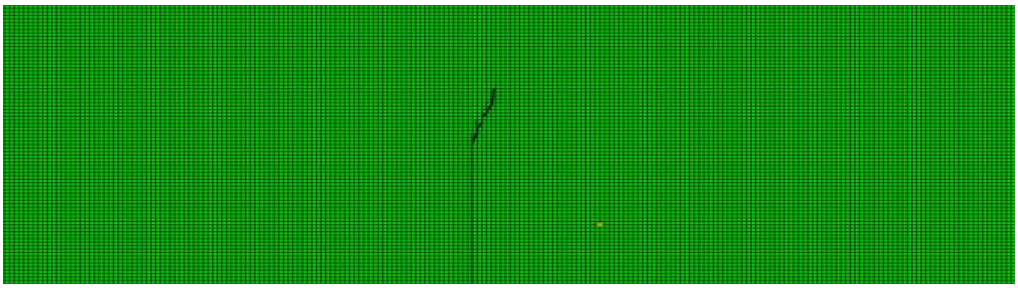

Fig 3.38: Crack growth propagation map in Mode B.

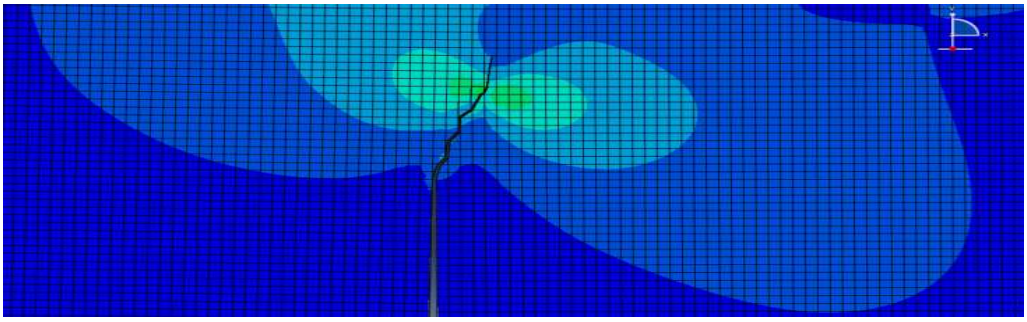

Fig 3.39: The stress distribution when crack growth in mode B

Crack propagation skewed of a 30-degree angle at tip, because of the location of initial crack, loads and constraints. Stress distribution around the crack tip is no more symmetric like it was in mode A although is here lower in magnitude.

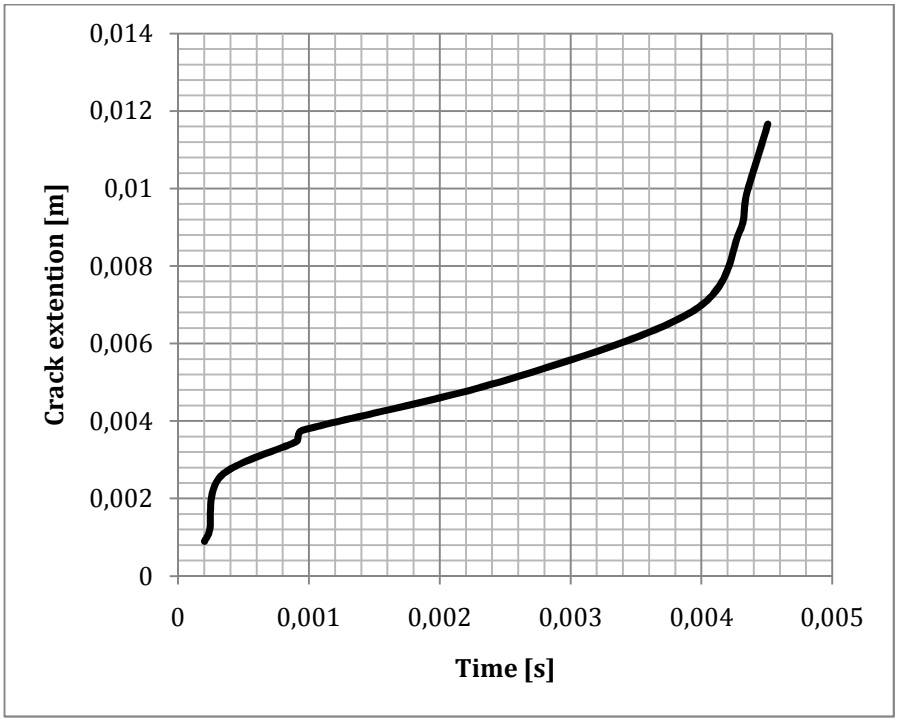

Fig 3.40: Crack length vs. time for Mode B

Fig 3.40 shows how is affected by the mode II and I. Crack propagation exhibits a sharp increase in the beginning then a controlled and stable propagation, up to a critical threshold at which it becomes instable.

C) Crack Propagation in case of Single mode– MODE C

As it was described in section1, 2 Mode C is characterized by a couple of action applied at different distance from the crack and even by the constraints are no more at the two ends of specimen. These conditions make the crack propagation mode mixed of II and I.

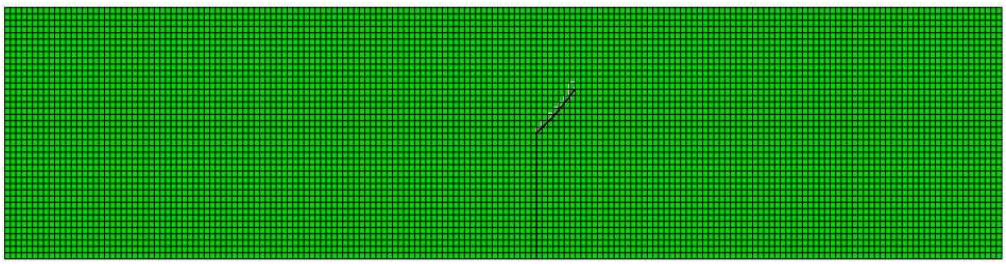

Fig 3.41: Crack growth propagation map in Mode C

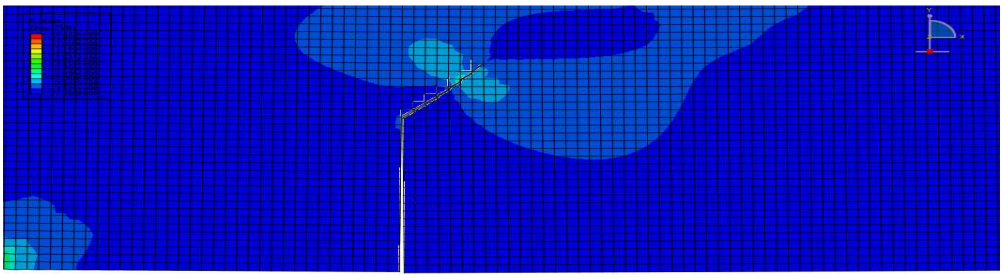

Fig 3.42: Stress distribution of crack growth in Mode C

As Fig 3.41 shows, direction of crack propagation is skewed of 45 degrees from the crack tip, therefore effect of mode II seems larger than in Mode B. Stress around the crack tip, is lower than in modes A and B and values of Stress Intensity Factor and energy release rate are also the lowest ones here among the three different cases.

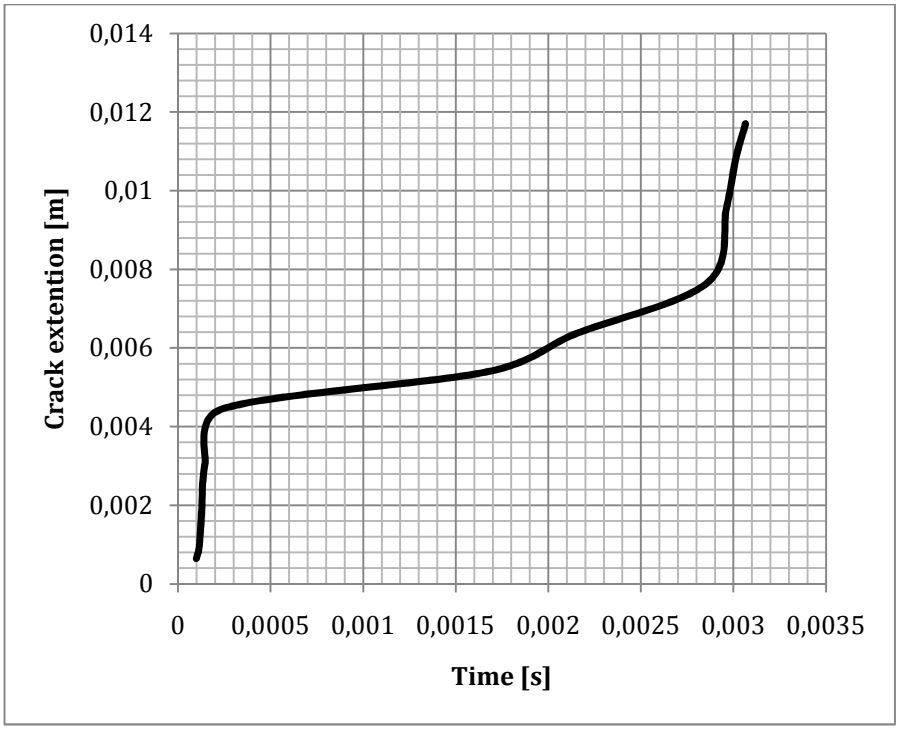

Fig 3.43: Crack length vs. time for Mode C

As in mode B even in this case propagation shows three regions, A first short trend presents a fast propagation at the beginning, then propagation become fairly slows up to a critical condition at which if finally becomes uncontrollable.

3.6 Discussion about crack propagation in mode A, B, C

Fig 3.45 summarizes the dependence of angle of crack propagation upon the failure mode analyzed. Element size at crack tip is even considered as sensitive parameters of the numerical method. Mode A shows a straight propagation along the Y-axis, while Mode B exhibits a deviation 30° which increases up to 45° in case of Mode C.

Unfortunately when the propagation is deviated, identifying the actual angle is rather difficult become a certain dependence work and the mesh refinement is shown, especially when angle is greater.

The analysis done in case of pure metal structure in both static and dynamic for different number of cycles was very useful to assures the protocol of fracture mechanics within the ABAQUS code and to apply in next chapters to the smart structure. The sensitivity

analysis shows that value of J-Integral and S.I.F increase if the load magnitude and crack length are higher, while they decrease as thickness of specimen is larger. The J-integral allows a more effective prediction since it includes even the plastic behaviour of material. Crack propagation is very suitable upon the fracture mode in terms of speed and angle of propagation. Refinement of FEM mode is a crucial detail for this kind of analysis. Element size in FEM is obviously very important for an effective prediction of stresses or strains inside the structure, in this case it is remarked that even the angle of paragraph is affected by the mesh refinement.

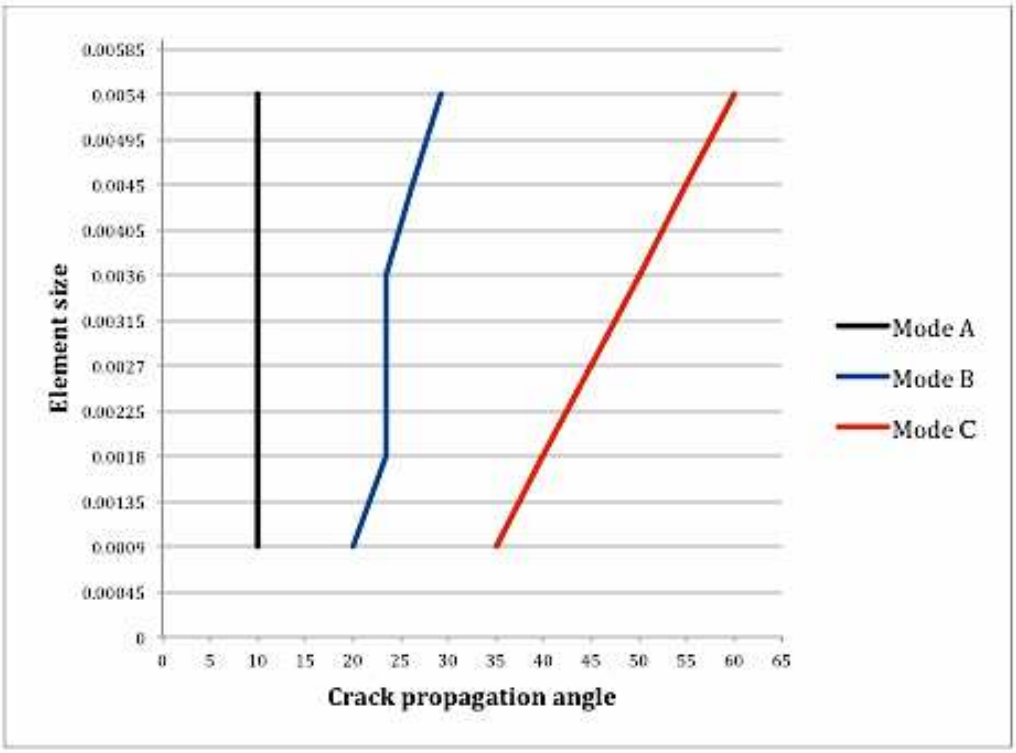

Fig 3.45: Direction of crack propagation in different modes A, B and C

CHAPTER 4

VALIDATION OF THE NUMERICAL PROTOCOL DEVELOPED IN ABAQUS FOR FRACTURE OF WELDED JOINTS

1 Motivation

Previous chapters described how some classical approaches developed in the literature for fracture mechanics can be effectively implemented into the ABAQUS code by resorting to the latest improvements introduced in some recent version of the code. At this point of the thesis a validation of the proposed numerical tool looked strictly required to assure an effective application to the unexplored field of fracture of piezoceramic materials. It was performed thanks to the collaboration between the Politecnico di Torino and the EPF School of Engineering in Sceaux, France, and its international partner in research activity such as Prof. Tom Lassen's laboratory in Norway. The field of application was the prediction of crack propagation in welded joints, particularly for offshore engineering. Therefore in this chapter a short description of the application is introduced before discussing the benchmarking operated among the ABAQUS and other FEM codes are the validation performed directly upon several experimental results.

Welding joints two or more metallic components by means of used metal (welding rod) into a fillet between the components or by raising the temperature of their surfaces or edges to the fusion temperature and applying pressure (flash welding).

Three are most the common types of welded joints [69]: butt, corner and T (Fillet), being shown in Fig 4.1. Each type provides specific function in product engineering.

Butt Joints are commonly used for pressure vessels, piping, tanks and other applications, which require a smooth weld face. Butt joints extend the length or width of a part by connecting the edges of two pieces of material in the same plane.

T-Joints consist of two pieces of material connected to form a "T" shape. They require a fillet weld and are common in many fabrication and construction applications, including structural steel, piping systems, and equipment fabrication.

Corner Joint consists of two pieces of material joined at their edges to form an "L" shape.

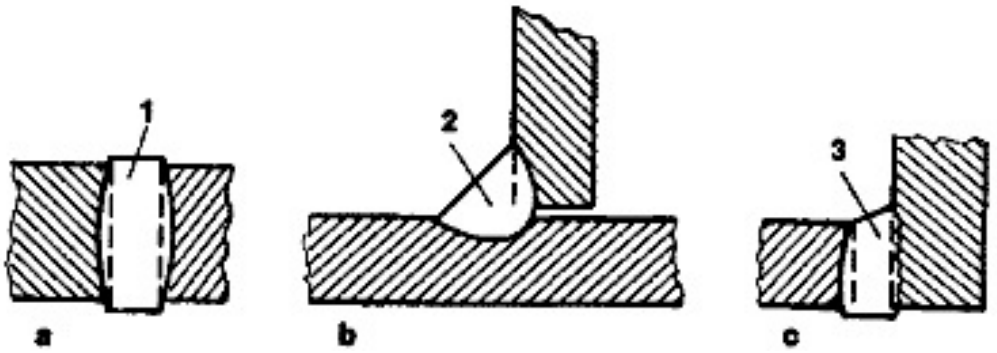

Fig 4.1: Types of welded joints and welds used in electro slag welding: (a) butt joint, (b) T-joint, (c) corner joint; (1) butt weld, (2) fillet weld, (3) weld for corner joint [70]

There are many welding processes, which are briefly described here:

- *Oxyacetylene welding (gas welding):* combustion of a gas is used as thermal source; the most common gas used is the acetylene. It is extremely versatile and affordable. Oxy-acetylene welding is simple in concept - two pieces of metal are brought together, and the flame with or without the addition of filler rod melts the touching edges.

- *MIG and MAG welding:* heat for welding is produced by forming an arc between a consumable metal electrode and the work piece. Electrode melts to form the weld. The main difference is that the metal electrode is a small diameter wire fed from a

spool, and a shielding gas is fed through the torch. As the wire is continuously fed, the manual process is sometimes referred to as semi-automatic welding.

- *Submerged arc welding (SAW):* Similar to MIG welding, SAW involves formation of an arc between a continuously fed bare wire electrode and the work piece. Process uses a flux to generate protective gasses and slag, and to add alloying elements to the weld pool. A shielding gas is not required.

- *Electric arc:* it is the most used in manual welding. The base metal and an electrode made a circuit electrical energy are released at the electrode tip where the operator can weld.

- *TIG welding*: Tungsten Inert Gas (TIG) welding is the process of blending together reactive metals, such as magnesium and aluminum. During the welding process, an arc is formed between a pointed tungsten electrode and the area to be welded (it is not consumable).

- *Resistance welding−point welding:* heat is given by the Joule's effect through the current following between the electrodes and pieces to be joint under pressure effect. Welding is given by a localized melting of metal between the two pieces. It is really used in a lot of industrial and automatized applications.

- *Laser welding, Arc plasma welding, Electronic beam welding:* heat generated by a laser in case of laser welding, or by gas in plasma state in arc plasma welding or an electron beam in the electron beam welding, the filling material is welded and the joint components are connected. To give rough impression of those processes Fig 4.2 is proposed.

Fatigue life prediction of welded joints is very complex, costly and time consuming. Welding process naturally might introduce some crack inside the joint, therefore an effective prediction of crack propagation in this case is even more important than analysis of damage nucleation. Computation of Stress Intensity Factor (SIF) range, ΔK, is therefore a key issue of design.

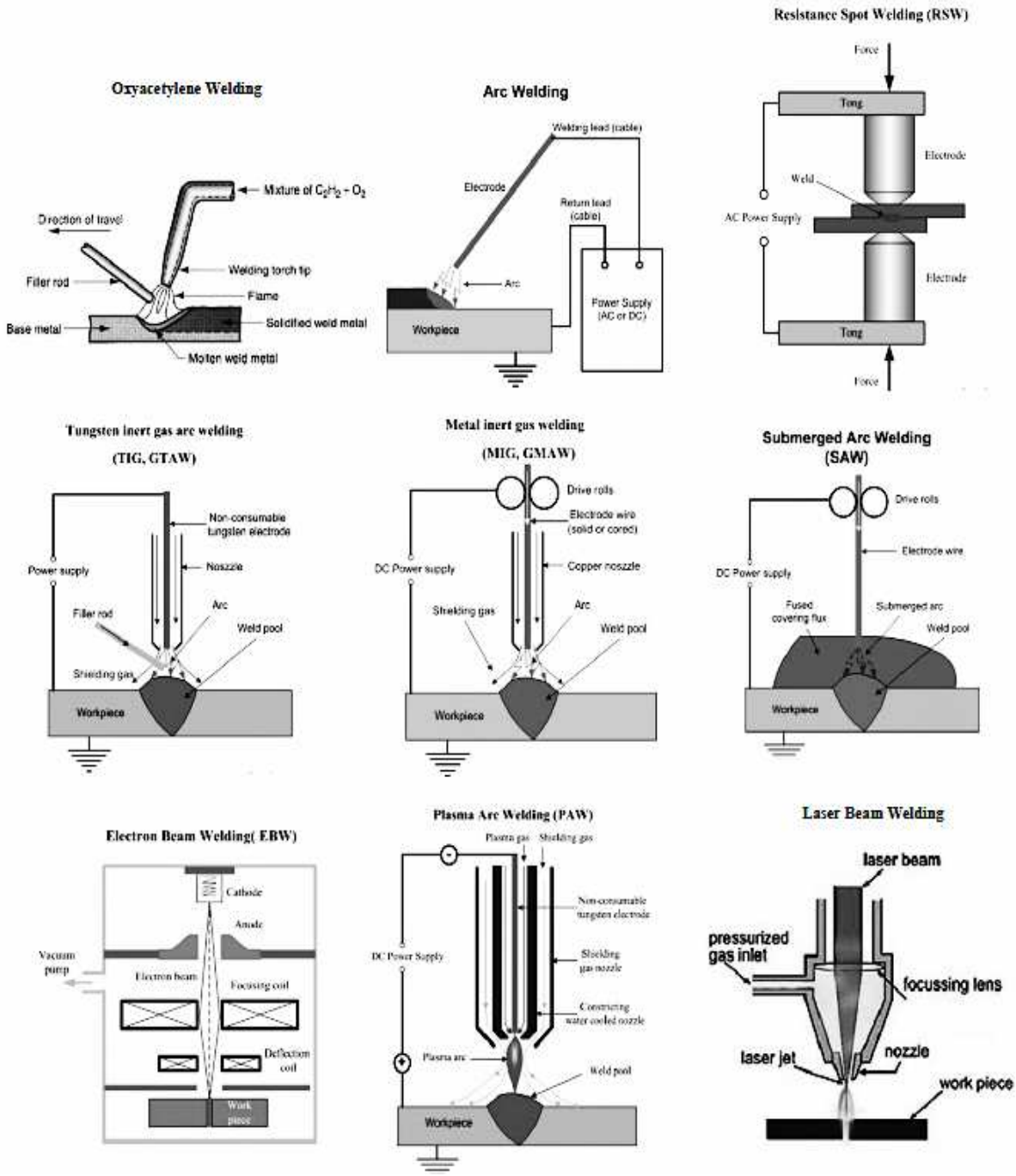

Fig 4.2: Impression of some industrial applications used in welding processes [72]

Non-destructive testing techniques usually are applied to measure the existing cracks inside the welded joint. Design activity needs an effective prediction of time to failure and crack growth histories leading to the failure [71].

This estimation can be compared to the planned service life and plan the maintenance activity. This activity can allow a scheduling of inspections and making more efficient and cheaper the maintenance operation.

2 EXPERIMENTS ON WELDED JOINTS

A preliminary experimental activity was performed by Prof Tom Lassen, at Norwegian University of Science and Technology. Description of tests was deeply performed by Mr. M. Fraldi in his M.Sc.D thesis [72].
Metallurgical properties of welded joint are resumed in Table 4.1 [73].

Table 4. 1: Chemical composition of the steel used in welded joint [72]

Element	C	Si	Mn	P	S	Cu	Ni	Cr	Mo	Nb
%	0.08	0.15	1.40	0.006	0.002	0.01	0.02	0.02	0.01	0.008

Yielding strength of this material is 416 MPa while tensile strength is up to 500 MPa. Hardness has been investigated in many points resumed in Table 4.2. “Base” refers the two base materials; “weld” is associated to the welded toe, “HAZ” (Heat affected zone) indicating several cross sections at different distance from nearest to welded toe.

Table 4. 2: Brinnel hardness of the tested welded joint [72]

ZONE	Base 1	Base 2	Weld 1	Weld 2	HAZ 1	HAZ 2	HAZ 3	HAZ 4
HARDNESS (HB)	142	147	175	178	213	181	173	165

Tests have been made on a cruciform welded joint structural in Fig 4.3. Plate has been cut by flame and welded; furthermore has been made a thermal relieving at 570 °C for one

hour. Steel is a typical material used in construction of off shore North Sea platforms, being characterized by, a low carbon and accelerated cooling. These steels are also used in artic building and in nuclear domain.

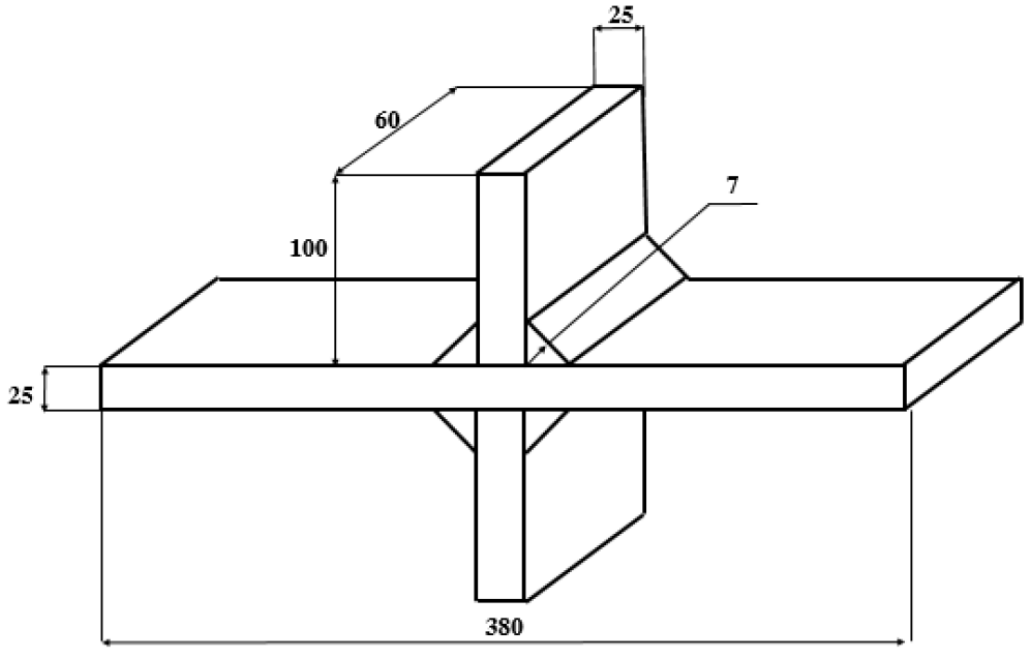

Fig 4. 3: Test specimen of welded joint [mm].

Several specimens were built up even to investigate the component life for some welding processes used in those applications as:

- Saw;
- Fcaw (Flux-cored arc welding);
- Smaw (Shielded metal arc welding) 57 and 76.

Saw, Fcaw and Smaw are all techniques of electric arc welding. Difference among those methods is use of flux in the Fcaw and of stick in Smaw. Measurement methodology used in experimental activity is the so-called “Alternating Crack Potential Drop” (ACPD); Alternate current potential drop (ACPD) is measured at surface of the conductive plate and used to determine, by a non-destructive approach, some parameters such as thickness of plate, electrical conductivity and linear effective magnetic permeability. To relate the measured potential drop to values of those parameters, a model is needed. Closed form analytical expressions are derived for the ACPD measured between the two voltage

electrodes of a four-point probe. Alternate current is injected and extracted by two current electrodes. In this procedure allows measuring and the growing dimension of crack, cycle by cycle. Experimental setup is depicted in Fig 4.4:

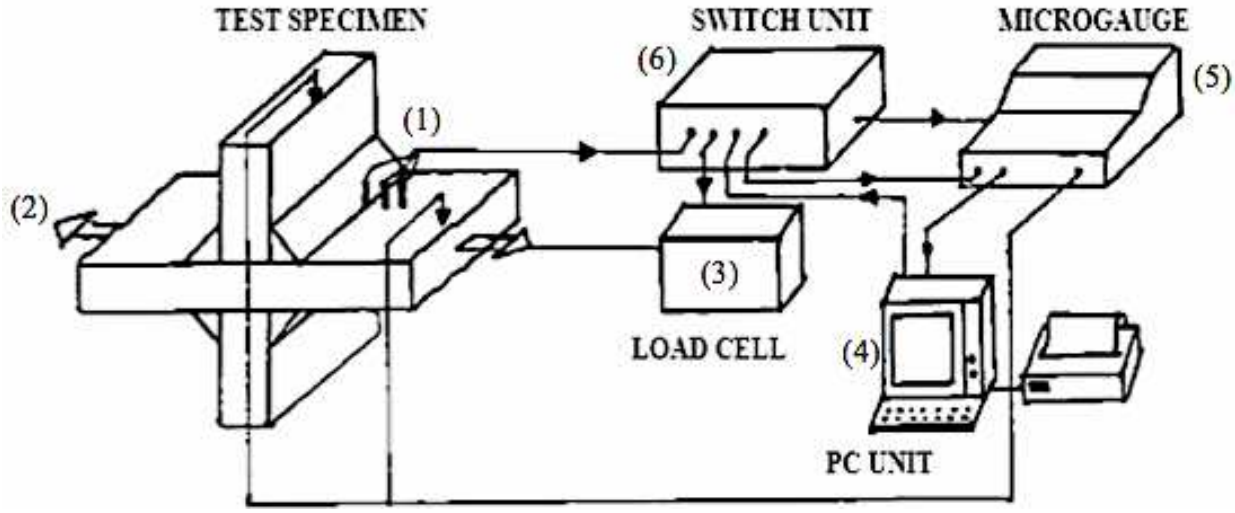

Fig 4. 4: Experimental set-up [74]

Some electrodes (1) are made in contact with the conductive surface of welded joint, some works as a sensor and other as an actuator to inject the current. Tensile actions (2) are applied by the testing machine and load is imposed and monitored by the load cell (3). Loading condition can be regulated by a controller (4). Measurement of displacement is done by the micro gauge (5). Switch unit (6)regulates forces under commands of “load cell” [74].

This architecture allows controlling step by step the crack propagation and applied load.

- Magnitude of tensile axial stress is about 150 MPa;
- Stress ratio of 0,5 (Stress ratio: ratio of minimum stress to maximum stress in one cycle of loading in a fatigue test);
- Frequency of applied load is 8 Hz;
- Strain gauges are disposed at 10 mm from the welded toe;
- Frequency of AC current is 6 kHz;
- Other environmental variables are set at normal laboratory conditions.

As relevant result of test is the monitored evolution of crack length versus the cycle's number as shown in Fig 4.5. Specimens used were 44 and for each one a number of 60 to 300 measures of crack length were performed.

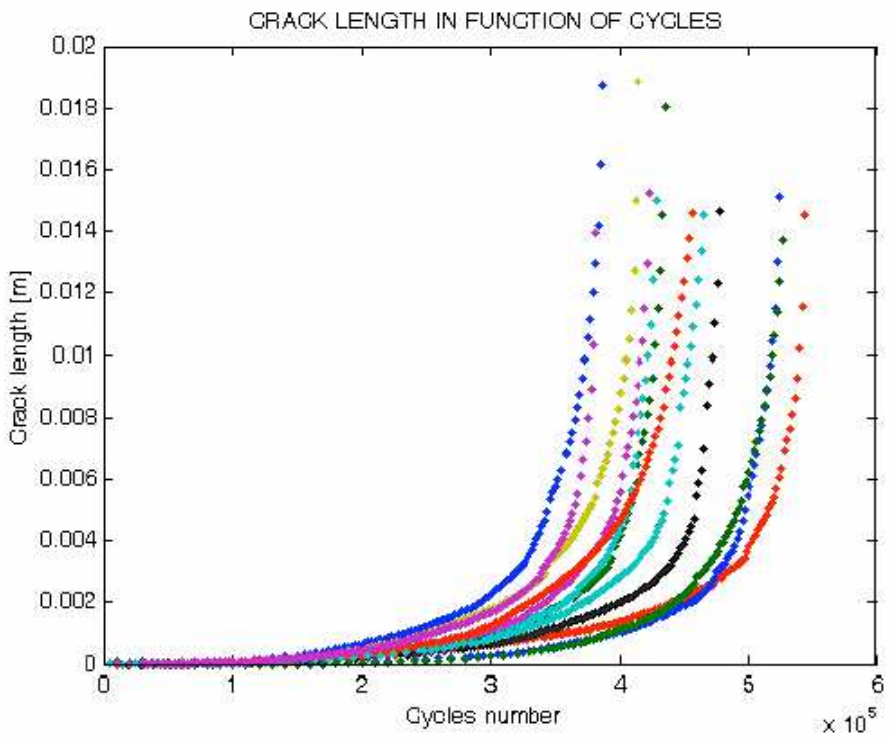

Fig 4. 5: Experimental results: crack length as function of cycle's number.

Fig 4.5 shows several curves, which differ for the amplitude of applied load. Each curve includes a number of points, each one being corresponding to a crack measurement performed.

3 Numerical prediction of experimental behaviour

Model of the welded joint tested was developed in the ABAQUS code and all the required inputs were provided to calculate the Stress Intensity Factor for different length of crack. Some discrete values of initial crack length were used as 3, 5, 7, 10, 12 and 15 mm. After simulation performed by ABAQUS, the EXCEL program was used to draw the diagram of Stress Intensity Factor versus Crack length and an interpolation was performed inside the Excel to obtain the value of K, for different values of crack length. The MATLAB code was then used to extract numerical data from the Excel files and to

draw all the diagrams related to this analysis such as the Paris' law, life prediction and those is shown in this section.

A) Modeling inside ABAQUS

Welded joint used as specimen was drawn inside the "part module", two dimensions were sufficient to explore the crack propagation, and only half of the whole specimen was modeled since symmetry along the y-axis was imposed. Properties of the steel were inputted as E=210 GPa (Young's modulus) and Poisson's ratio is ν=0.3.
For each value of initial crack lengths crack geometries direction and length were set up. A suitable mesh size and distribution was imposed after some preliminary attempts, to assure the required accuracy in results. Some details of selected mesh are described in Fig 4.6. Actually up to 20351 elements and 20814 nodes were used.

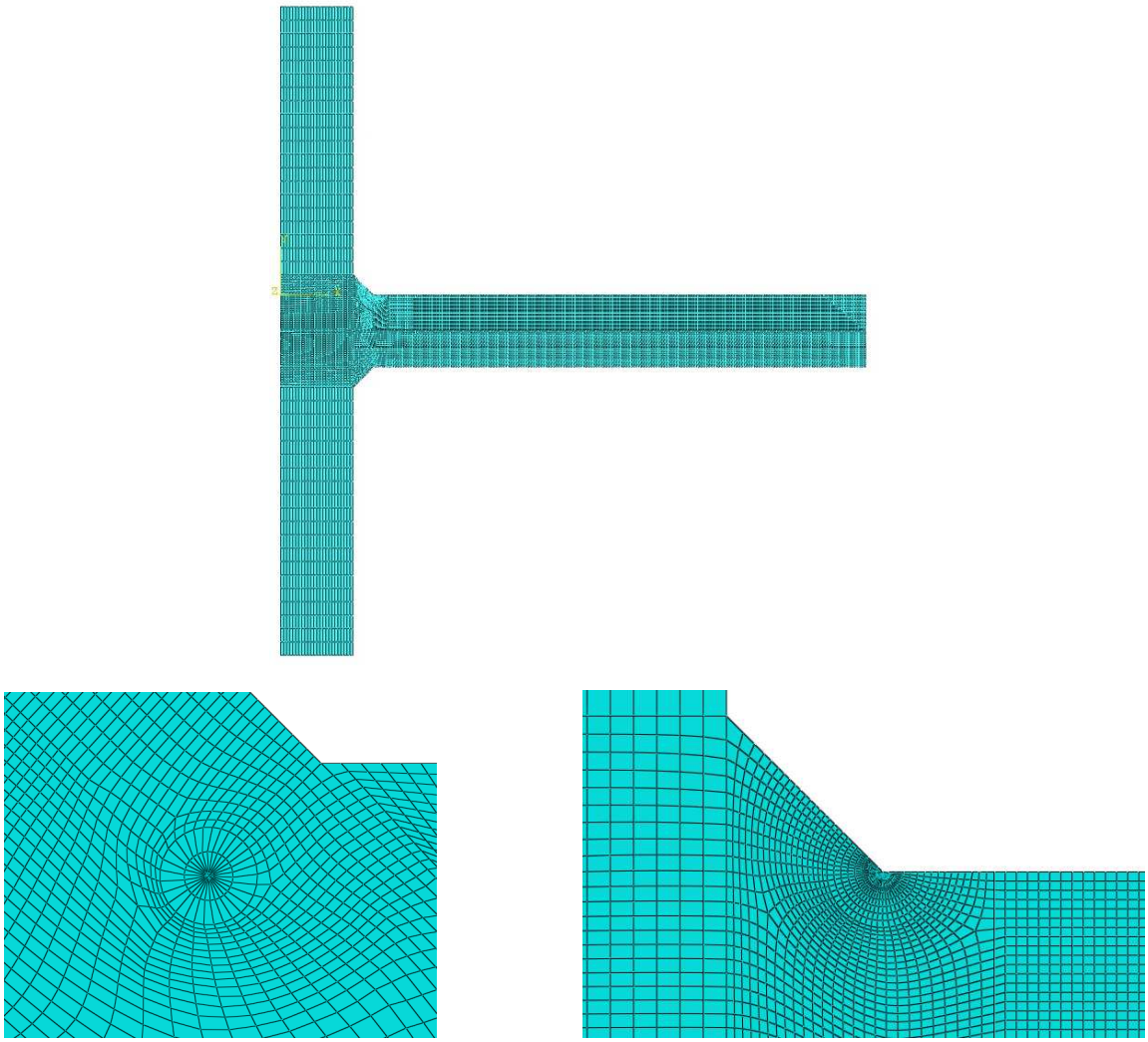

Fig 4.6: Mesh details in the ABAQUS model performed of the tested welded joint.

Table 4.3 shows values of Stress Intensity Factor completed by ABAQUS for the list of crack length above mentioned

Table 4.3: SIF computed by ABAQUS code

Crack Length [m]	K [MPa$\sqrt{m}$]
0	6.26
0.003	21.05
0.005	28.05
0.007	36.90
0.01	56.15
0.012	75.71
0.015	125.59

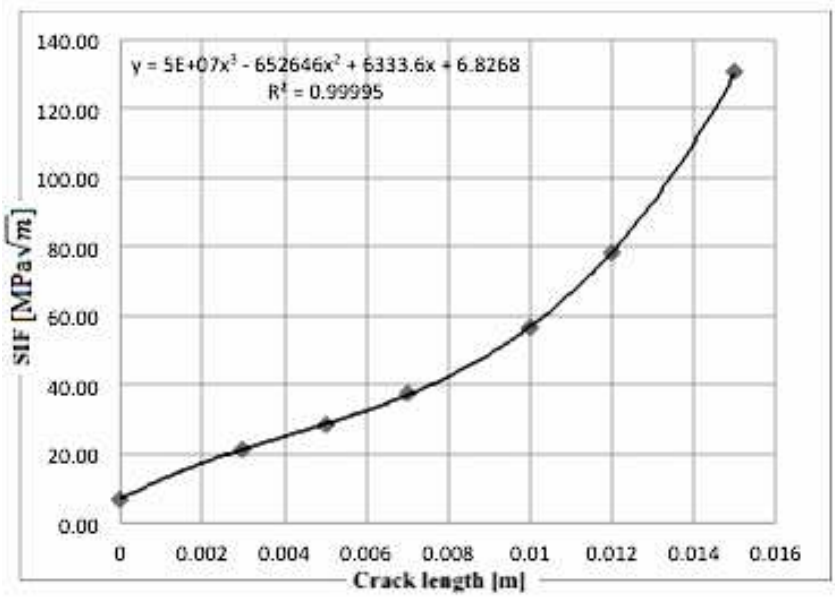

Fig 4.7: Interpolation of stress intensity factor value in excel

Interpolation function in Excel program allowed describing the SIF directly as function of crack length. Dynamic analysis was performed by computing the ΔK function vs. the crack length as is described in Fig 4.8. Each set of result with different colors is related to different welded technique.

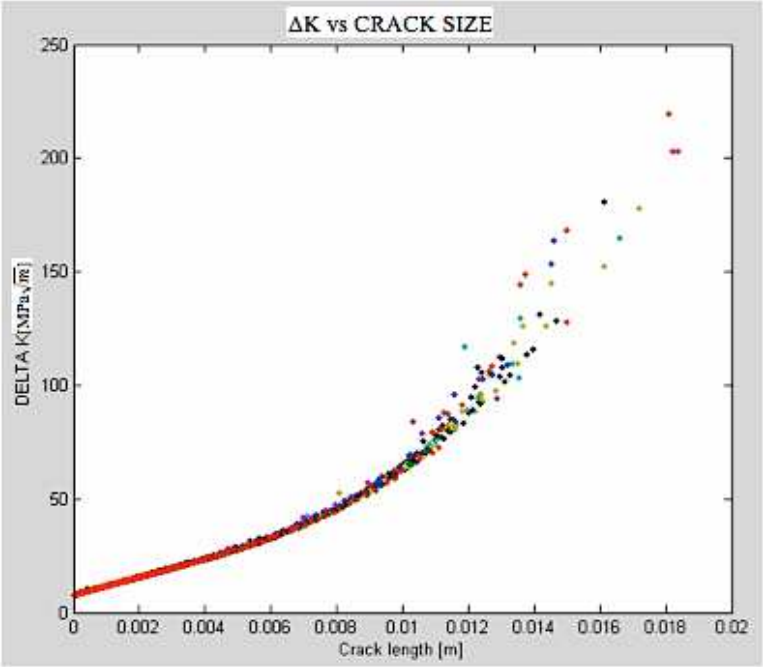

Fig 4. 8: Stress intensity factor for different crack lengths

Trend of SIF is either shown in case of a single case as described in Fig 4.9. It is very interesting to remark that these analyses show that behaviour is quiet different in case of very short crack length as the curve shows. It can be appreciated that trend is fairly different in the first part up to 0.0004 m, in comparison to the next part of the curve; these effect is a goal of some research activity [29].

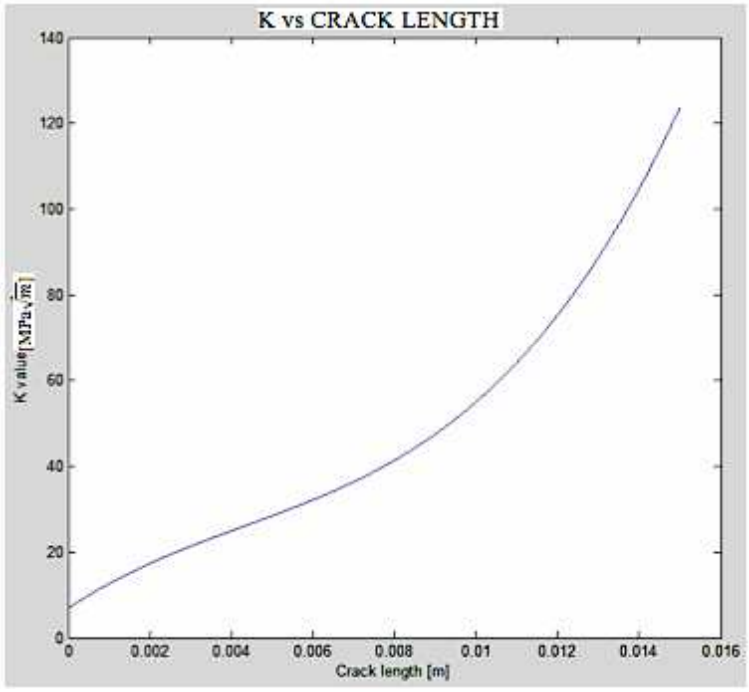

Fig 4. 9: Stress intensity factor value with Matlab code.

Crack propagation is described in diagrams like Fig 4.10 in which relation between da/dN and Δk is plotted. As it was deeply discussed above this relation can be predicted by the Paris' low and its recent elaboration. The Fig 4.10 all the tests were repurposed the interpolation rather difficult. Each case could be separated and represented as a standalone test.

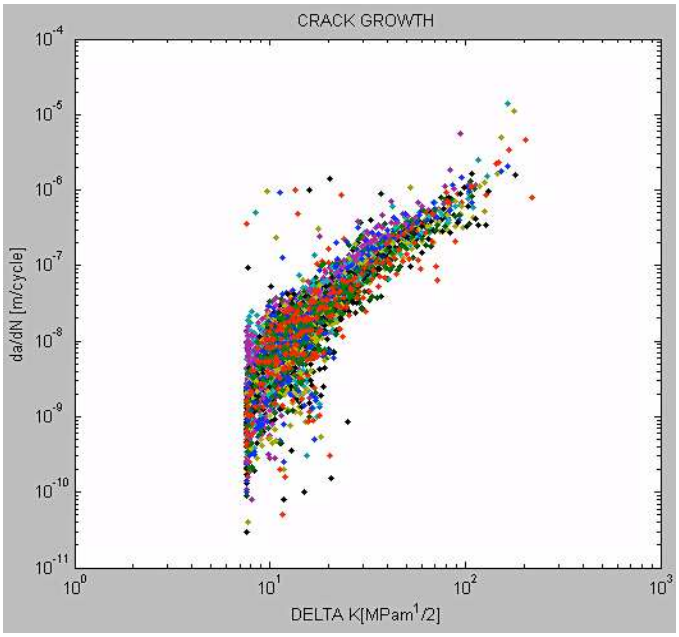

Fig 4. 10: Logarithmic plot of K as a in function of da/dN

From the previous analysis total number of cycles applied to a crack length of 15 mm could be found easily as in Fig 4.11.

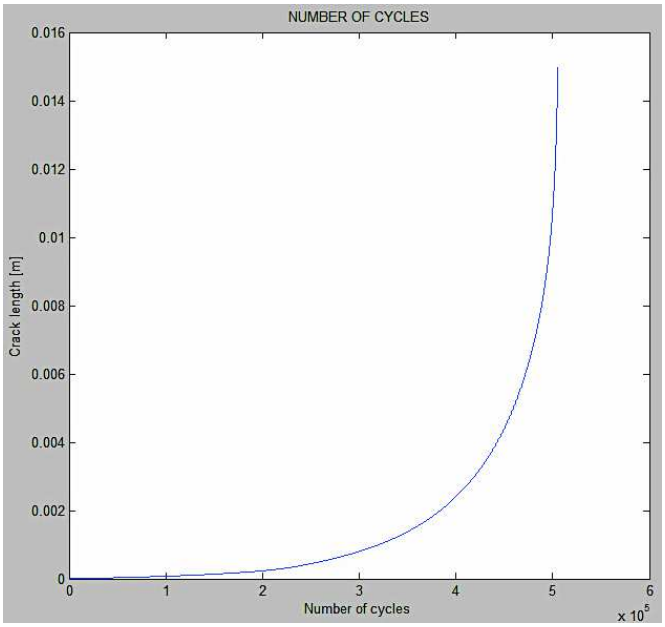

Fig 4. 11: Crack propagation in terms of number of cycles vs crack length

4 Model validation

Once that fracture analysis was performed by the ABAQUS code and outputs were elaborated by means of EXCEL and MATLAB codes, life prediction of this tested welded joint was finally presented. To validate the numerical results of ABAQUS perfectly, relation between number of cycles and crack length was analyzed and compared between numerical and experimental procedure, respectively.

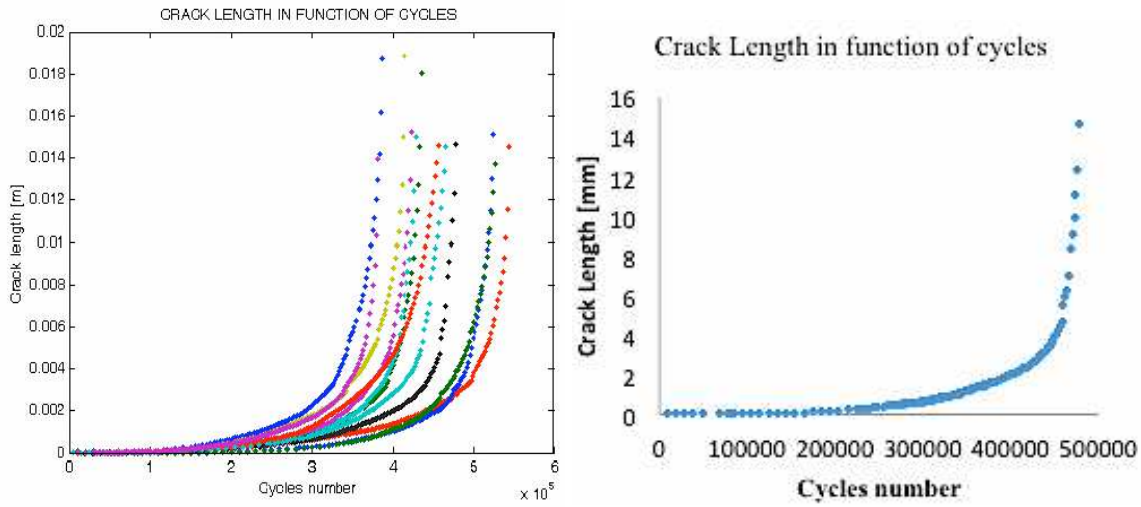

(a)

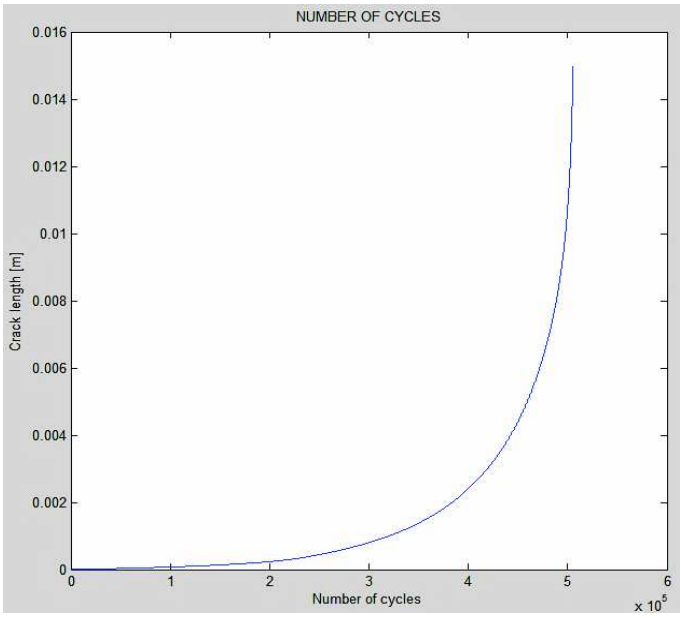

(b)

Fig 4.12: Number of cycle vs. crack length in experimental results (a) and numerical results (b)

As Fig 4.12 shows numerical prediction of specimen life agrees fairly well with experimental results, provided that material parameters are accurately set up.

This is the crucial issue of this modeling technique, because material properties were deeply analyzed in laboratory, while sometimes in real affliction it looks rather difficult having a precise characterization of the material.

As a result of this validation it can be remarked that computation of J-Integral is fast and automatable, by modeling the specimen inside the software and even complicated geometries can be easily analyzed by means of this approach. Accurate results are assured by a suitable selection of Mesh size and refinement. Moreover a good agreement between numerical prediction and experimental activity was found because of the precise characterization of material, which is not always available in practice.

CHAPTER 5

FRACTURE ANALYSIS OF PASSIVELY COUPLED COMPOSITE MATERIALS

1 Description of the composite specimen: ceramic and metallic materials

In this part of the thesis the fracture mechanic is studied in case of a composite structure, equipped with two layers of different material. Many practical cases concern a bounding between metal and ceramic, without functional capabilities. A sort of mechanical coupling is created and interface is present between layers. Moreover material properties, the crack growth direction and the speed of propagation are quite different, therefore investigation is particularly remarkable when crack is passing through the interface. In this thesis a simple case was analyzed by assuming that a layer of AlN ceramic is perfectly bounded upon the AISI 4340 steel.

New specimen is depicted in Fig 5.1. It is worthy noticing that ceramic does not exhibit any functional capability, therefore coupling is inactive as simply passive, while in case of piezoceramic it could be even active if some electrical boundary condition is applied.

A basic assumption in the following analysis is that field of displacement is complete coherent and there is no possibility of delamination, this could be a focus of study.

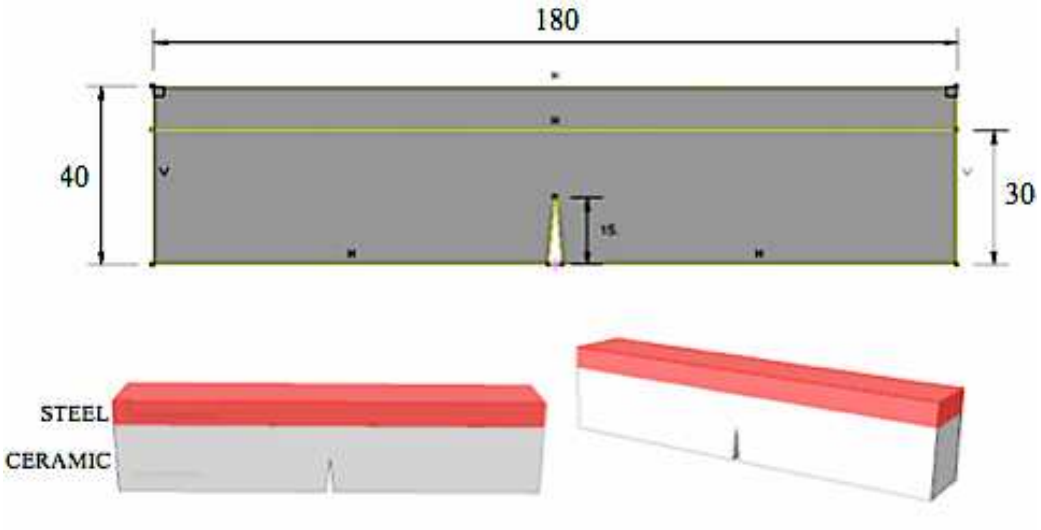

Fig 5.1: Sketch of composite ceramic-steel specimen

Procedure followed to this specimen model inside the ABAQUS code is the same of the structure with one layer only, but in the “property module”, properties of two materials were defined separately and section was assigned for each of them. Properties of steel are the same of previous investigation and while this ceramic material exhibits a maximum principal stress of 330 MPa and fracture toughness of 2.4 MPa. The Young’s modulus of AlN is 330 GPa while the Poisson’s ratio is 0.24 [75]. Numerical simulation even in this case was aimed at computing the stress distribution around crack tip, crack propagation speed and direction, respectively.

2 Numerical analysis

A) Composite specimen – Mode A

Fig 5.2 describes the composite specimen and loading and boundary conditions. Upper layer is made of steel and lower one is ceramic.

This arrangement was assumed to simulate the case in which the covering layer of ceramic material is damaged and to investigate whether and how crack can propagate through the main metallic structure.

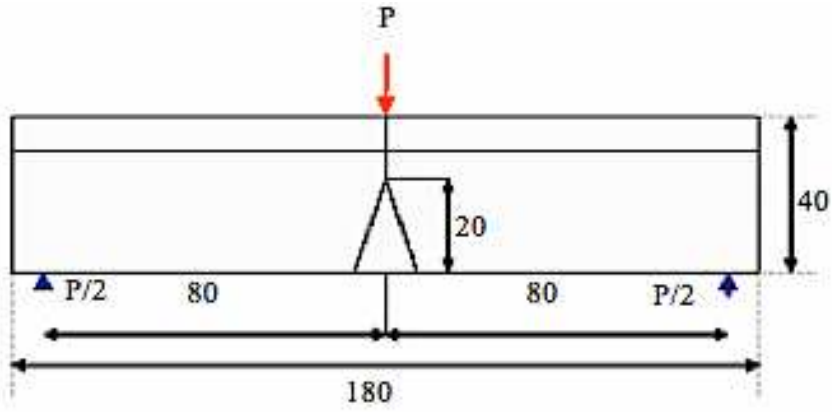

Fig 5.2: The sketch of composite in single mode A

Maps provided by the ABAQUS code show the crack growth direction. Crack passes from the ceramic to steel layer where applied force is 25 KN. Direction of crack does not change even when it passes through the interface between materials.

Stress distribution at the end of propagation looks like in Fig 5.3. Concentration is greater all along the crack edges.

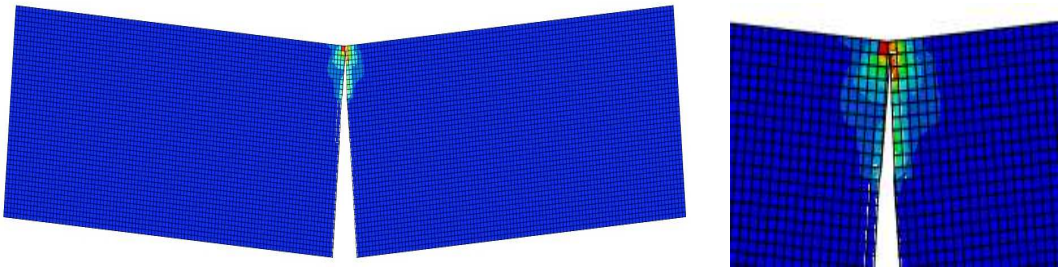

Fig 5.3: Stress distribution inside the composite material when crack growth in mode A.

Crack propagation expressed as a function of time in Fig 5.4 shows clearly two trends. A very high slope at the begining of propagation is shown and corresponds to inside the ceramic layer. This trend is due to lower stiffness of AlN, as soon as crcak passes to steel layer, crack growth proceeds slower with a moderate slope and it does n't become unstable.

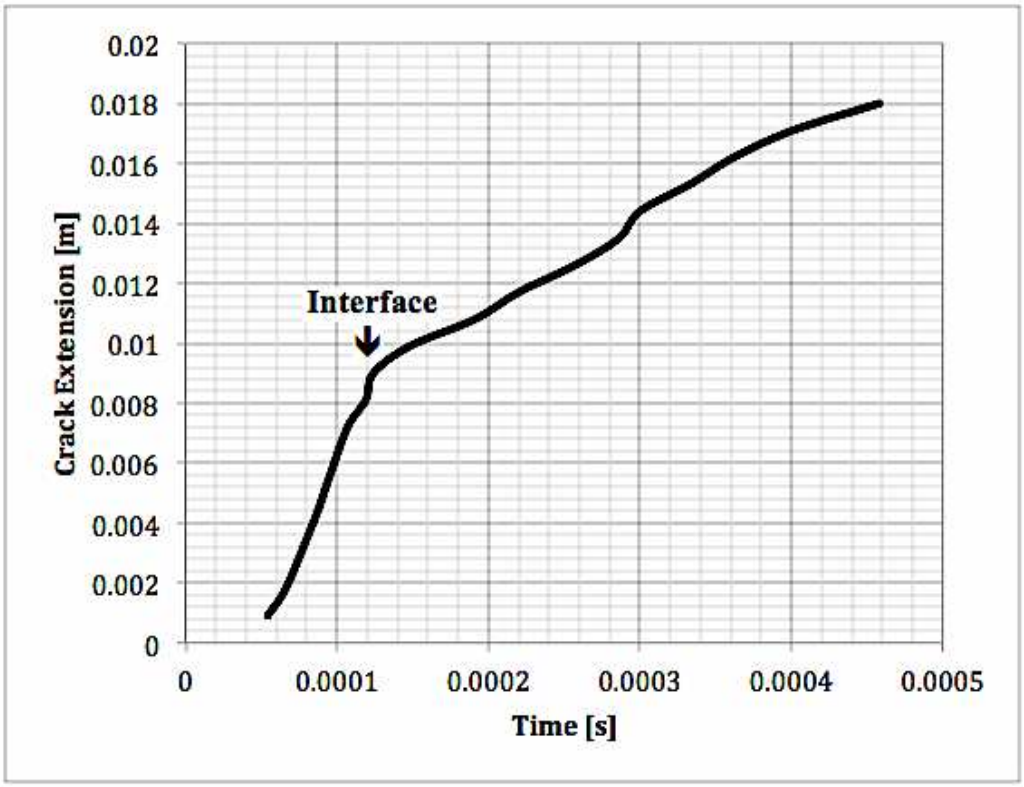

Fig 5.4: Crack length versus time for mode A

B) Composite specimen – Mode B

As Fig 5.5 shows even for mode B specimen is similar to those of tests performed on a single layer. Steel is upper and ceramic is lower.

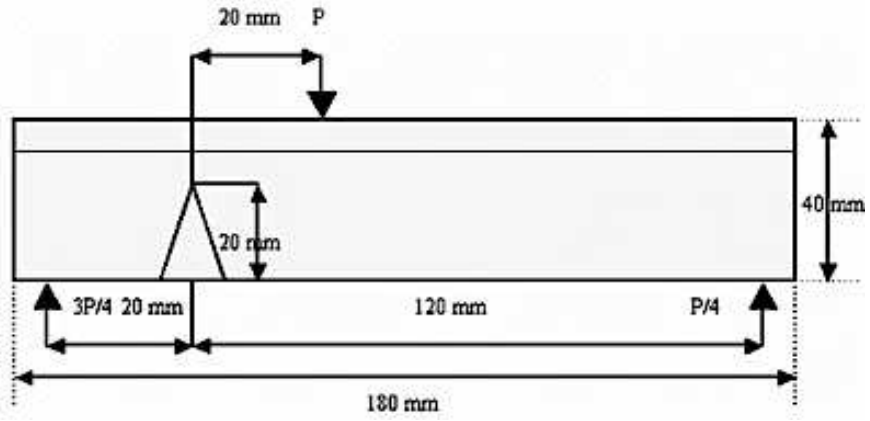

Fig 5.5: Sketch of specimen in composite material for mixed mode B tests

In this case a relevant result is for load of 45 KN. Crack propagation exhibits when it goes inside the ceramic layer and it goes into the steel structure. As Fig 5.6 shows the stress distribution after propagation and its clear that when the crack goes inside the steel the stress is more than inside ceramic. A sudden change of direction is detected of interface between the two materials.

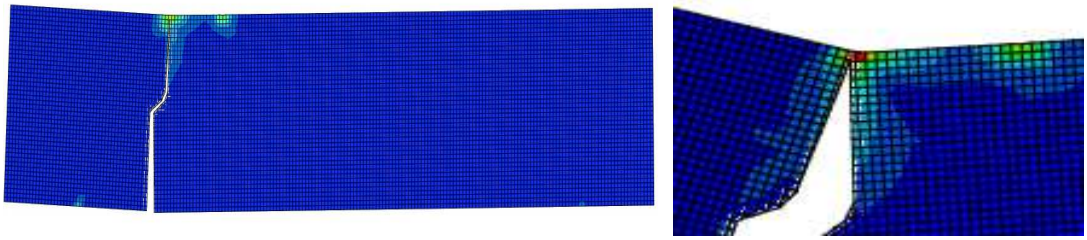

Fig 5.6: Stress distribution when crack growth in mode B

Once again in diagram showing the crack length vs. Time, speed of crack propagation in ceramic is very fast in comparison to propagation across the steel layer. A considerable slope in the first part of this graph, while after crossing the interface propagation is slower, inside the steel layer.

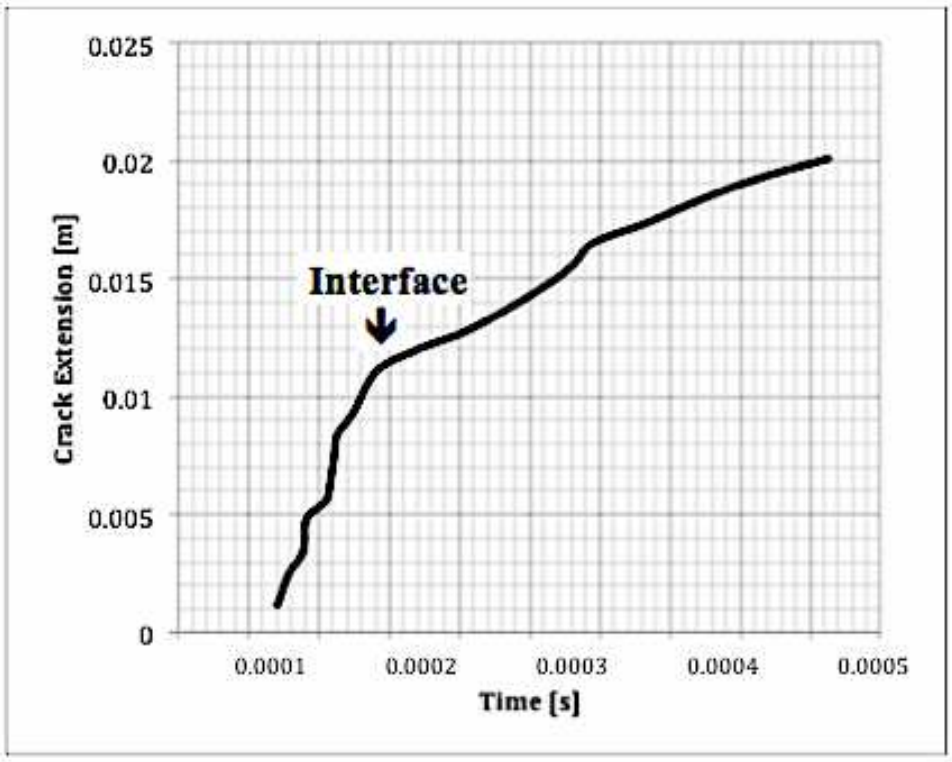

Fig 5.7: Crack length versus time for Mode B

C) Composite specimen – Mode C

Specimen used for testing in case of mode C is sketched in Fig 5.8 by including loads and boundary conditions. Like in previous composite cases steel is upper and ceramic lower.

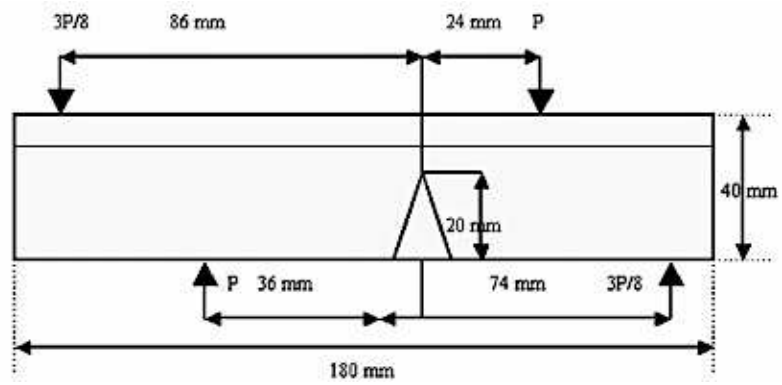

Fig 5.8: Sketch of composite for mixed Mode C

Results (Fig 5.9) show that under load of 140 KN angle of propagation is almost 45° in the ceramic layer. When cracks reach the steel layer, it doesn't immediately from the ceramic layer. A horizontal propagation at first occurs like in a sort of delamination then it continues through the steel layer.

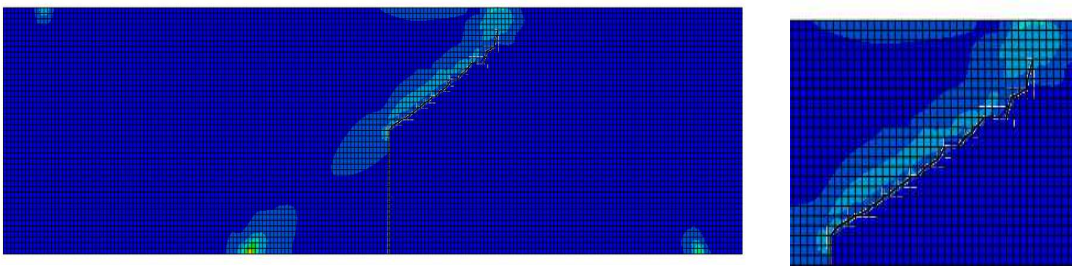

Fig 5.9: Stress distribution when crack growth in Mode C

In this case the most interesting result is the path followed by crack in propagation, while the change in speed propagation is similar to that of other cases. Although a sort of almost stop condition was detected when crack cross the inteface between materials.

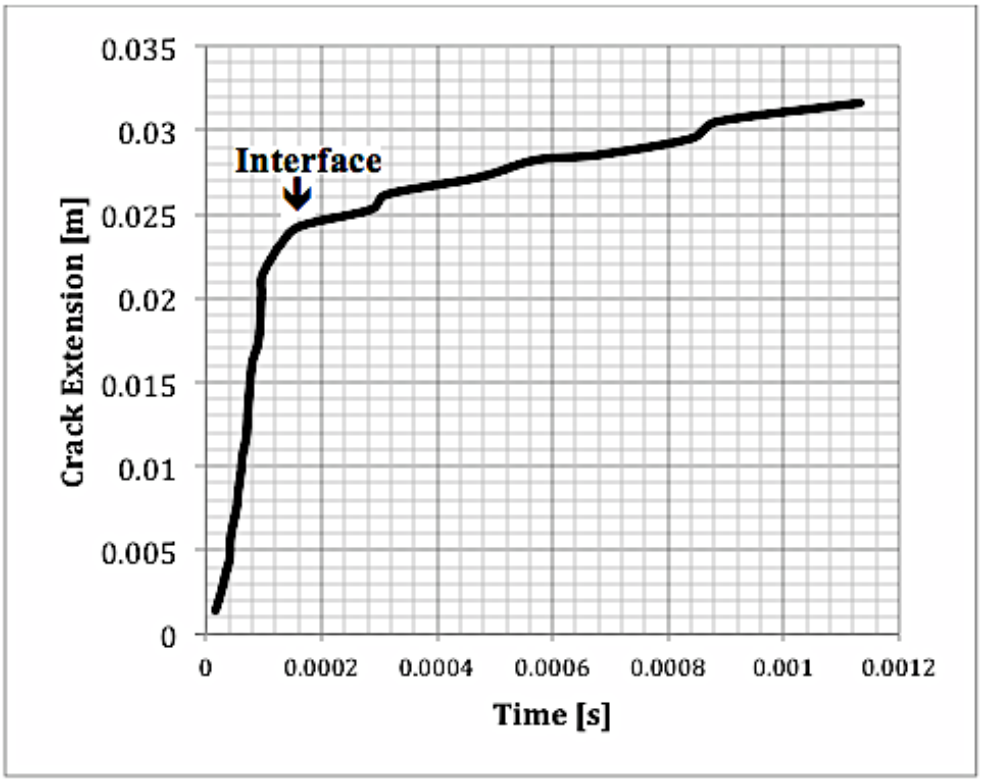

Fig 5.10: Crack length versus time for Mode C

3 Limits and problems of the numerical tool

Main goal of this research activity is the analysis of fracture mechanics inside passive and active structures composite, although until now only passive structure were analyzed, i.e. materials do not exhibit functional capabilities like piezoceramic does.

In case of active materials some problems and limitations were found, when the ABAQUS software was used. It is not able to connect the electro-mechanical properties and the analysis of materials to the fracture analysis. A multi-physics module allows the prediction of static and dynamic behaviors of piezoelectric material, even when it is connected to a voltage generator. Another efficient module allows prediction of fracture mechanics and the crack propagation, stress intensity factor and J-integral but never in association with the multi-physics analysis.

Connecting the two modules for a complete multi-physics analysis of fracture inside piezoceramics is a main focus of next chapters.

CHAPTER 6

OVERVIEW OF PROPERTIES AND FUNCTIONS OF PIEZOELECTRIC MATERIALS

1 Introduction

Piezoelectric materials are used to convert electrical into mechanical energy and vice versa. This technology has enabled a wide variety of commercially successful sensors, actuators and energy harvesters. They belong various classes of materials such as: single crystal materials, piezo-ceramics, piezo-polymers, piezo-composites, and piezo-films [76].

A) Single crystal

Single crystal is a regularly arranged material, includes some minute particles exhibit a regular structure. They are different from ceramics, being an assembly of irregularly distributed particles. Some examples of single crystal piezoelectric material are silicone crystals, being used as a semiconductor substrate material, gallium-arsenic crystals, being used as a LED substrate material, and quartz crystals.

These materials are often used for frequency stabilized oscillators and surface acoustic devices applications [76]. Single crystals exhibit five times the strain energy density of conventional piezoceramics. Thus, unlike piezoceramic actuators, which employ some strain magnification schemes, single crystal actuators can deliver higher strain without generative force.

B) Piezo-ceramics

Many applications of piezoelectricity are based on polycrystalline ceramics instead of natural piezoelectric crystals. Piezoelectric ceramics are more versatile since their physical, chemical, and piezoelectric properties can be tailored to specific applications. Piezo-ceramics have a wide range of applications. Piezo-ceramics are used in the automotive industry in a number of devices such as in knock and oil level sensors or as actuators for precise control of injection processes in engines. In medical technology piezo-ceramic components can be found in lithotripters, devices for plaque removal and in inhalers. Common applications in mechanical engineering include ultrasonic cleaning, ultrasonic welding and active vibration damping and control. The piezoelectric properties of the perovskite-structured materials can be easily tailored for applications by incorporating various cautions in the perovskite structure [76]. Most of the piezoelectric ceramics have structure of the perovskite. Lead Zirconate Titanate (PZT), Barium Titanate ($BaTiO_3$) and Lead Titanate ($PbTiO_3$) are the most popular piezoelectric ceramic materials.

C) Piezo-polymers

A polymeric film that has the ability to reversibly convert heat and pressure to electricity is known as pyroelectric and piezoelectric respectively. Polymers like polypropylene, polystyrene, poly (methyl methacrylate), vinyl acetate, and odd number nylons are known to possess piezoelectric properties. However, strong piezoelectric effects have been observed only in polyvinylidene fluoride (PVDF). These materials are mostly used for directional microphones and ultrasonic hydrophones applications [76]. PDVF is used even for distributed sensors (strain, vibration).

D) Piezo-composites

A piezoelectric composite material is fabricated by interleaving a cut or preshaped piezoceramic with a passive polymer or epoxy host matrix compound. These materials have many advantages including high coupling factors, low acoustic impedance, mechanical flexibility and a broad bandwidth in combination with low mechanical quality factor. They are especially useful for underwater sonar and medical diagnostic ultrasonic transducers [76].

E) Piezo-films

Basically this class includes zinc oxide (ZnO) and aluminum nitride (AlN), being simple binary compounds that have Wurtzite type structure, which can sputter-deposited in a c-axis oriented thin film on variety of substrates. ZnO has moderate piezoelectric coupling and its thin films are widely used in bulk acoustic and SAW (Surface Acoustic Wave) devices [76].

2 Piezoelectric phenomenon

Piezoelectric direct and converse effect

Certain single crystal materials: when mechanically strained, or deformed by external loads exhibit a distribution of electric charges on crystal surfaces. Moreover when direction of strain reverses, polarity of electric charges is reversed too. This is the so-called "*direct piezoelectric effect*" and crystals that exhibit this phenomenon are classed as "*piezoelectric crystals"*. (Fig 6.1)

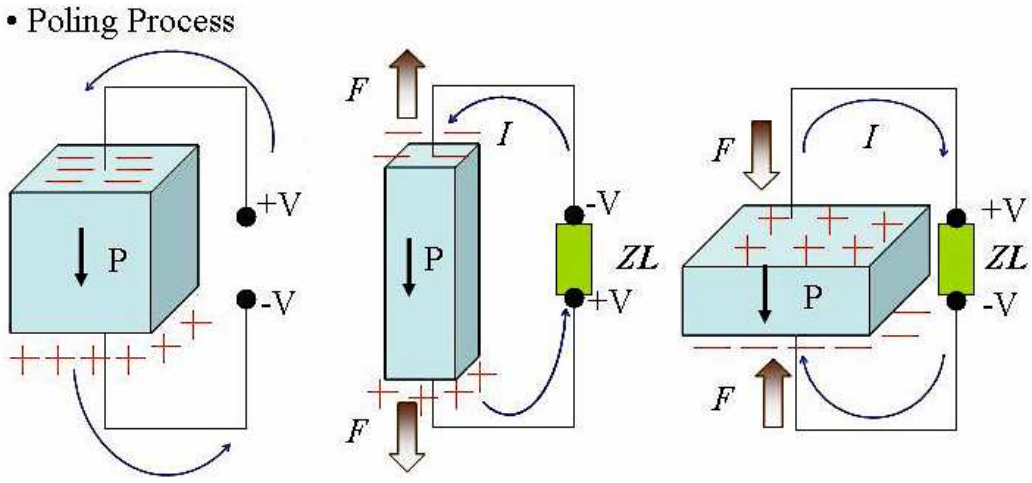

Fig 6.1 Direct piezoelectric effect [77]

By converse, when a piezoelectric crystal is placed in to an electric field, or charges are applied to its faces, crystal exhibits a mechanical strain, i.e. dimensions of the crystal change, either leading to an elongation or a compression depending on the polarization of

the solid. When direction of the applied electric field is reversed, even strain is reversed. This is the so-called "*converse piezoelectric effect*". (Fig 6.2)

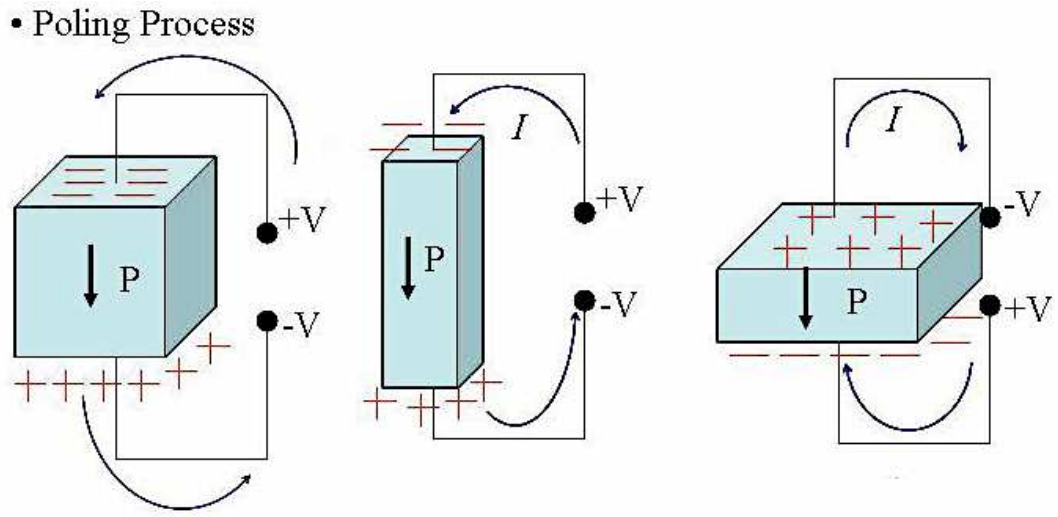

Fig 6.2 Converse piezoelectric effect [77]

Piezoelectric coefficient

Several piezoelectric coefficients are used in the literature to describe this phenomenon (d_{ij}, g_{ij}, S_{ij}, k_{ij}, and e_{ij}) and will be discussed in this section. These coefficients allow measuring the performance of the piezoelectric coupling and energy conversion [78].

A) Piezoelectric charge Constant (d_{ij})

The "piezoelectric charge or strain constant", d_{ij} is a measure of the elastic charge induced in response to a mechanical stress, or the achievable mechanical strain when an electric field is applied for a stress constant.

B) Piezoelectric voltage constant (g_{ij}**)**

The piezoelectric "voltage constant", g defines the ratio of the electric field strength E to the effective mechanical stress T.

$$\frac{d_{ij}}{\varepsilon}=g_{ij} \qquad (6.1)$$

where ε is the dielectric permittivity.

C) Elastic Compliance (S_{ij})

The elastic constant or compliance is a measure of the ratio of the relative deformation to the mechanical stress. Because it depends on the interaction of mechanical and electrical energy, the electrical boundary conditions must be taken into consideration.

D) Dielectric Coefficient (ε_{ij})

The permittivity or relative dielectric constant is a measure of the polarizability of material. The directionary of the permittivity is expressed by tensor components, whereby the same component indexes are used as for the electric field and dielectric displacement.

E) Piezoelectric Coupling Coefficient (k_{ij})

The coupling factor k is a measure of the effectiveness of the piezoelectric effect. It describes the ability of a piezoelectric material to transform electrical energy into mechanical energy and vise versa. Mathematically, the size of the coupling factor is determined by the square root of the ratio stored mechanical energy to the total energy applied.

$$D_i = d_{mi}\sigma_j + \varepsilon_{ik}E_k \quad (6.2)$$

$$\varepsilon_i = S_{ij}\sigma_j + d_{mi}E_m \quad (6.3)$$

where D_i refrers to electrical polarization, E_k is vector of apllied electric field and the indexes i, j = 1, 2, . . . ,6 and m, k = 1, 2, 3 refer to different directions within the material coordinate system.

3 Material Applications of Piezoelectric

Applications of the piezoelectric materials are in many fields. Lead Zirconate Titanate (PZT) ceramics, which was discovered on 1954 is the material dominating in this field until today [78]. Nevertheless many piezoelectric devices are currently used as Table 6.1 shown [79, 80].

Table 6.1 Applications of piezoelectric materials

Technology	Application
Piezo devices	Emitter and receiver for sonar applications Flow & distance measurement Non Destructive Testing Ultrasonic cleaning Ultrasonic welding
Piezo actuators	Micro- & nano positioning Vibration & noise control Valves & pumps Optics and photonics Ultrasonic motors Instrumentation
Piezo sensors	Vibration and shock measurement Pressure and force measurement Flow and distance measurement Sound and noise measurement
Piezo generators	Energy source for munitions Energy source for wireless sensors, e.g. in tyres Energy source for lightning switches Gas igniters
Piezo transducers	Communication devices Sonars Ultrasonic welding Ultrasonic cleaning
Energy harvester	Vibration harvesters in configuration of bimorph benders

3.1 LEAD ZIRCONATE TITANATE (PZT)

Lead Zirconate Titanate is an inorganic compound with the chemical formula Pb $[Zr_xTi_{1-x}]O3$ ($0 \leq x \leq 1$), this ceramics consolidates an excellent piezoelectric material position, PZT ceramics are commercially the most important materials because of their superior properties and also because of the ability of tailoring their properties. They are known to be simultaneously ferroelectric–ferroeleastic materials [82].

Mechanical properties of PZT ceramics are of considerable importance in the design of transducers and other piezoelectric devices. They are conventionally distinguished in SOFT and HARD piezoceramic. Words "soft" and "hard" refer to mobility of the dipoles or domains and hence also to the polarization and depolarization behaviors. Hard and soft PZT's generally differ in their piezoelectric constants. Figs 6.2 and 6.3 show the structure of PZT.

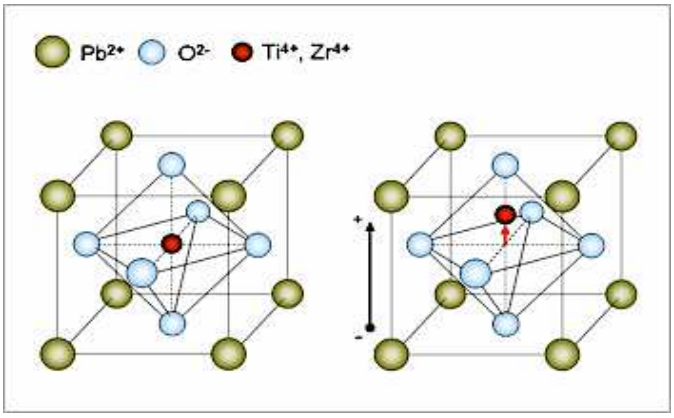

Fig 6.2 Structure of PZT [83]

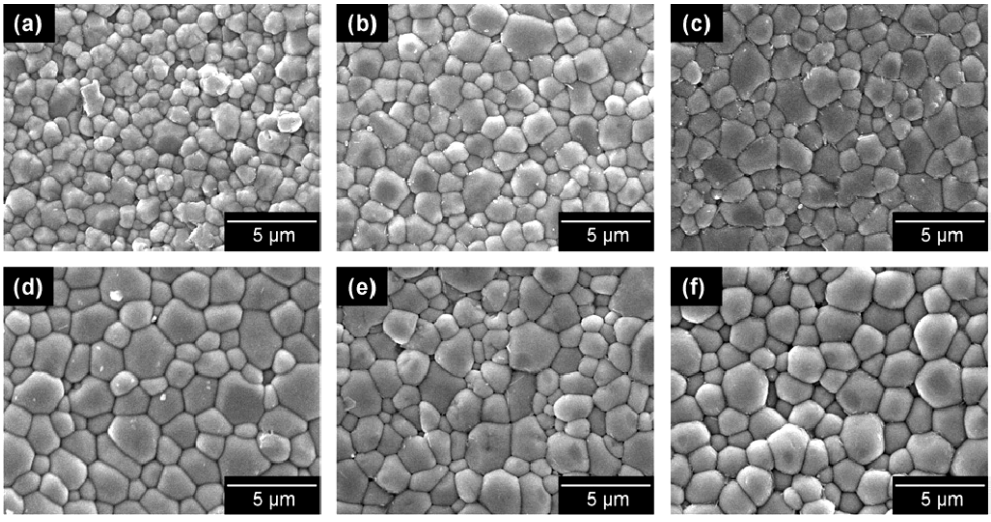

Fig 6.3 SEM images of PZT ceramics at different temperatures: (a) 900°C, (b) 950°C, (c) 1000°C, (d) 1050°C, (e) 1100°C, (f) 1150°C [84]

Characteristics of PZT:

- Wide range of frequencies in transmitting and receive (sub-audible, audible, ultrasonic)
- High output, low drive material
- High frequency, fast response time
- High sensitivity for active or passive use
- Ability to use with low voltage or high voltage drive circuits
- Good mechanical and acoustic coupling
- Wide variety of shapes and sizes that can be customized to fit specific requirements and applications
- Wide variety of compositions that can be selected to fit specific requirements and applications

Applications of PZT:

- Undersea exploration (sonar, beacons, imaging, current meters)
- Aerospace (gyroscopes, accelerometers, fuel level sensing)
- Medical products (Doppler blood flow, oncology therapeutics, level sensing, intra-operative tools for ophthalmology, dental descaling, general surgery, tissue ablation, medication delivery, hearing enhancement, bubble detection)
- Consumer products (ultrasonic toothbrushes, jewellery cleaners, contact lens cleaners, computer hard drives, touch screen displays, integrated, ultra-thin speakers and cosmetic enhancement)
- Industrial and commercial (flow and level sensors, ultrasonic cleaning, ultrasonic welding, intrusion alarms, fabric needle positioning, solder dispensing, machine vibration monitoring, bubble detection, sonochemistry for improved chemical mixing)
- Telecommunications (optical switching of telecom lines, buzzers and alarms, Haptics feedback, mobile phone cameras)
- Automotive (power seat controls, reversing/collision avoidance sensors, anti-knock sensors)
- Scientific research (nano positioning stages and analytical tools, scanning probe microscopy, advanced acoustics)

Mechanical and electrical properties of PZT are shown in the Table 6.2.

Table 6.2 Mechanical and electrical properties of PZT

Piezoelectric Coefficient d_{31}	Piezoelectric Coefficient d_{32}	Piezoelectric Coefficient d_{33}	Piezoelectric Coefficient d_{15}	Coupling factor K_{31}	Coupling factor K_{33}
(-121) ÷ (-175) pC/N	(-121) ÷ (-175) pC/N	300 ÷ 500 pC/N	495 ÷ 585 pC/N	0.3 ÷ 0.35	0.69
Young's Modulus	Flexural Strength	Poisson Ratio	Dielectric Constant	Dielectric Strength	Density
110 ÷ 120 GPa	73 MPa	0.34	1200 ÷ 3000 MHz	3900 Kv/m	7.8 Kg/m^3
Tensile Strength	Thermal Conductivity	Thermal Expansion	Hardness	Fracture Toughness K_{IC}	
425 ÷ 495 MPa	1.1 ÷ 1.5 W/m.k	4-8 * 10^{-6} $°C^{-1}$	5 ÷ 8 GPa	1.02 MPa.$\sqrt{m}$	

3.2 POLYVINYLIDENE FLUORIDE (PVDF)

Polyvinylidene fluoride (PVDF) is a highly non-reactive and thermoplastic fluoropolymer. It was developed primarily for applications demanding excellent chemical resistance, high levels of purity and superior mechanical properties. PVDF is often used as a lining or protective barrier in chemical industry applications. Compared to other fluoropolymers, it has relatively low melting point which in-fact enables easier melt processing [85]. It can also be injection moulded and welded and hence it is commonly used in the chemical, semiconductor, medical and defense industries. Also it has a relatively low density and it is of low cost too.

PVDF is a ferroelectric polymer too and hence it can exhibit efficient piezoelectric and pyroelectric properties, they making it useful in sensor and battery applications. Thin films of PVDF are used in some newer thermal camera sensors [86].

PVDF is also used as a principal ingredient in many high-end paints for metals. These PVDF paints have extremely high gloss look and good color retention too.

The main purpose of including PVDF in this screening is because it is known for its excellent resistance to creep and fatigue, excellent thermal stability, excellent radiation resistance, superior tensile properties and impact strengths, excellent resistance to reduce high dielectric strength over a wide temperature ranges.

Strong piezoelectricity is observed in PVDF, piezoelectric coefficients of poled (placed under a strong electric field to induce a net dipole moment) thin films are 10 times larger than that observed in any other polymer. Structure and SEM image of PVDF are shown in Figs 6.4 and 6.5.

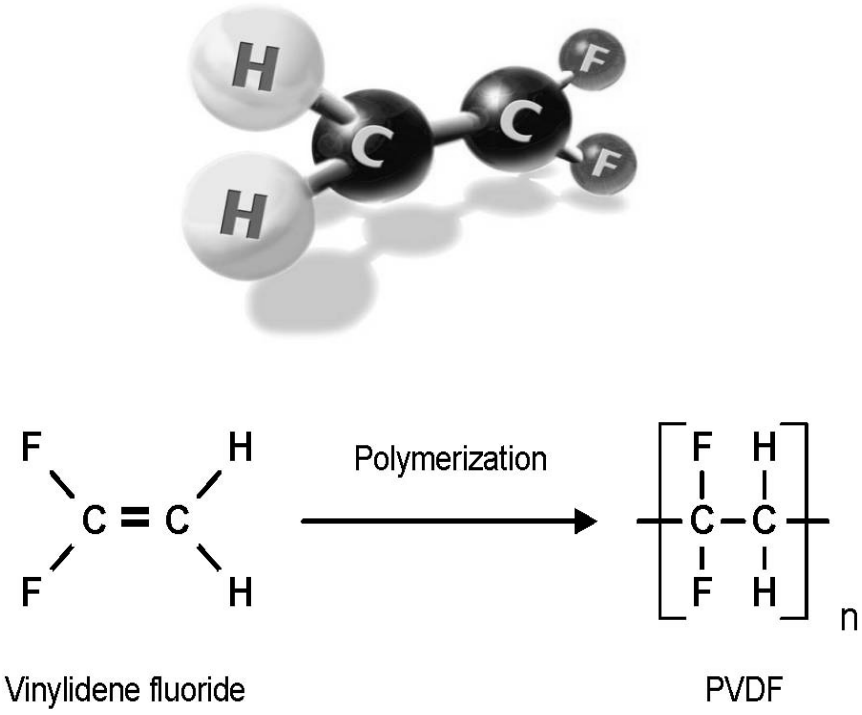

Fig 6.4 Structure of PVDF [87]

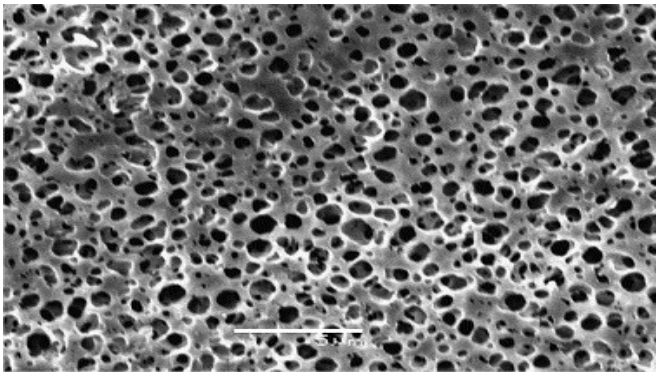

Fig 6.5 SEM of PVDF membrane [88]

Characteristics of Polyvinylidene fluoride (PVDF):

- High-performance material
- Low flammability in accordance with DIN 4102
- Excellent chemical resistance
- Physiologically safe
- Exceptionally good ageing resi stance

Application of Polyvinylidene fluoride (PVDF):

- High temperature and chemical resistance industry.
- Chemical industry
- Food industry
- Nuclear industry
- Tank and apparatus construction
- Electroplating industry
- Paper and textile industry
- Semi-conductor industry
- Environmental protection

Mechanical and electrical properties of PVDF are shown in Table 6.3.

Table 6.3 Mechanical and electrical properties of PVDF

Piezoelectric Coefficient d_{31}	Piezoelectric Coefficient d_{32}	Piezoelectric Coefficient d_{33}	Piezoelectric Coefficient d_{15}	Coupling factor K_{31}	Coupling factor K_{33}
-33 pC/N	2 pC/N	25 pC/N	27 pC/N	0.15 ÷ 0.20	0.12
Young's Modulus	Flexural Strength	Poisson Ratio	Dielectric Constant	Dielectric Strength	Fracture Toughness K_{IC}
2 GPa	60 ÷ 65 MPa	0.225	6.8 ÷ 7.7 MHz	40 ÷ 80 Kv/m	0.7 ÷ 1.6 MPa.$\sqrt{m}$
Tensile Strength	Yield Strength	Density	Hardness	Thermal Conductivity	Thermal Expansion
50 ÷ 57 MPa	45 ÷ 55 MPa	1.78 Kg/m^3	58 MPa	0.17 ÷ 0.19 W/m.k	$5÷7 * 10^{-5}$ $°C^{-1}$

3.3 ALUMINUM NITRIDE (AlN)

Aluminum nitride (AlN) is a high thermal conductivity electrical insulator ceramic. Among the piezoelectric materials, in particular, AlN has drawn researchers strong attention turning out to be a powerful material, because of its great number of advantages [89]. Aluminum nitride is considered as the most preferred material for acoustic application that allows to obtain the high sound velocity because of its wide band gap E_g=62 (eV). This parameter and high mechanical quality factor are also one of the demanded properties for fabrication of filters for high frequency and wide band, respectively. For both above-mentioned applications, electromechanical coupling is the most limiting property of AlN. Other piezoelectric material such as PZT and ZnO, which belongs to the ferroelectric group, exhibit much larger coupling coefficient. However, they do not assure high quality factors. Moreover, AlN exhibits lower piezoelectric coefficients than any other material [90]. Aluminum nitride has a hexagonal crystal

structure and is a covalent bonded material. It is stable at very high temperature in inert atmosphere. Most current applications are in electronics area where heat removal is important. However, AlN is an excellent material for IC integration. It is much more compatible with conventional Si manufacturing technology than other thin films. This is due to its thermal stability, chemical composition and possibility to achieve a low deposition temperature [91]. It has very good piezoelectric properties and low dielectric permittivity, nearly 100 times lower than PZT. Therefore, AlN is used in MEMS fabrication [92]. It exhibits a large voltage to break down and low leakage current, with high electrical resistance. It has good temperature compensation with good thermal stability. Chemical stability, very high hardness and melting point ensure that AlN thin layers do not degrade during processing. AlN does not require poling for activating piezoelectric phenomenon [93]. Structure and SEM image of AlN are shown in Figs 6.6 and 6.7 and properies in Table 6.4.

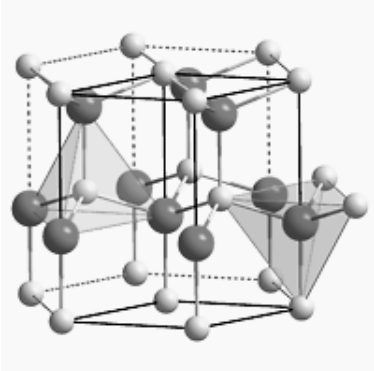

Fig 6.5. Structure of ALN [94]

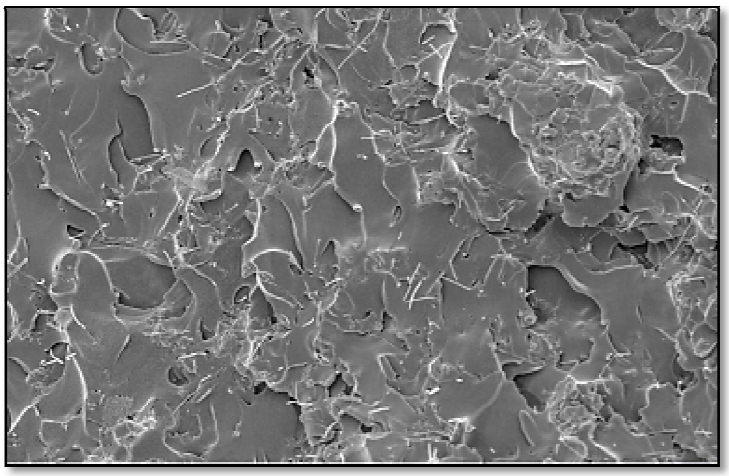

Fig 6.7. SEM of ALN membrane [95]

Characteristics of Aluminum Nitride (ALN):

- Very high hardness
- High elastic stiffness
- Good dielectric properties
- High thermal conductivity and low thermal expansion
- High temperature stability
- Corrosion resistance and chemically resistant material
- High electrical resistivity and low electric losses
- High breakdown voltage (U_b>800 kV/cm)
- High ultrasonic velocity

Application of Aluminum Nitride (ALN):

- Piezoelectric applications
- In-vitro biosensors
- Actuators and acoustic wave devices
- Power transistor bases
- MEMS application and microwave device packages
- Substrates for electronic packages
- Heat sinks
- Semiconductor processing chamber fixtures and insulators
- Molten metal handling components

Table 6.4 Mechanical and electrical properties of AlN

Piezoelectric Coefficient d_{31}	Piezoelectric Coefficient d_{32}	Piezoelectric Coefficient d_{33}	Piezoelectric Coefficient d_{15}	Coupling factor K_{31}	Coupling factor K_{33}
-2.1 pC/N	-2.1 pC/N	5.4 pC/N	3.6 pC/N	0.23	0.31
Young's Modulus	Flexural Strength	Poisson Ratio	Dielectric Constant	Dielectric Strength	Fracture Toughness K_{IC}
310 GPa	320 ÷ 350 MPa	0.21 ÷ 0.28	8-9.1 MHz	More than 20 kV/mm	3.3 MPa.$\sqrt{m}$
Hardness	Thermal Conductivity	Thermal Expansion	Tensile Strength	Density	
10.7 GPa	170 W/mK	4.5 * 10^{-6} $^{o}C^{-1}$	300 ÷ 400 MPa	3.3 g/cm^3	

3.4 BaTiO3

Barium Titanate was the first developed piezoelectric ceramic and even now it is still widely used. It is also a well-known material used for capacitors. BaTiO3 is the first piezoelectric transducer ceramic ever developed; however, its use in recent years has shifted away from transducers to an almost exclusive use as high-dielectric constant capacitors of discrete and multilayer (MLC) types. Reasons for this are strategy two: its relatively low TC (critical temperature) of 120°C, which limits its use as high-power transducers, and its low electromechanical coupling factor in comparison to PZT (0.35 vs 0.65). Unlike PZT, which is a solid-solution composition containing a volatile component (PbO), BaTiO3 is a definite chemical compound possessing relatively high stability components, making it easy to sinter while maintaining good chemical stochiometry. Nevertheless, these materials are often used combined with special additives to improve their basic properties. When BaTiO3 is used in its primary application as a capacitor, a

different group of additives is used. In this case the goal is suppressing the ferroelectric and piezoelectric properties as much as possible while maintaining or increasing its dielectric constant. Applications include switches, sensors, motor starters, and controllers [96]. Structure and SEM image of BaTiO3 are shown in Figs 6.8 and 6.9 and properties in Table 6.5.

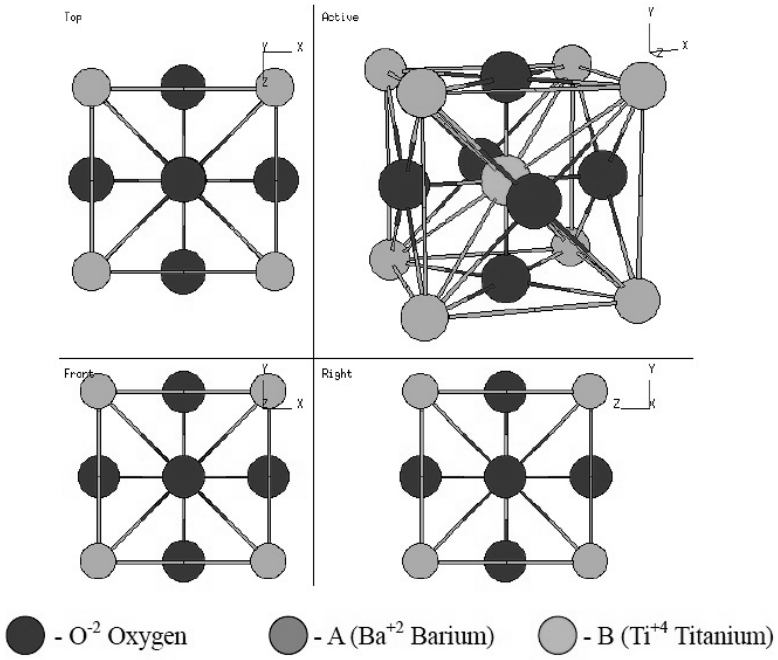

Fig 6.8. Perovskite Structure of BaTiO3 [97]

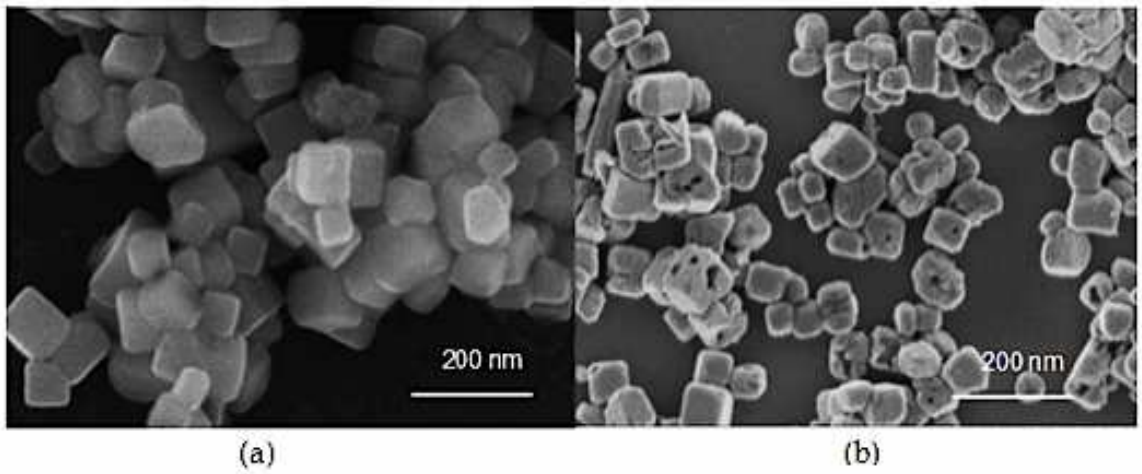

Fig 6.9. SEM images of BaTiO3 micro crystallites synthesized [98]

Applications of (BaTiO3):

- Capacitors
- Microphones
- Transducers
- Thermistors and self-regulating electric heating systems
- Nonlinear optics
- Photorefractive applications
- Uncooled sensors for thermal cameras

Table 6.5 Mechanical and electrical properties of BaTiO3

Piezoelectric Coefficient d_{31}	Piezoelectric Coefficient d_{32}	Piezoelectric Coefficient d_{33}	Piezoelectric Coefficient d_{15}	Coupling factor K_{31}	Coupling factor K_{33}
-58 pC/N	-58 pC/N	145 pC/N	245 pC/N	0.19	0.46
Young's Modulus	Flexural Strength	Poisson Ratio	Dielectric Constant	Dielectric Strength	Fracture Toughness K_{IC}
100 ÷ 125 GPa	98 MPa	0.37	640 kHz	181 kV/cm	0.49 MPa.$\sqrt{m}$
Hardness	Thermal Conductivity	Thermal Expansion	Density	Tensile Strength	
5 mohs	2.90 W/mK	(7 ÷ 8) *10^{-6} $^{o}C^{-1}$	5.5 g/cm3	52 MPa	

3.5 ZINC OXIDE (ZnO)

ZnO is formed in natural as the mineral zincite. Zinc oxide is a piezoelectric material with hexagonal Wurtzite crystal structure. ZnO crystals are composed of alternate layers of zinc and oxygen atoms disposed in wurtzite hexagonal close-packed structure, with a longitudinal axis. However, most of ZnO used commercially is synthetically produced. ZnO is widely used as an additive in a variety of applications including ceramics, plastics, cement, glasses, lubricants, paints, pigments, and ointments. Recently, due to its semiconducting properties, ZnO has been considered very attractive as an emerging material for electronics applications [99]. It is also widely used in gas sensors, “resisting coating against UV (Ultra-Violet) radiation”, piezoelectric devices, varistors, surface acoustic wave (SAW) devices and transparent conductive oxide electrodes. Recently ZnO has also attracted attention for its possible application in short wavelength light emitting diode (LEDs) and laser diodes because the optical properties of ZnO are similar to those of GaN [100, 101]. Pure zinc oxide, carefully prepared in a laboratory is a good insulator; however, it can be increased in electrical conductivity many fold by special heat treatments and by the introduction of specific impurities into the crystal lattice. ZnO can even be made to exhibit metallic conductivity as for transparent electrodes similar to ITO (Indium Tin Oxide) [102]. Coupling coefficient for ZnO is high which makes ZnO an excellent material to be used in wide variety of piezoelectric applications [103].

ZnO does not have the best piezoelectric coefficient compared with other piezoelectric materials like PZT (lead zirconate titanate) and BaTiO3 (barium titanate), although ZnO has several advantages. It has both semiconductor and piezoelectric characteristics, it is also biocompatible, and suitable for application in nanotechnology [104]. Structure and SEM image of ZnO are shown in Figs 6.10 and 6.11 as properties in Table 6.6.

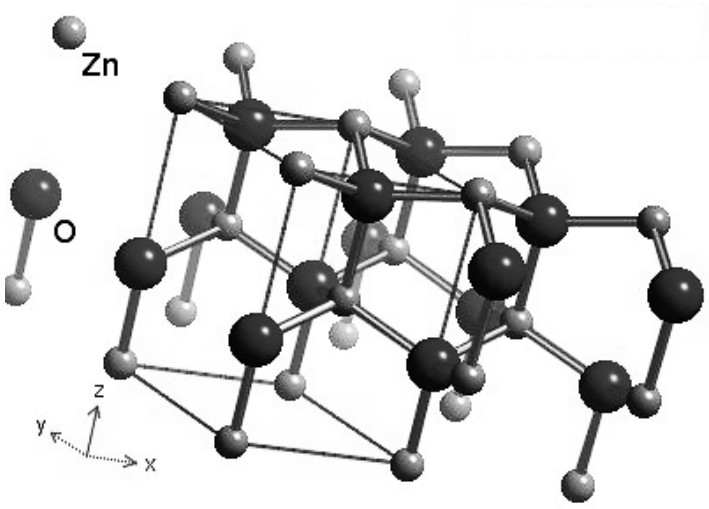

Fig 6.10. Structure of ZnO [105]

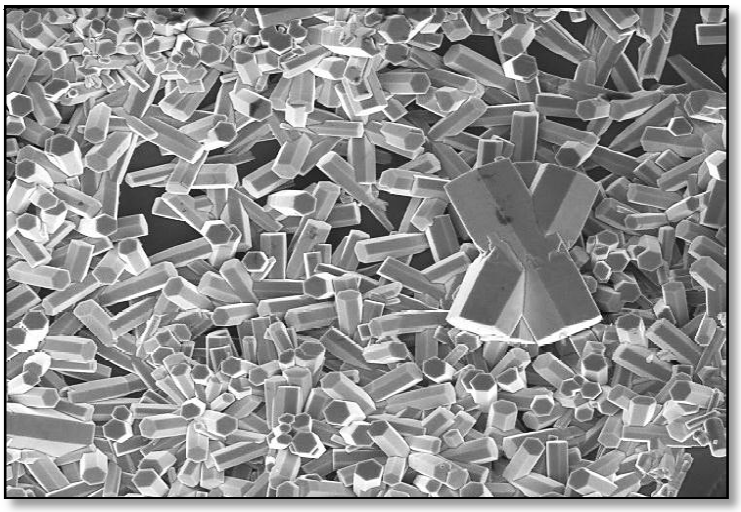

Fig 6.9. SEM images of ZnO [106]

Characteristics of Zinc Oxide (ZnO):

- High carrier mobility
- Transparency
- Wide band gap
- Low temperature process
- Cost saving

Applications of Zinc Oxide (ZnO):

- Variable sensor devices, which are used to prevent voltage surges in devices like cellphone.
- Pigments in paints. Chinese white is a special grade of white pigment based on zinc oxide.
- Filler for rubber products
- Metal-protective coating
- Batteries, fuel cells and photocells
- Coatings for paper
- Sunscreens and sunblocks for the prevention of sunburn
- Rubber industry
- Plastics and ceramic industry

Table 6.5. Mechanical and electrical properties of ZnO

Piezoelectric Coefficient d_{31}	Piezoelectric Coefficient d_{32}	Piezoelectric Coefficient d_{33}	Piezoelectric Coefficient d_{15}	Coupling factor K_{31}	Coupling factor K_{33}	Fracture Toughness K_{IC}
-5.43 pC/N	-5.43 pC/N	11.7 pC/N	-11.3 pC/N	0.18	0.47	1.2-1.4 MPa.$\sqrt{m}$
Young's Modulus	Flexural Strength	Poisson Ratio	Dielectric Constant	Dielectric Strength	Density	Thermal Expansion
20 GPa	100-125 MPa	0.36	4.5 MHz	106 V/Cm	5.6 g/cm^3	6.5*10^{-6} $^oC^{-1}$

CHAPTER 7

FRACTURE ANALYSIS OF SINGLE LAYER OF PIEZOELECTRIC MATERIAL

1 Specimens and analysis conditions

Set of specimens analyzed in case of smart piezoceramic PZT-4 has the same geometries used for steel, although piezoelectric coefficient had to be inputted.

Because of its wide use in industry such as: ultrasonic cleaners, ultrasonic atomizers, ultrasonic micro-bonding apparatus, underwater echo sounders, high frequency transducers, high stress pressure sensors, squeeze-type gas igniters, high power actuators, vibratory motors, transformers, ultrasonic welding, ultrasonic mixing, ultrasonic surgery, son chemistry and so on.

Electro-mechanical properties of PZT-4 such as elasticity, piezoelectric coupling and dielectric are defined as follows:

$$\text{Elasticity} = \begin{bmatrix} C_{11} & C_{12} & C_{13} & 0 & 0 & 0 \\ C_{12} & C_{11} & C_{13} & 0 & 0 & 0 \\ C_{13} & C_{13} & C_{33} & 0 & 0 & 0 \\ 0 & 0 & 0 & C_{44} & 0 & 0 \\ 0 & 0 & 0 & 0 & 55 & 0 \\ 0 & 0 & 0 & 0 & 0 & 2(C_{11} - C_{12}) \end{bmatrix} \text{[GPa]} \quad (7.1)$$

$$\text{Elasticity} = \begin{bmatrix} 115.4 & 74.28 & 74.28 & 0 & 0 & 0 \\ 74.28 & 139 & 77.84 & 0 & 0 & 0 \\ 74.28 & 77.84 & 139 & 0 & 0 & 0 \\ 0 & 0 & 0 & 25.64 & 0 & 0 \\ 0 & 0 & 0 & 0 & 25.64 & 0 \\ 0 & 0 & 0 & 0 & 0 & 25.64 \end{bmatrix} [\text{GPa}]$$

$$\text{Piezoelectric coupling} = \begin{bmatrix} d_{33} & 0 & 0 \\ -d_{31} & 0 & 0 \\ -d_{31} & 0 & 0 \\ 0 & d_{15} & 0 \\ 0 & 0 & d_{15} \\ 0 & 0 & 0 \end{bmatrix} [\text{c/m}^2] \quad (7.2)$$

$$\text{Piezoelectric coupling} = \begin{bmatrix} 15.08 & 0 & 0 \\ -5.207 & 0 & 0 \\ -5.207 & 0 & 0 \\ 0 & 12.71 & 0 \\ 0 & 0 & 12.71 \\ 0 & 0 & 0 \end{bmatrix} [\text{c/m}^2]$$

$$\text{Dielectric} = \begin{bmatrix} \varepsilon_{11} & 0 & 0 \\ 0 & \varepsilon_{22} & 0 \\ 0 & 0 & \varepsilon_{33} \end{bmatrix} 10^{-9} [\text{farad/m}] \quad (7.3)$$

$$\text{Dielectric} = \begin{bmatrix} 5.872 & 0 & 0 \\ 0 & 6.752 & 0 \\ 0 & 0 & 6.752 \end{bmatrix} 10^{-9} [\text{farad/m}]$$

Dimensions and geometries of specimens are the same of previous analysis. In particular specimen has length 180 mm, width 40 mm, thickness 30 mm and initial crack length 20 mm.

2 Modeling the fracture mechanics of piezoelectric inside the ABAQUS© code

Modeling of fracture inside the piezoelectric material is similar to the case of steel, but some modification to case with electromechanical coupling was required. Inside the “property module”, properties of piezoelectric have to be inputted. In particular PZT exhibits behaviour of an orthotropic material. Therefore orientation is strictly important in the numerical investigation.

In case of piezoelectric material in addition to the mechanical loads input voltage, electrical potential and electrical boundary conditions are even defined. To proceed special elements being piezoelectric are selected to build up the mesh.

Unfortunately the Abaqus software is unable to perform the fracture analysis in case of piezoelectric material by taking into account the electro mechanical behaviour of this material. As above mentioned fracture and piezoelectric analysis can be run separately but never in combination.

To solve this problem, a suitable procedure creates a link between the fracture and the piezoelectric model, respectively. The ISIGHT program was used to solve this problem and connect the electro mechanical coupling together with the fracture mechanics analysis inside the Abaqus.

3 The ISIGHT program

In computer-aided product development, engineers are currently using a wide range of softwares to design and simulate their products. Often results computed by one package are inputs for another code. Manual process may introduce some errors in modeling and simulations. SIMULIA© provides some market-leading solutions to improve the process of leveraging the power of various software packages. ISIGHT is used to combine cross-disciplinary models and applications together in a simulation process flow, and automate their execution. ISIGHT's ability is manipulating and mapping parametric data between some process steps. It can make automatic a numerical simulation made of several steps and based on some cooperation softwares. Moreover it reduces manual errors and accelerates the evaluation of product design alternatives.

ISIGHT is a desktop solution that provides a suite of visual and flexible tools for creating simulation process flows-consisting of a variety of applications, including commercial CAD/ CAE software, internally developed programs, and Excel spreadsheets. If the ISIGHT code provides a standard library of components, which provides some blocks to create a simulation process flow. Each component is a sort of container with its own interface for integrating and running a particular model or simulation. It is even provided a set of protocols to correct outputs to applications like Excel™, Word™, MATLAB®, Text I/O applications, Scripting, and Databases. An open "API" and a "Component

Generator" allow the development of some components for simulation. The "Component Generator" creates custom GUIs for wrapped components, and extends the ISIGHT capabilities.

This open architecture allows SIMULIA and its partners to offer application components that provide a tighter integration with models developed in popular engineering software applications, such as Abaqus™, CATIA V5™, Pro/ENGINEER™, Unigraphics™, ENOVIA™, Teamcenter™, ANSYS™, LS-DYNA™, MADYMO™, Price-H™, SEER™, STAR-CCM+™, AVL™, Adams™, and different versions of Nastran™. It also enables partners and customers to add custom design driver techniques including DOE, approximation error analysis, optimization, Monte Carlo sampling methods, and random variable distributions. This approach makes it easier to create process flows, reduces maintenance costs, and provides timely access to new components or updates through an independent release process.

The intuitive "Design Gateway" graphical user interface enables users to quickly create integrated simulation process flows, which couple simulation programs regardless of discipline, programming language, or format. It provides drag-and-drop process flow creation, parameter mapping, and problem formulation. This process editor supports powerful file parameters that can represent simulation models as variables, as well as dynamically sizable arrays for both inputs and outputs. The software also provides branching, looping, conditional, and other execution logic. This flexibility, combined with scripts to alter the runtime behavior of the model as a function of changing parameter values, allows the creation of highly reusable processes. Once the process flow is defined, the user interface enables easy import of externally defined parameter values and problem formulations. Utilities such as model search, model content viewer, parameter search, and parameter grouping are also available.

The "Runtime Gateway" enables local execution of engineering process flows and creation of graphs and tables to visualize results. All job results are saved automatically to a locally managed MySQL database. The user interface supports the creation of visual tools for real-time post processing of data such as tables, 2D and 3D plots, and statistical analysis. Run data can be filtered and graded with a flexible set of criteria before post processing. All scatter plots allow easy one-click visualization of the virtual prototype by dedicated simulation results viewers. It provides interactive tools for visualizing parameter relationships as well as performance attribute tradeoffs with interactive approximations. Users can share these approximations with non-ISIGHT users by

exporting them to Excel. ISIGHT is offered as a standalone desktop product. However, any simulation process flow created with ISIGHT can be seamlessly executed on the SIMULIA Execution Engine from the Ru time Gateway. ISIGHT offers an extensive library of parallel process drivers, such as Design of Experiments, Optimization, Approximations, and Design for Six Sigma that enables engineers to thoroughly and quickly explore the design space.

Two main steps to integrating the Design Process are; first, understand the codes or tools used to solve the problem and the order in which they are executed and Second, “teach” ISIGHT how to run those codes or tools in the proper order. The procedure of using simcode component is as follow, which is shown in the picture:

Fig 7.1. Sequence of procedure simulation in the ISIGHT code.

Architecture of the ISIGHT tool includes (Fig 7.1):

- Simcode component
  i. Specifying the command
  ii. Defining how input and output data is created/captured
- Data Exchange component
  i. File wizards
  ii. Menu layout
  iii. Read vs. write
  iv. Template files
  v. Parameter modes, types and structures
- OS Command component
  i. Basic and Advanced options
  ii. Required Files

The Simcode component is used to integrate any simulation code that uses ASCII-based input and output. Internally, the Simcode component consists of three smaller components: two Data Exchange modules and one OS Command.

4 Prediction of SIF and J-Integral through the ISIGHT code

To solve the problem of fracture mechanics of piezoelectric material inside the ABAQUS code feature of fracture and piezoelectric analysis were connected together by means of ISIGHT tool, this procedure is here in described.

In the first step of this research activity a single layer of piezoceramic undergoing a single mode of fracture was analyzed.

A preliminary operation consists of modeling the specimen as it is inside the ABAQUS code, by providing all the mechanical properties of material as well as the relevant information about the crack, such as loading and boundary conditions, crack geometry, length and the GEM mesh.

To input the electrical properties and piezoelectric coefficients the same model is developed as a separated case, by introducing piezoelectric elements and by inputting all the required parameters.

To practice how similar models are pre-processed in the ABAQUS code. One is conceived for the fracture analysis and the other for the static and dynamic analysis of piezoelectric material. To perform the fracture analysis in presence of piezoelectric phenomenon the two analyses have to be run in sequence and the two models have to be made interacting each other.

Connection between the two analyses and related model is done by ISIGHT tool, by resorting to some components like a calculator loop, sub model and connector.

Fig 7.2 shows the architecture of the whole toolbox as it was developed, assembled and used by the author for this thesis. This model is aimed at computing only the stress intensity factor and the J-integral as it was done in pervious chapters for steel and composite specimens.

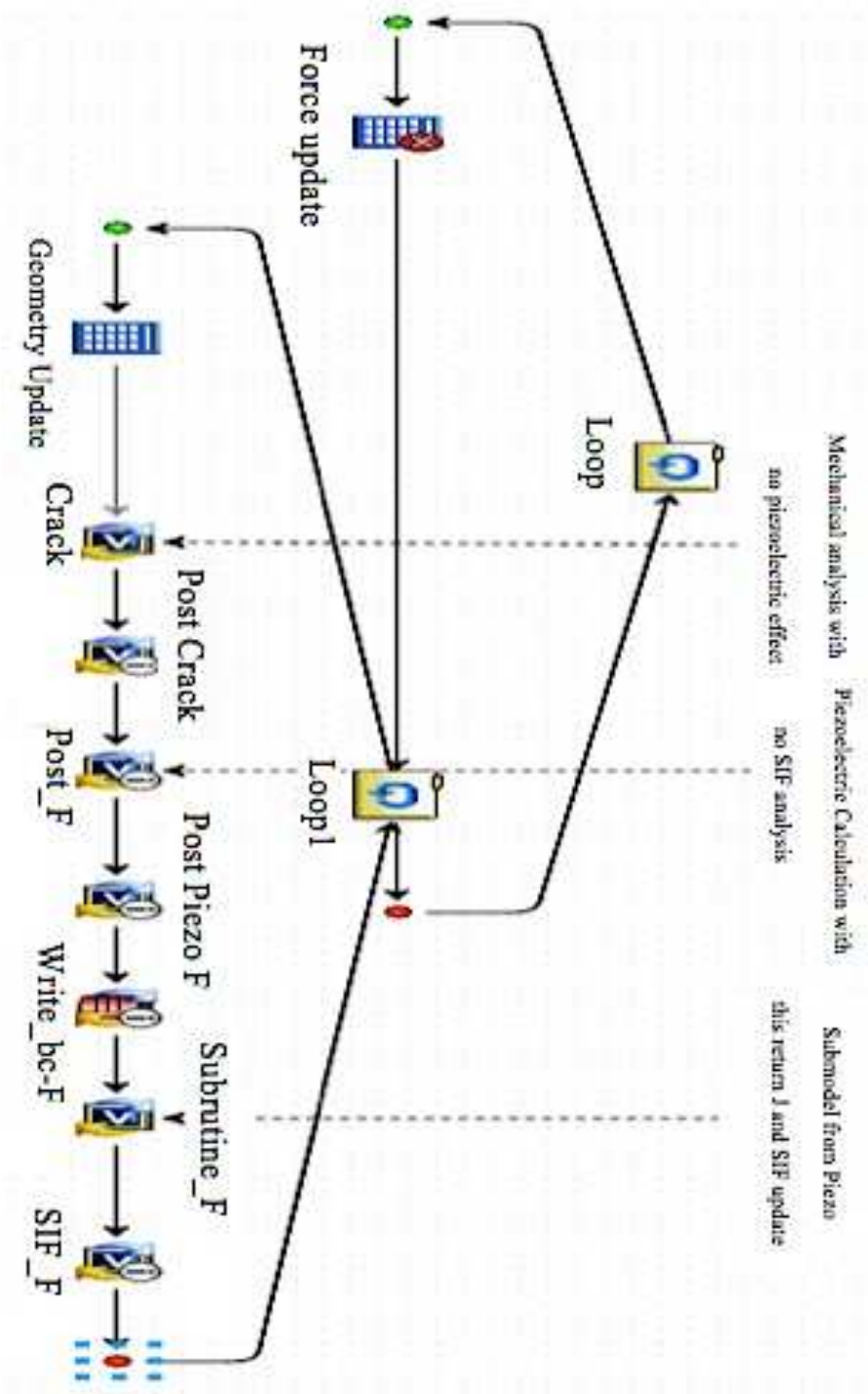

Fig 7.2: The model to obtain the value of J-Integral and SIF

Looking at the flow described in Fig 7.2, the first block to be considered is “crack”. This component consists of an active window, which can be opened into ISIGHT as Fig 7.3.

Users can save from ABAQUS code the first model above mentioned where only mechanical properties and loads were considered in '. py' files, i.e. by resorting to the Python code format available in ABAQUS. This command list can be copied and pasted inside the window called "crack" of ISIGHT code, as Fig 7.3 shows.

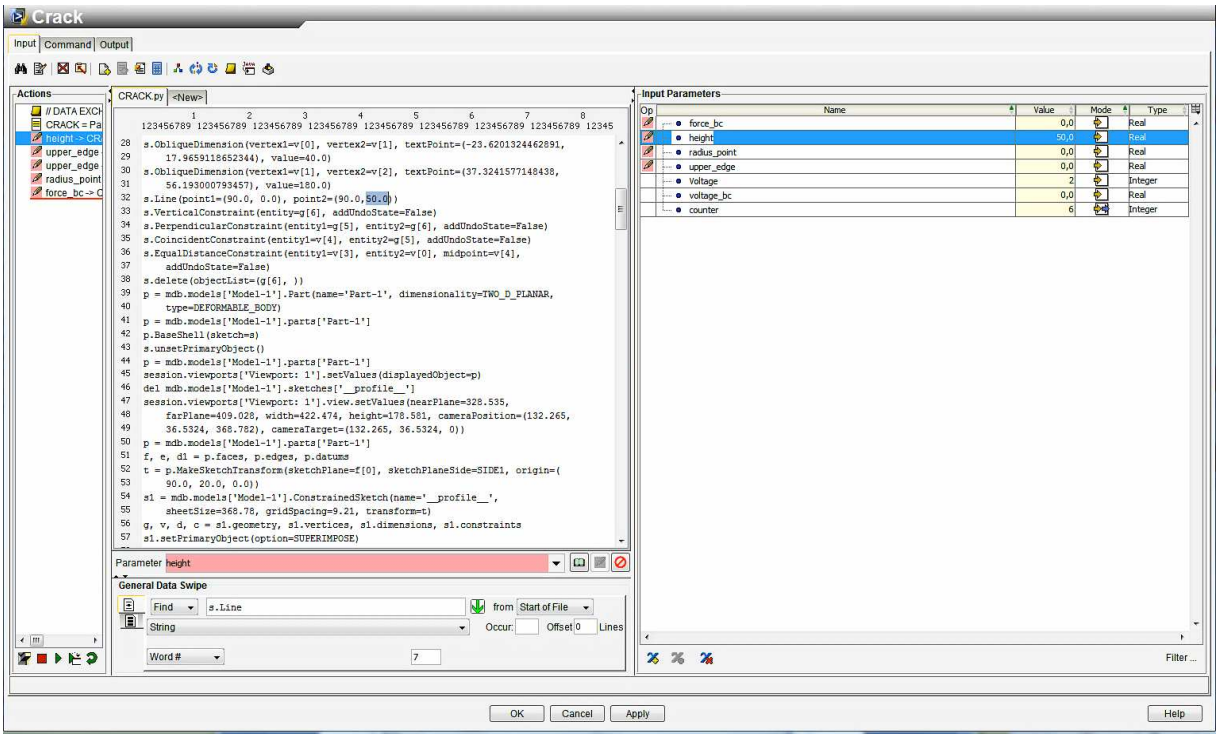

Fig 7.3: Using Python code coming from Abaqus model (Appendix 1)

In this module a first window includes all the INPUTS, a second one the commands for the analysis and a third one collects the outputs. When this first component "crack" is run in practice the fracture analysis is started, only mechanical loads and properties of piezoceramic are considered and SIF and J-integral are computed as in previous case of steel material.

A second active component, referred to as " POST-CRACK" collects the outputs of the first run above described, as well as all the inputs useful to run the piezoelectric analysis. This operation is foreseen by creating a suitable flow of data as Fig 7.4 shows. Parameter by parameter a connecting line is there drawn to tell the toolbox where required inputs for the next steps of numerical investigation have to be found.

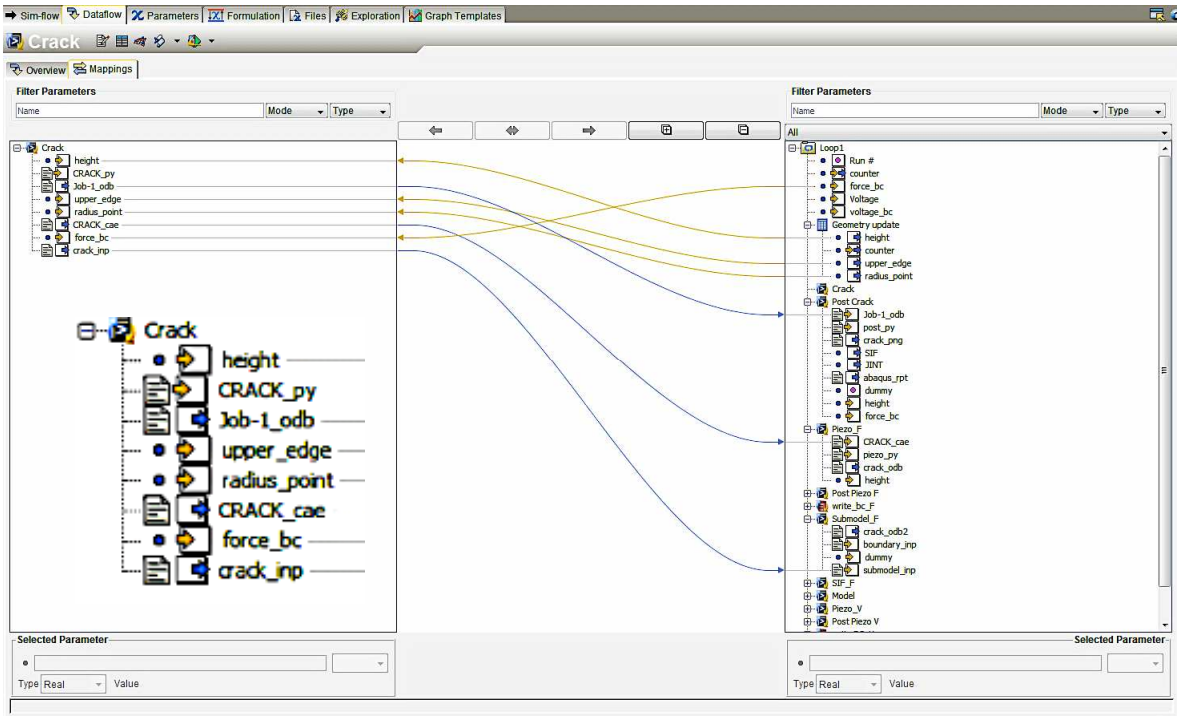

Fig 7.4: The element to connect different parameters together inside the program

A third action is performed by the component here referred to as “PIEZO-F”. This is an active window similar to the “CRACK” component. User copies and pastes here the model of piezoceramic specimen pre-processed in ABAQUS just to run the piezoelectric analysis and saved as a ‘.py’ file, by resorting to the python format. In this case model works by using only electromechanical and electrical properties of piezo to compute the displacements of the FEM model of specimen under the forces applied to the specimen. In this part no computation of SIF or J-integral is performed.

In “POST-PIEZO-F” flow of data, output and inputs for the loop is prepared by drawing the connecting lines among parameters as in Fig 7.5.

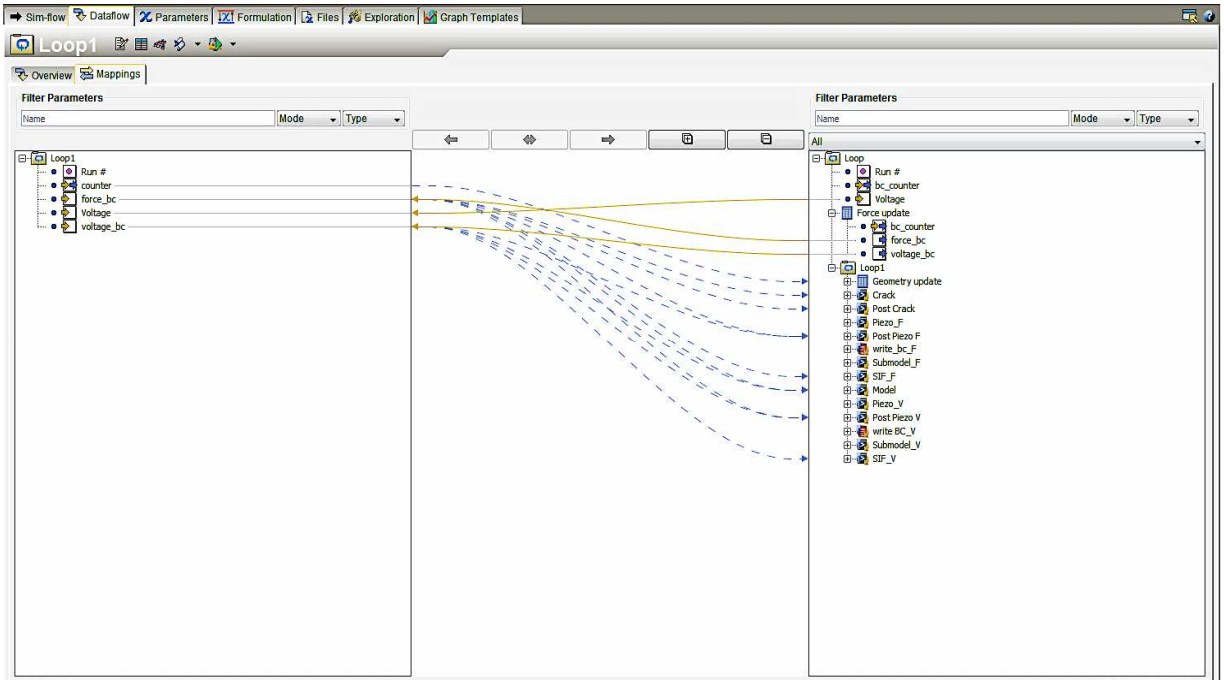

Fig 7.5: Connecting the parameters to make a loop for different conditions

Voltage distribution is even an output of this analysis. This is important because it changes the boundary conditions around the crack tip because sections are driven by the created electrical field induced the piezo electric phenomenon. So far boundary conditions are written and updated in the “WRITE BC-F” component.

“SUB MODEL F” collects the displacements due to the piezoelectric phenomenon and computed by the electromechanical analysis and converts this information into an updated value of SIF and of J-integral, which now includes the electromechanical coupling. In particular, SIF and J-integral are added in the solutions coming from the initial fracture analysis.

“SIF” component is conceived to store the final values of relevant parameters and of SIF and J-integral corresponding to this step of the simulation. This sequence only describes what it is done for a given geometry of crack and loading force. To be able to perform the analysis this calculator is divided in several steps.

A first level of loop is foreseen to subdivide in small increments of external loading condition the whole analysis. Therefore when convergence is reached for each value of

force a next step is started, by updating the force applied as the upper part of “BLOCK DIAGRAM” in Fig 7.2 shows and Fig 7.6 describes in detail.

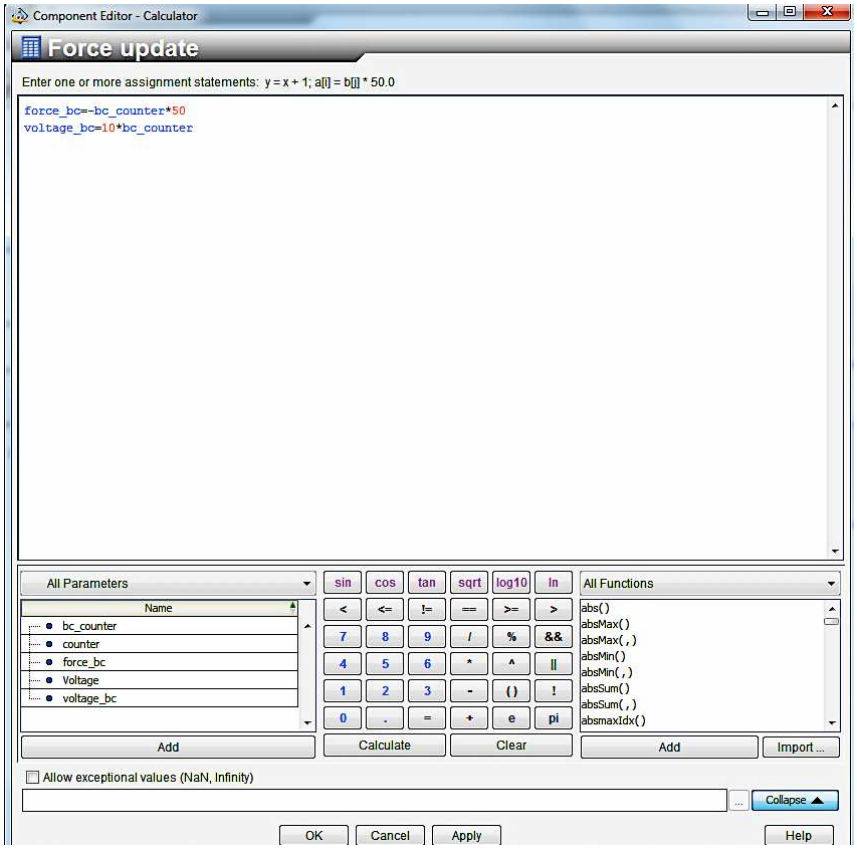

Fig 7.6: Calculator element to control the loads magnitude and boundary conditions

Nevertheless, the final crack length for each force magnitude is reached by an iterative solution by updating the geometry of cracked structure as lower functional “loop1” does in Fig 7.2. Even in case of a computation of SIF and J-integral partial results have to converge before then external load can be increased.

The sequence above described assumes that excitation is due to some mechanical actions applied to the structure, Voltage is first an effect of mechanical strain applied to piezoelectric and its effect upon the values of SIF and J-integral is evaluated as a correction to the main contribution driven by force.

In this case piezoelectric layer works as a sensor or even as an energy harvester, but its behaviour can be considered passively coupled to the structure.

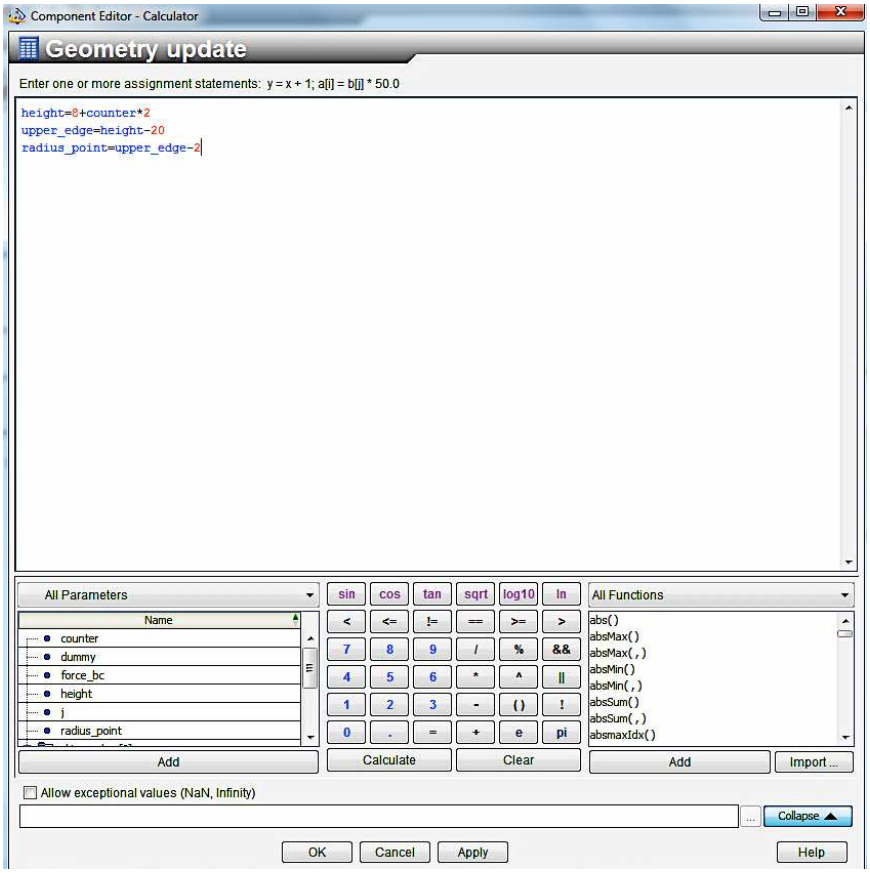

Fig 7.7: Geometry update in calculator module to loads magnitude and boundary conditions

When strain is induced by the applied electric field it is required dealing with the active a coupling between piezoelectric and structure. Therefore the ISIGHT model has to be updated to allow introducing this option, as Fig 7.8 shows. In particular the inner loop1 is equipped with a second path being activated in case of voltage driven response of the piezoelectric. A “MODEL” component collects inputs suitable to compute the actions applied to structure as a consequence of electric field excitation,

Sequence of operations is then similar to the other case, since SIF and J-integral are first computed by assuming that reformed shape is imposed by the electrical actuation. Nevertheless, piezoelectric does not loose its capabilities of sensing the strain applied to the structure and a feedback is provided in terms of created voltage, fairly lower than excitation but sufficiently high to motivate a separated evaluation and a correction of SIF and J-integral by means of “SUBMODEL-V” and “SIF-V” components which play the same role of pervious case, where response was driven by force.

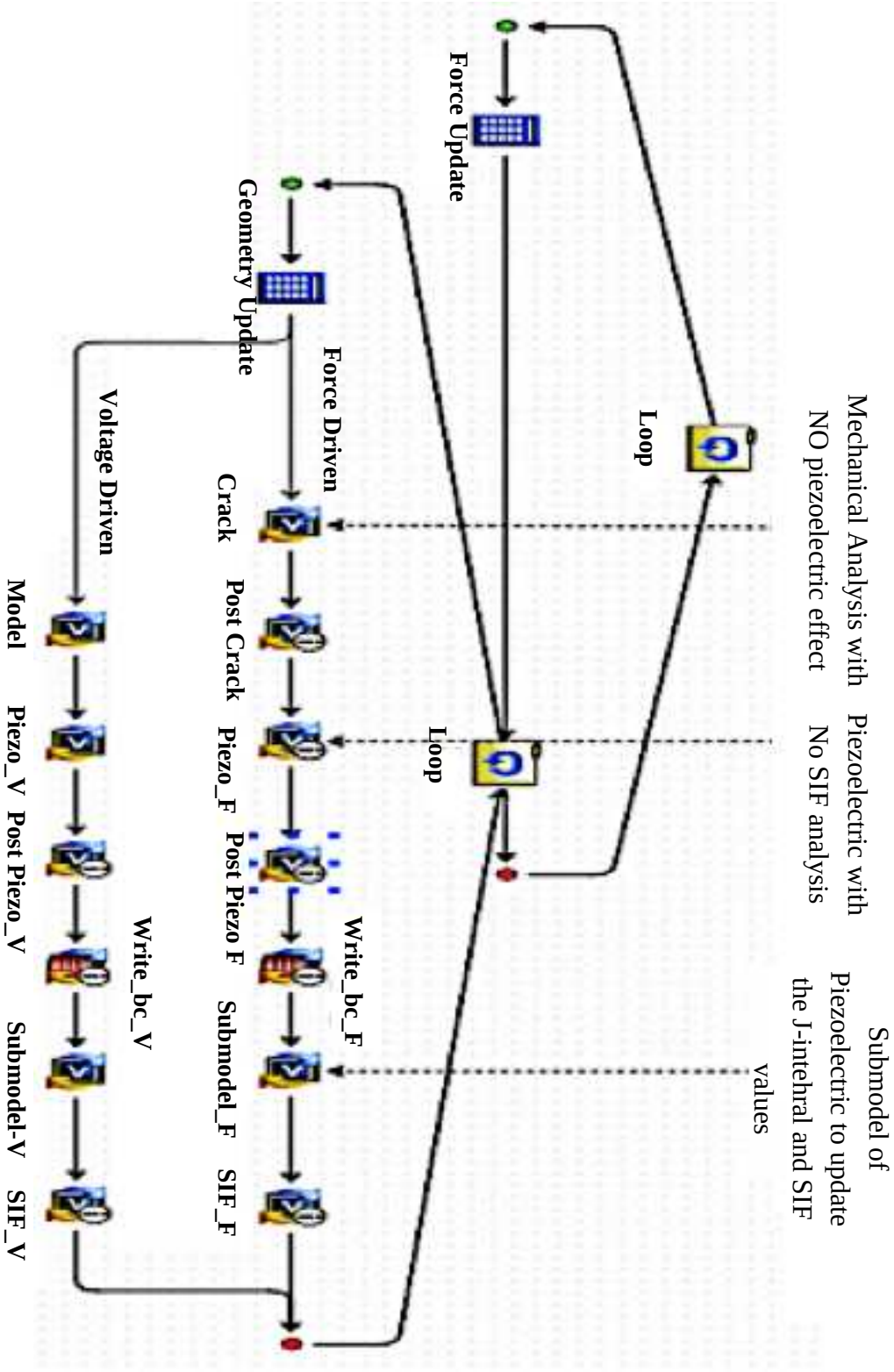

Fig 7.8: Final model to compute the value of j-Integral and SIF for different load condition

At the end of this run ISIGHT provides directly a post-processing of outputs in format of ordered lists of numbers as in Fig 7.9.

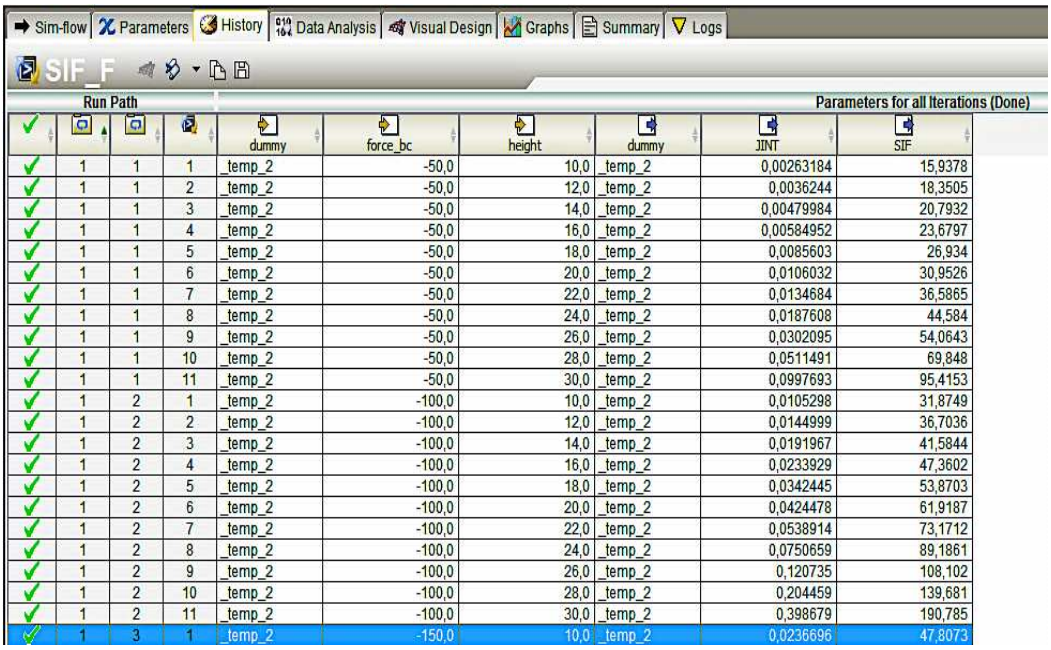

Sim-flow | Parameters | History | Data Analysis | Visual Design | Graphs | Summary | Logs

SIF_F

Run Path | Parameters for all Iterations (Done)

			dummy	force_bc	height	dummy	JINT	SIF
✓	1	1	1	_temp_2	-50,0	10,0	_temp_2	0,00263184	15,9378
✓	1	1	2	_temp_2	-50,0	12,0	_temp_2	0,0036244	18,3505
✓	1	1	3	_temp_2	-50,0	14,0	_temp_2	0,00479984	20,7932
✓	1	1	4	_temp_2	-50,0	16,0	_temp_2	0,00584952	23,6797
✓	1	1	5	_temp_2	-50,0	18,0	_temp_2	0,0085603	26,934
✓	1	1	6	_temp_2	-50,0	20,0	_temp_2	0,0106032	30,9526
✓	1	1	7	_temp_2	-50,0	22,0	_temp_2	0,0134684	36,5865
✓	1	1	8	_temp_2	-50,0	24,0	_temp_2	0,0187608	44,584
✓	1	1	9	_temp_2	-50,0	26,0	_temp_2	0,0302095	54,0643
✓	1	1	10	_temp_2	-50,0	28,0	_temp_2	0,0511491	69,848
✓	1	1	11	_temp_2	-50,0	30,0	_temp_2	0,0997693	95,4153
✓	1	2	1	_temp_2	-100,0	10,0	_temp_2	0,0105298	31,8749
✓	1	2	2	_temp_2	-100,0	12,0	_temp_2	0,0144999	36,7036
✓	1	2	3	_temp_2	-100,0	14,0	_temp_2	0,0191967	41,5844
✓	1	2	4	_temp_2	-100,0	16,0	_temp_2	0,0233929	47,3602
✓	1	2	5	_temp_2	-100,0	18,0	_temp_2	0,0342445	53,8703
✓	1	2	6	_temp_2	-100,0	20,0	_temp_2	0,0424478	61,9187
✓	1	2	7	_temp_2	-100,0	22,0	_temp_2	0,0538914	73,1712
✓	1	2	8	_temp_2	-100,0	24,0	_temp_2	0,0750659	89,1861
✓	1	2	9	_temp_2	-100,0	26,0	_temp_2	0,120735	108,102
✓	1	2	10	_temp_2	-100,0	28,0	_temp_2	0,204459	139,681
✓	1	2	11	_temp_2	-100,0	30,0	_temp_2	0,398679	190,785
✓	1	3	1	_temp_2	-150,0	10,0	_temp_2	0,0236696	47,8073

Fig 7.9: Results coming from ISIGHT program

Diagrams and trends are depicted in a collection of windows as in Fig 7.10 (Horizontal and vertical axis presents, JINT, SIF, force_bv and height).

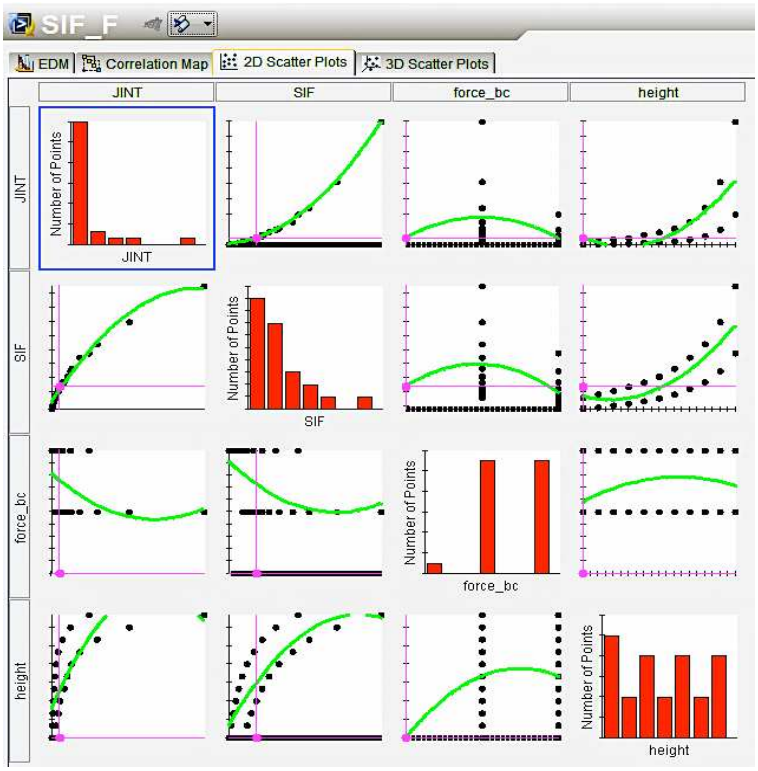

Fig 7.10: Diagrams coming from ISIGHT program

5 Analysis of crack propagation through the ISIGHT code

Prediction of crack propagation requires a different implementation of the ISIGHT tool above described. In this case propagation is investigated in terms of direction and speed. To provide those results the piezoelectric phenomenon is considered both in terms of applied strain when damage is driven by voltage and in terms of change in shape of layers.

As Fig 7.11 describes the crack propagation model developed inside the ISIGHT code includes some components. “CREATE PIEZO MODEL” introduces all the piezoelectric properties of material, voltage is applied and displacements of modes are recorded by running the model “RUN PIEZO”. Geometry of specimen imposed by the voltage, even in terms of shrinking effect is described in “GRAB UX” and inputted into the XFEM component.

As in case of metal XFEM assures the computation of crack path and propagation once that actual geometry, shape and loading condition are known. Crack propagation and geometry of specimen changes as component “STATUS” monitors.

The loop is then closed so as for increasing voltage the crack propagation is computed by an iterative solution at each value of voltage imposed and gradually up to the collapse of the structure.

It is remarkable that crack propagation can be even predicted by resorting to a piezo-thermal (electro-thermal) analogy.

In particular, it is known that strain induced along direction 1 by the electric field applied along direction 3 is:

$$\varepsilon_1 = d_{31}E_3 \qquad \text{where} \qquad E_3 = \frac{V}{t} \tag{7.1}$$

Above expression suggests that numerical procedure has to evaluate step by step values of applied voltage V and of piezoelectric layer thickness t (this motivates the updating of geometry). Moreover, under assumption of linear behaviour (small displacements) relation between strain and electric field is linear as well as that between strain and temperature in thermo mechanical analysis.

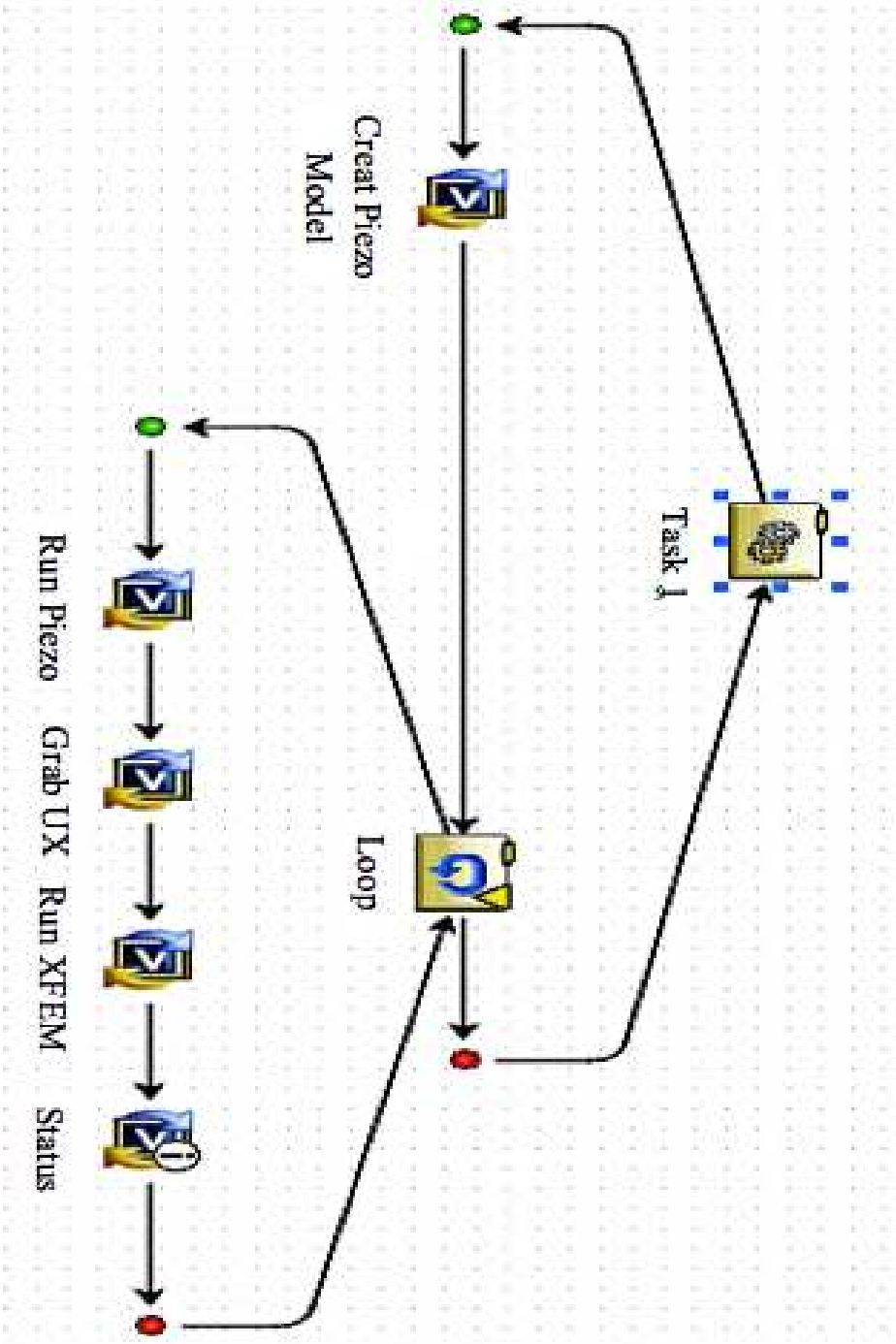

Fig 7.11: The ISIGHT model to analysis the crack propagation inside piezoelectric

Therefore one possibility suggested by the literature is resorting to an analogy between piezoelectric and thermal strain, by inputting inside the ABAQUS code an equivalent thermal expansion coefficient α instead of d_{31} and an equivalent distribution of

temperature t, instead of electric field, to run more easily thermo mechanical analysis instead of implementing this approach. Difference is that the ABAQUS code is already programmed to perform a prediction of crack propagation in case of thermal loads, which it doesn't in case of piezoelectric action. Analogy looks like:

$$\varepsilon_{Piezo} = d_{31}E = d_{31}\frac{V}{t} \qquad d_{31} \rightarrow \alpha_{eq}$$

$$\varepsilon_{thermal} = \alpha T \qquad \frac{V}{t} \rightarrow T_{eq} \qquad (7.2)$$

Procedure was tested to compare the results obtained by the new proposed protocol and this approach. Nevertheless, to make efficient the computation of equivalent temperature T_{eq} it was required analyzing the displacements induced by voltage for given thickness of piezoelectric layer and imposing their equivalence in case of thermo mechanical analysis. In practice sequence of operation was:

1) Running the piezo model with isostatic constraints and calculating the plate shrinking.
2) Running the mechanical model by using temperature to mimic the voltage. Thermal expansion coefficient was used to obtain the same displacements of the voltage driven deformation.
3) Running the mechanical model with temperature, with real constraints. Reactions were even checked and scaled by elastic properties of material assure to get the same effect of voltage. It was demonstrated that results and behavior of crack propagation in both the procedures based on ISIGHT program and thermal analysis are the same.

6 Numerical investigation: Fracture in single mode propagation

6.1 Influence of loading condition

Effect of magnitude of load and crack length was first analyzed without applying voltage stress intensity factor and J-integral were calculated to investigate the attitude of piezoceramic PZT to fracture. SIF and J-Integral for initial crack length of 20 mm are shown in Table 7.1.

Table 7.1: SIF and J-Integral with initial crack length of 20mm

Load [N]	50	100	150	200	250	300	350	400	450	500
SIF[MPa]	30.95	61.98	92.86	123.8	154.7	185.7	216.7	247.6	278.5	309.5
J-Integral [N/mm]	0.010	0.0424	0.0954	0.1697	0.2652	0.3811	0.5201	0.6788	0.8586	1.0603

It can be remarked that when piezoceramic is purely passive line a metal and no effect of voltage is considered SIF increases with load and J-integral is positive and increases too.

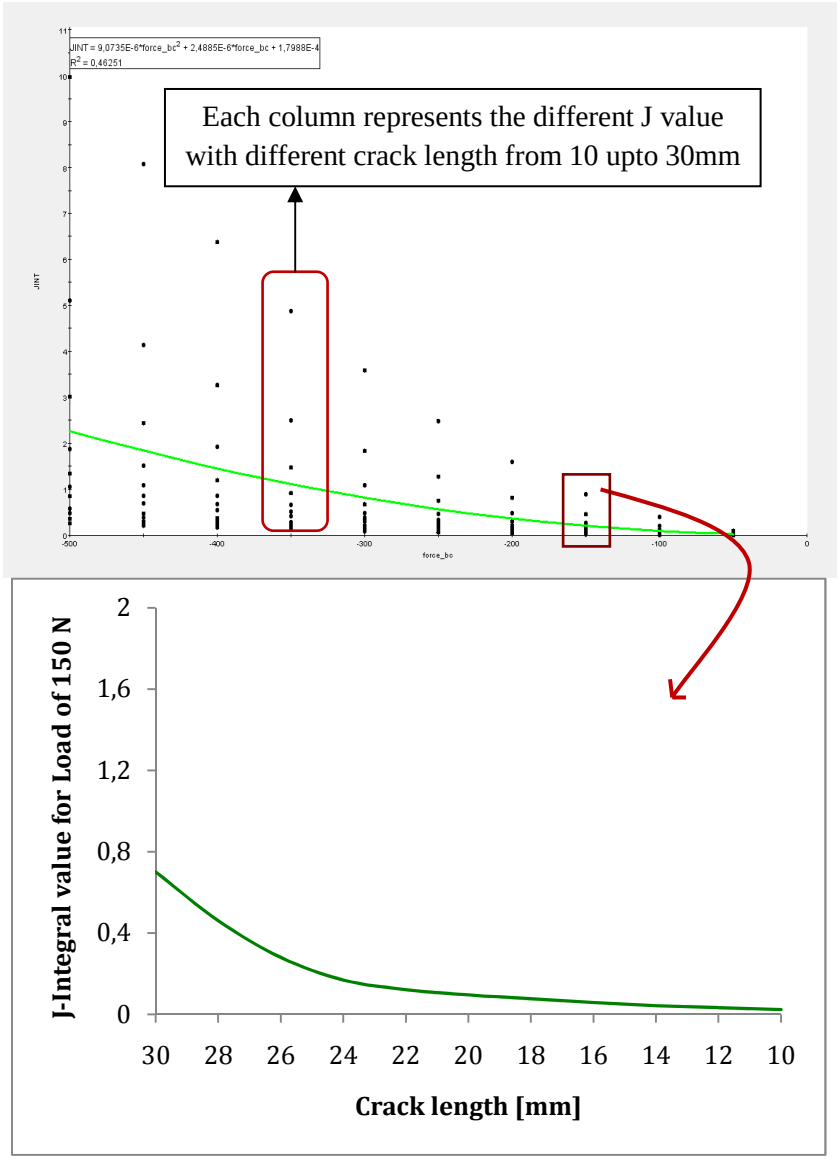

Fig 7.12: The value of J-Integral for different loads magnitude without applying voltage.

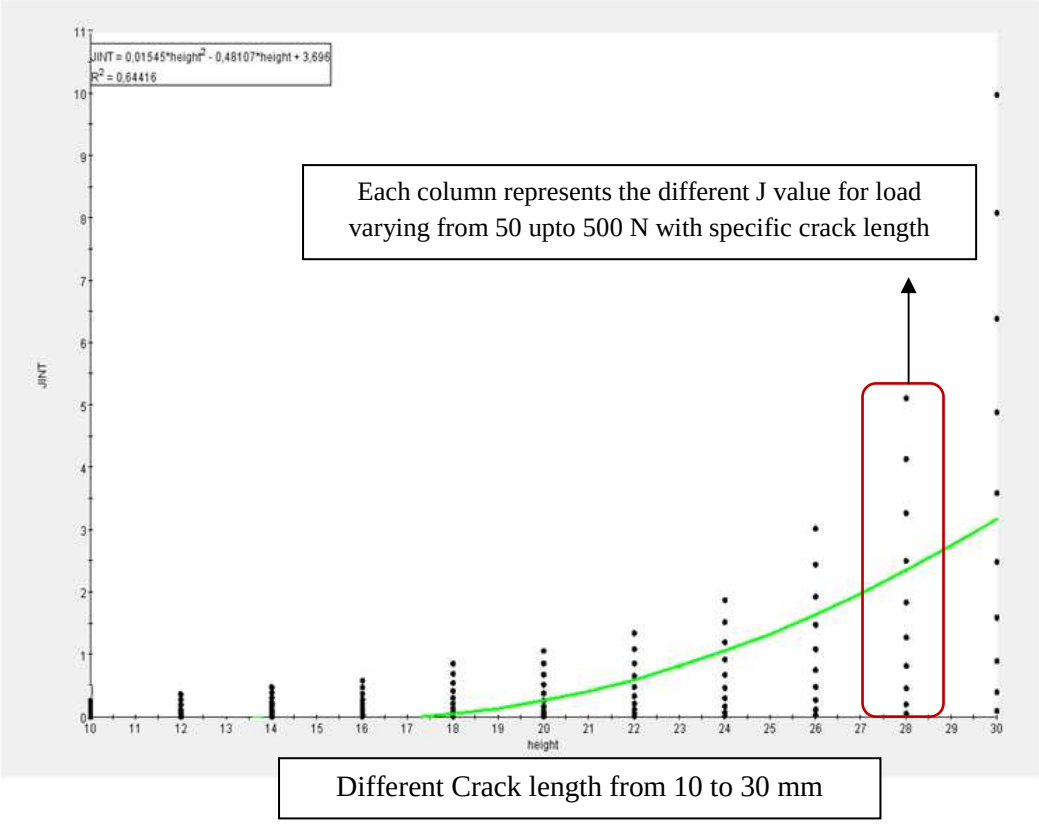

Fig 7.13: The value of J-Integral for different crack length without applying voltage.

In Fig 7.12 J-integral is plotted as a function of applied load. Each point of this plot corresponds to a value of crack length, whose range is spamming from 10 to 30 mm. The ABAQUS code drawn a line of tendencies to describe how the two coordinates of plot are related in this case it can be appreciated that:

1) J-integral non-linearly increases with load

2) Its value is greater when crack length is longer

In Fig 7.13 the same analysis was plotted, but J-integral is now a function of crack length. Values are bigger when crack is longer and relation appears non-linear as in pervious graph.

Stress Intensity Factor was analyzed as Figs 7.14 and 7.15 show. It is worthy noticing that Stress Intensity factor shows a nonlinear dependence upon crack length, while it is linearly related to load magnitude. In both cased SIF increases as load and crack length do.

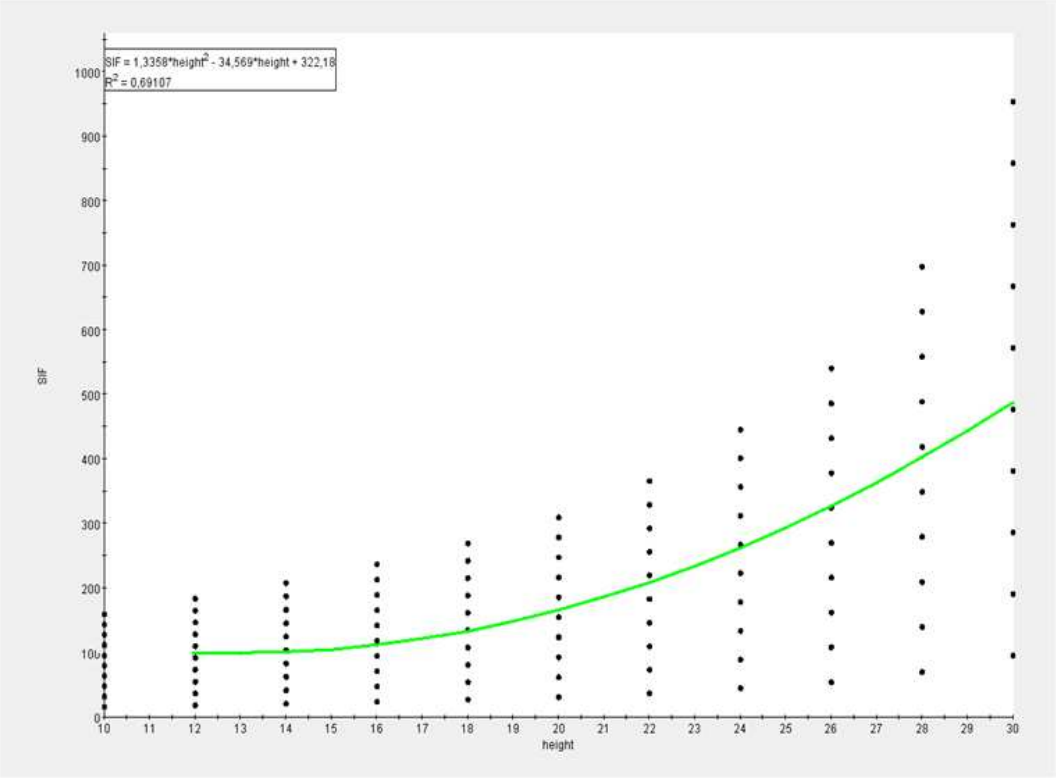

Fig 7.14: The value of SIF for different crack length without applying voltage.

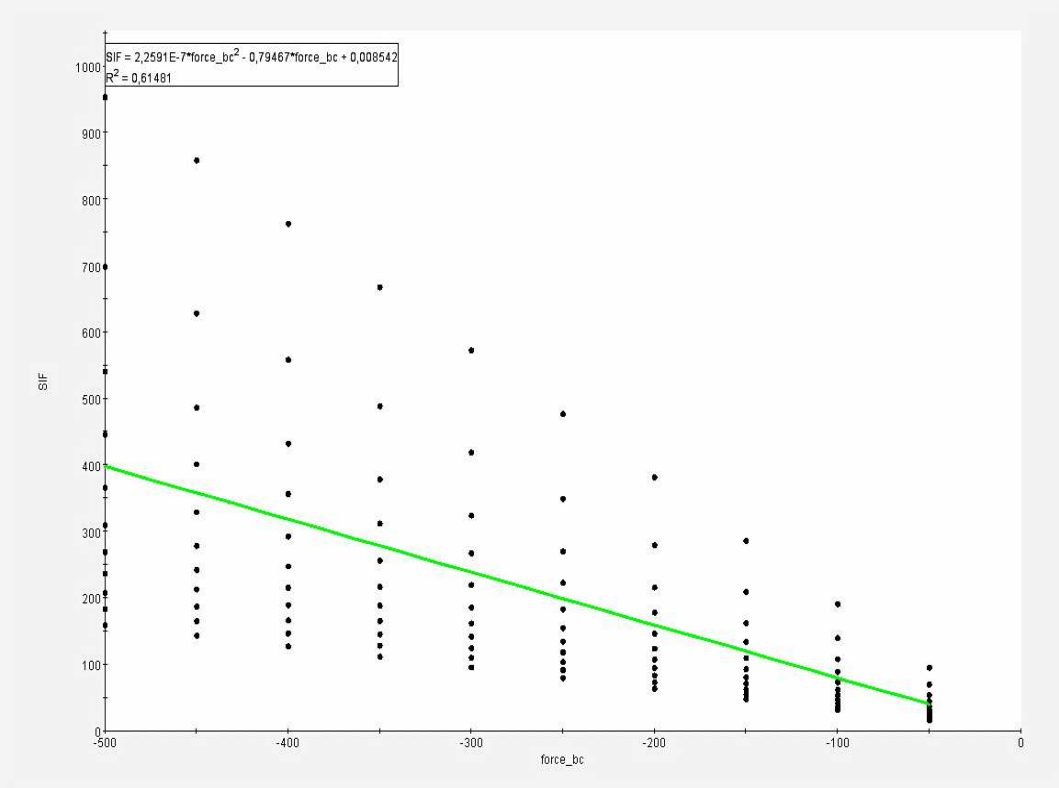

Fig 7.15: The value of SIF for different loads magnitude without applying voltage

A preliminary investigation about correlation between Stress Intensity factor and J-integral was done as it looks in Fig 7.16. Actually relation is complete with analytical prediction according which J-integral is proportional to square value of K (see chapter 1).

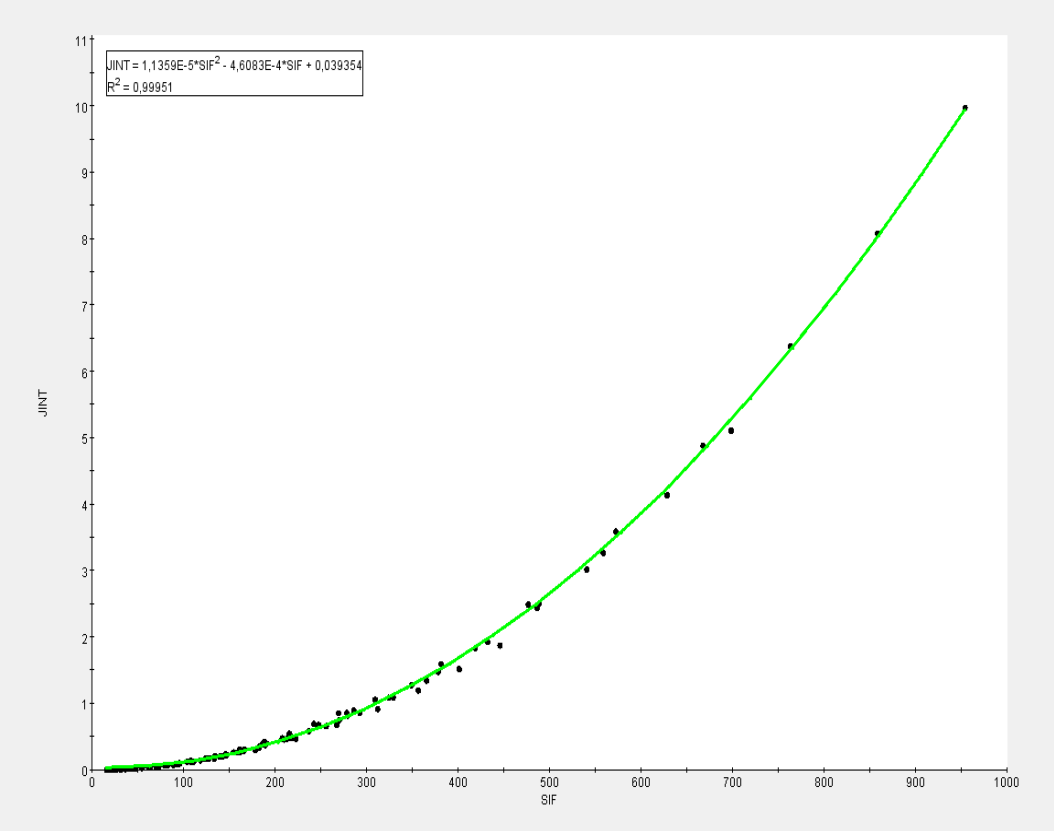

Fig 7.16: The value of J-Integral against SIF values in all point.

6.2 Influence of voltage

In this second part the effect of voltage applied to the piezoelectric layer is analyzed. It was assumed that no external load is applied to the structure.

Table 7.2 shows the calculated values of SIF and J-Integral for a crack length of 20 mm and voltage varying from 10 up to 100 V, then for variable crack length from 10 up to 30 mm.

Table 7.2: SIF and J-Integral with initial crack length of 20mm

Voltage [V]	10	20	30	40	50	60	70	80	90	100
SIF[MPa]	7.509	15.019	22.530	30.033	37.551	45.061	52.566	60.081	67.588	75.098
J-Integral [N/mm]	-3.8e-8	-0.001	-0.003	-0.006	-0.009	-0.014	-0.019	-0.024	-0.031	-0.038

Distribution of electric potential is described in Fig 7.17 and 7.18. As it can be observed voltage crosses the whole section of specimen, although it is affected by the crack length. Gradient in space of voltage and around the crack tip is more evident for a larger bending effect.

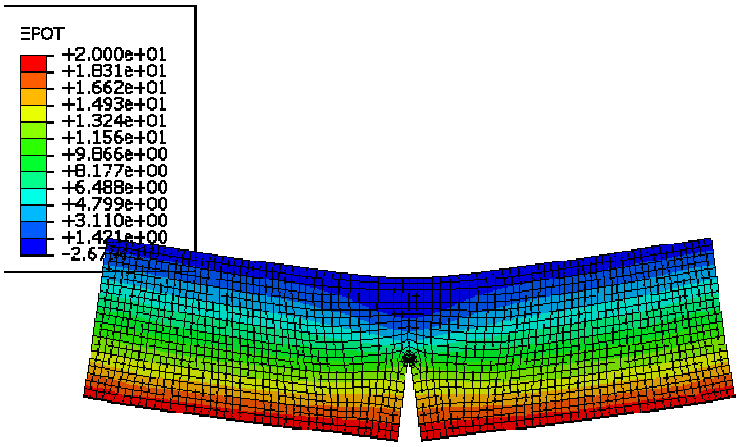

Fig 7.17: Electrical potential distribution for 20 volt and crack length 20 mm

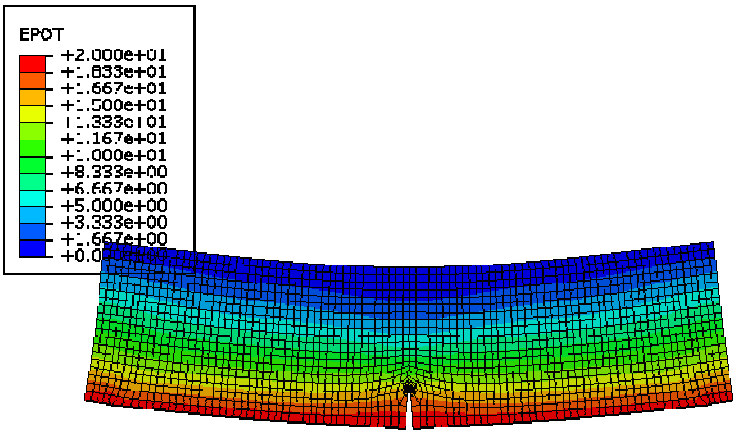

Fig 7.18: Electrical potential distribution for 20 volt and crack length 10 mm

As in previous case J-integral analyzed in Fig 7.20 and 7.21. Great news in those simulations is that J-integral is negative. About this result it was deeply focused the attention during this study to catch the meaning of such detail. It can be observed that loading conditions are fairly different in case of mechanical force applied or in case of active piezoelectric layer, although the some opening mode of fracture is excited. Fig 7.19 shows some differences.

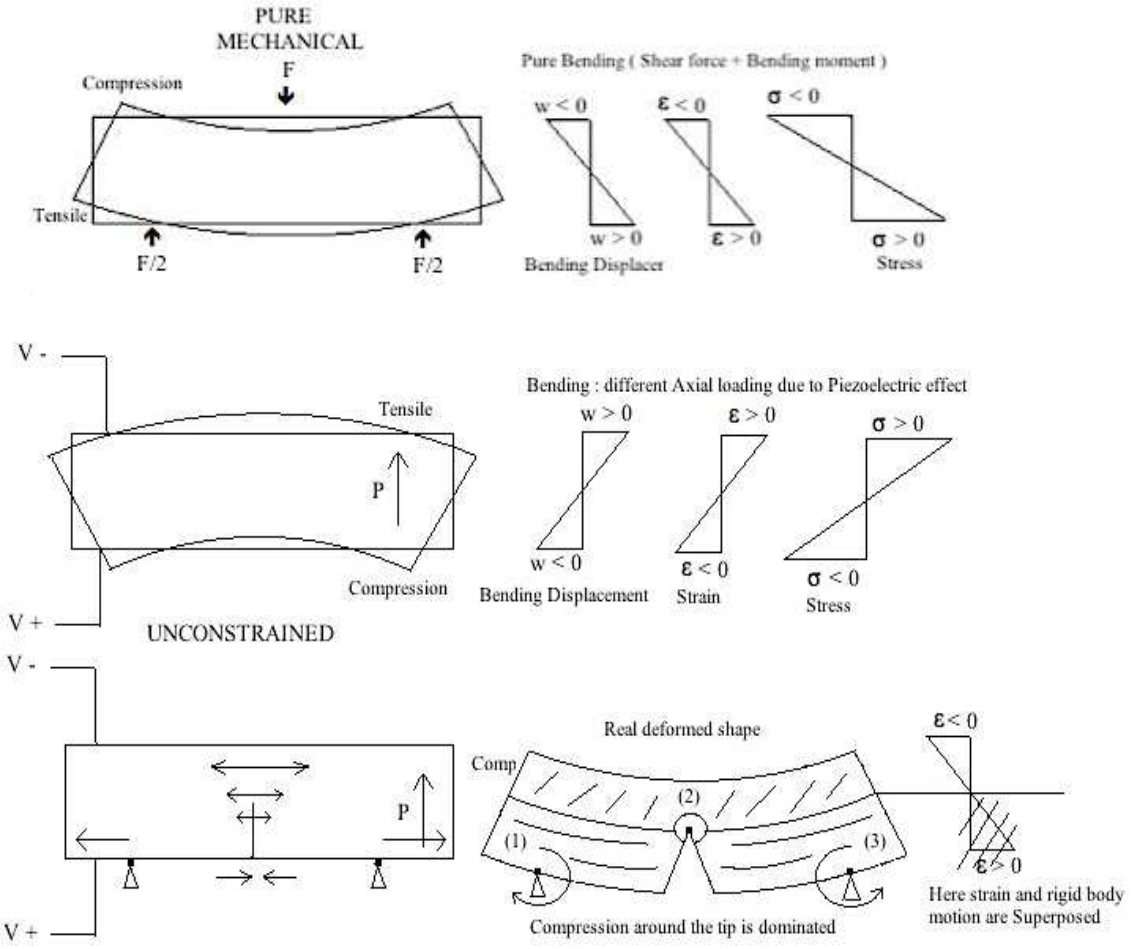

Fig 7.19: Loading condition in case of force and voltage applied.

According to Fig 7.19 in case of pure bending moment induced by a vertical force, distribution of strain is agreeing with distribution of displacement along the line axis. Therefore strain is part positive and in part negative and where crack occurs compatibility

is no more valid, i.e. theoretical distribution of strain and stress depicted cannot be applied, since crack generates two separated faces.

In case of voltage, distribution is linear from zero to the maximum value, once that polarization of piezoelectric layer is defined. For each level of voltage correspond an elongation ε and related stress σ. If a free body is considered tensile effect occurs at the upper surface and lower surface as ε=0, if polarization and voltage drop are those assumed in the above depicted example. By converse if the body is constrained by hinges at the bottom, each constraint applies a reaction. This effect makes lower fibers undergoing a tensile stress and crack opening occurs, while upper fibers undergo a state of compression or at least they are close to neutral axis of bending. Moreover, two blocks separated by crack rotate and add a contribution to the stress concentration around the tip. Obviously this is only a rough and preliminary interpretation of the phenomenon, but it allowed understanding results obtained by the Abaqus code.

In particular, those differences make state of compressive stress around the crack tip dominant. J-integral is therefore negative. Nevertheless, from the practical point of view amplitude of J-integral is relevant more than its sign, which only depends on the specific constraining conditions.

As in previous cases, if only amplitude of J-integral is considered, a similar nonlinear dependence upon the loading conditions, being here the voltage and on crack length is exhibited.

It will be remarked that trend automatically drawn by the ABAQUS code apparently suggests that amplitude increase indefinitely. This looks like a wrong perception because if one looks at value of 22-24 mm of crack length the trend suddenly changes and J-integral slightly decreases.

This behavior is even more evident in Fig 7.18 where SIF is plotted. It grows up with crack length until value of 21-23 mm and then it becomes smaller above this threshold.

This is a very significant result even from the practical point of view and it can be explained as follows. If one looks at Fig 7.17 and Fig 7.18 it can be realized that as much as it is long the crack tip is located inside a region dominated by the electric potential of the upper electrode of piezoelectric layer. State of stress is affected by the proximity with the upper and free surface where the electric charge is concentrated and the remaining

cross section suitable to bear the applied load is quite small. Work done by piezoelectric material in terms of compression, according even to Fig. 7.20 is dominating with respect to energy relapse rate or at least more relevant. Attitude of piezoelectric layer to propagate the crack is now lower as SIF and J-integral suggest. Therefore it can be remarked that piezoelectric actuator induces a state of stress around the crack tip when length is quite great that is in contrast with the crack propagation. This effect agrees with some experimental observations, which demonstrated that life is longer than prediction, because of some unexplained motivation.

A sort of “smart recovery” against the fracture of material is opposed by the piezoelectric layers when the available thickness is reduced below a critical value, provided that crack propagation is still stable. Relation between SIF and applied voltage is even linear as in Fig.7.23.

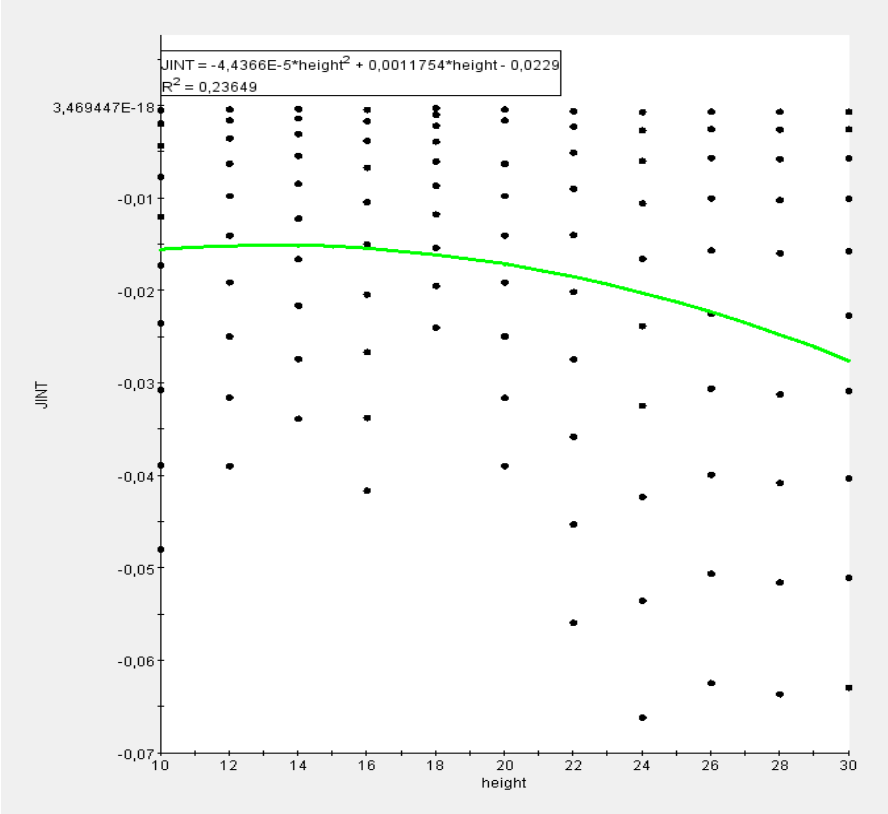

Fig 7.20: The value of J-Integral for different crack length with different voltage

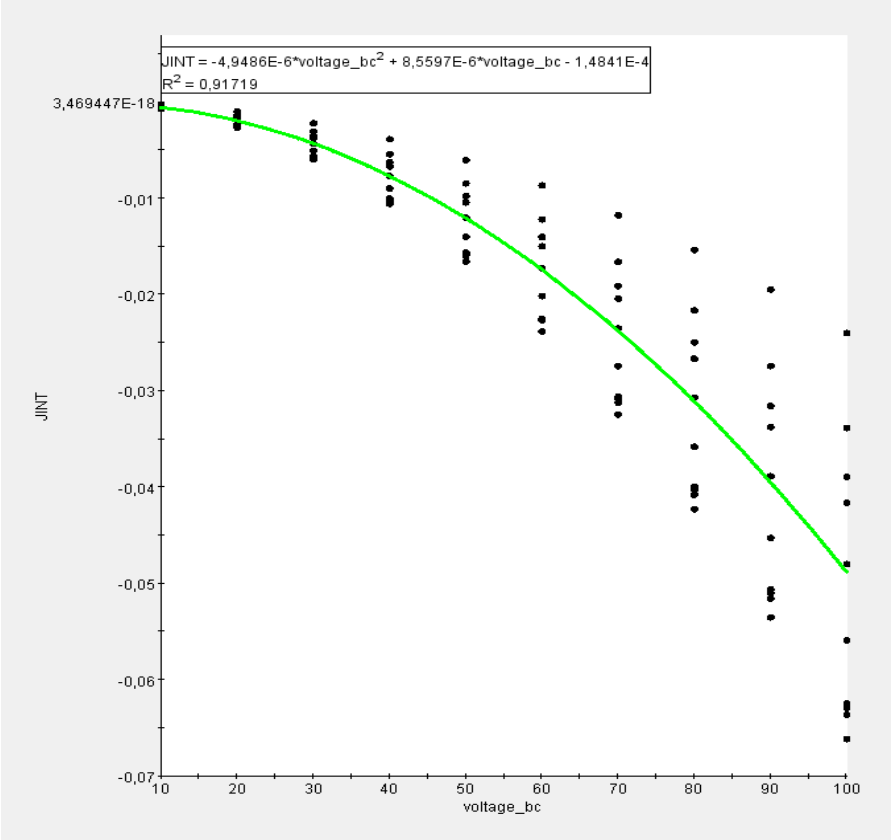

Fig 7.21: The value of J-Integral for different voltage magnitude without force.

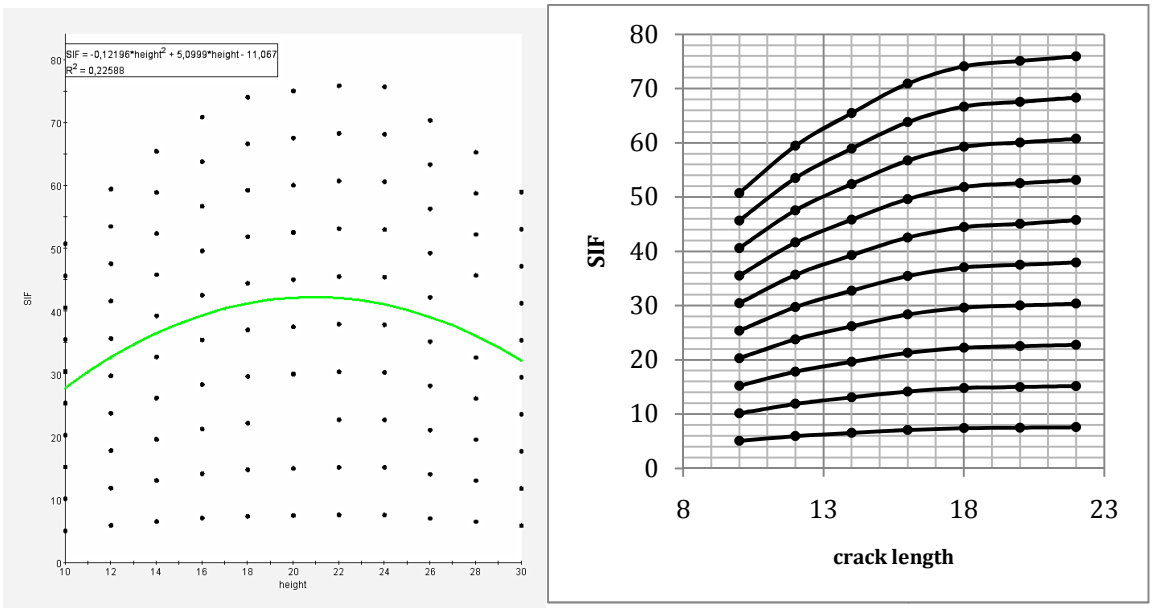

Fig 7.22: The value of SIF for different crack length without applying external force.

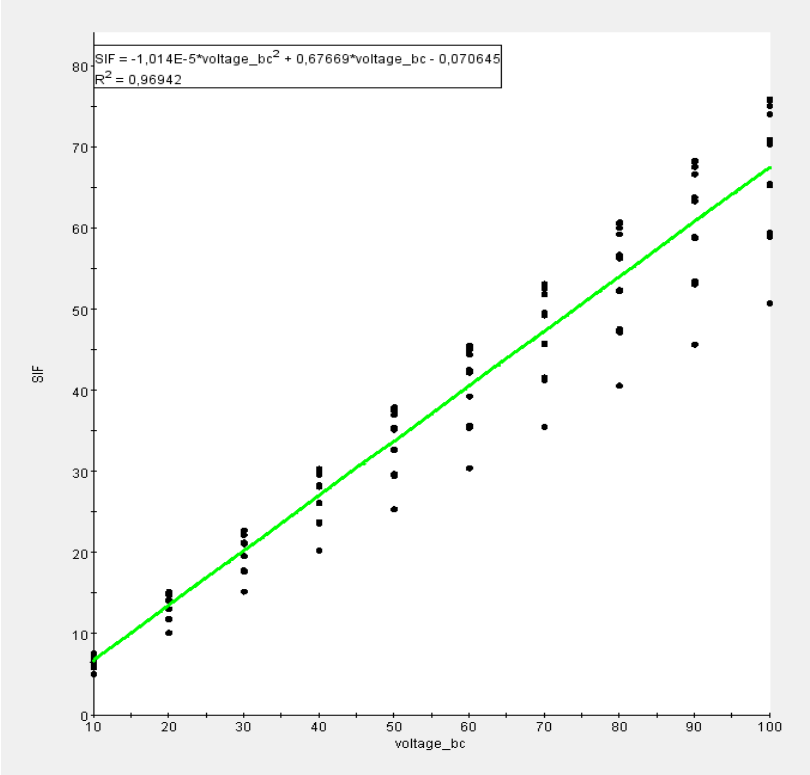

Fig 7.23: The value of SIF for different voltage magnitude force

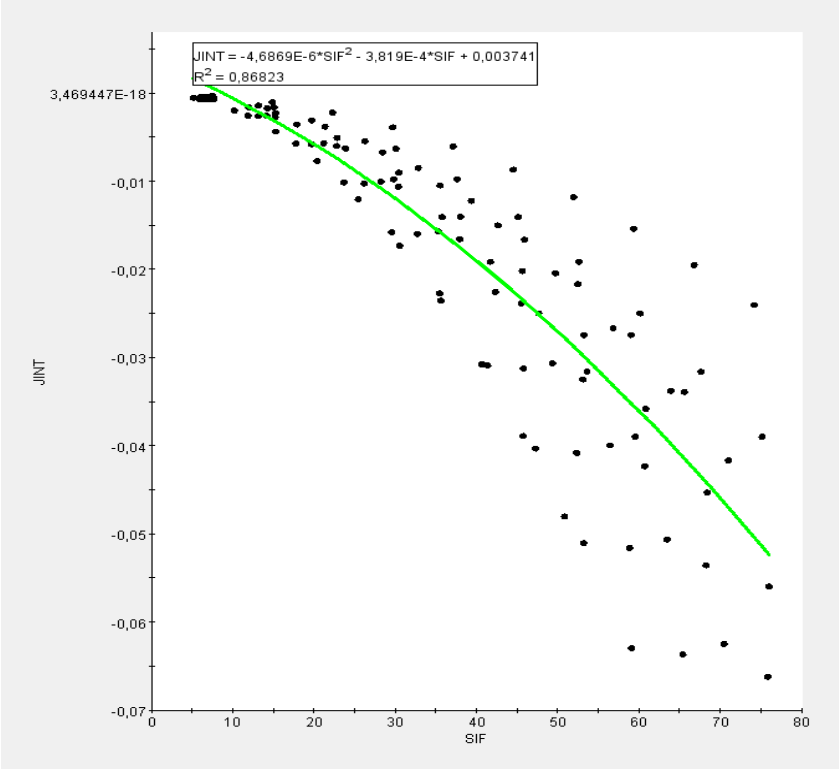

Fig 7.25: Relation between J-Integral and SIF

It can be noticed that Stress Intensity Factor has nonlinear growth with crack length. Although it has linear relation with voltage. Relation between J-integral and SIF is shown in Fig 7.23.

7 Numerical investigation: Mixed mode crack propagation

To make expedient this analysis mixed mode C is directly considered. Configuration is the same of the steel specimen. Two forces are applied and constraints are no more at the two ends of specimen but close to crack.
Procedure followed in the numerical investigation was the same of single mode crack propagation and sensitivity analysis was done by focusing the same parameters. Results are here in presented.

7.1 Influence of loading condition

In this case calculation of SIF includes both mode I and II. It was performed by analyzing first the pure mechanical loading condition. Range of values was from 10 up to 100, crack length was set at 20 mm when constant and long from 10 up to 30 mm was investigated when it is variable.

Table 7.3: The value of SIF and J-Integral with different load magnitude with crack length of 20mm

Load [N]	10	20	30	40	50	60	70	80	90	100
K_I[MPa]	31.472	62.898	94.302	125.645	157.109	188.4	219.631	250.841	281.984	313.094
K_{II}[MPa]	2.673	5.3774	7.533	10.1046	11.749	14.1609	16.612	19.078	21.5801	24.1254
J-Integral [N/mm]	0.01096	0.0438	0.0987	0.1756	0.27456	0.3955	0.5386	0.7038	0.8911	1.1009

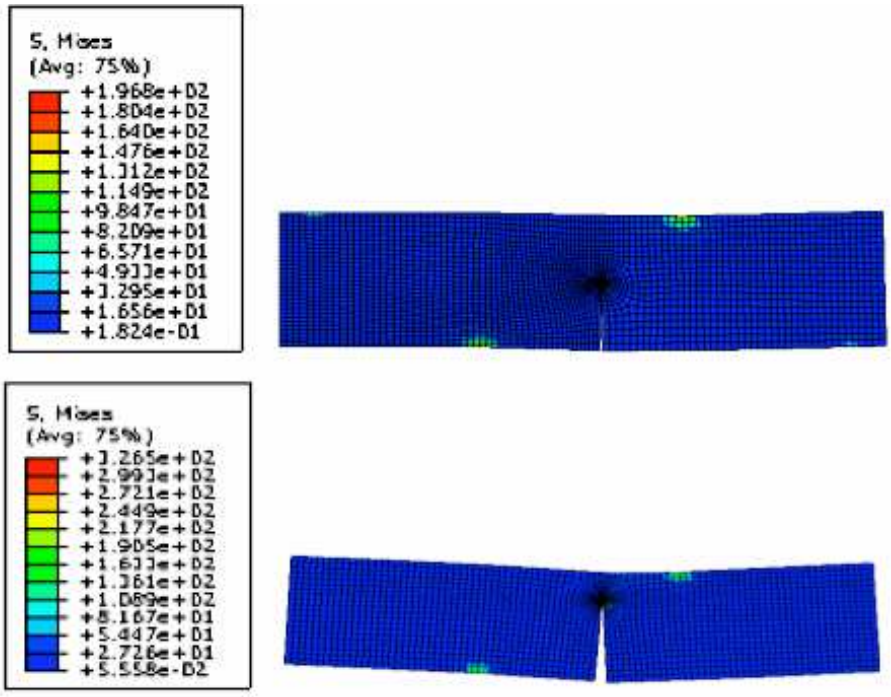

Fig 7.26: Stress distribution inside the model with10 N

As Fig 7.27 shows even in presence of mixed mode propagation crack follows a straight path.

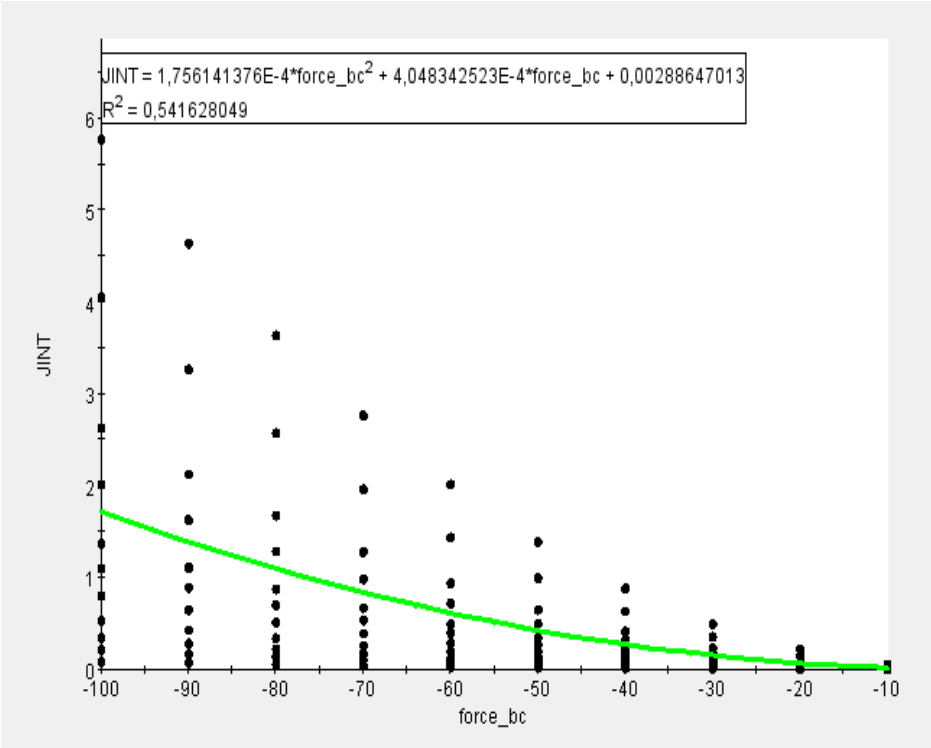

Fig 7.27: The value of J-Integral for different loads magnitude without applying voltage.

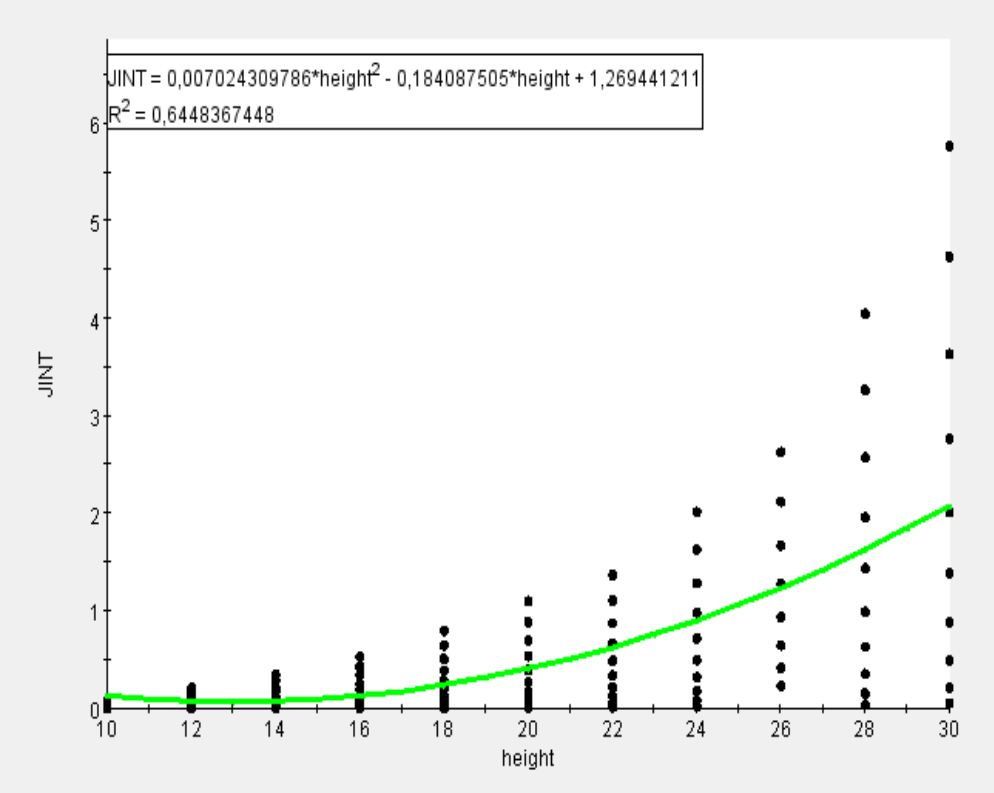

Fig 7.28: J-Integral vs. crack length (without applying voltage)

Trends of J-integral are similar to those of single mode, although it seems that a higher sensitivity upon load magnitude than on crack length is shown.

For Stress Intensity Factor two analyses were performed, and for each mode, as Fig 7.29 and 7.30 show.

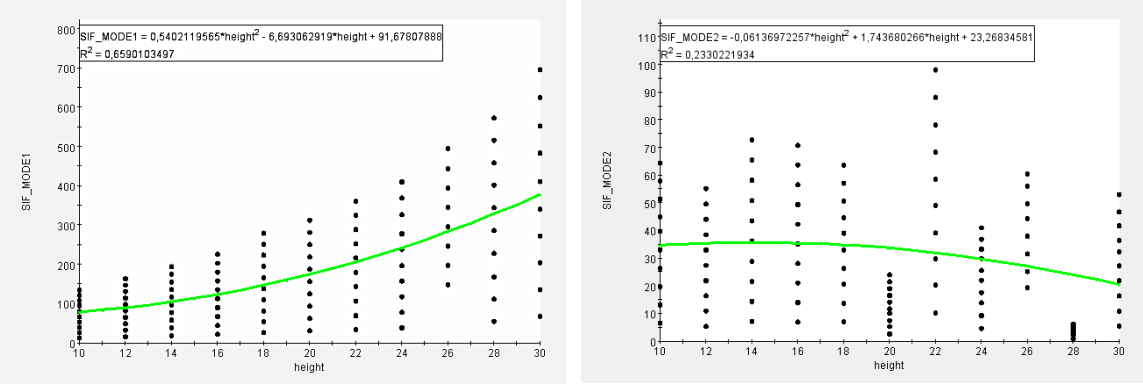

Fig 7.29: The value of SIF for different crack length without applying voltage.

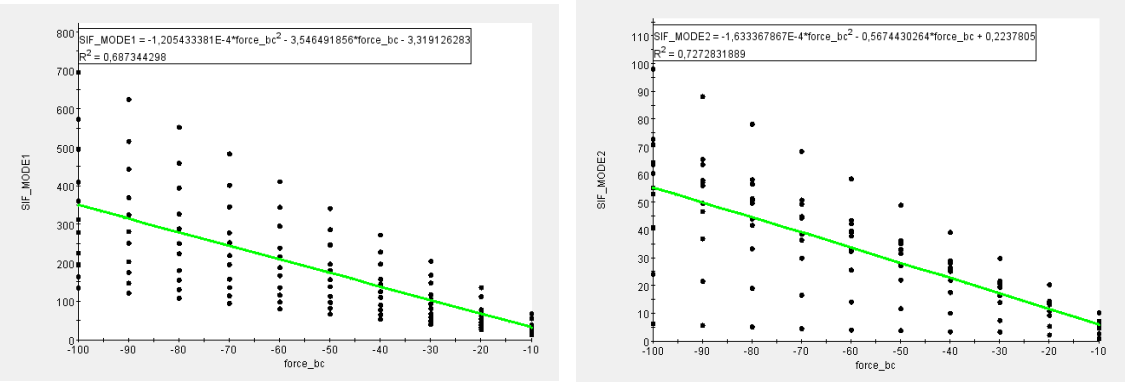

Fig 7.30: The value of SIF for different loads magnitude without applying voltage

Behaviour of K_I is quite regular, it increases with increasing crack length and applied load. K_{II} looks decreasing with increasing crack length. In particular behaviour damages quite a lot length by length. Crack of 20 and 28 mm show very different attitude to propagation, this effect could be related even to a convergence problem of the numeric tool.

If look one looks at Fig 7.31 (b) can realize that this mode is irregularly detected and convergence in the computation of K_{II} is rather difficult, This points out a limit of simulation but is motivating even the crack propagation so poorly affected by the II mode contribution, From this Fig, its clear from the relation between J-integral and SIF.

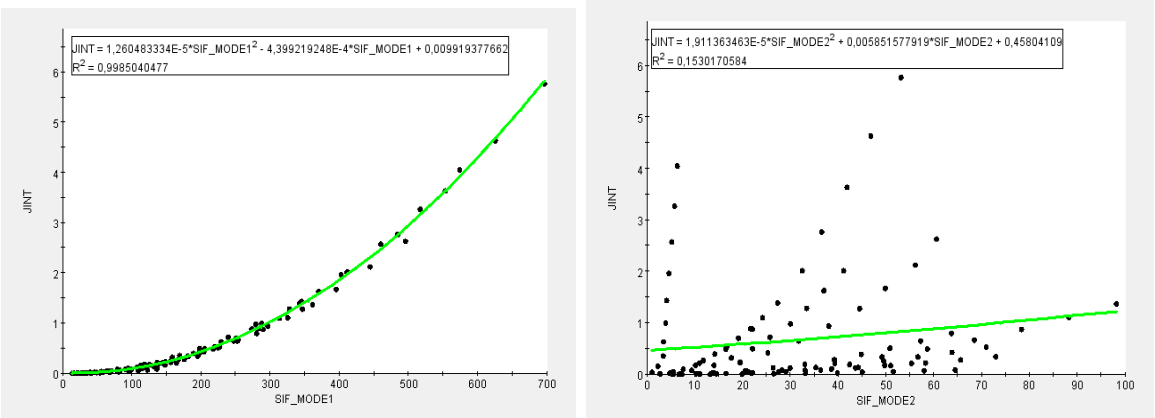

(a) (b)

Fig 7.31: The value of J-Integral against SIF values in all point.

7.2 Influence of voltage

Sensitivity upon applied voltage was investigated first for a crack length of 18 mm and voltage spamming constant from 20 to 200 V, therefore different crack lengths from 10 to 30 mm. results are shown in Table 7.4

Table 7.4: SIF and J-Integral for different Voltage with crack length of 18mm

Voltage [v]	20	40	60	80	100	120	140	160	180	200
K_I[MPa]	9.875	19.763	29.66	39.577	49.503	59.447	69.401	79.363	89.342	99.336
K_{II}[MPa]	9.148	18.302	27.46	36.6232	45.789	54.963	64.135	73.322	82.503	91.695
J-Integral [N/mm]	-0.003	-0.006	-0.03	-0.053	-0.083	-0.1199	-0.163	-0.212	-0.269	-0.332

Crack opening with 80 V and crack lengths of 10 and 20 mm is shown in Fig 7.32 together with stress distribution.

Fig 7.32: Stress distribution inside the model for 80V and crack length of 10 and 20 mm

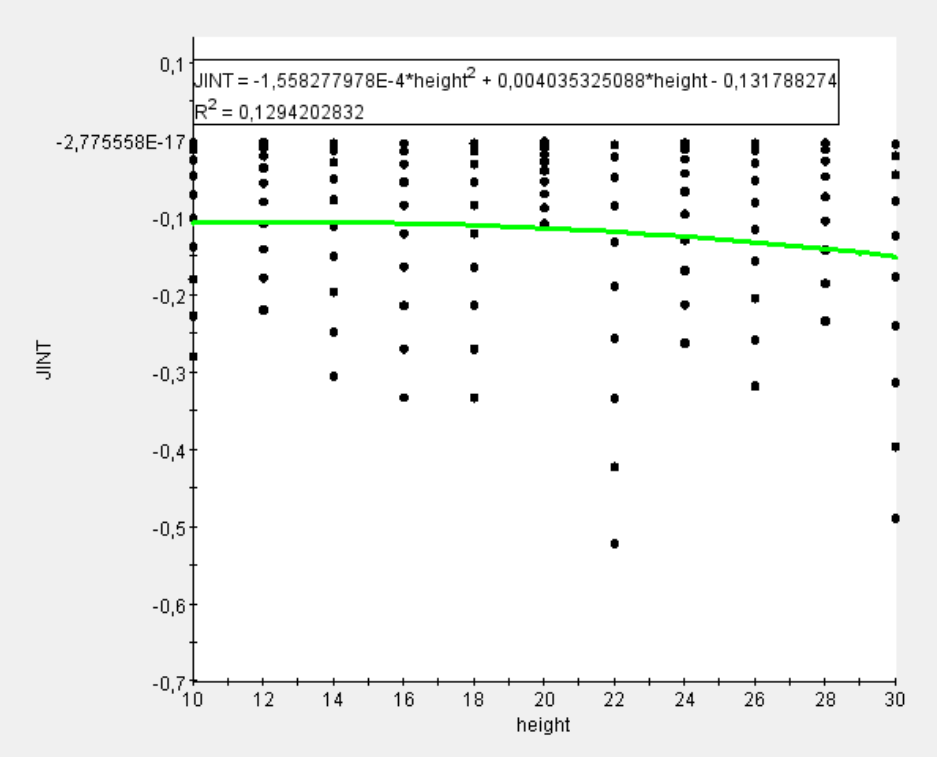

Fig 7.33: J-Integral for different crack length for different voltage

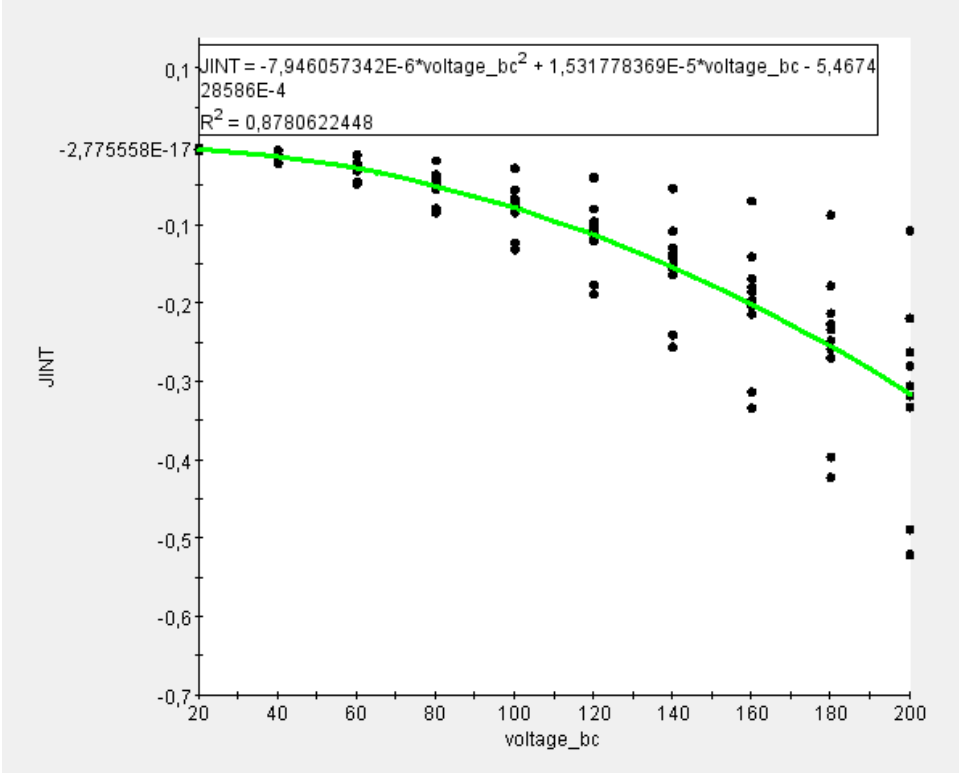

Fig 7.34: J-Integral for different voltage

As Fig 7.33 and 7.34 show j-integral increase with crack length, although as in single mode sign is negative because of constraining conditions described in Fig 7.20.

As in single mode a sort of “BARRIER EFFECT” in case of longer crack was detected even in this case and it affects both mode I and mode II as Fig 7.35 (a) and (b) show.

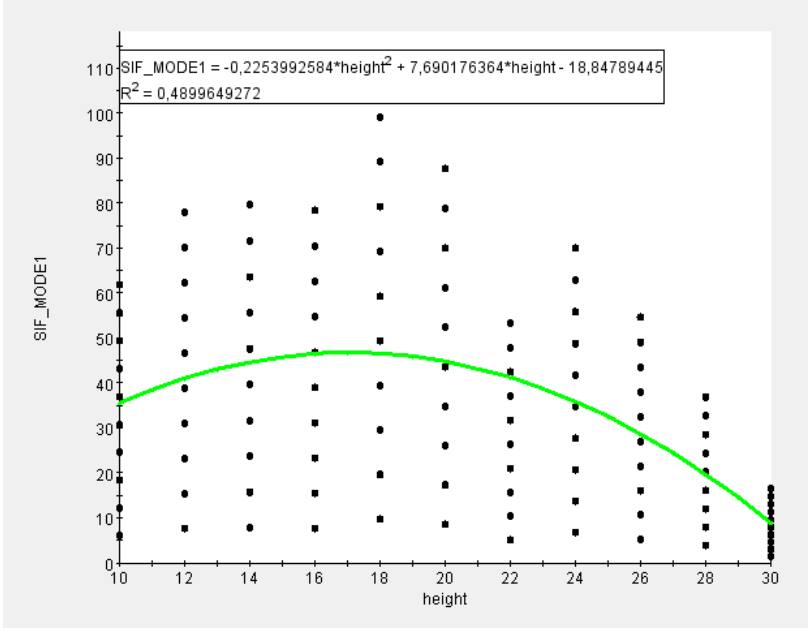

(a)

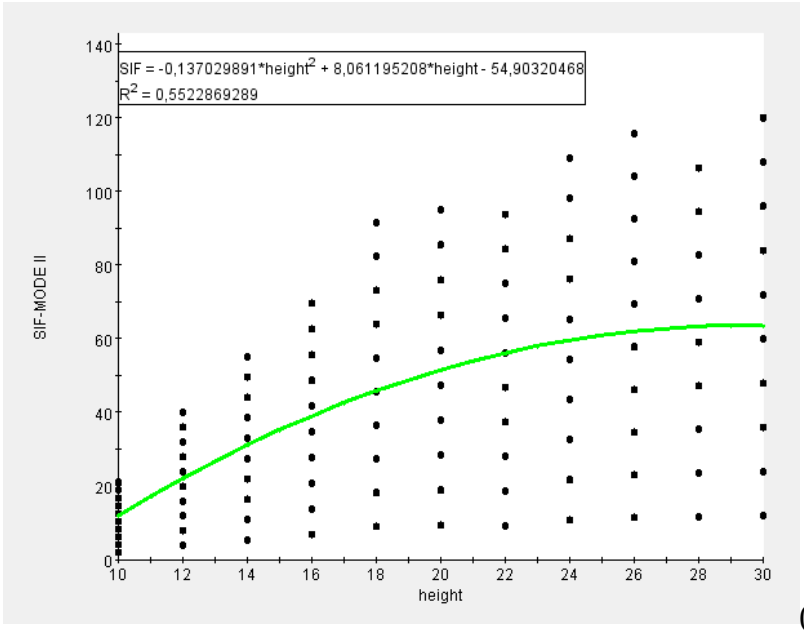

(b)

Fig 7.35: SIF for different crack length and mode of propagation I (a) and II (b)

(Without applying external force)

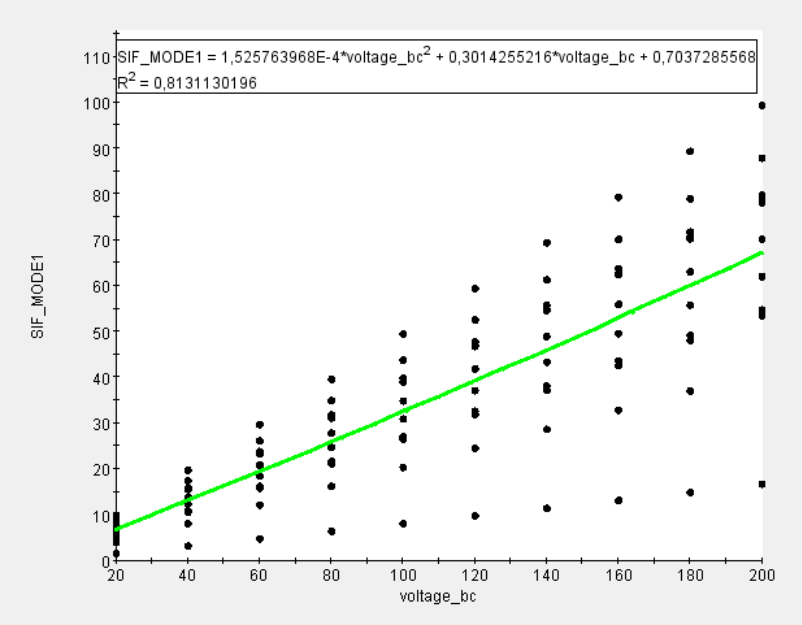

(a)

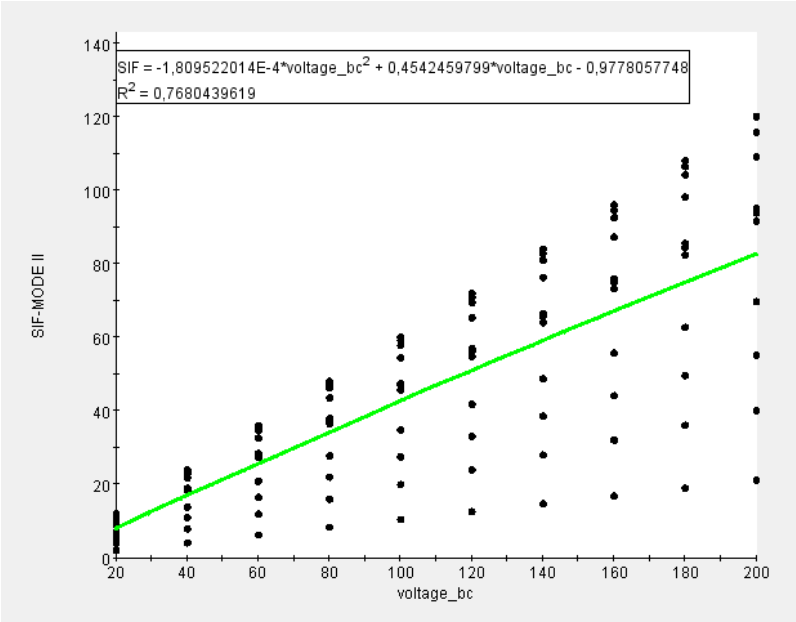

(b)

Fig 7.36: SIF for different voltage magnitude and mode of propagation I (a) and II (b)

(Without applying external force)

Trend of mode II is here well identified and is similar to that of mode I as Fig 7.36 states. Finally the below Fig 7.37 presents the correlation between Stress Intensity Factor and J-integral.

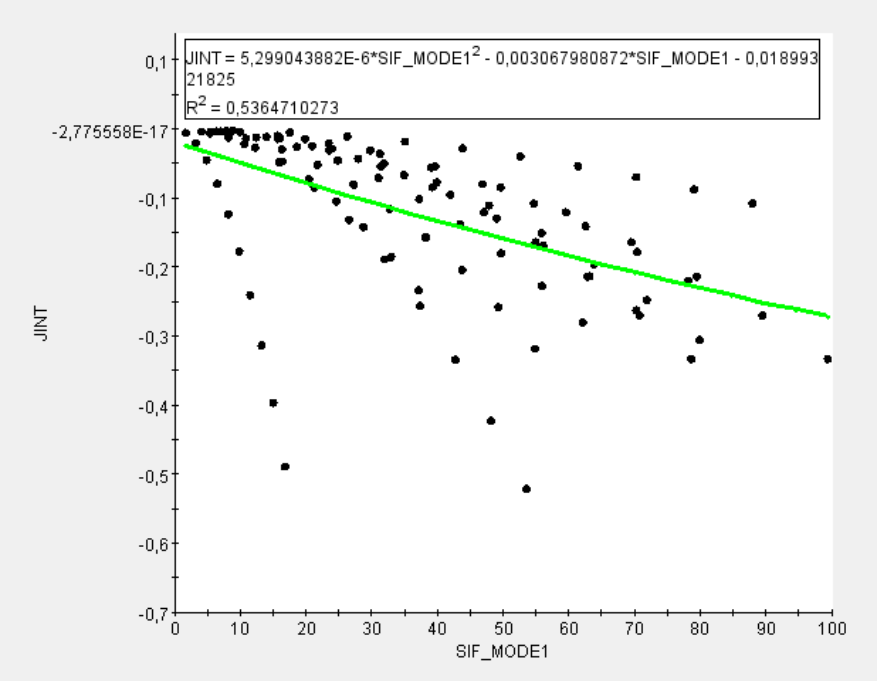

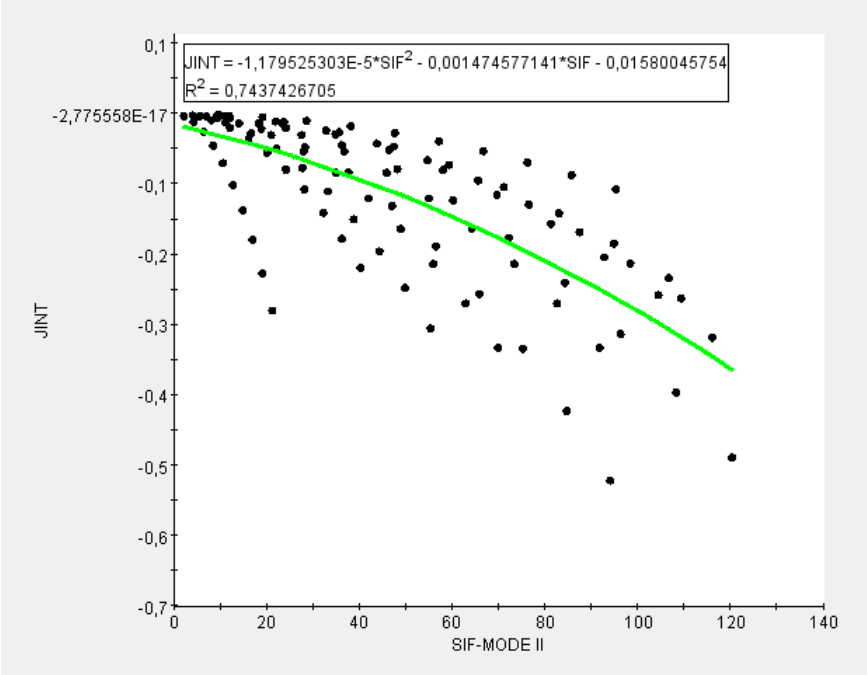

Fig 7.37: The value of J-Integral against SIF values in all point.

CHAPTER 8

FRACTURE OF SMART COMPOSITE STRUCTURE WITH PIEZOELECTRIC AND METALLIC LAYERS

The main goal of predicting the fracture mechanics of smart composite materials is coped in this chapter by focusing the attention upon the case of metallic structure equipped with surface bonded piezoelectric actuator. A thin layer of PZT-4 whose properties were already described in previous chapters and was bonded on a substrate of AISI 4340 steel.

1 Specimens and analysis conditions

Fig 8.1 shows a sketch of the composite structure modeled. Upper layer is made of PZT-4, while lower one is made of steel. Crack propagation in case of single and mixed modes are considered to analyze fracture mechanics in this case.

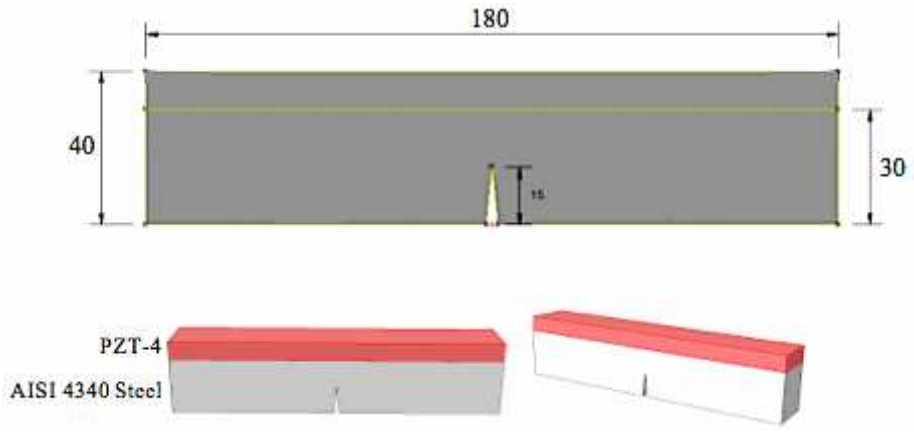

Fig 8.1: Sketch of composite smart specimen analyzed.

Main feature of this specimen is that only a part of structure is active and an interface between two materials is introduced. The modeling activities inside the ABAQUS code are almost the same of previous analyses. The ISIGHT protocol was even used to allow communicating the two tools fracture and piezoelectric analysis of the ABAQUS code.

2 Single mode crack propagation

Just in case the final configuration of specimen for the numerical investigation about single mode of crack propagation is described in Fig 8.2.

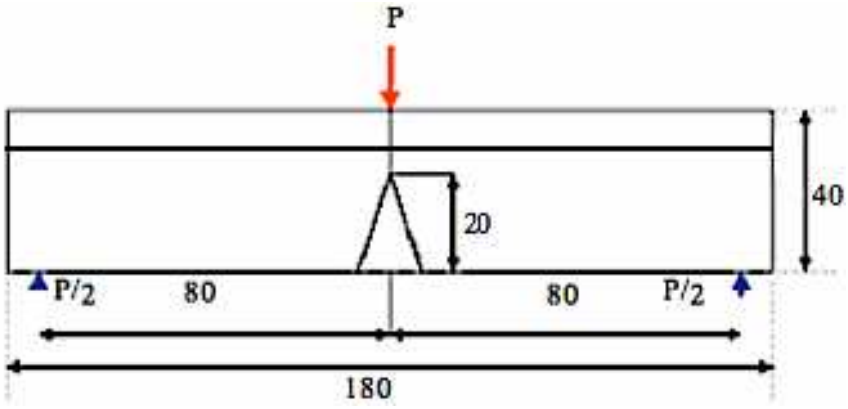

Fig 8.2: Sketch of composite in single mode A

As in chapter 7 the same flow of numerical investigation was followed to detect the sensitivity of fracture parameters upon loading and crack properties. Table 8.1 shows results of SIF and J-integral for a crack length of 19 mm, where load from 50 to 500 N, range of crack length for the sensitivity analysis is from 11 up to 27 mm. It is remarkable that from 20 to 27 mm crack propagates inside the piezoelectric material. Crack propagation is shown in Fig 8.3.

Table 8.1: SIF and J-Integral with varying load magnitude and crack length of 19 mm

Load [N]	50	100	150	200	250	300	350	400	450	500
SIF [MPa]	73.13	146.2	219.3	292.5	365.6	438.8	511.9	585.0	658.1	731.3
J-Integral [N/mm]	0.025	0.108	0.177	0.411	0.642	0.925	1.259	1.645	2.081	2.570

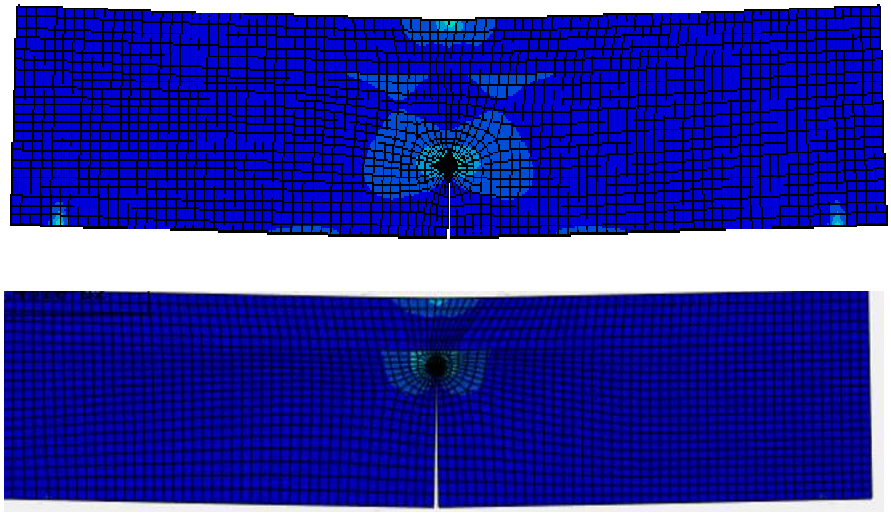

Fig 8.3: Stress distribution and crack propagation inside the composite specimen

In several steps of the numerical prediction made by ABAQUS, trends of J-integral are plotted as a function of applied mechanical load (Fig 8.4) and crack length (Fig 8.5) respectively. Nonlinear behaviour and sensitivity of composite specimen are both evident.

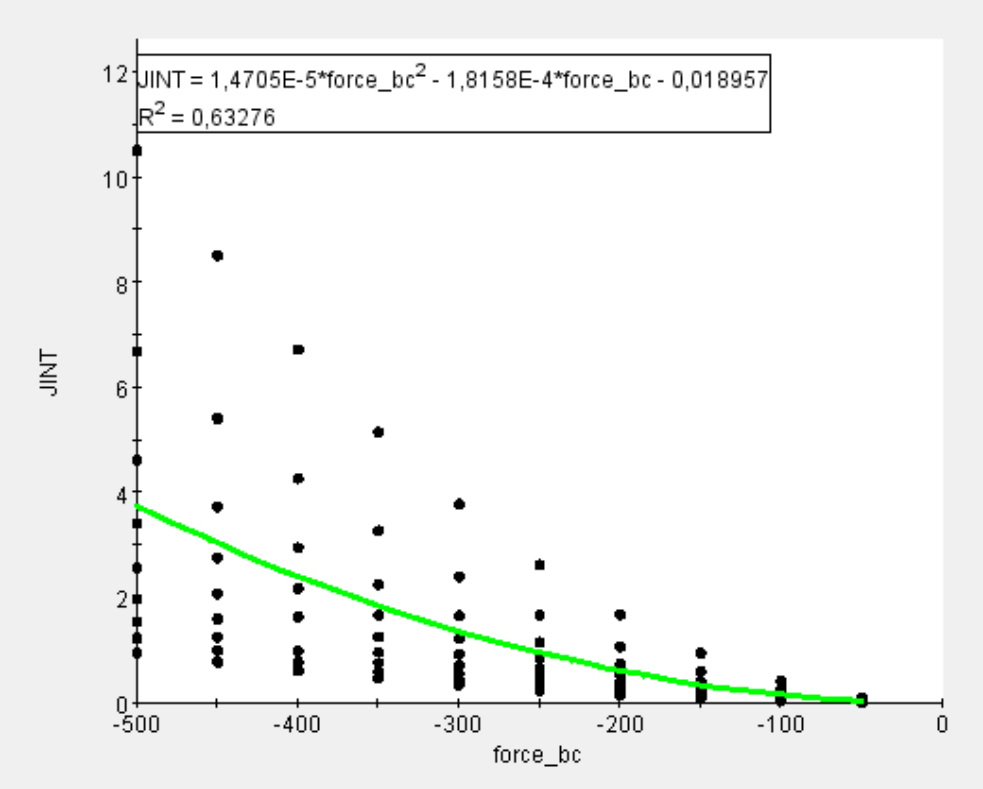

Fig 8.4: J-Integral vs. load magnitude (without applying voltage)

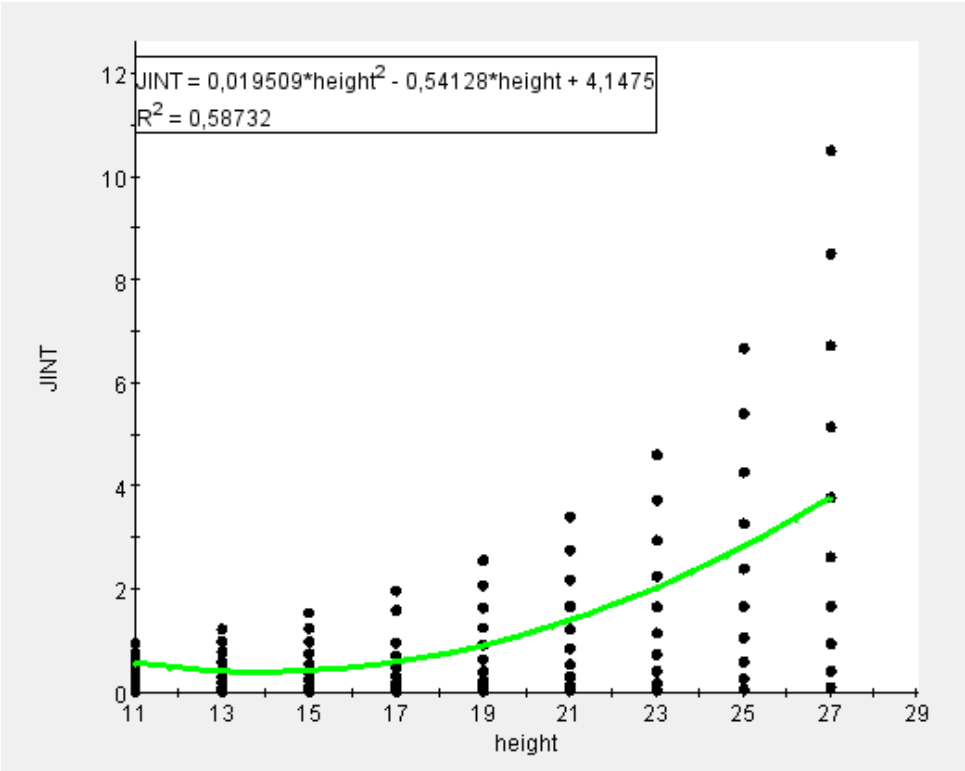

Fig 8.5: J-Integral vs. crack length (without applying voltage)

As Fig 8.6 shows the J-integral in each step exhibits a non-linear behaviour. Positive values of J-integral suggest that crack is opening in all the conditions. Nevertheless the last two points in each run are so distant because crack goes inside the piezo layer. In case of two layers of different materials the properties are changing, therefore values of J-integral depend on the contour and region of specimen, which is analysed.

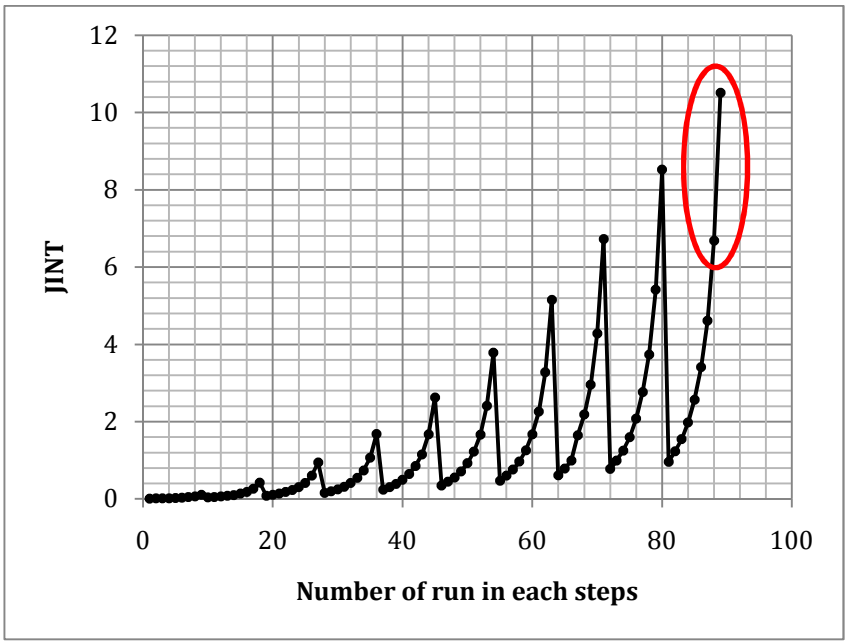

Fig 8.6: J-integral in all conditions of different loads and crack length

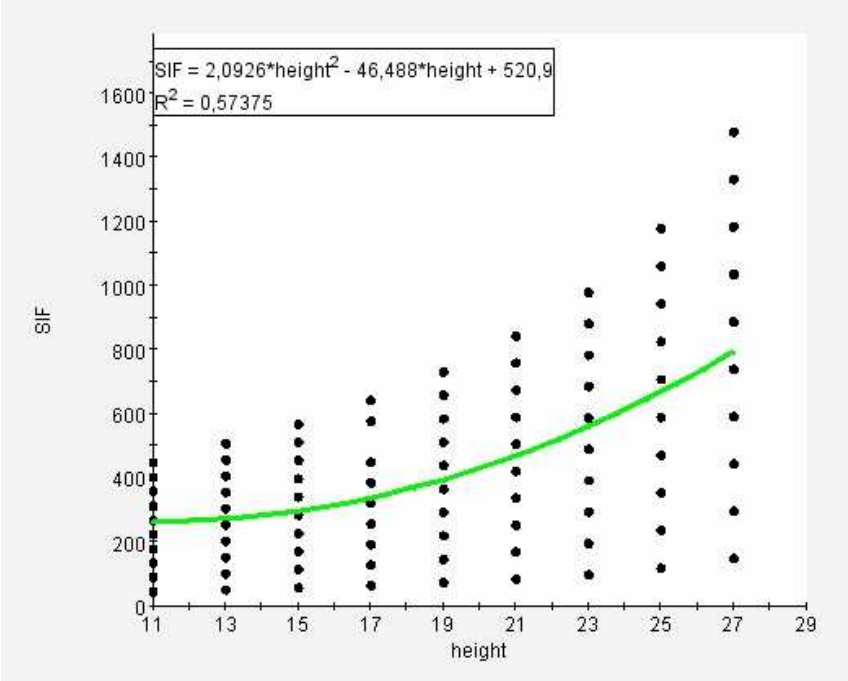

Fig 8.7: SIF for different crack length without applying voltage.

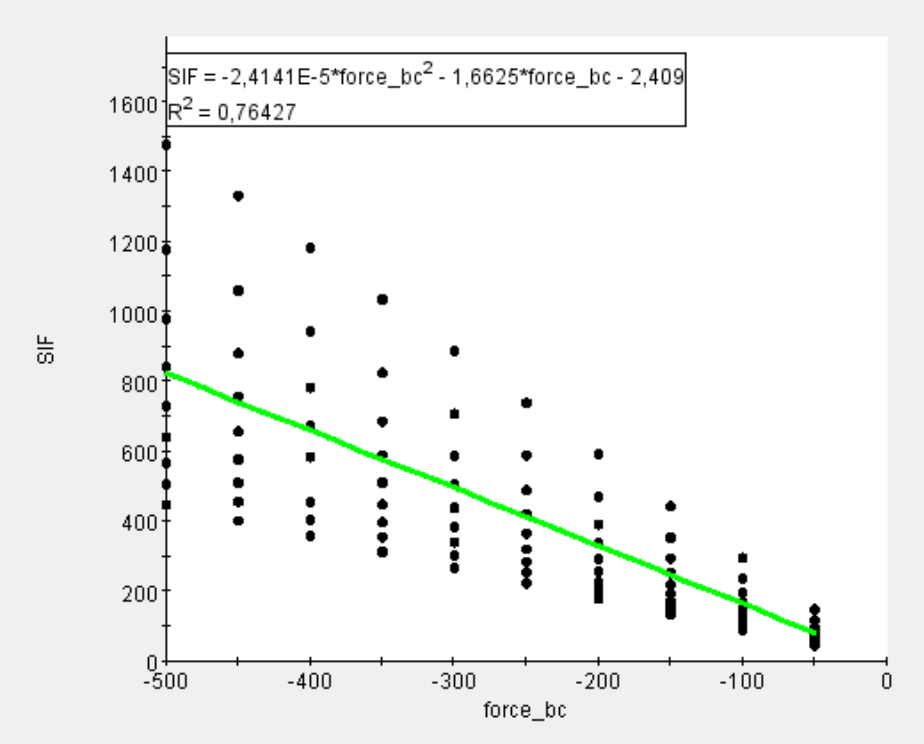

Fig 8.8: SIF for different loads magnitude without applying voltage

SIF depends nonlinearly upon the crack length and almost linearly on applied load (Fig 7.8 and 8.8). Even in Fig 8.9 increasing of values is more evident where piezoelectric layer is reached.

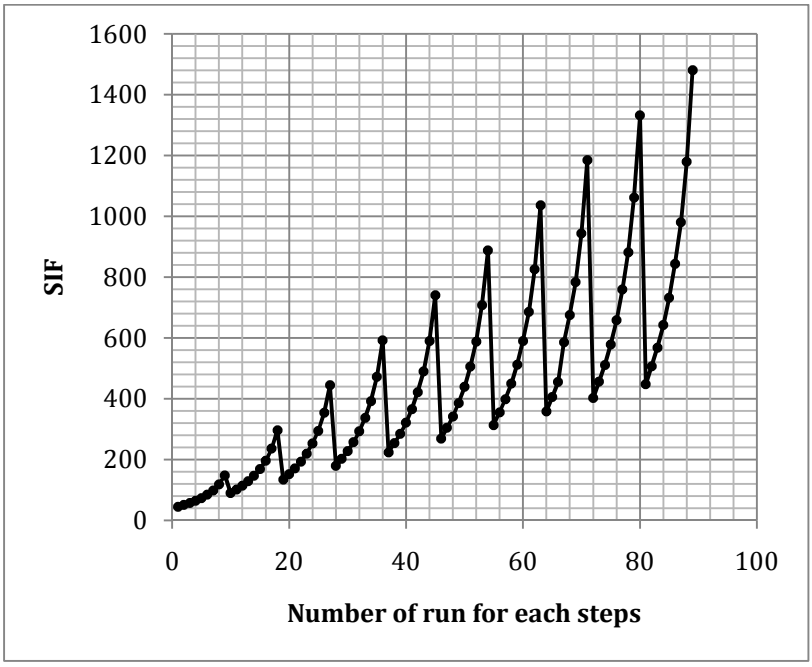

Fig 8.9: SIF in all conditions of different loads and crack length

Fig 8.10 presents the correlation between Stress Intensity Factor and j-integral.

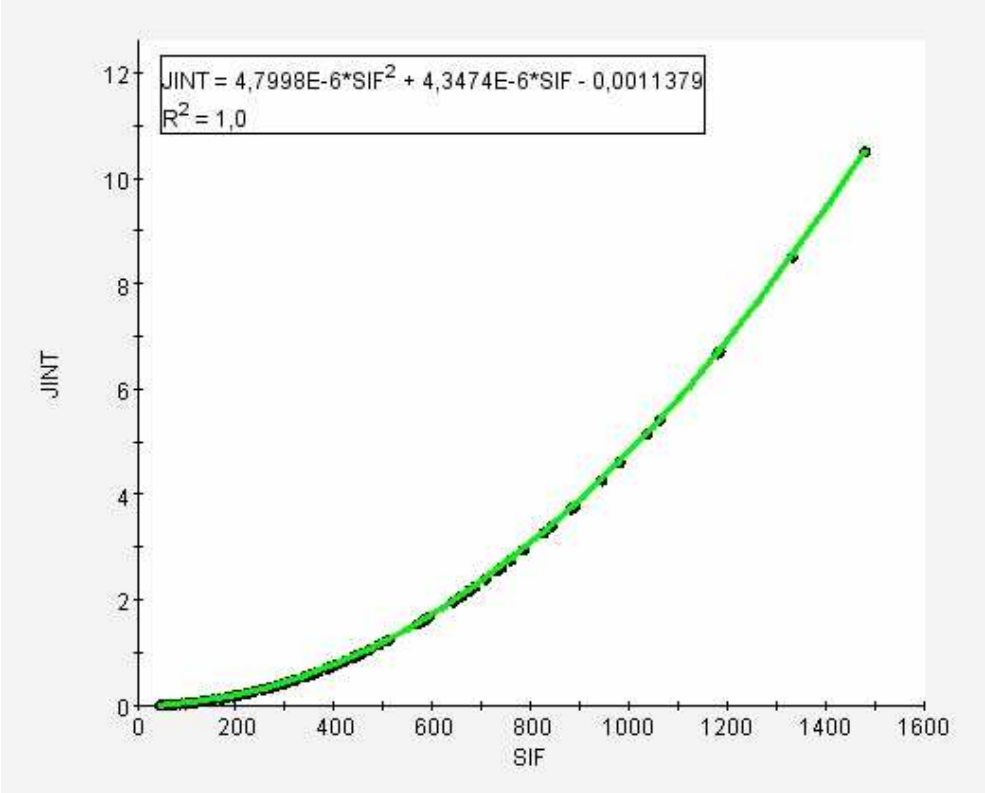

Fig 8.10: J-Integral vs. SIF

Behaviour of composite specimen looks similar to previous case when voltage is the excitation. Table 8.2 shows SIF and J-integral, for a crack length of 19mm, voltage variable from 10 to 100v and crack length range spamming from 11 to 27.

Table 8.2: SIF and J-Integral with different Voltage and crack length of 19mm

Voltage [V]	10	20	30	40	50	60	70	80	90	100
SIF [MPa]	30.53	61.07	91.604	122.15	152.72	183.24	213.80	244.30	274.83	305.38
J-Integral [N/mm]	0.004	0.018	0.0411	0.0732	0.1144	0.1647	0.2242	0.2928	0.3705	0.4575

Crack opening under 40 V is shown in following Fig 8.11.

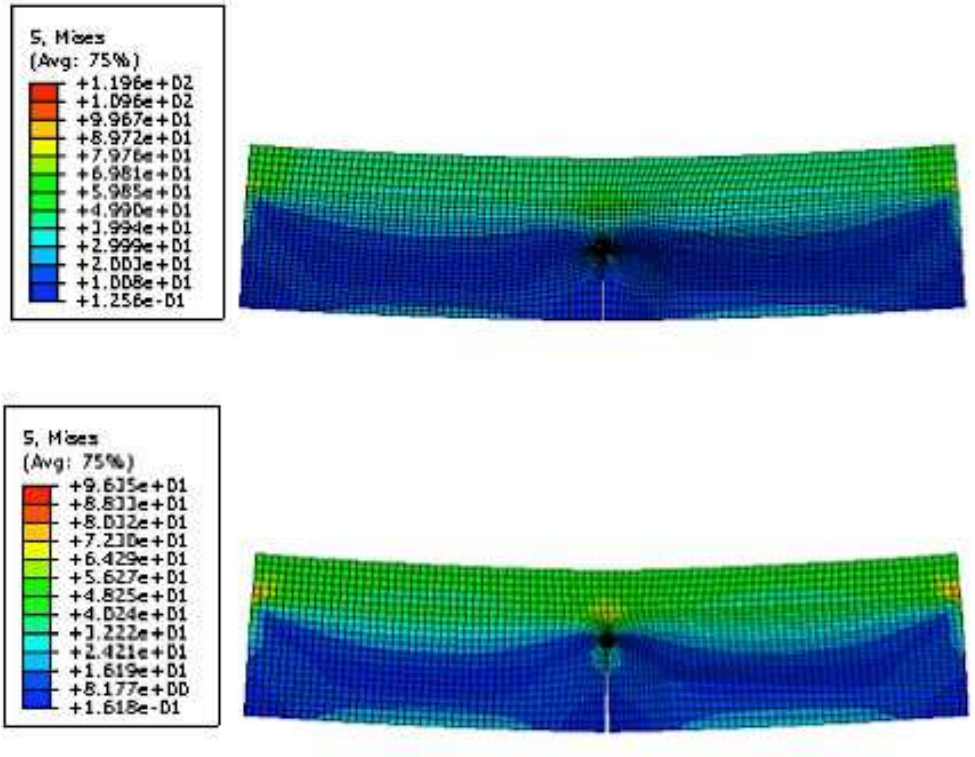

Fig 8.11: Stress distribution under voltage effect and crack propagation

It is worthy noticing that when crack reaches the interface between steel and piezoelectric material first it stops. At that point it is very important analyzing the bending of structure. In this case metal contributes only with its inertia and stiffness, therefore propagation needs of a strong electric field applied to piezo, so large to bend the whole structure and providing the required energy to the fracture of piezoelectric layer too. Nevertheless, stiffness of piezoelectric layer looks affected by the tensile stress applied by the piezoelectric effect. In practice a “BARRIER EFFECT” is opposed by the active layer. This behaviour is more evident if J-integral is plotted vs. crack length as it drops down very fast above a certain crack length (Fig 8.12), although it grows up nonlinearly with voltage (Fig 8.13).

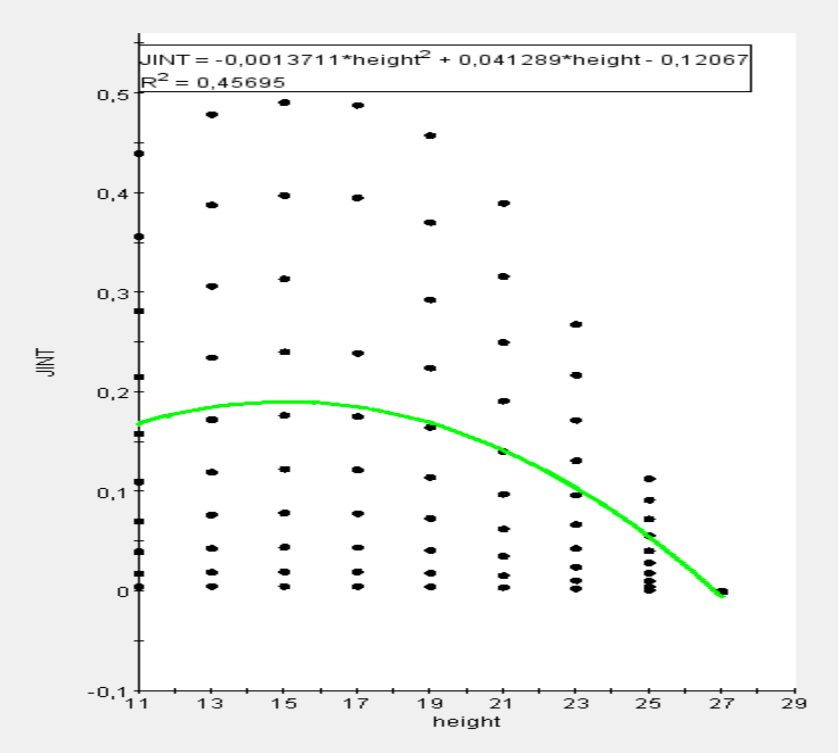

Fig 8.12: J-Integral vs. crack length

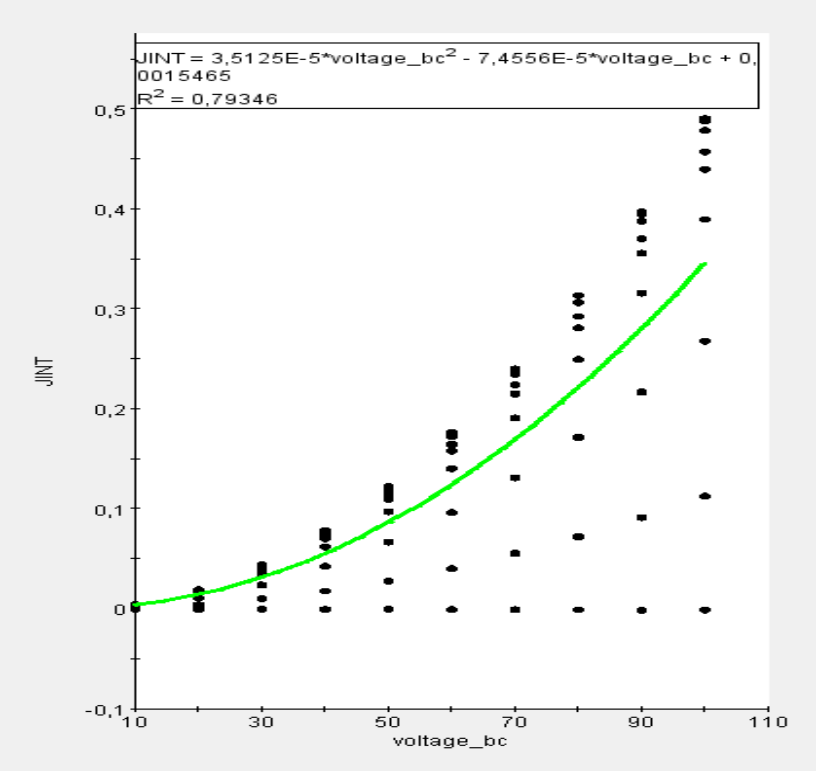

Fig 8.13: J-Integral vs. voltage

It is remarkable that J-integral when it is driven by voltage is positive while in pure piezo it was negative. Tensile stress in piezoelectric layer is dominating. The sudden decreasing of J-integral in to the barrier effect is evident when the history of simulation is plotted as in Fig 8.14.

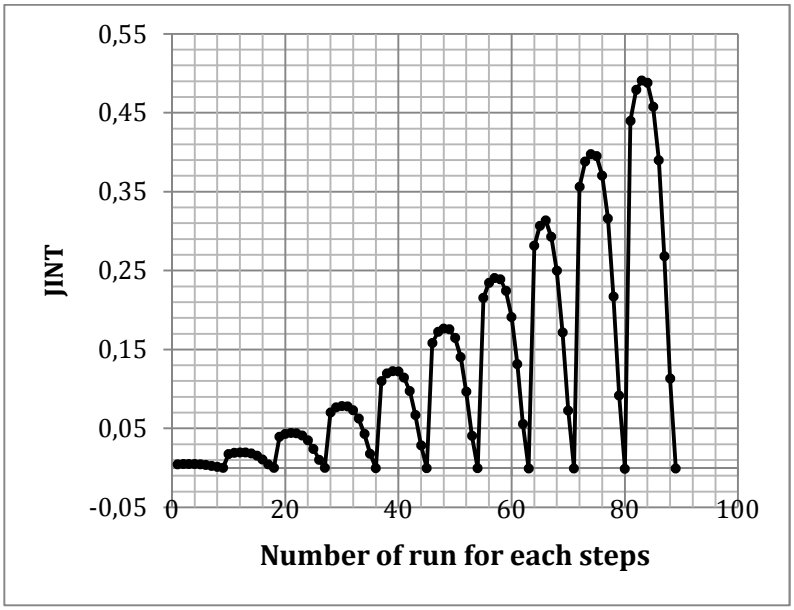

Fig 8.14: J-integral in all conditions of different loads and crack length

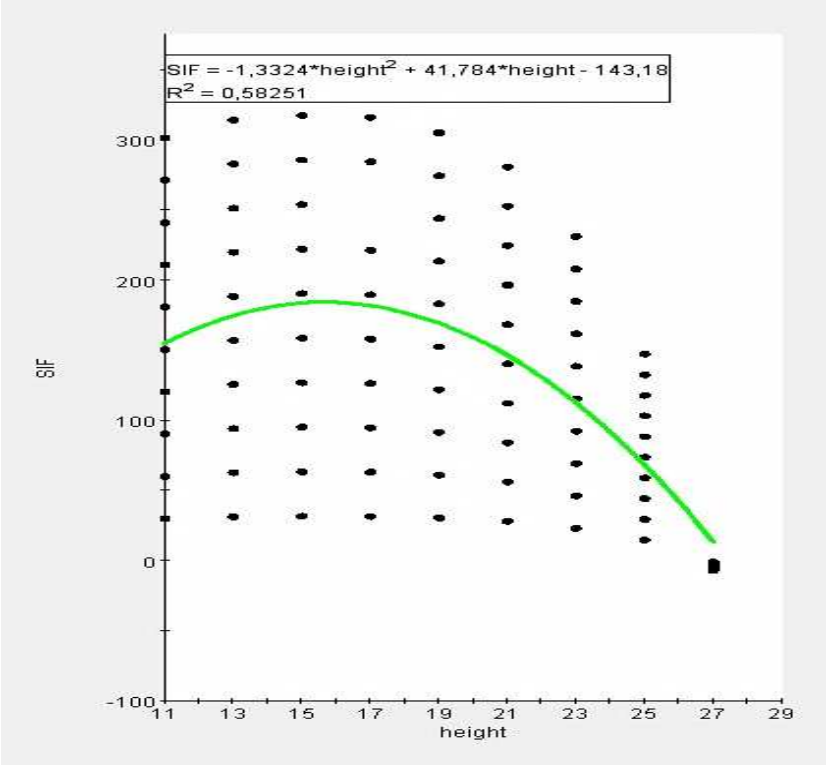

Fig 8.15: SIF for different crack length (without applying external force)

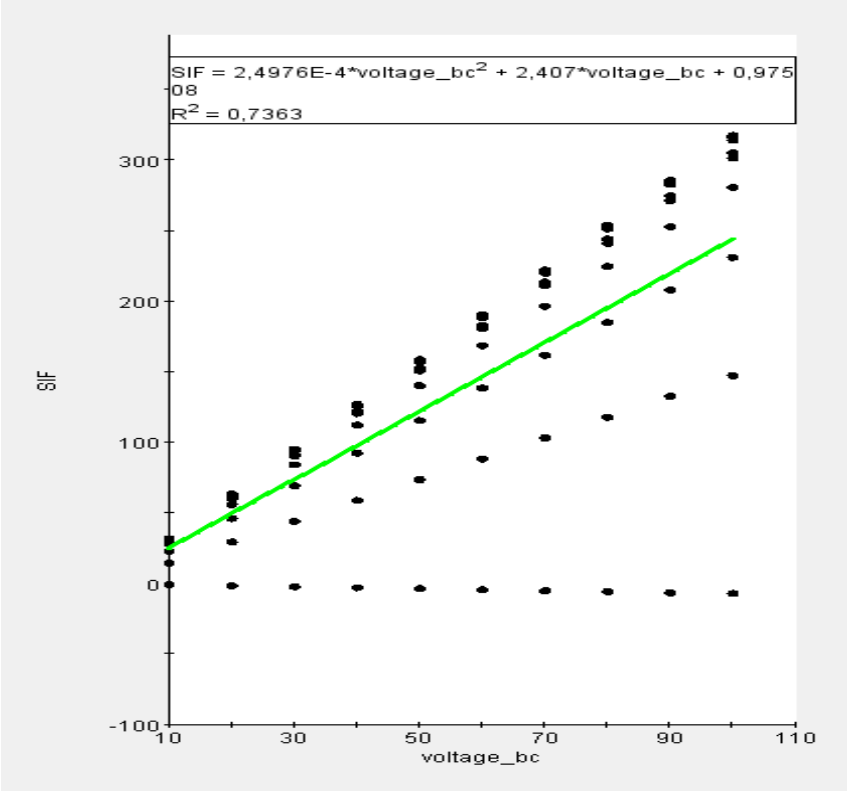

Fig 8.16: SIF for different voltage magnitude (without applying external force)

Fig 8.15 and 8.16 confirm the trend already seen for the J-integral even for the SIF. According to the Fig 8.17, barrier effect is evident. Correlation between J-integral and Stress Intensity factor is much more nonlinear in this case (Fig 8.18)

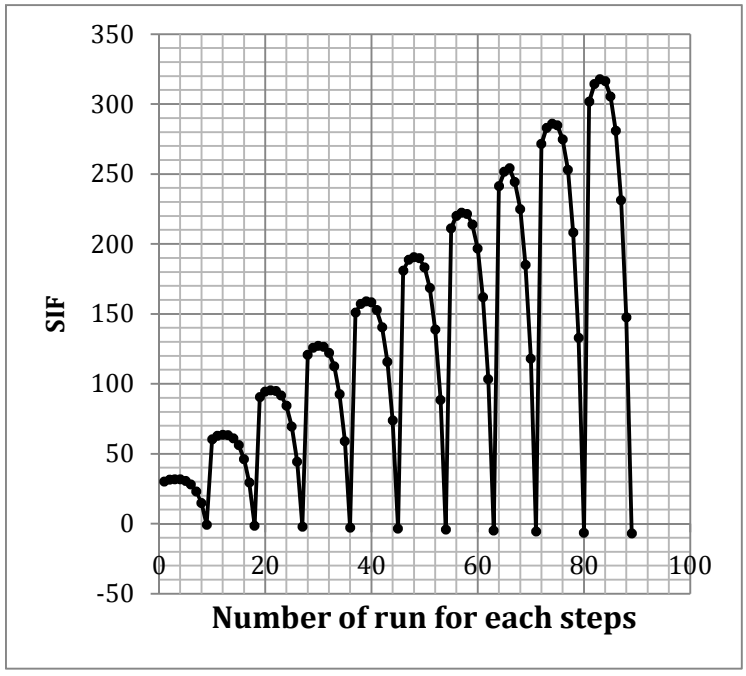

Fig 8.17: SIF in all conditions of different voltage and crack length

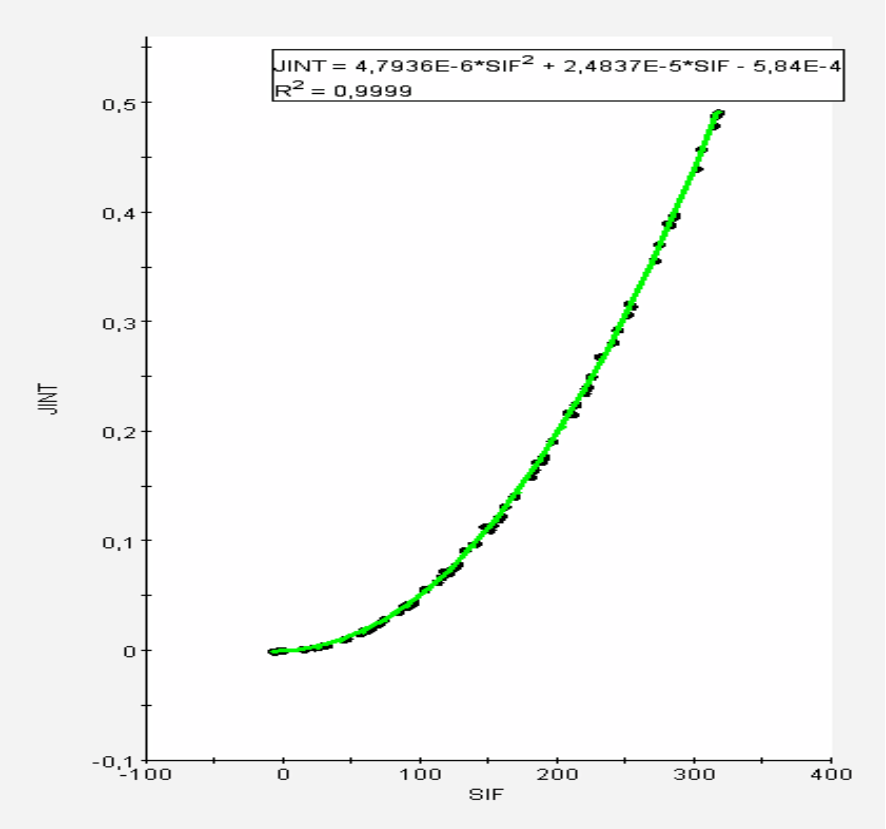

Fig 8.18: J-Integral against SIF values in all point

3 Mixed mode crack propagation

Mixed mode C was then analyzed upon specimen shown in Fig 8.19. 40 mm 74 mm 36 mm 20 mm

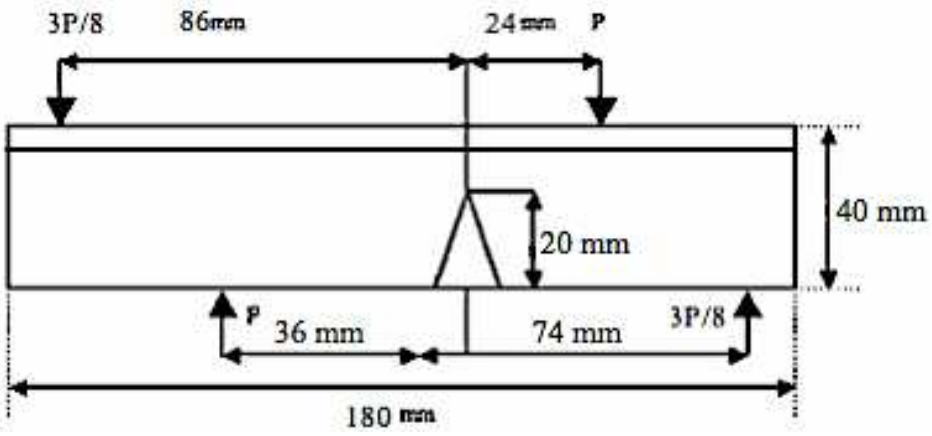

Fig 8.19: The sketch of composite specimen mixed mode C

Influence of pure mechanical load on the SIF and J-integral is analyzed in Table 8.3.

Table 8.3: SIF and J-Integral with different load magnitude with crack length of 19mm

Load (N)	10	20	30	40	50	60	70	80	90	100
K_I[MPa]	1.874	3.74	5.623	7.49	9.372	11.2	13.12	14.992	16.866	18.744
K_{II}[MPa]	-0.94	-1.8	-2.83	-3.77	-4.72	-5.66	-6.609	-7.555	-8.499	-9.443
J-Integral [N/mm]	2.1 e^{-5}	8 e^{-5}	1.88e^{-4}	3.3 e^{-4}	5.2 e^{-4}	7.5 e^{-4}	0.00102	0.00134	0.00169	0.00209

Local concentrations of stress and crack propagation are shown in Fig 8.20.

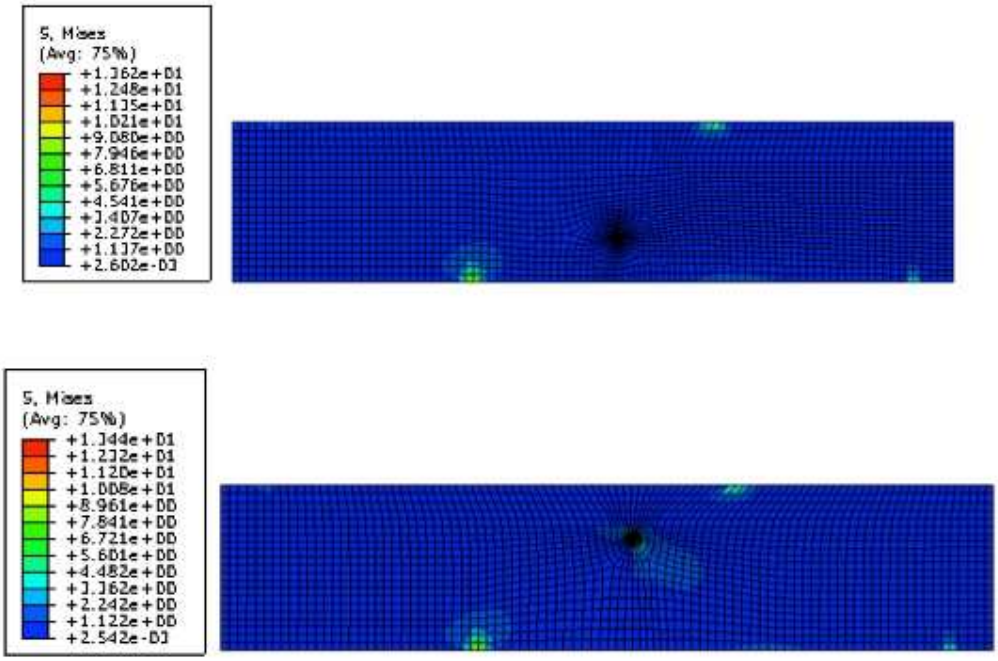

Fig 8.20: Stress distribution in composite specimen under load of 20 N and crack propagation

J-integral nonlinearly follows the applied load (Fig 8.2) and crack length growth (Fig 8.22) as usual even in metallic components.

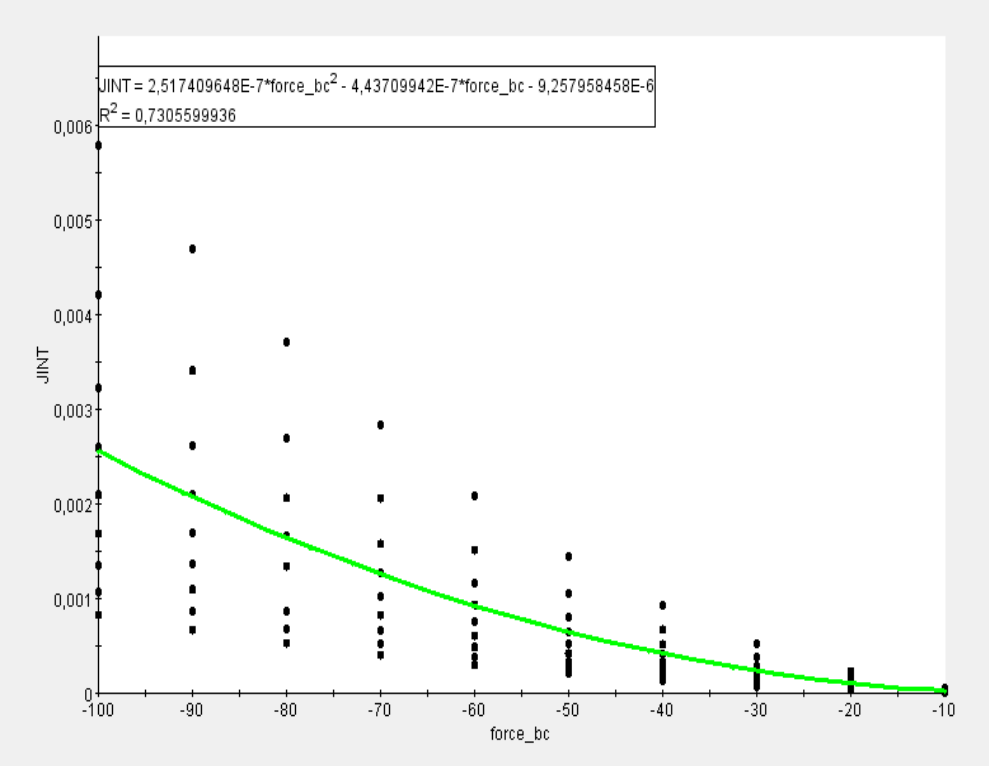

Fig 8.21: J-Integral vs. loads magnitude (without applying voltage)

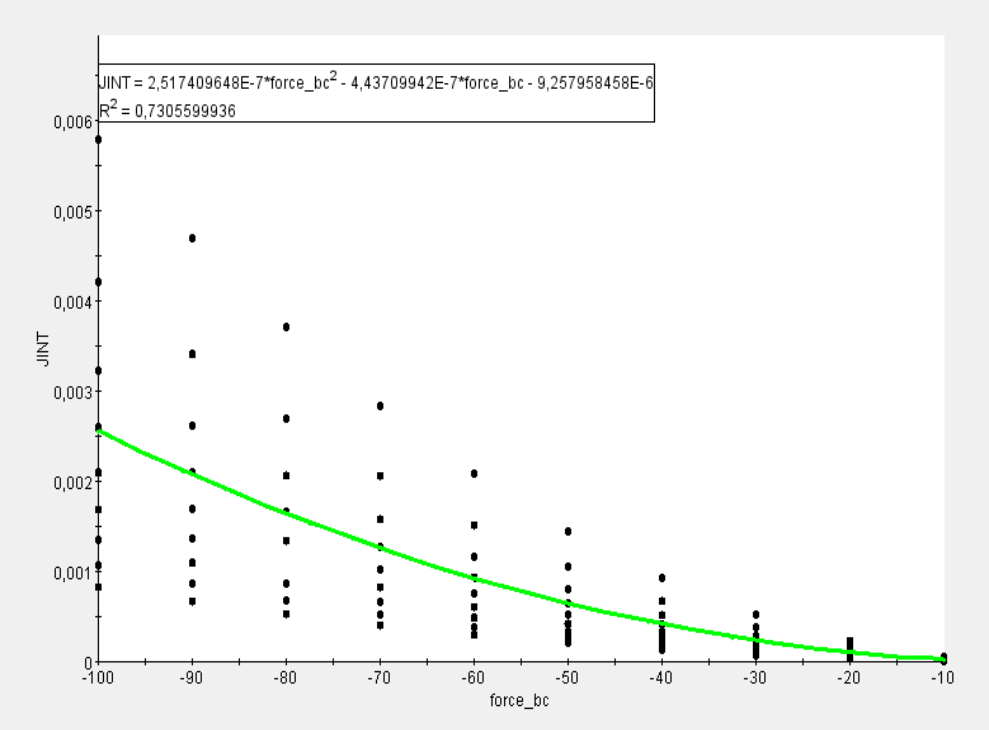

Fig 8.22: J-Integral vs. crack length (without applying voltage)

Trend of J-integral is monotonic. When Stress Intensity Factors are analyzed, it can be remarked that values increase both with crack length, although in mode II (Fig 8.23 and 8.24).

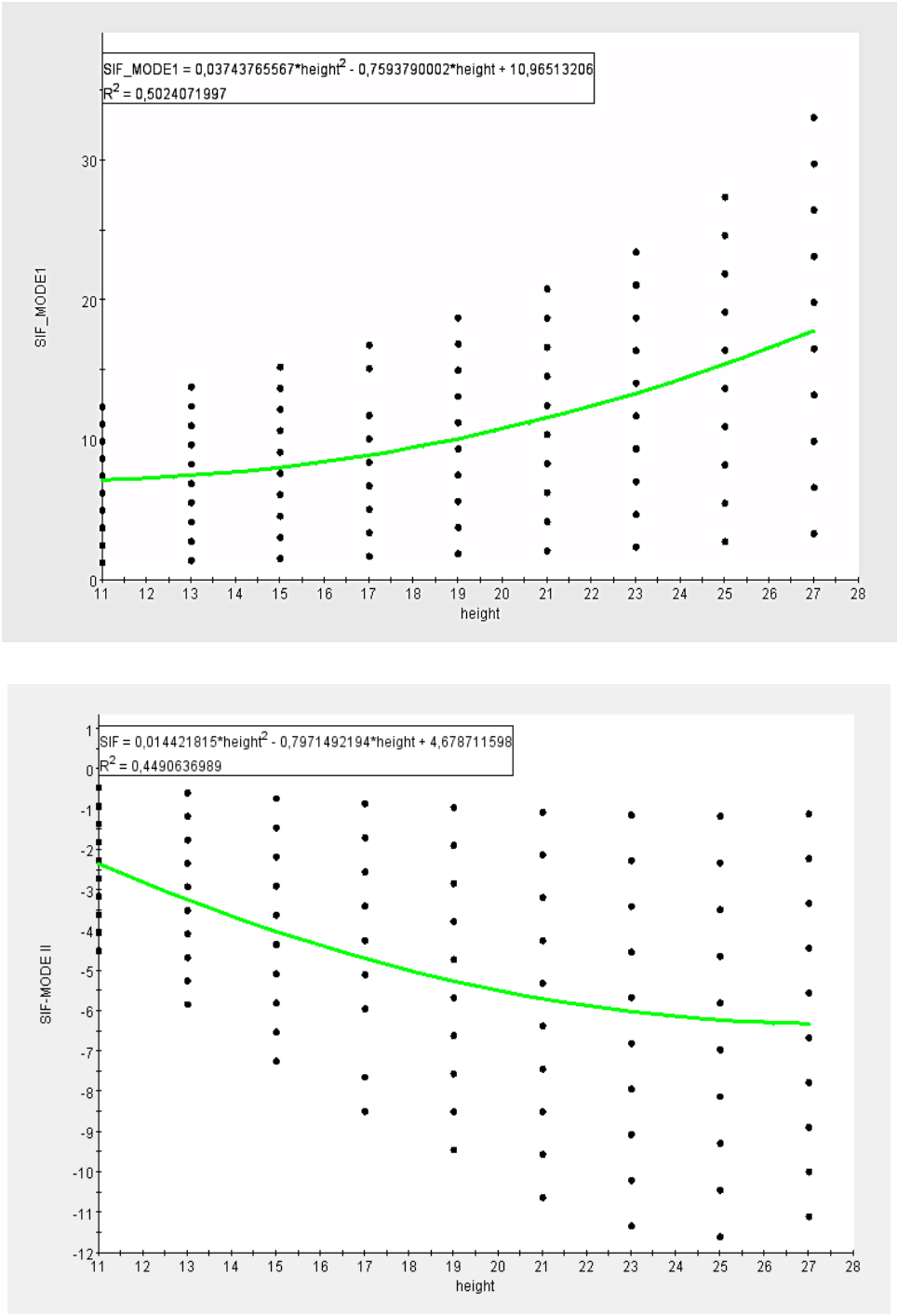

Fig 8.23: SIF for different crack length (without applying voltage)

The ABAQUS code releases a negative K_{II}, in this case since sliding mode is undergoing a relative motion of fracture goes instead of frontal decohesion, this sign is poorly relevant for the damage mechanism.

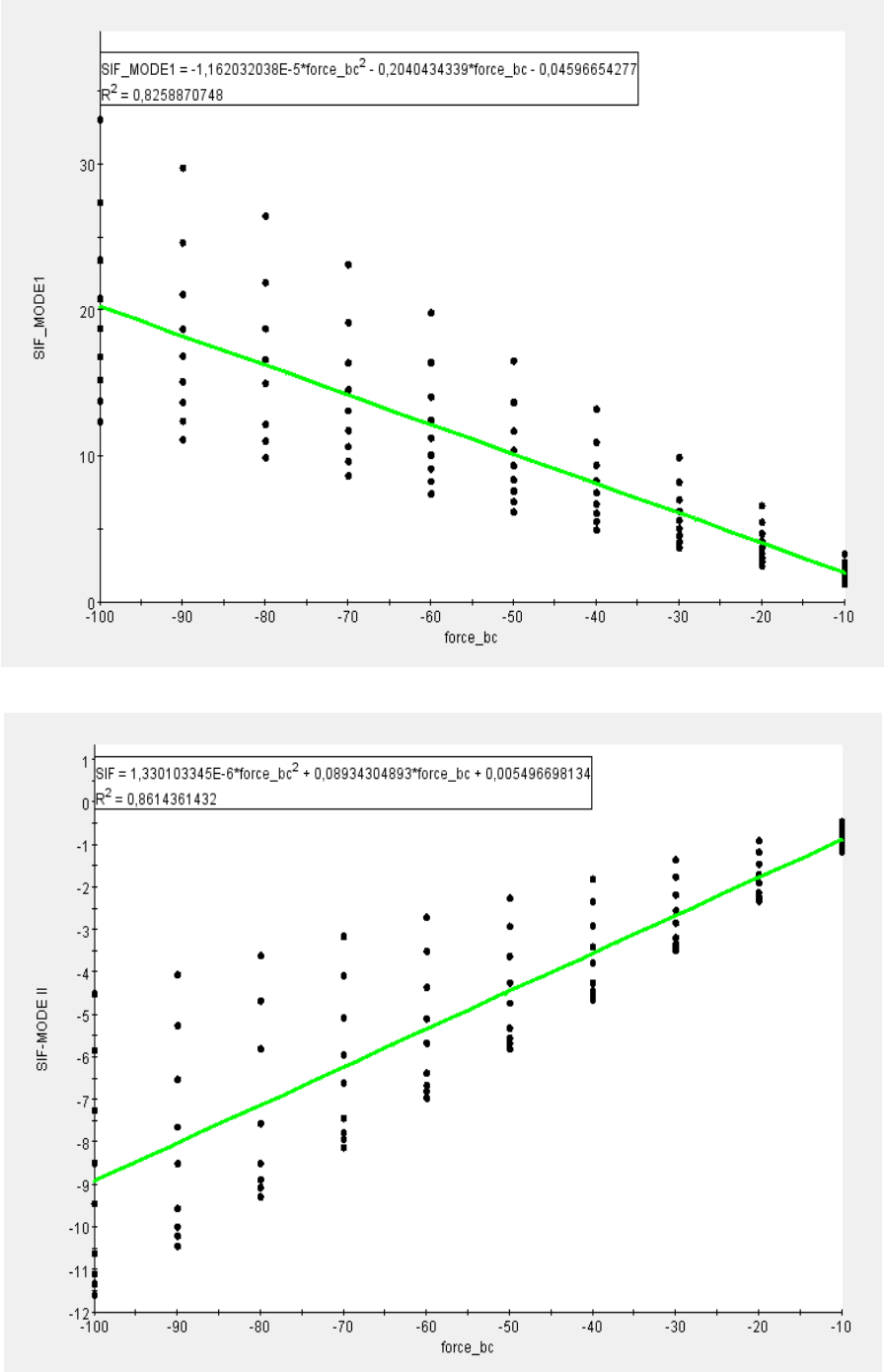

Fig 8.24: SIF vs. load magnitude without applying voltage

Convergence is good in each step of simulation, as Fig 8.25.

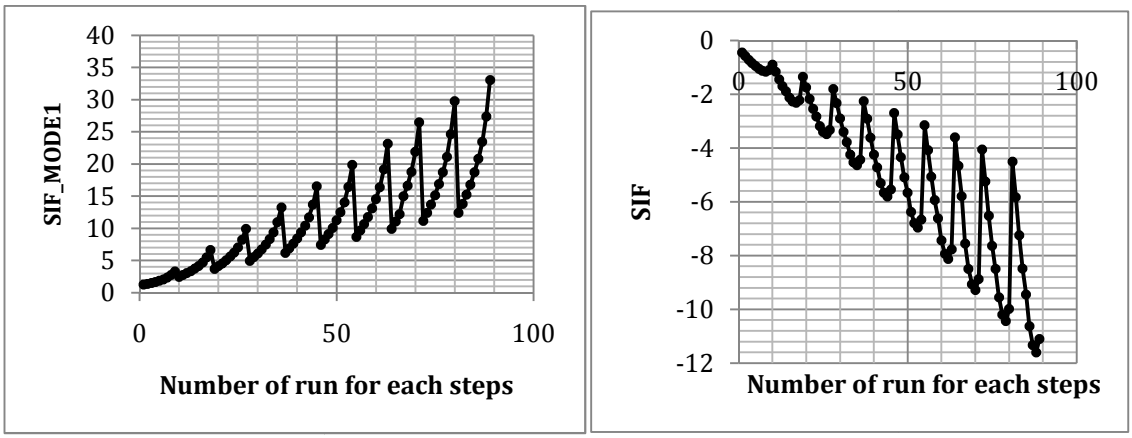

Fig 8.25: SIF in all conditions of different load and crack length

Relations between SIF and J-integral in both modes are smoothly nonlinear, as it was expected.

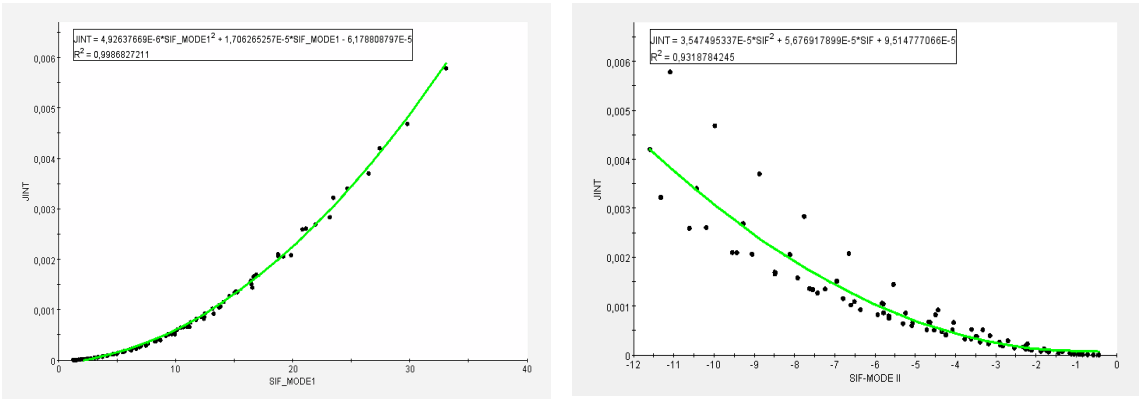

Fig 8.26: J-Integral vs. SIF

As soon as voltage is applied as excitation the barrier effect is found. Table 8.4 collects SIF and J-integral for crack length of 19mm, voltage spamming from 20 to 200 V, while crack length is 11 to 27 mm in sensitivity analysis.

Table 8.4: SIF and J-Integral with different Voltage and the crack length of 19mm

Voltage [V]	20	40	60	80	100	120	140	160	180	200
K_I[MPa]	78.19	142.82	207.4	272.1	336.74	401.36	466.00	530.50	595.39	659.75
K_{II}[MPa]	8.694	31.57	54.44	77.282	100.158	123.009	145.862	168.756	191.576	214.501
J-Integral [N/mm]	0.0294	0.1018	0.219	0.3810	0.5877	0.8391	1.1354	1.4757	1.8628	2.2918

Crack opening under 80 V is shown in Fig 8.27.

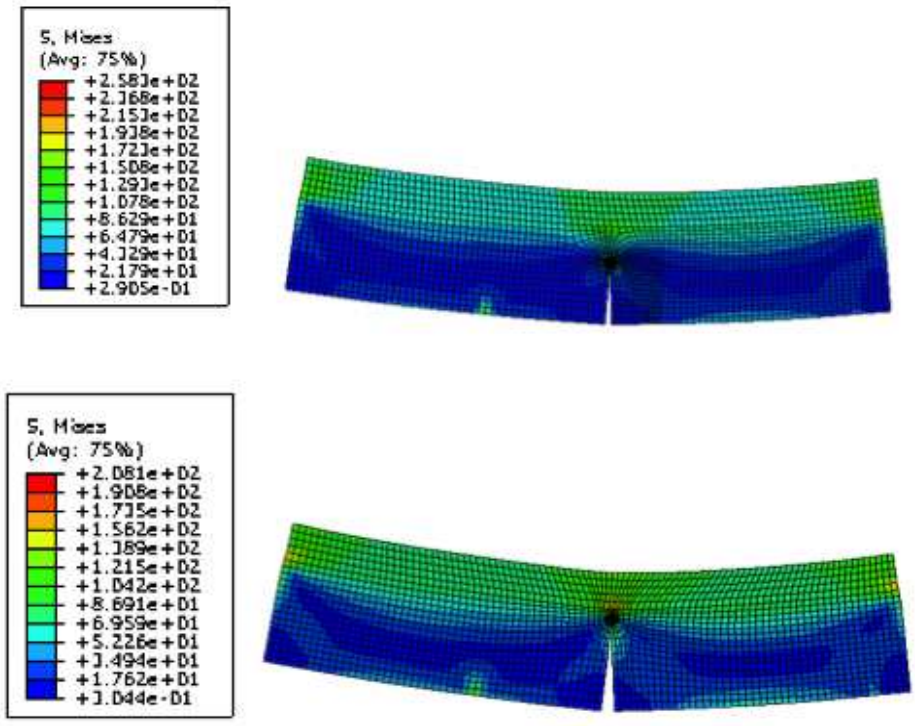

Fig 8.27: Crack propagation under 80V and electric potential

It can be remarked that crack propagation is slightly rotate at tip, although mixed mode propagation is analyzed. One again barrier effect motivated the trends of j-integral in fig 8.28, although it grows up as voltage increases.

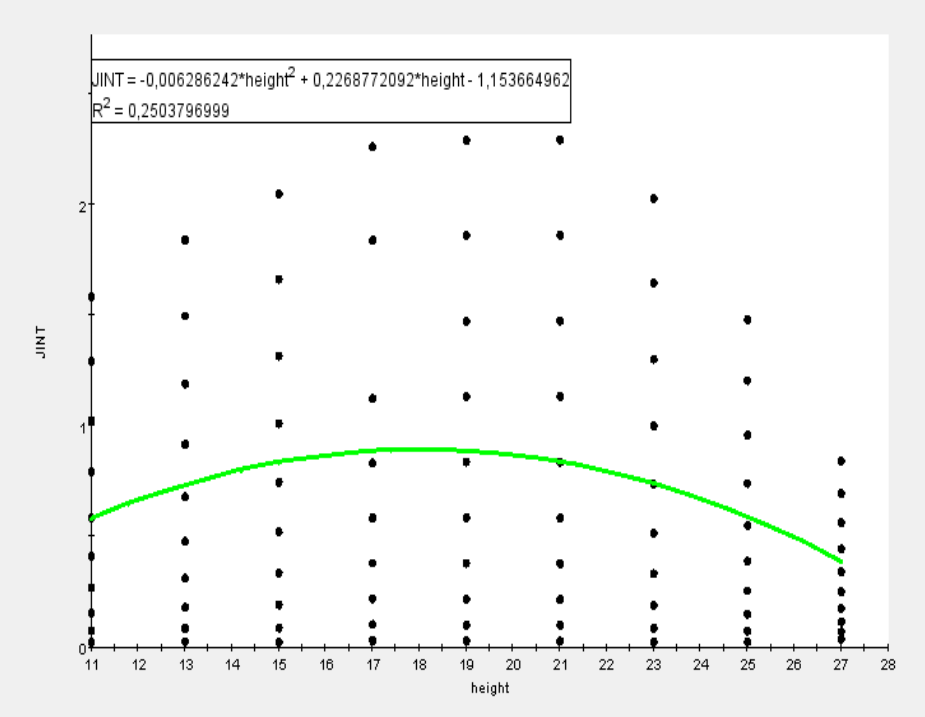

Fig 8.28: J-Integral vs. crack length with different voltage (without force)

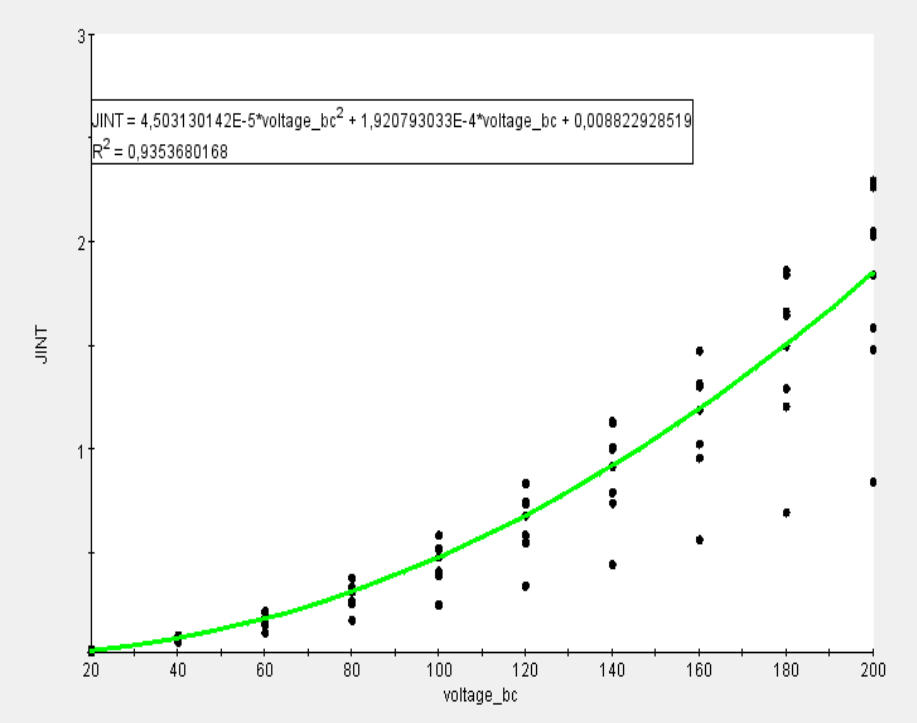

Fig 8.29: J-Integral vs. voltage magnitude (without force)

Similarly SIF diagrams in Fig8.30 show a very effective barrier effect in mode I and a smoother effect in mode II.

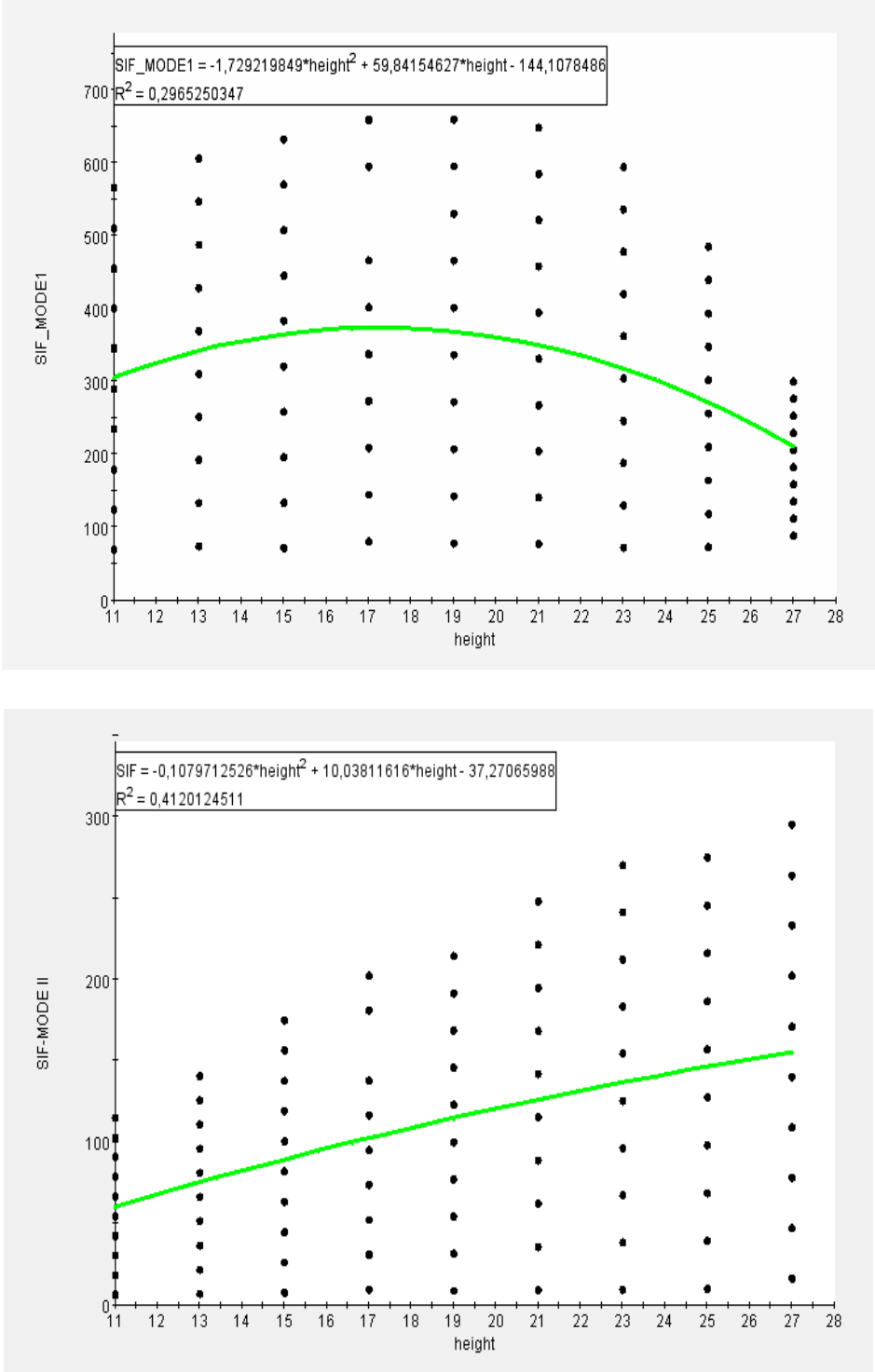

Fig 8.30: SIF vs. crack length (without applying external force)

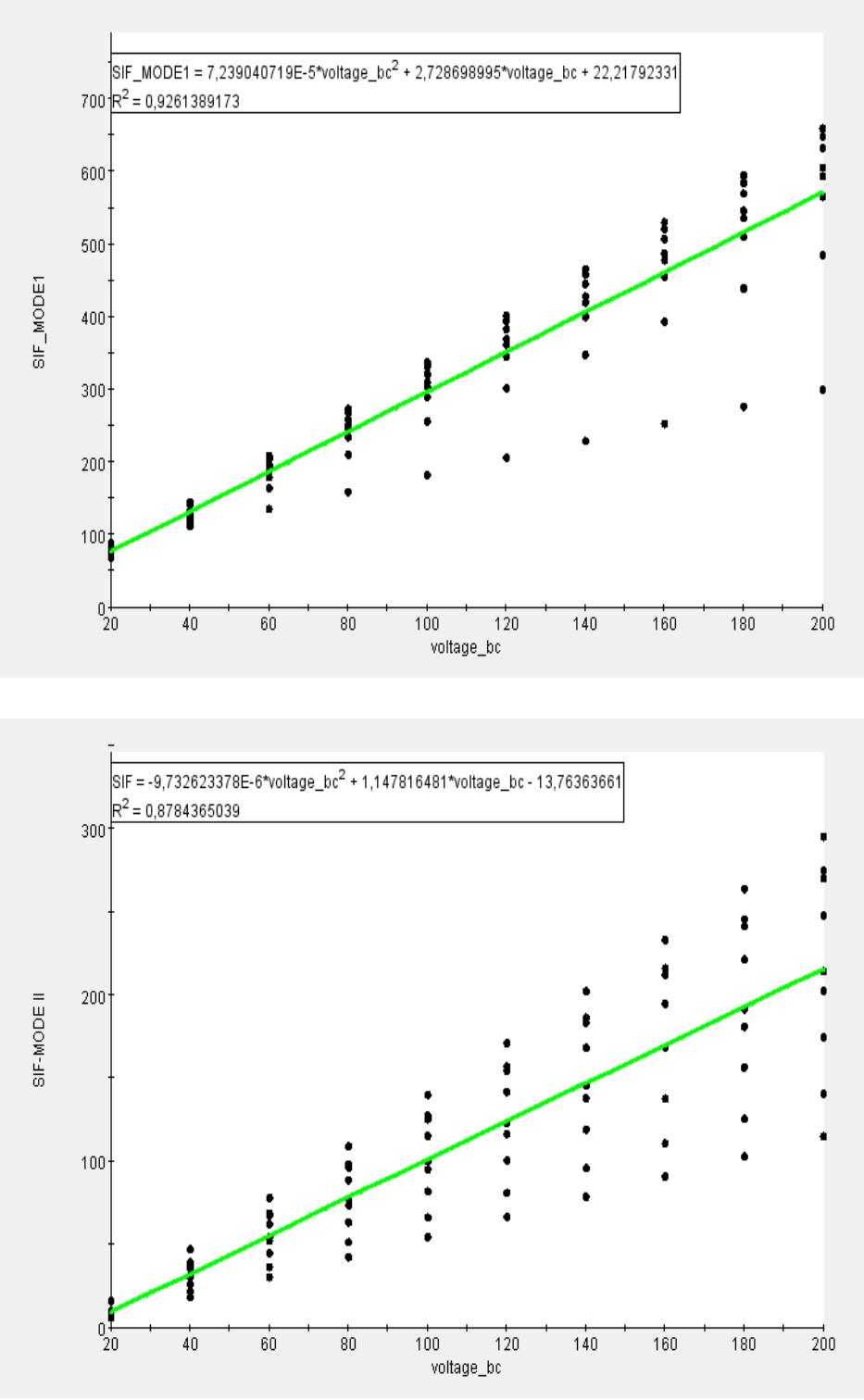

Fig 8.31: SIF vs. voltage magnitude (without applying external force)

Finally Fig 8.32 describes the correlation between Stress Intensity Factor and J-integral.

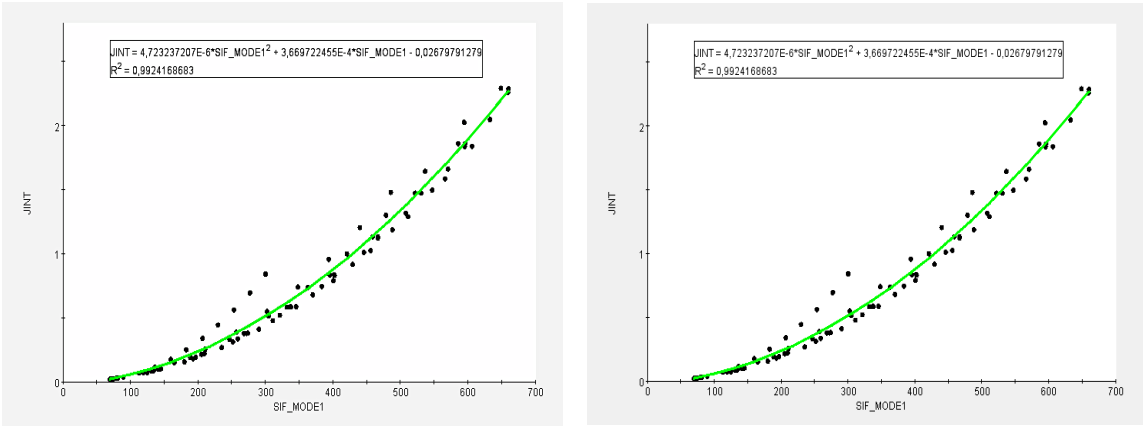

Fig 8.32: J-Integral vs. SIF

4 Crack propagation path

Since a main goal of the thesis is predicting the fracture behaviors inside piezoelectric layer and in smart components with surface bounded piezoelectric in both active and passive configuration a resume of relevant results is herein proposed.

4.1 Crack propagation in single fracture mode of pure piezoelectric layer

Crack growth in single mode of fracture inside a pure piezoelectric specimen was analyzed in both boundary conditions i.e. under a mechanical force and under the voltage of an applied electric field. As Fig 8.33 and 8.34 demonstrate when force is loading the specimen, crack growth proceeds up to rupture of specimen material. By convers when voltage acts as driving load, crack propagation stops when a certain length is reached. To start again and put the propagation up to rupture a large electric field is required. This looks like a “barrier effect”, being even related to the high charge concentration around the crack tip.

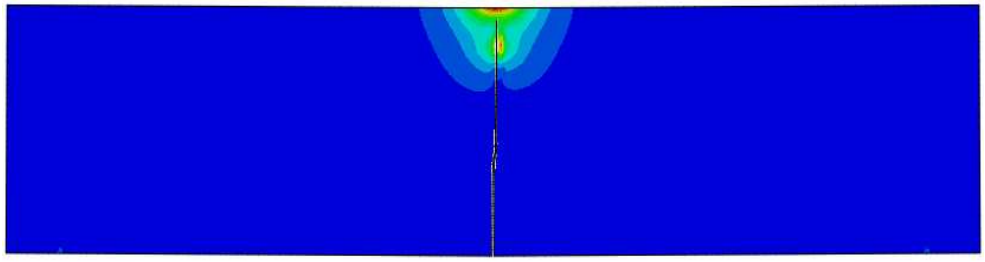

Fig 8.33: Crack propagation in single mode of fracture with mechanical force as in a sensor

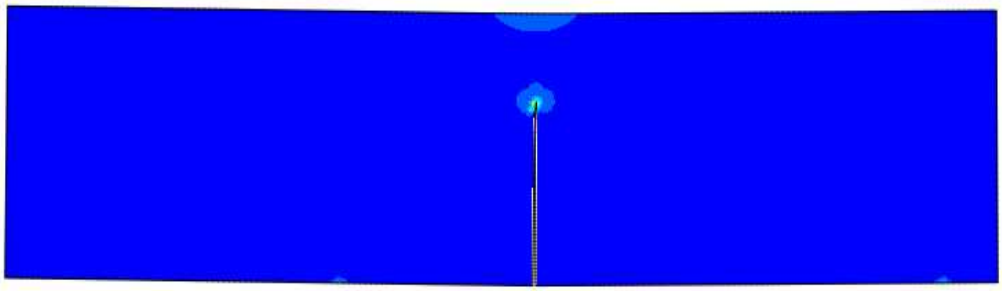

Fig 8.34: Crack propagation in single mode of fracture with voltage applied as in an actuator

4.2 Crack propagation in mixed mode fracture of pure piezo

In case of mixed of fracture mechanics (Fig 8.35 and 8.36), when mechanical load is applied, crack growth shows angle of 45 degree with x-direction. It is due to the stronger action of force being larger than voltage created inside the specimen because of piezoelectric effect. When voltage is driving crack propagation occurs along the vertical direction such as in single mode. Crack propagates according to displacements imposed by electric field around the crack tip without any deviation.

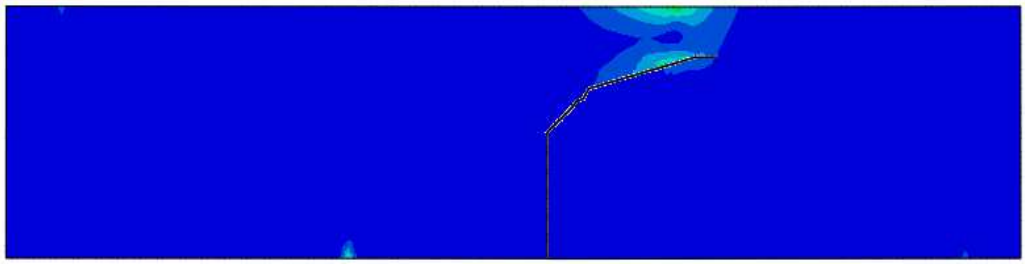

Fig 8.35: Crack propagation in mixed mode of fracture (with force)

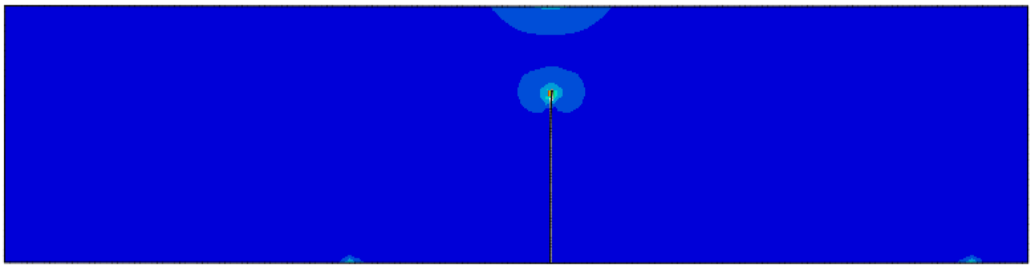

Fig 8.36: Crack propagation in mixed mode of fracture (with voltage)

4.3 Crack propagation in single mode fracture of composite piezoelectric specimen

In case of composite specimens with surface bounded piezoelectric layer (Fig 8.37 and 8.38). Crack propagates along the vertical direction in both cases, when force and voltage are loading the structure in single mode of fracture mechanics. In case of force driven crack propagates inside the steel then it passes through the piezo electric layer up to rupture. If voltage is applied crack propagates inside the steel then stops when it reaches the interface between the two materials.

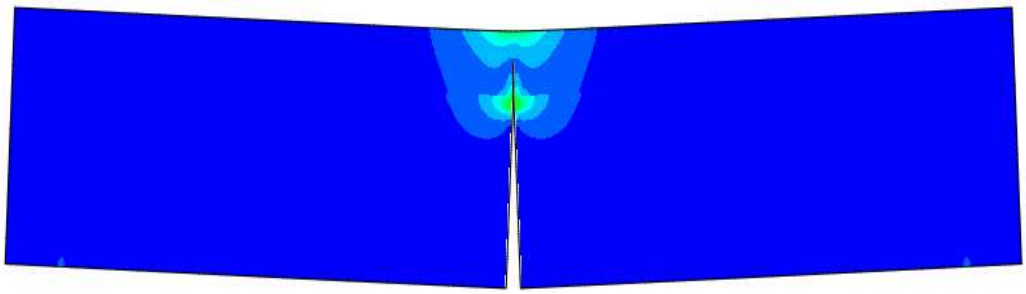

Fig 8.37: Crack propagation in single mode of fracture with force (composite material)

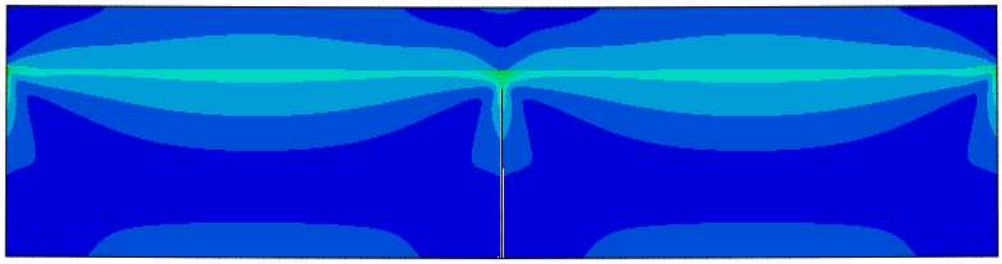

Fig 8.38: Crack propagation in single mode of fracture with voltage (composite material)

4.4 Crack propagation in mixed mode fracture of composite piezoelectric specimen

Finally crack propagation in mixed mode of composite piezoelectric is considered. Crack is propagated along a direction rotated of 45 degrees but under mechanical action, it breaks both materials, and its direction changes at interface (Fig 8.39). When voltage is applied to the specimen, crack never passes to the piezoelectric layer because the bending moment is applied to the steel part by the piezoelectric layer, being in this case under effect of tensile load and even structure (Fig 8.40).

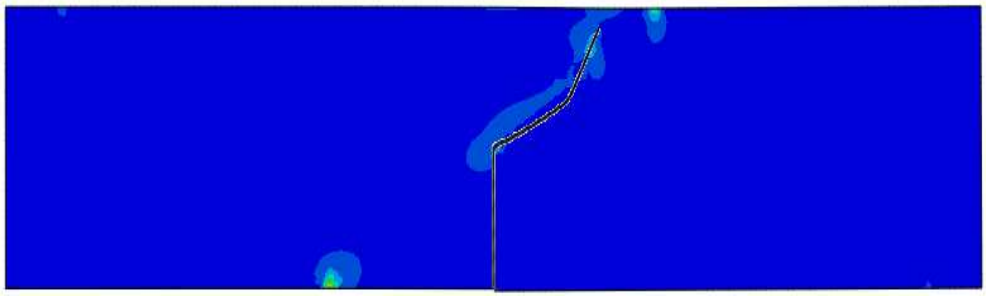

Fig 8.39: Crack propagation in mixed mode of fracture with force (composite material)

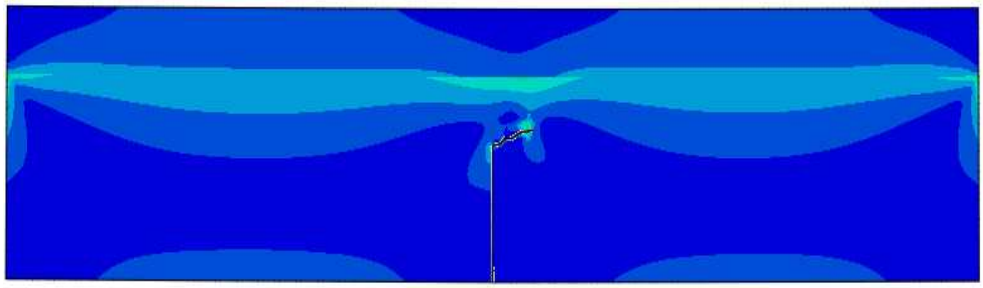

Fig 8.40: Crack propagation in mixed mode of fracture with voltage (composite material)

CONCLUSION

The main goal of this thesis was understanding better what are the typical behaviour of piezoelectric layer in case of either passively coupled (force driven-sensor) and actively coupled (voltage driven-actuator) undergoing crack propagation. Surprisingly the literature look still very poor of contributions in this field and only some preliminary elaboration of very well assessed analytical methods already available at the state of arts was proposed.

They are unsuitable for an effective prediction of fracture mechanics in smart structure having complex geometries as they are currently manufactured for several industrial applications. Need for a suitable numerical approach to be used in tight cooperation with some commercial tool immediately looked urgent. To cope with this first need the ABAQUS code was selected, because of the effectiveness demonstrated and tested by several authors of its modules dedicated to fracture analysis and piezoelectricity. Nevertheless a severe limitation occurred as soon as the two modules were tentatively connected by the author to investigate the fracture behaviour in piezoceramics. Even this problem was solved by resorting to the ISIGHT tool, which allows configuration a numerical protocol for a complex numerical investigation inside the ABAQUS code by listing and connecting the commands useful to start the required subroutine and to define a suitable flow of inputs and outputs for a coupled simulation as it is, in this case, that performed by the fracture mechanics and piezoelectric modules respectively.

This activity required a deep understanding and learning about both the ABAQUS modulus involved. Therefore fracture analysis was first performed on single and standard specimens for fracture bending tests mode of AISI 4340 steel, being already deeply studied and used in the literature.

Analysis was performed by calculating the Stress Intensity Factor and the J-integral as suggested in the literature, for mode I and mixed mode I and II. Results were checked

with experiments and numerical investigations available in the literature. Crack propagation was even predicted by resorting to the XFEM approach, as a first result, the thesis assessed suitable procedure for this kind of activity performed by means of ABAQUS code. It was immediately used for a benchmarking with other tools used by the EPF-School of Engineering in Sceaux for prediction of the crack propagation and life of welded joint. Experimental validation was even performed thus confirming the effectiveness of the numerical tool proposed. After this second original contribution a third task was developed. Crack propagation in some piezoelectric structure made of PZT-4 was analyzed for the same cased of steel specimen and by considering a pure piezoelectric layer and a composite made with a upper piezoelectric layer and lower metallic structure. Two loading conditions were compared. A first case in which some mechanical action is applied to the bimorph of piezoelectric and steel material and a second one corresponding to a direct activation operated by the electric field through the voltage applied to the piezoelectric electrodes.

The relevant results are that crack propagation is fairly different across the steel and piezoceramic because of their different properties. In particular, in passive configuration a crack propagation through the steel easily breaks the piezoceramic if only a mechanical force is applied, speed of propagation increases and might make unstable the fracture. By converse when bending is driven by voltage a sort of “BARRIER EFFECT” is opposed by the piezoelectric layer because of a superposition of phenomenon. Local distribution of stress around the tip is greatly affected by the piezoelectric phenomenon, which can reduce the capability of material to allow cracking. In some cases starching of the piezoelectric layer increases its stiffness and toughness, by reducing the crack propagation. Somehow proximity of crack tip to free surface with concentrated electric charges seems to be favorable to reduce the crack propagation. This phenomenon looks the most original observation of this study, which simultaneously assessed a suitable numerical tool for fracture analyses, A deep experimental validation of specimens of smart composite is required to confirm the above described prediction. To develop this task a dedicated design of experiments is required as well as a suitable number of specimens.

Last but not least such as experimental activity requires a suitable amount of financial supports and a tight cooperation together with a manufacturer of PZT structure. This motivation made unpractical adding this experimental validation to the first performed on

the welded joints, although the numerical predictions obtained look agreeing with some typical observations documented in the literature about the failure of PZT patches used in smart material systems.

Performing some experimental tests to validate the results in case of fracture mechanics inside piezoelectric materials, even when the piezoelectric material is cracking at the begining and also designing the specimen in the way that the boundary condition in composite specimen has a possible displacement between two layers can be considered as future work.

REFERENCES

1. G.T. Hahn, B. L. Averbach, W. S Owen, and M. Cohen. “Fracture”. *MIT press*. Swampscott. MA. p.91, 1959.
2. E. Smith, “Nucleation of Cleavage Cracks in Solids – Fracture at Screw Dislocation Pile-ups”. Volume 1 Issue, pp. 119-121, 1967.
3. Y.Q. Chen, S.P. Pan, M.Z. Zhou, D.Q. Yi and Y.F. Xu. “Effects of inclusions, grain boundaries and grain orientations on the fatigue crack initiation and propagation behavior of 2524-T3 Al alloy”. *Materials Science & Engineering* A vol. 580. pp. 150-158, 2013.
4. Ted L. Anderson. “Fracture Mechanics: Fundamentals and Application”. *Taylor and Francis publishing*, Florida, 2004.
5. A. Chabot, M. Hun and F. Hammoum. “Determination of energy release rate for a mixed-mode deboning test for composite pavements”. *6th International Symposium on defect and Material Mechanics*, Centrale Nantes, France, July 1-3, 2013.
6. G.R. Irwin. “Fracture. Encyclopedia of physics (handbuch der Physic)”. Vol VI, Flugge (Ed.), *Springer Verlag*, Berlin, pp. 551-590, 1985.
7. A.A. Griffith. “The phenomena of rupture and flows in solids”. *Phil. Trans. Roy. Soc*. London, A221: 163-197, 1921.
8. H.A. Wood and R.M. Engle. “USAF Damage Tolerance Design Handbook”. *Report AFFDL-TR-79-3021*, United Air Force, Ohio, 1971.
9. T. Yasuoka, Y. Mizutani and A. Todoroki. “Small scale yielding conditions for steep residual stress distribution”. *Engineering Fracture Mechanics*, 96, pp. 392–400, 2012.
10. http://www-mdp.eng.cam.ac.uk/
11. G. Legrain, N. Moes, E. Verron. “Stress analysis around crack tips in finite strain problems using the extended Finite Element Method”. *International Journal for Numerical Methods in Engineering* 63, 2, pp. 290 – 314, 2005.

12. G.R. Irwin. “Plastic zone near a crack and fracture toughness”. *Proc. 7th Sagamore Conference*, IV-63, New york, August 16-19, 1960.
13. P.A. Lagace. “Plane Stress and Plane Strain”. *Lecture note Aeronautics & Astronautics and Engineering Systems*, MIT, 2001.
14. Meyers and Chawla. “Mechanical Behavior of Materials”. *Cambridge University Press*, New york, 2009.
15. S.K. Kudari and K.G. Kodancha. “3D finite element analysis on crack-tip plastic zone”. *International Journal of Engineering, Science and Technology*, Vol. 2, No. 6, pp. 47-58, 2010.
16. J. Kert´esz and H.J. Hermann. “Stability analysis of crack propagation”. *Physica A*, 178, pp. 227-235, 1991.
17. P. Ljustell. “Fatigue crack growth experiments and analyses-from small scale to large scale yielding at constant and variable amplitude loading”. *Doctoral Thesis*, KTH University, Sweden, 2013.
18. A.G. Miserez. “Fracture and Toughening of High volume Fracture Ceramic Particle Reinforced Metals”. *Doctoral Thesis*, Lausanne, EPFL, 2003.
19. P.C. Paris and F. Erdogan. “A critical analysis of crack propagation laws”. *J. Basic Eng*. 85, pp. 528–534, 1960.
20. http://www-materials.eng.cam.ac.uk
21. K. Wallin. “Fracture Toughness of Engineering Materials – estimation and application”, *EMAS publishing*, Engelska, 2011.
22. M.J. Patr´ıcio Dias. “Crack propagation on highly heterogeneous composite materials”. *Doctoral Thesis*, Technische Universiteit Eindhoven, 2008.
23. H.M. Westergaard. “Bearing Pressures and Cracks”, *Journal of Applied Mechanics*, Vol. 6, pp.49-53, 1939.
24. http://www.efunda.com
25. S. Al Laham. “Structural Integrity Branch, Stress Intensity Factor and Limit Load”. *British Energy Generation Ltd. Handbook*, United Kingdom, 1998.
26. http://en.wikipedia.org/wiki/Fracture_toughness
27. A.R. Boccaccini, S. Atiq, D.N. Boccaccini, I. Dlouhy and C. Kaya. “Fracture behaviour of mullite fibre reinforced-mullite matrix composites under quasi-static and ballistic impact loading”. *Composites Science and Technology*, 65, pp. 325–333, 2005.

28. J. Phalippou, T. Woignier and R. Rogier. “Fracture toughness of silica aerogels”. *Journal de Physique Colloques*, 50, C4–191, 1989.
29. N. Recho. “Fracture mechanics and crack growth”. *Editions: John WILEY*. ISBN: 978-1-84821-306-7, Mars 2012.
30. T.D. Araújo, D. Roehl and L. Fernando Martha. “An adaptive strategy for elastic-plastic analysis of structures with cracks”. *J. Braz. Soc. Mech. Sci. & Eng*. vol.30 no.4, 2008.
31. W. Ramberg and W.R. Osgood. “Description of stress-strain curves by three parameters.” *Technical Note, National Advisory Committee For Aeronautics*, Washington DC, 1943.
32. M. Fashang, D. Xiaomin, A. Micheal. “Sutton and James Newman. A CTOD based mixed-mode fracture criterion, mixed-mode crack behavior, American society for testing and materials”. West Conshohocken, pp. 86-110, 1999.
33. O. Plekhov, M. Paggi, O. Naimark and A. Carpinteri. “Dimensional analysis interpretation to grain size and loading frequency dependencies of the Paris and Wöhler curves”. *International Journal of Fatigue*. 33:477–483, 2011.
34. D. Roylance. “Fatigue”. Dept of Material science and Eng, MIT, Cambridge, 2001.
35. H. Tada, P.C. Paris and G.R. Irwin. “The Stress Analysis of Cracks Handbook”. *Del Research Corporation*, Hellertown, Pennsylvania, 1973.
36. M. F. Kanninen and C. H. Popelar. “Dynamic fracture mechanics in Advanced Fracture mechanics”. *Oxford University press*, New York, pp. 192-280, 1985.
37. C. Abdennour, and S.Y. Zamrik. “Prediction of Crack Initiation Direction for Surface Flaws Under Biaxial Loading”. *J. Pressure Vessel Technol*. 125(1), pp. 65-70, 2003.
38. M. Ramulu and A.S. Kobayashi, “Strain energy density fracture criterion in elastodynamic mixed mode crack propagation”. *Engineering Fracture mechanics*, 18, pp. 1087-1098, 1983.
39. K.B. Broberg. “On crack paths”. *Engineering Fracture Mechanics*, Vol. 28, No. 5-6, pp. 663-679, 1987.
40. W. Wang. “Smart materials”. *Lecture note*, University of Washington, 2008.
41. Y. Shindo, Professor, M. Oka and K. Horiguchi. “Analysis and Testing of Indentation Fracture Behavior of Piezoelectric Ceramics Under an Electric Field”. *J. Eng. Mater. Tech*, 123(3), pp. 293-300, 2001.

42. B. Lawn. “Fracture of Brittle solids”. *Cambridge University Press.* Cambridge, 1993.
43. A.R. Ingraffea. “Theory of Crack initiation and propagation in rock. In: Fracture Mechanics of Roc”. *Atkinson B.K. (Ed.), Academic Press*, London, pp. 71-110, 1987.
44. D.D. Pollard and G. Holzhausen. “On the mechanical interaction between a fluid-filled fracture and the earth's surface”. *Tectonophysics*, 53, pp. 27-57, 1979.
45. A.R. Ingraffea. “Mixed-mode crack propagation in mortar and concrete”. *Report No. 81-13*: Department of Structural Engineering, Cornell University, 1983.
46. L.C. Murdoch. “Hydraulic fracturing of soil during laboratory experiments”. *Propagation. Geo technique*, 43, pp. 267–276, 1993.
47. R.M. McMeeking. “Crack Tip Energy Release Rate for a Piezoelectric Compact Tension Specimen”. *Eng. Fract. Mech,* 64, pp. 217–244, 1999.
48. Y.M. Desai, T.I. Eldho and A.H. Shah. “Finite Element Method with applications in engineering”. *Pearson Education India,* 2011.
49. Y. Liu. “An Introduction to the Boundary Element Method (BEM) and Its Applications in Engineering”. *CAE Research Lab*, University of Cincinnati Cincinnati, Ohio, U.S.A. 2013
50. S.R. Idelsohn , E. Oñate , N. Calvo and F. Pin. “The meshless finite element method”. *Iternational Journal for Numerical Methods in Engineerin*. vol. 58-4, 2003.
51. A. Ahmed. “eXtended Finite Element Method (XFEM)- Modeling arbitrary discontinuities and Failure analysis”. *Master Thesis*, Universit a degli Studi di Pavia, 2009.
52. L. Gavete, F. Michavila, F. Díez. “A new singular finite element in linear elasticity”. *Computational Mechanics*, Volume 4, Issue 5, pp 361-371, 1989.
53. B. Davis, “Simulation of Arbitrary Delamination Growth in Composite Structures Using the Virtual Crack Extension Method”, *27th Technical Conference of the American Society for Composites*, Texas, 2012.
54. D. Potyondy, P. Wawrzynek, and A. Ingraffea, “Discrete crack growth analysis methodology for through cracks in pressurized fuselage structures,” *Int J Numerical Meth Engng*, 38, pp. 1611-1633, 1995.

55. F. Pengcheng, S.M. Johnson, R.R. Settgast and C.R. Carrigan. “Generalized displacement correlation method for estimating stress intensity factors”. *Engineering Fracture Mechanics*, Volume 88, pp. 90–107, 2012.
56. D.M. Parks. “The virtual crack extension method for nonlinear material behavior”. *Computer Methods in Applied Mechanics and Engineering*, Volume 12, pp. 353–364, 1977.
57. E. F. Rybicki and M. F. Kanninen. “Finite-element calculation of stress intensity factors by a modified crack closure integral”. *Engineering Fracture Mechanics*, 9(4), pp. 931-938, 1977.
58. A. Miravete and M.A. Jiménez. “Application of the finite element method to prediction of onset of delamination growth”. *Appl. Mech.* Rev. 55(2), pp. 89-106, 2002.
59. D. Lebaillif, X. Zhang and N. Recho. “Use of a Crack Box Technique for Crack Bifurcation in Ductile Material”. *Proceedings of the 16th European Conference of Fracture*, Alexandroupolis, Greece, July 3-7, 2006.
60. W.S. Gan. “Acoustical Imaging: Techniques and Applications for Engineers”. *John Wiley & Sons*, Chichester, 2012.
61. A. Ern, J.L. Guermond, “Theory and practice of finite elements”, *Springer*, New york, 2004.
62. A. Becker. “The Boundary Element Method in Engineering”. *McGraw-Hill publisher*. London, 1992.
63. 63. http://www.suppliersonline.com (Metal Suppliers)
64. D. Lebaillif , S. Ma, M. Huther, H.P. Lieurade, E. Petitpas and N. Recho “Fatigue Crack Propagation and Path Assessment in Industrial Structures”. *International conference on Fatigue Crack Path/FCP*, 18-20 September, Parma, Italy, 2003.
65. R. Juvinall, K. Marshek. “Fundamentals of Machine Component Design”, *John Wiley & Sons Inc*, 5th Ed, New York, 2011.
66. A.S. Kobayashi, S.T. Chiu, R. Beeuwkes. “A numerical and experimental investigation on the use of Jintegral”. J Appl Mech, 15:293–305, 1973.
67. D. Kwiatkowski, H. Dębski. “Numerical Simulation of Cracking Process of polymer Composites on Examples of SENB Sample”. *Kompozyty* 11:4, 299-303, 2011.
68. G. Venkatachalam, R. Harichandran, S. Rajakumar, C. Dharmaraja and C. Pandivelan. “Determination of J-integral and stress intensity factor using the

commercial FE software ABAQUS in austenitic stainless steel (AISI 304) plates". *Int. J. Advanced Manufacturing Technology*, 1-4, 2008.

69. S. Kalpakjian and S. Schmid. "Manufacturing Processes for Engineering Materials". *Pearson Education*, 5th edition, Singapore, 2008.
70. G. Nikolaev, S.A. Kurkin, and V.A. Vinokurov. "Raschet, proektirovanie Iizgotovlenie svarnykh konstruktsii". *Moskovskoe vysshee tekhnicheskoe uchilishche*, Moscow, 1971.
71. A. Mukhtar, H. Biermann, P. Hübner and S. Henkel. "Fatigue Crack Propagation Life Calculation in Welded Joints". *International Conference on Crack Paths*, Vicenza, Italy, 23 - 25 September, 2009.
72. M. Faraldi. "Fatigue life of welded joints as function of their singularity degree". *Master Thesis*, Politecnico di Torino, 2013.
73. T. Lassen and N. Recho. "Proposal for a more accurate physically based S–N curve for welded steel joints". *International Journal of Fatigue*. 31(1), pp, 70-78, 2009.
74. T. Lassen and N. Recho. "Fatigue Life Analyses of Welded Structures: Flaws". *Wiley-ISTE.* Oakland, CA, 2006.
75. http://accuratus.com (Accuratus Corporation)
76. M. Schwartz. "Smart Materials", *CRC Press*. Boca Raton, 2009.
77. http://bme240.eng.uci.edu (Clinical Medicine website-University of California)
78. S. Moheimani, and A. Fleming. "Piezoelectric Transducers for Vibration Control and Damping", *Springer*, London, 2006.
79. S. Fujishima. "The History of Ceramic Filters", *IEEE Transactions on Ultrasonics, Ferroelectrics, and Frequency Control*, 47(1), pp. 1–7, 2000.
80. J. Nuffer and T. Bein. "Application of Piezoelectric materials in Transportation Industry" *Global Symposium on Innovative Solutions for the Advancement of the Transport Industry*, 4-6. San Sebastian, Spain, October 2006.
81. http://www.noliac.com/Application_overview-161.aspx
82. S.C. Abrahms and E.T. Kave, Ferroelectrics 2, 1971.
83. http://dspace.jorum.ac.uk
84. D. van den Ende, W. Groen and S. van der Zwaag. "The effect of calcining temperature on the properties of 0-3 piezoelectric composites of PZT and a liquid crystalline thermosetting polymer". *Journal of Electroceramics*, 27, 1. 13-19, 2010.

85. O. Kenji, O. Hiroji and K. Keiko. “Properties and Structural Applications of Poly Vinylidene Fluoride”. *Journal on Applied Physics*, 81, 2760, 1996.
86. Q. Zhang, V. Bharti, G. Kavarnos and M Schwartz. “Poly Vinylidene Fluoride (PVDF) and its Copolymers”. *Encyclopedia of Smart Materials; John Wiley & Sons*. Volumes 1-2, pp. 800- 825, 2002.
87. www.coleparmer.co.uk (Cole.Parmer group)
88. www.sustainable-desalination.net (Membranes & Sustainable Desalination Research Group)
89. X. XU, H. Wu and C. Zhang and Z. Jin. “Morphhological properties of ALN piezoelectric thin films deposited by DC reactive magnetron sputtering”, *Thin Solid Films* 388,pp.62-67, 2001.
90. P.Muralt, J. Antifacos and M. Cantoni, “Is there a better material for thin film BAW application than ALN?”, *IEEE Ultrasonic Symposium* 1, pp.315-320, 2005.
91. D. A. Dubois and P. Muralt, “Stress and piezoelectric properties od ALN thin films deposited onto metal electrodes by pulsed direct current reactive sputtering”, *Journal of Applied Physics* 89, pp.6389-6395, 2001.
92. A. Andrei, K. Krupa, P. Delobelle, L. Hirsinger, M. Jozwik, C. Gorecki and L. Nieradko, “ALN as an actuation material for MEM applications: the case of ALN driven multilayered cantilivers”, *Sensor and Actuators* A 141,pp.565-576, 2008.
93. T. Palacios, f. Calle, E. Monroy, J. Grajal, M. Eickhoff, C.prieto, “Nanotechnology for SAW devices on ALN epilayers”, *Material Science and Engineering* B93, pp154-158, 2002.
94. Wikipedia.org/wiki/Aluminium_nitride (Aluminum Nitride Accuratus. Retrieved 01, 2014)
95. S. Choi, H. Im and J. Kim. “The thermal conductivity of embedded nano-aluminum nitride-doped multi-walled carbon nanotubes in epoxy composites containing micro-aluminum nitride particles”. *Nanotechnology,* vol. 23 issue 6, pp. 065303-065303, 2012.
96. G.H. Haertling. “Ferroelectric Ceramics: History and Technology”. *J. Am. Ceram. Soc*, 82 (4), pp. 797-818, 1999.
97. Alexander K. Tagantsev, L. Eric Cross, Jan Fousek. “Fundamentals of Ferroic Domain Structures”. *Domains in Ferroic Crystals and Thin Films*, pp 11-107, 2010.

98. B.D. Liu. “Microstructural Defects in Ferroelectrics and Their Scientific Implications”. *State Key Laboratory of Crystal Materials*, Shandong University, Shandong, 2011.

99. Caglar, Y. “Crystalline structure and morphological properties of undoped and Sn doped ZnO thin films”. *Superlattices and Microstructures*, 46 (3), pp. 469-475, 2009.

100. M. Komatsu, N. Ohashi, I. Sakaguchi, S. Hishita and H. Haneda. “GaN solubility limit in co-implanted ZnO measured by secondary ion mass spectrometry” *applied Surface Sience*, 189 pp.349-452, 2002.

101. S. Tuzemen. G. Xiong, J.Wilkinson, B.Mischuck, K.B. Ucer and R. T. Williams, “Production and properties of p-n junctions in reactively sputtered ZnO” *Physica*, B. 308-310m pp.1197-1200, 2001.

102. R. Brook. “Concise Encyclopedia of Advanced Ceramic Materials”. *The MIT Press*, Cambridge.1991.

103. R. Riedel and I.W. Chen. “Ceramics Science and Technology: Materials and Properties”. Wiley-VCH, vol. 2, Weinheim, Germany, 2010.

104. Z. Wang and J. Song. “Piezoelectric Nano generators Based on Zinc Oxide Nanowire Arrays”, *Science* Vol. 312, pp.242-245, 2006.

105. www.webelements.com (WebElemnts group)

106. J. Schwartz, J. Perez and Y. Mo. “Growth and Characterization of Wide Band Gap Semiconductors (Zinc Oxide, Zinc Sulfide)”. *American Physical Society (APS)*, Texas, 2007.

APPENDIX A

The python code, which is used to model the crack propagation inside the piezoelectric specimen inside the ABAQUS.

```
*Heading
** Job name: Crack-propagation Model name: Model-1
** Generated by: Abaqus/CAE 6.12-1
*Preprint, echo=NO, model=NO, history=NO, contact=NO
**
** PARTS
**
*Part, name=crack
*End Part
**
*Part, name=plate
*Node
      1,          180.,           0.
      2,          180.,           1.
       .
       .
   7420,           0.,          39.
   7421,           0.,          40.
*Element, type=CPE4E
  1,    1,    2,   43,   42
  2,    2,    3,   44,   43
   .
   .
7199, 7378, 7379, 7420, 7419
7200, 7379, 7380, 7421, 7420
*Nset, nset=_PickedSet3, internal, generate
   1,  7421,     1
*Elset, elset=_PickedSet3, internal, generate
   1,  7200,     1
*Nset, nset=_PickedSet5, internal, generate
   1,  7421,     1
*Elset, elset=_PickedSet5, internal, generate
   1,  7200,     1
*Nset, nset=_PickedSet9, internal, generate
   1,  7421,     1
*Elset, elset=_PickedSet9, internal, generate
   1,  7200,     1
*Orientation, name=Ori-2
        1.,          0.,          0.,          0.,          1.,          0.3,                    0.
** Section: plate
*Solid Section, elset=_PickedSet3, orientation=Ori-2, material=pzt
1.,
*End Part
**
```

```
** ASSEMBLY
**
*Assembly, name=Assembly
**
*Instance, name=crack-1, part=crack
*End Instance
**
*Instance, name=plate-1, part=plate
*End Instance
**
*Nset, nset=_PickedSet6, internal, instance=plate-1, generate
   1,  7421,     1
*Elset, elset=_PickedSet6, internal, instance=plate-1, generate
   1,  7200,     1
*Nset, nset=_PickedSet8, internal, instance=plate-1
 3731,
*Nset, nset=_PickedSet9, internal, instance=plate-1
 6971,
*Nset, nset=_PickedSet10, internal, instance=plate-1
 411,
*Enrichment, name=Crackpiezo, type=PROPAGATION CRACK, elset=_PickedSet6, interaction=IntProp-
1
*End Assembly
**
** MATERIALS
**
*Material, name=pzt
*Damage Initiation, criterion=MAXPS
90.,
*Damage Evolution, type=ENERGY, mixed mode behavior=POWER LAW, power=1.
 0.06, 0.06, 0.06
*Dielectric, type=ANISO
 7e-09,    0., 6e-09,    0.,    0., 6e-09
*Elastic, type=ORTHOTROPIC
 1.45e+11, 7.98e+10, 1.45e+11, 7.86e+10, 7.86e+10, 1.13e+11, 2.56e+10, 2.56e+10
 3.06e+10,
*Piezoelectric
0.,    0.,    0.,   14.,    0.,    0., -6.98,   14.
-6.98,    0.,    0.,    0.,    0.,    0.,    0.,    0.
0.,  14.1
**
** INTERACTION PROPERTIES
**
*Surface Interaction, name=IntProp-1
1.,
*Initial Conditions, type=ENRICHMENT
plate-1.3580, 1,Crackpiezo, -1., -1.
plate-1.3580, 2,Crackpiezo, -1., 0.
plate-1.3580, 3,Crackpiezo, 1e-06, 0.
plate-1.3580, 4,Crackpiezo, 1e-06, -1.
plate-1.3561, 1,Crackpiezo, -1.
plate-1.3561, 2,Crackpiezo, -1.
plate-1.3561, 3,Crackpiezo, 1e-06
plate-1.3561, 4,Crackpiezo, 1e-06
**
** BOUNDARY CONDITIONS
**
** Name: BC-1 Type: Displacement/Rotation
*Boundary
_PickedSet9, 2, 2
```

```
** Name: BC-2 Type: Displacement/Rotation
*Boundary
_PickedSet10, 1, 1
_PickedSet10, 2, 2
** ----------------------------------------------------------------
**
** STEP: crackgrowth
**
*Step, name=crackgrowth, nlgeom=YES, inc=100000
*Static
0.01, 1., 1e-09, 0.01
**
** LOADS
**
** Name: Force   Type: Concentrated force
*Cload
_PickedSet8, 2, -250.
**
** INTERACTIONS
**
** Interaction: Int-1
*Enrichment Activation, name=Crackpiezo, activate=ON
**
** CONTROLS
**
*Controls, reset
*Controls, analysis=discontinuous
*Controls, parameters=time incrementation
, , , , , , , 20, , ,
**
** OUTPUT REQUESTS
**
*Restart, write, frequency=0
*Print, solve=NO
**
** FIELD OUTPUT: F-Output-1
**
*Output, field
*Node Output
CF, PHILSM, PSILSM, RF, U
*Element Output, directions=YES
LE, PE, PEEQ, PEMAG, S, STATUSXFEM
*Contact Output
CDISP, CSTRESS
**
** HISTORY OUTPUT: H-Output-1
**
*Output, history, variable=PRESELECT
*End Step
```

APPENDIX B

The python code, which is used to model the crack propagation inside the composite specimen (metal + ceramic) inside the ABAQUS.

```
*Heading
** Job name: bb50 Model name: Model-1
** Generated by: Abaqus/CAE 6.12-1
*Preprint, echo=NO, model=NO, history=NO, contact=NO
**
** PARTS
**
*Part, name=Part-1
*Node
      1,  0.180000007, 0.0301251542
      2,  0., 0.0301251542
       .
       .
   9044,  0.178203478, 0.0391022861
   9045,  0.179101735, 0.0391022861
*Element, type=CPE4R
   1,    1,   10,  688,  469
   2,   10,   11,  689,  688
    .
    .
8799, 9044, 9045,  545,  546
8800, 9045,  479,    8,  545
*Nset, nset=Set-3
    1,   2,   7,   8,   9,   10,   11,   12,   13,   14,   15 . . . 7044, 7045, 7046, 7047, 7048, 7050.
*Elset, elset=Set-4, generate
    1,  6600,     1
** Section: Section-2
*Solid Section, elset=Set-4, material=ceramic
0.03,
** Section: Section-1
*Solid Section, elset=Set-3, material=Material-1
0.03,
*End Part
**
*Part, name=Part-2
*End Part
**
** ASSEMBLY
**
*Assembly, name=Assembly
**
*Instance, name=Part-1-1, part=Part-1
*End Instance
**
```

```
*Instance, name=Part-2-1, part=Part-2
*End Instance
**
*Nset, nset=_PickedSet8, internal, instance=Part-1-1
 7,
*Nset, nset=_PickedSet9, internal, instance=Part-1-1
 4,
*Nset, nset=_PickedSet10, internal, instance=Part-1-1
 3,
*Nset, nset=_PickedSet11, internal, instance=Part-1-1, generate
    1,  9045,     1
*Elset, elset=_PickedSet11, internal, instance=Part-1-1, generate
    1,  8800,     1
*Enrichment, name=Crack-1, type=PROPAGATION CRACK, elset=_PickedSet11, interaction=IntProp-1
*End Assembly
**
** MATERIALS
**
*Material, name=Material-1
*Damage Initiation, criterion=MAXPS
 7.45e+08,
*Damage Evolution, type=ENERGY, mixed mode behavior=POWER LAW, power=1.
 11904.7, 11904.7, 11904.7
*Damage Stabilization
1e-05
*Density
7850.,
*Elastic
 2.1e+11, 0.29
*Plastic
    4e+07,    0.
  2.2e+08, 0.001
  4.5e+08, 0.002
  6.6e+08, 0.003
    9e+08, 0.004
 1.15e+09, 0.005
 1.35e+09, 0.006
 1.46e+09, 0.007
  1.5e+09, 0.008
 1.52e+09, 0.009
 1.53e+09,  0.01
 1.54e+09, 0.015
 1.55e+09,  0.02
*Material, name=ceramic
*Damage Initiation, criterion=MAXPS
 3.6e+08,
*Damage Evolution, type=ENERGY, mixed mode behavior=POWER LAW, power=1.
 20.46, 20.46, 20.46
*Damage Stabilization
1e-05
*Density
3300.,
*Elastic
 3.3e+11, 0.24
**
** INTERACTION PROPERTIES
**
*Surface Interaction, name=IntProp-1
1.,
*Surface Interaction, name=IntProp-2
```

```
1.,
*Initial Conditions, type=ENRICHMENT
Part-1-1.2356, 1,Crack-1, -0.000350001, 8.34371e-05
Part-1-1.2356, 2,Crack-1, 0.000549999, 8.34361e-05
Part-1-1.2356, 3,Crack-1, 0.000563636, -0.000829448
Part-1-1.2356, 4,Crack-1, -0.000336364, -0.000829447
Part-1-1.2556, 1,Crack-1, -0.000336364
Part-1-1.6356, 4,Crack-1, -6.36354e-05
Part-1-1.6556, 1,Crack-1, -6.36354e-05
Part-1-1.6556, 2,Crack-1, 0.000836361
Part-1-1.6556, 3,Crack-1, 0.000849999
Part-1-1.6556, 4,Crack-1, -5.00008e-05
**
** BOUNDARY CONDITIONS
**
** Name: BC-1 Type: Displacement/Rotation
*Boundary
_PickedSet9, 1, 1
_PickedSet9, 2, 2
** Name: BC-2 Type: Displacement/Rotation
*Boundary
_PickedSet10, 2, 2
**
** STEP: Step-1
**
*Step, name=Step-1, nlgeom=YES, inc=100000
*Dynamic
0.01,2.,1e-09
**
** LOADS
**
** Name: Load-1   Type: Concentrated force
*Cload
_PickedSet8, 2, -50000.
**
** CONTROLS
**
*Controls, reset
*Controls, parameters=time incrementation
8, 10, , , , , , 20, , ,
**
** OUTPUT REQUESTS
**
*Restart, write, frequency=0
*Print, solve=NO
**
** FIELD OUTPUT: F-Output-1
**
*Output, field
*Node Output
A, CF, PHILSM, PSILSM, RF, U, V
*Element Output, directions=YES
LE, PE, PEEQ, PEMAG, S, STATUSXFEM
*Contact Output
CDISP, CSTRESS
**
** HISTORY OUTPUT: H-Output-1
**
*Output, history, variable=PRESELECT
*End Step
```

APPENDIX C

The python code, which is used to model the welded structure inside the ABAQUS to analysis the Stress Intensity factor and J-Integral.

```
*Heading
** Job name: 111 Model name: Model-1
** Generated by: Abaqus/CAE 6.12-1
*Preprint, echo=NO, model=NO, history=NO, contact=NO
**
** PARTS
**
*Part, name=Part-1
*End Part
**
** ASSEMBLY
**
*Assembly, name=Assembly
**
*Instance, name=Part-1-1, part=Part-1
*Node
      1, 0.0250000004, -0.0319999754
      2,          0., -0.0319999754
       .
       .
  20813, 0.0345993713, -0.00146585598
  20814, 0.0343711637, -0.00137293909
*Element, type=CPS4R
  1,    1,   24, 1560,  107
  2,   24,   25, 1561, 1560
   .
   .
20350,    19,    19, 18757, 18764
20351,    19,    19, 18764,  1421
*Element, type=CPS3
18087, 18797, 18789, 18786
*Nset, nset=Set-1, generate
     1,  20814,      1
*Elset, elset=Set-1, generate
     1,  20351,      1
** Section: Section-1
*Solid Section, elset=Set-1, material=Material-1
0.06,
*End Instance
**
*Nset, nset=_PickedSet79, internal, instance=Part-1-1
 19,
*Nset, nset=_PickedSet80, internal, instance=Part-1-1
 19,
```

```
*Nset, nset=Set-62, instance=Part-1-1
   2,   3,   6,   8,   9,  12,  23,  47,  48,  49,  50,  51,  52,  53,  54,  55
  56,  57,  58,  59,  60,  61 … 1499, 1500, 1501, 1502, 1503, 1504, 1505, 1506, 1507.
*Elset, elset=Set-62, instance=Part-1-1
   24,   48,   72,   96,  120,  144,  168,  192,  216,  240,  264,  288,  312,  336,  360,  384
  408,  432,  456,  480,  504,  528 . . . 19214, 19238, 19262, 19286, 19310, 19334
*Elset, elset=_Surf-4_S4, internal, instance=Part-1-1, generate
 1609,  7567,   331
*Elset, elset=_Surf-4_S3, internal, instance=Part-1-1, generate
 17798,  17827,      1
*Surface, type=ELEMENT, name=Surf-4
_Surf-4_S4, S4
_Surf-4_S3, S3
*End Assembly
**
** MATERIALS
**
*Material, name=Material-1
*Elastic
 2.1e+11, 0.3
**
** BOUNDARY CONDITIONS
**
** Name: BC-1 Type: Symmetry/Antisymmetry/Encastre
*Boundary
Set-62, PINNED
**
** STEP: Step-1
**
*Step, name=Step-1, inc=100000
*Static
0.1, 1., 1e-05, 0.1
**
** LOADS
**
** Name: Load-1   Type: Pressure
*Dsload
Surf-4, P, -1.5e+08
**
** OUTPUT REQUESTS
**
*Restart, write, frequency=0
**
** FIELD OUTPUT: F-Output-1
**
*Output, field, variable=PRESELECT
*Output, history, frequency=0
**
** HISTORY OUTPUT: H-Output-1
**
*Contour Integral, crack name=H-Output-1_Crack-1, contours=5, crack tip nodes, type=K FACTORS,
direction=MERR
_PickedSet79, _PickedSet80, 0., -1., 0.
*End Step
```

APPENDIX D

Matlab code, which is used to calculate different fracture mechanics parameters in case of welded structure according to the ABAQUS results.

```
%%%%%%%%%% J-INTEGRAL %%%%%%%%%%%%
%IT'S NECESSARY TO GIVE FILENAME.*** IN THE CORRECT ZONE
format short e
clear all
clc
close all
%%%%%%%%%%%%%%%%%PLANE STRESS%%%%%%%%%%%%%%%
%%GENERAL DATA
v= 0.36 ; %POISSON COEFFICIENT
E= 2300 ; % YOUNG MODULUS [MPa]
op=0 ; % OPENING ANGLE [degree]
lambda=0.5; %DEGREE OF SINGULARITY
ray=[1;1.1;1.2;1.3;1.55;1.8;2.05;2.3;2.8;3.3]; %VECTOR OF MESH RADIUS
results=xlsread('SPECIMEN_CRACK.xlsx','STRESS'); %READING RESULTS
FROM EXCEL
psi=pi/2; %ANGLE FROM CRACK AND CAE
FRAME
Annexe I
A2
cont=0; %INITIALIZATION
%% CYCLES OF ALL COMBINATION
for kk=10:-1:1
r=ray(kk); %RADIUS OF FEM COMPUTATION
%DATA ACQUISITION FROM MATRIX RESULTS
dist=results(:,1);
Ux= results(1:end,(kk*5-3)); %X DISPLACEMENT
Uy= results(1:end,(kk*5-3)+1);% Y DISPLACEMENT
Sx= results(1:end,(kk*5-3)+2); % STRESS ALONG X AXIS
Sy= results(1:end,(kk*5-3)+3); % STRESS ALONG Y AXIS
Sxy= results(1:end,(kk*5-3)+4); % STRESS ALONG XY DIRECTION
for ww=(kk-1):-1:1;
ra=ray(ww); % RADIUS OF ASYMPTOTIC
COMPUTATION
cont=cont+1;
%%%%%%%%%% J FEM COMPUTATION
%%GEOMETRY CONSIDERATION
n=size(Ux,1); %NUMBER OF DIVISION
cpsi=cos(psi);
spsi=sin(psi);
```

```
op=op*pi/180;
b=2*pi-op;
for i=1:n %ANGLE TETA OF EACH DATA
teta(i)=dist(i)*b+op/2-pi;
end
deltax=zeros(n,1);
deltay=zeros(n,1);
dteta=zeros(n,1);
dl=zeros(n,1);
for i=1:n-1 % ANGLE BETWEEN EACH DATA
dteta(i)=teta(i+1)-teta(i);
dl(i)= dteta(i)*r; %ARC LENGHT
deltax(i)=dl(i)*cos(dteta(i)); %X DISTANCE IN CRACK FRAME
deltay(i)=dl(i)*sin(dteta(i)); %Y DISTANCE IN CRACK FRAME
end
dteta(n)=dteta(n-1);
dl(n)=dl(n-1);
deltax(n)=deltax(n-1);
deltay(n)=deltay(n-1);
deltaX=cpsi*deltax-spsi*deltay; %X DISTANCE IN CAE FRAME
deltaY=cpsi*deltay+spsi*deltax; %Y DISTANCE IN CAE FRAME
%STRAIN COMPUTATION FROM DISPLACEMENT
Ex=zeros(n,1);
Ey=zeros(n,1);
Exy=zeros(n,1);
for i=1:n-1
Ex(i)= (Ux(i+1)-Ux(i))/deltaX(i);
Ey(i)= (Uy(i+1)-Uy(i))/deltaY(i);
Exy(i)=0.5*((Ux(i+1)-Ux(i))/deltaY(i)+(Uy(i+1)-Uy(i))/deltaX(i));
end
Ex(n)=Ex(n-1);
Ey(n)=Ey(n-1);
Exy(n)=Exy(n-1);
Annexe I
A3
%J COMPUTATION
W=0.5*(Sx.*Ex+Sy.*Ey+2*Exy.*Sxy);
W2=W.*deltay;
T=Sx.*cpsi.*Ex.*deltaY+Sx.*spsi.*Exy.*deltaY+Sxy.*cpsi.*Exy.*deltaY+Sxy.*sp
si.*Ey.*deltaY -
(Sxy.*cpsi.*Ex.*deltaX+Sxy.*spsi.*Exy.*deltaX+Sy.*cpsi.*Exy.*deltaX+Sy.*sps
i.*Ey.*deltaX);
J=W2-T;
JFEM(cont)=sum(J);
%%ASYMPTOTICAL DEDUCTION
Uxa=Ux*((ra/r)^lambda);
Uya=Uy*((ra/r)^lambda);
Sxa=Sx*((ra/r)^lambda);
Sya=Sy*((ra/r)^lambda);
Sxya=Sxy*((ra/r)^lambda);
dista=dist;
for i=1:n %ANGLE TETA OF EACH DATA
tetaa(i)=dista(i)*b+op/2-pi;
end
deltaxa=zeros(n,1);
```

```
deltaya=zeros(n,1);
dtetaa=zeros(n,1);
dla=zeros(n,1);
for i=1:n-1 % ANGLE BETWEEN EACH DATA
dtetaa(i)=teta(i+1)-teta(i);
dla(i)= dtetaa(i)*r; %ARC LENGHT
deltaxa(i)=dla(i)*cos(dtetaa(i)); %X DISTANCE IN CRACK FRAME
deltaya(i)=dla(i)*sin(dtetaa(i)); %Y DISTANCE IN CRACK FRAME
end
dtetaa(n)=dtetaa(n-1);
dla(n)=dla(n-1);
deltaxa(n)=deltaxa(n-1);
deltaya(n)=deltaya(n-1);
deltaXa=cpsi*deltaxa-spsi*deltaya; %X DISTANCE IN CAE FRAME
deltaYa=cpsi*deltaya+spsi*deltaxa; %Y DISTANCE IN CAE FRAME
%STRAIN COMPUTATION FROM DISPLACEMENT
Exa=zeros(n,1);
Eya=zeros(n,1);
Exya=zeros(n,1);
for i=1:n-1
Exa(i)= (Uxa(i+1)-Uxa(i))/deltaXa(i);
Eya(i)= (Uya(i+1)-Uya(i))/deltaYa(i);
Exya(i)=0.5*((Uxa(i+1)-Uxa(i))/deltaYa(i)+(Uya(i+1)-Uya(i))/deltaXa(i));
end
Exa(n)=Exa(n-1);
Eya(n)=Eya(n-1);
Exya(n)=Exya(n-1);
%J COMPUTATION
Wa=0.5*(Sxa.*Exa+Sya.*Eya+2*Exya.*Sxya);
W2a=Wa.*deltaya;
Annexe I
A4
Ta=Sxa.*cpsi.*Exa.*deltaYa+Sxa.*spsi.*Exya.*deltaYa+Sxya.*cpsi.*Exya.*delta
Ya+Sxya.*spsi.*Eya.*deltaYa -
(Sxya.*cpsi.*Exa.*deltaXa+Sxya.*spsi.*Exya.*deltaXa+Sya.*cpsi.*Exya.*deltaX
a+Sya.*spsi.*Eya.*deltaXa);
Jaa=W2a-Ta;
JA(cont)=sum(Jaa);
end
end
JFEM
JA
Jratio=JFEM./JA;
figure
plot(JFEM)
hold on
plot(JA,'r')
title 'PLANE STRESS JA-JEM CRACK'
legend 'Jfem' 'Ja'
xlabel 'Combinations of contours'
ylabel 'J value [MPamm]'
figure
plot(Jratio)
title 'PLAINE STRESS J RATIO CRACK'
xlabel 'Combinations of contours'
```

```
ylabel 'Ratio between FEM and asymptotic'
figure
plot(JFEM/0.00055)
title 'RATIO WITH ABAQUS RESULTS'
xlabel 'Combinations of contours'
ylabel 'Ratio between FEM and Abaqus'
clear all
%%%%%%%%%% PARIS COEFFICIENTS %%%%%%%%%%%
%%%%%%%%II APPROACH J-INTEGRAL%%%%%%%%%%%%
format short e
clear all
clc
close all
%DATA READING
%Experimental results loading and data definitions
results=xlsread('RESULTS_A.xlsx','NOUT');
results=abs(results);
nn=size(results,2);
E=210000; %YOUNG MODULUS [MPa]
v=0.3; %POISSON MODULUS
i=1;
ind=1;
sigma=150 ; %AXIAL STRESS [MPa]
partition=[0.95,0.8,0.7,0.5,0.3,0.2,0.1,0.05]; %CRACK LENGTH PARTITION
%K INTERPOLATION
k=@(x)30000000*(x.^3)-197316*(x.^2)+4249*x+7.6; %INTERPOLATING K VIA
JINTEGRAL
FUNCTION
Annexe I
A5
%DATA EXTRAPOLATION
%Creating a vector of cycles and crack length data
while i<= nn-1
crac(:,ind)=results(:,i+1)/1000;
cycl(:,ind)=results(:,i);
i=i+2;
ind=ind+1;
end
nn=size(crac,2);
mm=size(crac,1);
%%%%%%%%%%%PARIS PLOT%%%%%%%%%%%%%%%%
%Once made the numerical derivative and computed the K values the
%Paris plot of all the specimens is plotted
for i=1:nn
for j=1:mm-1
dadN(j,i)=abs((crac(j+1,i)-crac(j,i))/(cycl(j+1,i)-cycl(j,i)));
dK(j,i)=k((crac(j+1,i)+crac(j,i))/2);
end
end
dadN(j+1,:)=dadN(j,:);
dK(j+1,:)=dK(j,:);
figure
loglog(dK,(dadN),'.','MarkerSize',5)
title 'CRACK GROWTH'
ylabel 'dadN [m/cycle]'
```

```
xlabel 'deltaK[MPam^1/2]'
figure
plot(crac,dK,'.','MarkerSize',5)
title 'DELTAK IN FUNCTION OF CRACK SIZE'
ylabel 'DELTA K[MPam^1/2]'
xlabel 'Crack length [m]'
%%%%%%%%%%%%%%%%%%%%C,n
INTERPOLATION%%%%%%%%%%%%%%%%%%%%%%%%%%
%For each specimen the C ,n with R-square values are computed
%thanks to the least square methods.
%Logarithmic transformation
logda=log10(dadN);
logdk=log10(dK);
CONT=0;
%cycle for different crack lengths
for k=1:7
alfa=partition(k);
CONT=CONT+1;
%cycle for all specimens
for i=1:nn
Aproto=logdk(:,i);
Bproto=logda(:,i);
%elimination of Nan and Inf values
Aproto(isnan(Aproto))=[];
Bproto(isnan(Bproto))=[];
Aproto(isinf(Bproto))=[];
Bproto(isinf(Bproto))=[];
%setting the crack length
vita=length(Bproto);
quantile=round(vita*alfa);
Annexe I
A6
iniz=round(vita*partition(8));
%Interpolation
A=Aproto(iniz:quantile);
B=Bproto(iniz:quantile);
p=polyfit(A,B,1);
n(i)=p(1,1);
C(i)=p(1,2);
Bstim=C(i)+n(i).*A;
Bmed(i)=mean(B);
devt=(B-Bmed(i)).^2;
devsp=(Bstim-Bmed(i)).^2;
DT(i)=sum(devt);
DSP(i)=sum(devsp);
%R,n,C values
R2(i)=DSP(i)/DT(i);
A=10.^A;
B=10.^B;
Bstim=10.^Bstim;
%figure
%loglog(A,B,'*')
%hold on
%loglog(A,Bstim,'r')
clear A B Aproto Bproto p Bstim devt devst vita quantile
```

```
end
R2;
n;
C=10.^C;
meanR2(CONT)=median(R2);
meann(CONT)=median(n);
meanC(CONT)=median(C);
end
meanR2
meann
meanC
```